

Heterogenization of Molecular Electrocatalysts for Small Molecule Transformations

by

Jeremy D. Kallick

A dissertation submitted in partial fulfillment
of the requirements for the degree of
Doctor of Philosophy
(Chemistry)
in the University of Michigan
2022

Doctoral Committee:

Assistant Professor Charles C. L. McCrory, Chair
Associate Professor Neil Dasgupta
Professor Stephen Maldonado
Professor Melanie Sanford

Jeremy D. Kallick

kallick@umich.edu

ORCID iD: 0000-0002-6937-9181

© Jeremy D. Kallick 2022

Acknowledgements

The last 6 years I have spent working on my dissertation could not have been accomplished without the help and support of many exceptional individuals both within and outside of graduate school. First and foremost I would like to thank my advisor, Professor Charles C. L. McCrory, for his help, guidance, and patience throughout my PhD process. He was always willing to spend hours talking about science, the politics of graduate school, and life beyond the campus. Learning from his analytical approach to science has made me a much stronger chemist.

I would also like to thank the members of my committee: Professor Melanie Sanford, Professor Stephen Maldonado, and Professor Neil Dasgupta. Their help and guidance were instrumental in my Graduate school publications. I would also like to thank the current and past members of my lab for all the discussions, fun, and necessary beers we have had throughout the last 6 years: Dr. Chia-Cheng Lin, Dr. Yingshou Liu, Dr. Kwan Leung, Dr. Weixuan Nie, Dr. Libo Yao, Robert Bonsall, William Dean, Samuel Michaud, Taylor Soucy, Lirong Shi, Maiko Lunn, Kevin Riverva-Cruz, Jukai Zhou, Drew Tarnopol, Ammar Ibrahim, Ziqiao Xu, Weijie Feng, Grace Clinger, Lesley Escobar, and Michael Riehs. I would like to especially thank Weijie Feng for his help with interpreting XPS spectra.

The Chemistry Department staff has also been extremely helpful throughout my time here. I would like to thank the Graduate Student Coordinators Elizabeth Oxford and Katie Foster for their help in navigating the graduate school bureaucracy and making sure I always had everything I needed done mostly on time. I would like to thank Roy Wentz for his help in designing and constructing the various electrochemical cells that made my research possible. I would also like to

thank Debashish Sahu for his assistance in figuring out how to run ammonia quantification NMR, even when the instrument went down at 10:00 PM at night.

Lastly, but certainly not least, I would like to thank all of my friends and family. Their unconditional support and friendship throughout the last 6 years has made this thesis possible. Having friends to spend time with outside of the lab was an invaluable resource that made surviving graduate school possible. I would like to also acknowledge Daniel Holland who was the first friend I made in Michigan and taught me how to go sailing, Joe Meadows who helped keep me sane during the terrible combination of a pandemic *and* Graduate School, and especially Bernadette Schneider whose constant friendship and support was a blessing for which I am eternally grateful.

I would also like to include a special thanks to my undergraduate advisor Professor Mike Hill who helped and inspired me as both a researcher and a friend and is the reason I came to Graduate School in the first place.

Table of Contents

Acknowledgements.....	ii
List of Tables	viii
List of Figures.....	ix
Abstract.....	xxii
Chapter 1 : Research Motivation and Introduction to Electrode Modification with Molecular Catalysts.....	1
1.1 Introduction	1
1.2 Non-Covalent Attachment Methods.....	8
1.2.1 Physisorption	8
1.2.2 Pyrene Attachment	11
1.3 Covalent Attachment Methods.....	13
1.3.1 Pyrazine Bond Formation.....	13
1.3.2 Amide Bond Formation.....	14
1.3.3 Diazonium Coupling	16
1.3.4 Copper(I) Catalyzed Azide Alkyne Cycloaddition	18
1.3.5 Electropolymerization	21
1.3.6 Multi-Layer Approach.....	23
1.4 References	24
Chapter 2 Major Electrochemical and Surface Techniques.....	30
2.1 X-Ray Photoelectron Spectroscopy	30
2.1.1 Introduction	30

2.1.2 XPS Principles.....	31
2.1.3 Basic XPS Instrumentation.....	32
2.1.4 Modern XPS Instrumentation.....	35
2.1.5 XPS Data Analysis	37
2.1.6 XPS Relative Sensitivity Factors.....	37
2.1.7 Spin Orbit Splitting.....	38
2.1.8 ‘Shakeup’ Satellite Peaks	40
2.1.9 Determining the Baseline	41
2.1.10 Peak Fitting.....	42
2.2 Rotating Disk Electrode Voltammetry	43
2.3 Rotating Ring Disk Electrode Voltammetry	49
2.4 Additional Resources	53
2.4.1 Resources for XPS.....	53
2.4.2 Resources for Electrochemistry.....	54
2.5 References	55
Chapter 3 Controlled Formation of Multilayer Films of Discrete Molecular Catalysts for the Oxygen Reduction Reaction using a Layer-by-Layer Growth Mechanism Based on Sequential Click Chemistry	58
3.1 Preface.....	58
3.2 Abstract	59
3.3 Introduction	60
3.4 Experimental	62
3.4.1 Materials and General Instrumentation	62
3.4.2 Synthetic Procedures	64
3.4.3 General Procedure for Preparation of Modified Glassy Carbon Electrodes with Multilayer Films	66

3.4.4 XPS Measurements	69
3.4.5 Electrochemical Methods	70
3.5 Results and Discussion	71
3.6 Conclusions	84
3.7 Supplementary Information.....	85
3.7.1 Optimization of Layer-by-Layer Synthesis: SL-Cu(DEphen)	85
3.7.2 Optimization of Layer-by-Layer Synthesis: DL-Cu(DEphen).....	90
3.8 References	112
Chapter 4 Heterogenization of TEMPO for Electrocatalytic Alcohol Oxidation.....	116
4.1 Preface	116
4.2 Abstract	117
4.3 Introduction	118
4.4 Experimental Methods	120
4.4.1 Materials and General Instrumentation	120
4.4.2 Synthetic Procedures	121
4.4.3 General Procedure for Glassy Carbon Electrodes Modified with Monolayer TEMPO Films.....	123
4.4.4 Electrochemical Methods	125
4.5 Results and Discussion.....	125
4.6 Conclusions	133
4.7 References	134
Chapter 5 Selective Reduction of Aqueous Nitrate to Ammonia with an Electropolymerized Chromium Molecular Catalyst.....	136
5.1 Preface.....	136
5.2 Abstract	137
5.3 Introduction	138

5.4 Experimental	141
5.4.1 Materials and General Instrumentation	141
5.4.2 Synthetic Procedures	143
5.4.3 XPS Measurements	146
5.4.4 Electrochemical Methods	146
5.4.5 Product Detection	150
5.5 Results and Discussion	154
5.6 Conclusion	163
5.7 Supporting Information	165
5.8 References	204
Chapter 6 Conclusions and Future Directions	209
6.1 Introduction	209
6.2 Next Steps for NO ₃ RR by TPTCrCl ₃ Films	210
6.3 Alternative Catalyst Systems	215
6.4 References	218

List of Tables

Table 1.1 Redox potential (E_{cat}^0), oxygen reduction peak potential (E_{O_2}), and measured kinetic current ($\frac{i_k(E_{\text{cat}}^0)}{q_{\text{cat}}}$) of a series of 1,10-phenanthroline copper complexes adsorbed on edge plane graphite. ⁴⁴ Reproduced from J. Phys. Chem. A., 2007 , 111, 12641-12650. with permission from the American Chemistry Society.	9
Table 2.1 Spin Orbit Splitting	39
Table S3.1 Cleaning Procedures	90
Table S5.1 Average XPS ratios of p-TPTCrCl ₃ films both directly after polymerization and after a standard 2-hour electrolysis. The lack of Cl ratios for post electrolysis polymers is due to an absence of the chlorine peak in those samples. All reported values are averages of at least 3 independently prepared samples and all errors are standard deviations	178
Table S5.2 Faradaic efficiencies and current densities for the potential dependent reduction of nitrate by electropolymerized p-TPTCrCl ₃ films. All electrolyses were conducted for 2 hours in argon sparged 0.1 M pH 6 phosphate buffer containing 0.1 M Na ¹⁵ NO ₃ . The stir rate was 250 RPM. All reported values are the average of 3 independently conducted electrolyses and all errors are standard deviations. The data in this table corresponds to Figures 5.3a and 5.3b in the main text.....	180
Table S5.3 Faradaic efficiencies and current densities for the stir rate dependent reduction of nitrate by electropolymerized p-TPTCrCl ₃ films. All electrolyses were conducted for 2 hours in argon sparged 0.1 M pH 6 phosphate buffer containing 0.1 M Na ¹⁵ NO ₃ . The applied potential was -0.75 V vs RHE. All reported values are the average of 3 independently conducted electrolyses and all errors are standard deviations. The data in this table corresponds to Figures 5.3c and 5.3d in the main text.	181
Table S5.4 Faradaic efficiencies and current densities for the reduction of select NO _x species by electropolymerized p-TPTCrCl ₃ films. All electrolyses were conducted for 2 hours in argon sparged 0.1 M pH 6 phosphate buffer containing 0.1 M substrate except for the reduction of ¹⁵ NH ₂ OH•HCl which was conducted for 1 hour. The applied potential was -0.75 V vs RHE and the stir rate was 250 RPM. All reported values are the average of 3 independently conducted electrolyses and all errors are standard deviations. The data in this table corresponds to Figures 5.3e and 5.3f in the main text.....	182
Table S5.5 Activity and Selectivity Measurements of selected State-of-the-Art Solid-State Electrocatalysts for Nitrate Reduction to Ammonia ¹	202

List of Figures

- Figure 1.1** Potential dependent product distribution for CO₂RR on polycrystalline copper in aqueous electrolyte.¹⁴ Reproduced from *Energy Environ. Sci.*, **2012**, 5, 7050-7059. with permission from the Royal Society of Chemistry..... 3
- Figure 1.2** Potential dependence product distribution of the CO₂RR on silver in aqueous electrolyte.¹⁵ Reproduced from *Phys. Chem. Chem. Phys.*, 2014, 16, 13814-13819. with permission from the Royal Society of Chemistry..... 6
- Figure 1.3** Figure demonstrating proposed effects of the poly-4-vinyl pyridine on CO₂RR by CoPc including 1) pyridine coordination to the cobalt center, 2) H-bonding stabilization of the CO₂RR intermediates and 3) proton relay through the polymer film.³¹ Reproduced from *Chem. Sci.*, 2016, 7, 2506-2515. with permission from the American Chemistry Society..... 10
- Figure 1.4** Noncovalent attachment of a pyrene modified TEMPO complex to a MWCNT. 11
- Figure 1.5** Synthetic scheme for the pyrene modified iron porphyrin used by Robert and co-workers for the CO₂RR in aqueous electrolyte.⁵⁷ Reproduced from *J. Am. Chem. Soc.*, **2016**, 138, 2492-2495., with permission from the American Chemistry Society. 12
- Figure 1.6** Pyrazine conjugation between a glassy carbon electrode and a molecular catalyst containing an o-diamine moiety.⁵⁸ Reproduced from *J. Am. Chem. Soc.*, **2018**, 140, 1004-1010., with permission from the American Chemistry Society..... 14
- Figure 1.7** Amide bond formation between an amine-functionalized glassy carbon electrode and a carboxylic acid containing nickel catalyst.⁵⁹ EDC stands for 1-Ethyl-3-(3-dimethylaminopropyl)carbodiimide which is used to activate the carboxylic acid. Note that this reaction is performed in water. Reproduced from *Angew. Chem. Int. Ed.*, **2015**, 54, 12303-12307., with permission from John Wiley & Sons..... 15
- Figure 1.8** Mechanism of diazonium salt grafting of molecular complexes to glassy carbon. Note that because it is a radical based mechanism there is minimal control over the surface structure and multi-layer grafting can occur..... 16
- Figure 1.9** Diazonium salt modification of a carbon electrode with azide and ethynyl functional groups. These groups can then be used to attach complexes to the electrode using the Cu(I) Catalyzed Azide Alkyne Cycloaddition (CuAAC).⁶² Reproduced from *Chem. Eur. J.*, 2008, 14, 9286-9291., with permission from John Wiley & Sons..... 17
- Figure 1.10** Synthesis procedure for attaching Re and Mn bipyridine catalysts to glassy carbon using diazonium salt grafting. Note how the diazonium salt is formed from the parent amine

prior to surface attachment.⁶⁴ Reproduced from *ACS Appl. Mater. Interfaces.*, **2016**, 14, 4192-4198., with permission from the American Chemistry Society..... 18

Figure 1.11 A generalized reaction scheme for modification of an azide modified carbon electrode with the CuAAC “click” reaction..... 19

Figure 1.12 The proposed binuclear intermediate in the 4 e⁻ reduction of O₂ to H₂O by copper phenanthroline.⁷⁰ Reproduced from *J. Am. Chem. Soc.*, **2011**, 133, 3696-3699., with permission from the American Chemistry Society. 21

Figure 1.13 Electropolymerization of vinyl terpyridine metal complexes. 22

Figure 1.14 Polyterthiophene containing a ruthenium terpyridine catalyst. 22

Figure 2.1 Basic XPS instrumentation..... 34

Figure 2.2 A modern XPS Instrument. Reproduced from "Electron Spectroscopy for Chemical Analysis," In *Surface Analysis – The Principal Techniques 2009*, p 47-112. with permission from John Wiley and Sons.¹⁶ 35

Figure 2.3 A representative XPS spectrum from Cu₂p. Within this spectrum can be seen the following: a) the peaks arising from Cu_{2p(1/2)} energy state; b) the peaks arising from the Cu_{2p(3/2)} energy state; and c) the ‘shakeup’ satellite peaks due to the presence of Cu(II). The splitting of the peaks designated a and b are due to the presence of both Cu(I) and Cu(II) within the sample which have slightly different binding energies. The satellite peaks are a unique feature of Cu(II) and are discussed further in section 2.1.8. Note that the ratio of a to b is approximately 1:2. 40

Figure 2.4 Background fitting for a Nitrogen 1s peak using three different methods: a) Linear, b) Shirley, and c) Tougaard..... 42

Figure 2.5 Comparison of Gaussian and Lorentzian standardized line shapes..... 43

Figure 2.6 Basic construction of a rotating disk electrode..... 44

Figure 2.7 Representative rotating disk electrode voltammogram showing O₂ reduction by copper diethynylphenanthroline covalently attached to a glassy carbon electrode in pH 4.8 0.1 M acetate buffer with 1.0 M sodium perchlorate as a supporting electrolyte. 45

Figure 2.8 Diagram showing the change in measured current as a function of the applied rotation rate for a theoretical electrochemical reaction with a slow kinetic rate..... 46

Figure 2.9 Example of Koutecký-Levich analysis of a single potential of the RDEV measurement shown in Figure 2.6. Each square represents the current at a single rotation rate. The y-intercept of the best fit line is circled in blue and is the inverse of the kinetic current. 48

Figure 2.10 Potential dependent kinetic current obtained from Koutecký-Levich analysis of the RDEV measurement shown in Figure 2.6. 48

Figure 2.11 A typical rotating ring disk electrode setup showing the additional ring electrode surrounding the central disk working electrode. 49

Figure 2.12 An example RRDEV measurement for ORR by copper diethynylphenanthroline covalently attached to glassy carbon in a 100 mM acetate buffer (50 mM NaOAc•3H₂O and 50 mM HOAc) at pH 4.8 containing 1 M NaClO₄ supporting electrolyte under an O₂ atmosphere. The rotation rate was 400 RPM and the platinum ring was held at 0.73 V vs Ag/AgCl/KCl(sat.). The scan rate of 10 mV/s. The ring current is not corrected for collection efficiency ($N = 0.175$). 53

Figure 3.1 Multilayer catalyst films on electrode surfaces grown from sequential Cu(I) catalyzed Azide-Alkyne Cycloaddition (CuACC) reactions. 62

Figure 3.3 (a) Representative CVs of SL-Cu(DEphen), DL-Cu(DEphen), and TL-Cu(DEphen) film samples. The coverage of each surface was estimated by integrating the charge under the Cu^{III} redox features. (b) A box and whisker plot of coverages of the SL-Cu(DEphen), DL-Cu(DEphen), and TL-Cu(DEphen) estimated from integrated charges from cyclic voltammograms. The small white box represents the average (mean) coverage while the horizontal line represents the median value. The larger shaded box represents the coverage range in which 50% of the measurements occur, and the error bars represent the 1.5 IQR range. N is the number of coverage measurements from independently-prepared electrodes. The estimated coverage of the DL-Cu(DEphen) system is roughly double that of the SL-Cu(DEphen). However, the average coverage of the TL-Cu(DEphen) is roughly equivalent to that of the DL-Cu(DEphen). 76

Figure 3.4 Representative CVs of (a) SL-Cu(DEphen), (b) DL-Cu(DEphen), and (c) TL-Cu(DEphen) film samples under N₂ (blue line) and O₂ (red line). The large increase in the magnitude of the reductive current in the presence of O₂ is indicative of catalytic turnover. Kinetic current densities (j_K) estimated from Koutecky-Levich analysis of rotating disk voltammetry data are shown in (d) for SL-Cu(DEphen), (e) for DL-Cu(DEphen), and (f) for TL-Cu(DEphen). The central data points in each plot are the average potential-dependent j_K values, and the exterior error bars are the standard deviations at each potential. The area within the error bars is the ~68% confidence interval of the measurement set, and N is the number of j_K estimates from independently prepared electrodes in each measurement set including data collected using both Pt and BDD auxiliary electrodes. 79

Figure 3.5 (a-b) Fraction of the ORR current going to H₂O₂ production as a function of potential based on RRDE measurements at 400 rpm for (a) SL-Cu(DEphen) and (b) DL-Cu(DEphen). (c-d) Postulated mechanisms explaining the decreased H₂O₂ production observed for DL-Cu(DEphen) due to (c) increased likelihood of bimetallic activation of O₂ or (d) possibility of cascade (or tandem) catalysis involving sequential reduction of O₂ to H₂O₂ to H₂O..... 83

Figure S3.1 N:Cu ratio for SL-Cu(DEphen) electrodes synthesized with varying amounts of NaN₃ in the azidification solution used for the initial preparation of the N₃-terminated glassy carbon electrode. The ideal ratio of 5:1 is denoted by the dashed line. Based on the results 100 mg of NaN₃ was used for the optimized synthesis conditions..... 86

Figure S3.2 N:Cu ratios for SL-Cu(DEphen) synthesized with varying DMSO:H₂O ratios in the CuACC click solution. Increasing the amount of H₂O beyond a 1:1 ratio resulted in precipitation of reagents. Based on these results a DMSO:H₂O ratio of 1:1 was used in the optimized conditions. 86

Figure S3.3 N:Cu ratios for SL-Cu(DEphen) synthesized with varying copper amounts in the CuACC click solution. The concentration of copper plays a critical role in the synthesis because of the high stability of the bis Cu(DEphen)₂ complex. To promote formation of the mono complex an excess of Cu must be used. Based on these results 2.7 mg of Cu was used for the optimized conditions. 87

Figure S3.4 N:Cu ratios for SL-Cu(DEphen) synthesized using CuAAC solutions at either 0 C or room temperature (RT). Elevated temperatures (not shown) resulted in decomposition of the azide. Based on these results room temperature was used for subsequent reactions. 87

Figure S3.5 N:Cu ratios for SL-Cu(DEphen) synthesized with varying reaction times (e.g. times of exposure to the CuAAC click solution). Each CuAAC reaction was done in a separate vial to avoid contamination when removing electrodes for cleaning. Although 12 hours shows the appropriate N:Cu ratio, we used 14 hours in the optimized synthesis conditions to remain consistent with the optimized double-layer film synthesis procedure as described in Figure S3.10. 88

Figure S3.6 N:Cu ratios for SL-Cu(DEphen) synthesized with varying cleaning procedures. The four cleaning procedures 1-4 are outlined in **Table S1**. There are two points in the synthesis that require cleaning. First, after the azidification step used to prepare the N₃-terminated glassy carbon surfaces, a cleaning step is required to remove hexanes and unreacted sodium azide. Failure to clean the electrode after the azidification step resulted in the formation of precipitates in the CuAAC click solution. Second, after the CuAAC click reaction is completed, a cleaning step is required to remove any unclicked physisorbed species from the electrode surface. Based on these results cleaning procedure 3 was used in the optimized procedure. 89

Figure S3.7 NMR spectrum of 1,4-diazidobenzene in CDCl₃ showing characteristic peak at 7.02 ppm. 91

Figure S3.8 NMR depicting decomposition of 1,4-diazidobenzene to 1,4-diaminobenzene in DMSO:H₂O mixture. 1.3 mg of 1,4-diazidobenzene was first dissolved into 5 mL of DMSO, and then the resulting solution was added to 5 mL of H₂O. There was a noticeable heating of the solution upon mixing the DMSO and H₂O. The resulting 1,4-diaminobenzene was then extracted into CDCl₃. The resulting NMR shows a peak at 6.81 ppm consistent with the formation of 1,4-diaminobenzene. The peak at 7.27 is due to CDCl₃. 92

Figure S3.9 1.3 mg of 1,4-diazidobenzene was first dissolved into 5 mL of d₈-THF, and then the resulting solution was added to 5 mL of D₂O. There was no noticeable heating of the solution upon mixing the d₈-THF and D₂O. An NMR of the resulting 1:1 d₈-THF:D₂O solution shows a peak at 7.02 ppm consistent with 1,4-diazidobenzene, confirming the reactant does not decompose during mixing of these solvents. 93

Figure S3.10 N:Cu ratios for DAB terminated SL-Cu(DEphen) synthesized with varying reaction times (e.g. times of exposure to the DAB CuAAC click solution). The ideal N:Cu ratio of 9 assumes X-ray promoted photodecomposition of the terminal azide to a terminal amine. ^{38, 39} Based on these results 14 hours was used for the reaction time.	94
Figure S3.11 N:Cu ratios for SL-Cu(DEphen), DAB terminated SL-Cu(DEphen), and DL-Cu(DEphen) using the optimized conditions outlined in the experimental section of the main text as derived from the experiments in Figures S1-S10. The ideal ratios for each are denoted with a dashed line.	94
Figure S3.12 Representative scan rate dependence of a SL-Cu(DEphen) film.	95
Figure S3.13 Representative scan rate dependence of a DL-Cu(DEphen) film.	95
Figure S3.14 Representative scan rate dependence of a TL-Cu(DEphen) film.	96
Figure S3.15 Representative rotating disk electrode voltammogram of a SL-Cu(DEphen) film in a 100 mM acetate buffer (50 mM NaOAc•3H ₂ O and 50 mM HOAc) at pH 4.8 containing 1 M NaClO ₄ supporting electrolyte under an O ₂ atmosphere. A 400 RPM scan is performed at the beginning and end of the experiment to ensure stability of the film.	97
Figure S3.16 Representative rotating disk electrode voltammogram of a DL-Cu(DEphen) film in a 100 mM acetate buffer (50 mM NaOAc•3H ₂ O and 50 mM HOAc) at pH 4.8 containing 1 M NaClO ₄ supporting electrolyte under an O ₂ atmosphere. A 400 RPM scan is performed at the beginning and end of the experiment to ensure stability of the film.	98
Figure S3.17 Representative rotating disk electrode voltammogram of a TL-Cu(DEphen) film in a 100 mM acetate buffer (50 mM NaOAc•3H ₂ O and 50 mM HOAc) at pH 4.8 containing 1 M NaClO ₄ supporting electrolyte under an O ₂ atmosphere. A 400 RPM scan is performed at the beginning and end of the experiment to ensure stability of the film.	99
Figure S3.18 Control experiment in which the synthesis was stopped after the azidification step resulting in an azide terminated surface. The sonication steps in combination with exposure to light during cleaning likely resulted in the decomposition of the azides to amines prior to analysis.	100
Figure S3.19 Control experiment in which a heat-treated glassy carbon disk electrode was exposed to optimized click conditions without the azidification step. Without the azide present the click reaction cannot occur.	101
Figure S 3.20 Control experiment in which CuSO ₄ •5H ₂ O was not added to the click solution. All other steps were not changed from optimized conditions. Note that a large amount of precipitate formed when the DMSO solution and H ₂ O were mixed due to the decreased stability of the ligands in the absence of copper.	102
Figure S3.21 Control experiment in which 3,8-diethynyl-1,10-phenanthroline was not added to the click solution. All other steps were not changed from optimized conditions. Note that the	

solution was clear upon the addition of ascorbic acid due to the absence of the reduced Cu(DEphen).	103
Figure S3.22 Single Layer Cu(DEphen) which has been stripped of copper using sodium diethyldithiocarbamate as described in the experimental section of the main paper.....	104
Figure S3.23 Double Layer Cu(DEphen) which has been stripped of copper using sodium diethyldithiocarbamate as described in the experimental section of the main paper.....	105
Table S3.2 Catalyst loading and ORR activities at selected potentials for multilayer Cu(DEphen) films and representative activities for control experiments	106
Figure S3.24 Kinetic current densities (j_K) estimated from Koutecky-Levich analysis of rotating disk voltammetry data for (a) a SL-Cu(DEphen) film measured using a Pt auxiliary electrode, (b) a SL-Cu(DEphen) film measured using a BDD auxiliary electrode, (c) a DL-Cu(DEphen) film measured using a Pt auxiliary electrode and (d) a DL-Cu(DEphen) film measured using a BDD auxiliary electrode. The central data points in each plot are the average potential-dependent j_K values, and the exterior error bars are the standard deviations at each potential. N is the number of measurement sets of independently-prepared electrodes that went towards determining each j_K value. Importantly, there is no observed dependence of ORR activity based on choice of auxiliary electrode (Pt or BDD), suggesting the ORR activity is not a result of trace Pt contamination.....	107
Figure S3.25 Representative rotating ring disk electrode voltammogram of a SL-Cu(DEphen) film in a 100 mM acetate buffer (50 mM NaOAc•3H ₂ O and 50 mM HOAc) at pH 4.8 containing 1 M NaClO ₄ supporting electrolyte under an O ₂ atmosphere. The rotation rate was 400 RPM and the platinum ring was held at 0.73 V vs Ag/AgCl/KCl(sat.).....	108
Figure S3.26 Representative rotating ring disk electrode voltammogram of a DL-Cu(DEphen) film in a 100 mM acetate buffer (50 mM NaOAc•3H ₂ O and 50 mM HOAc) at pH 4.8 containing 1 M NaClO ₄ supporting electrolyte under an O ₂ atmosphere. The rotation rate was 400 RPM and the platinum ring was held at 0.73 V vs Ag/AgCl/KCl(sat.).....	109
Figure S3.27 Representative rotating ring disk electrode voltammogram of a TL-Cu(DEphen) film in a 100 mM acetate buffer (50 mM NaOAc•3H ₂ O and 50 mM HOAc) at pH 4.8 containing 1 M NaClO ₄ supporting electrolyte under an O ₂ atmosphere. The rotation rate was 400 RPM and the platinum ring was held at 0.73 V vs Ag/AgCl/KCl(sat.).....	110
Figure S3.28 Fraction of the ORR current going to H ₂ O ₂ production as a function of potential based on RRDE measurements at 400 RPM for the TL-Cu(DEphen) films.	111
Figure 4.1 Ethynyl-modified TEMPO complexes used for covalent attachment to glassy carbon surfaces via the Cu(I)-Catalyzed Azide-Alkyne Cycloaddition.	120
Figure 4.2 Surface modification of a glassy carbon electrode with Complex I using the Cu(I)-Catalyzed Azide-Alkyne Cycloaddition reaction.	126

Figure 4.3 Representative Cyclic Voltammogram of a glassy carbon electrode covalently modified with TEMPO complex (I).....	127
Figure 4.4 Representative cyclic voltammograms of all bases tested for background effects when cycled with a TEMPO complex (I) modified glassy carbon electrode. The bases tested were (a) Tetrabutylammonium Acetate, (b) Tetrabutylammonium Benzoate, (c) Tetrabutylammonium Hydroxide, (d) Piperidine, (e) 2,6-Lutidine, and (f) N-methyl Imidazole.....	128
Figure 4.5 Representative Cyclic Voltammograms of alcohol oxidation with glassy carbon electrodes modified with TEMPO complex I using either 2,6-Lutidine (left) or N-methyl Imidazole (right), as the sacrificial base.	129
Figure 4.6 Representative CVs demonstrating instability of the TEMPO complex I under oxidative aqueous conditions. The CVs on the left are of the complex in acetonitrile where the redox peak is visible both before and after a single positive sweep in pH 10 carbonate buffer (right).	130
Figure 4.7 Representative Rotating Disk Electrode Voltammograms (RDEV) of a glassy carbon electrode covalently modified with TEMPO complex I used for alcohol oxidation in acetonitrile with 0.1 M tetrabutylammonium hexafluorophosphate as the electrolyte and N-methyl Imidazole as the sacrificial base.	131
Figure 4.8 Representative CVs demonstrating instability of the TEMPO complex II under oxidative aqueous conditions. The CVs on the left are of the complex in acetonitrile where the redox peak is visible both before and after a single positive sweep in pH 10 carbonate buffer (right).	132
Figure 4.9 Representative CVs demonstrating instability of the TEMPO complex III under oxidative aqueous conditions. The CVs on the left are of the complex in acetonitrile where the redox peak is visible both before and after a single positive sweep in pH 10 carbonate buffer (right).	132
Figure 5.1 Electropolymerized terthiophene films with appended chromium terpyridine moieties (p-TPTCrCl ₃) are selective for the electrochemical reduction of NO ₃ ⁻ to NH ₃ via a stepwise mechanism with an overall rate of 0.29 ± 0.053 mol NH ₃ g _{cat} ⁻¹ h ⁻¹	140
Figure 5.2 (a) General scheme for the synthesis of the TPTCrCl ₃ monomer. Further synthetic details are in the experimental section of the supplemental information. (b) Single crystal structure of the TPTCrCl ₃ monomer complex, based on single crystals suitable for X-ray analysis grown from acetonitrile/hexanes/diethyl ether. (c) Representative CVs of p-TPTCrCl ₃ films in 0.1 M phosphate buffer at a scan rate of 0.1 V/s in the absence and presence of 0.1 M NaNO ₃ . The p-TPTCrCl ₃ film was formed from a 20 mC electrodeposition. (d) Representative XPS of a p-TPTCrCl ₃ film formed from a 20 mC electrodeposition.	156
Figure 5.3 Product distributions from CPE measurements of NO ₃ RR by p-TPTCrCl ₃ films formed from a 20 mC electrodeposition. Unless otherwise noted, all CPEs were conducted in pH 6 phosphate buffer with 0.1 M of ¹⁵ N-labeled substrate for 2 h. (a) Faradaic efficiencies and (b) average partial current densities for products of ¹⁵ NO ₃ ⁻ reduction as a function of applied	

potential at a stir rate of 250 rpm. **(c)** Faradaic efficiencies and **(d)** average partial current densities products of $^{15}\text{NO}_3^-$ reduction as a function of stir rate at -0.75 V vs RHE. **(e)** Faradaic efficiencies and **(f)** average partial current densities for products of the reduction of 0.1 M $^{15}\text{NO}_3^-$, 0.1 M $^{15}\text{NO}_2^-$, and 0.1 M $^{15}\text{NH}_2\text{OH}$ at -0.75 V vs RHE and a stir rate of 250 rpm. The CPEs for $^{15}\text{NO}_3^-$ and $^{15}\text{NO}_2^-$ were conducted for 2 h, and the CPEs for NH_2OH were conducted for 1 h. All data in these figures are also included in Table S5.2-S5.4..... 159

Figure 5.4 Comparison of NO_3RR activity to NH_3 by p-TPTCrCl₃ films from this study (blue stars) to that of selected previously reported catalysts (black squares). All data from this figure along with relevant citations are included in Tables S5.5. 163

Figure S5.1 Calibration curve for absorbance at 548 nm versus sodium nitrite concentration as obtained using the Greiss method for nitrite quantitation. All reported values are averages of 3 independently prepared samples, and all errors are standard deviations. 165

Figure S5.2 Calibration curve for absorbance at 700 nm versus hydroxylamine hydrochloride concentration as obtained using the 8-hydroxyquinoline method for hydroxylamine quantitation. All reported values are averages of 3 independently prepared samples, and all errors are standard deviations. 166

Figure S5.3 Representative data showing the concentration of hydroxylamine in the electrolyte solution over time after reduction of NaNO_3 by p-TPTCrCl₃. All values are reported as a percent of the initial concentration determined immediately after electrolysis completed. The electrolyte was 100 mM phosphate buffer titrated to various pH values. Due to the drastic increase in stability of hydroxylamine at pH 6 all electrolyses in this paper use pH 6 100 mM phosphate buffer as the electrolyte..... 167

Figure S5.4 Calibration curve for the quantification of isotopically labeled $^{15}\text{NH}_4\text{Cl}$ via H-NMR. All values are reported as a ratio between the $^{15}\text{NH}_4$ peaks and the maleic acid internal standard. All reported values are averages of 3 independently prepared samples, and all errors are standard deviations. 168

Figure S5.5 Representative H-NMR of a calibration standard containing 2 mg L^{-1} isotopically labeled $^{15}\text{NH}_4\text{Cl}$. The peaks at 7.23 and 7.11 ppm are from the $^{15}\text{NH}_4\text{Cl}$ and the peak at 6.25 ppm is the maleic acid internal standard. 169

Figure S5.6 Representative H-NMR of a calibration standard containing 4 mg L^{-1} isotopically labeled $^{15}\text{NH}_4\text{Cl}$. The peaks at 7.23 and 7.11 ppm are from the $^{15}\text{NH}_4\text{Cl}$ and the peak at 6.25 ppm is the maleic acid internal standard. 170

Figure S5.7 Representative H-NMR of a calibration standard containing 6 mg L^{-1} isotopically labeled $^{15}\text{NH}_4\text{Cl}$. The peaks at 7.23 and 7.11 ppm are the from $^{15}\text{NH}_4\text{Cl}$ and the peak at 6.25 ppm is the maleic acid internal standard. The small triplet interspaced with the $^{15}\text{NH}_4\text{Cl}$ doublet is due the presence of trace amounts of $^{14}\text{NH}_4$ 171

Figure S5.8 Representative H-NMR of a calibration standard containing 10 mg L^{-1} isotopically labeled $^{15}\text{NH}_4\text{Cl}$. The peaks at 7.23 and 7.11 ppm are from the $^{15}\text{NH}_4\text{Cl}$ and the peak at 6.25 ppm

is the maleic acid internal standard. The small triplet interspaced with the $^{15}\text{NH}_4\text{Cl}$ doublet is due the presence of trace amounts of $^{14}\text{NH}_4$ 172

Figure S5.9 Representative H-NMR of a calibration standard containing 15 mg L^{-1} isotopically labeled $^{15}\text{NH}_4\text{Cl}$. The peaks at 7.23 and 7.11 ppm are from the $^{15}\text{NH}_4\text{Cl}$ and the peak at 6.25 ppm is the maleic acid internal standard. The small triplet interspaced with the $^{15}\text{NH}_4\text{Cl}$ doublet is due the presence of trace amounts of $^{14}\text{NH}_4$ 173

Figure S5.10 Representative H-NMR of calibration standard containing 25 mg L^{-1} isotopically labeled $^{15}\text{NH}_4\text{Cl}$. The peaks at 7.23 and 7.11 ppm are from the $^{15}\text{NH}_4\text{Cl}$ and the peak at 6.25 ppm is the maleic acid internal standard. The small triplet interspaced with the $^{15}\text{NH}_4\text{Cl}$ doublet is due the presence of trace amounts of $^{14}\text{NH}_4$ 174

Figure S5.11 Representative H-NMR of a calibration standard containing 30 mg L^{-1} isotopically labeled $^{15}\text{NH}_4\text{Cl}$. The peaks at 7.23 and 7.11 ppm are from the $^{15}\text{NH}_4\text{Cl}$ and the peak at 6.25 ppm is the maleic acid internal standard. The small triplet interspaced with the $^{15}\text{NH}_4\text{Cl}$ doublet is due the presence of trace amounts of $^{14}\text{NH}_4$ 175

Figure S5.12 Representative potentiostatic p-TPTCrCl₃ deposition. The deposition solution consisted of 1 mM TPTCrCl₃ dissolved in dichloromethane with 0.1 M tetrabutylammonium hexafluorophosphate as the electrolyte. The deposition potential was 1.06 V vs $\text{Fc}^{+/0}$ and the total charge passed was 0.02 C. 176

Figure S5.13 Representative cyclic voltammetry data showing the growth of the TPTCrCl₃ polymer during oxidative electropolymerization. The deposition solution consisted of 1 mM TPTCrCl₃ dissolved in dichloromethane with 0.1 M tetrabutylammonium hexafluorophosphate as the electrolyte. 177

Figure S5.14 Representative SEM of a bare glassy carbon electrode (Left) and a glassy carbon electrode coated with a film of electropolymerized TPTCrCl₃ (Right). The white bars represent 100 μm 179

Figure S5.15 Representative raw (prior to any processing) H-NMR of the electrolyte solution obtained after a 2-hour controlled potential electrolysis (CPE) at -0.75 V vs RHE and 250 RPM of isotopically labeled NO_3^- on a glassy carbon electrode modified with p-TPTCrCl₃. The electrolysis was conducted in a sealed cell containing 100 mM $\text{Na}^{15}\text{NO}_3$ dissolved in 0.1 M pH 6 phosphate buffer that was sparged with Argon for 30 minutes. The peaks at 7.23 and 7.11 ppm are from $^{15}\text{NH}_3$ and the peak at 6.25 ppm is from the maleic acid internal standard. The peak at 4.41 ppm is from water, and the peak at 2.55 ppm is from DMSO. 183

Figure S5.16 Representative H-NMR of the electrolyte solution obtained after a 2-hour controlled potential electrolysis (CPE) at -0.55 V vs RHE and 250 RPM of isotopically labeled NO_3^- on a glassy carbon electrode modified with a p-TPTCrCl₃ film. The electrolysis was conducted in a sealed cell containing 100 mM $\text{Na}^{15}\text{NO}_3$ dissolved in 0.1 M pH 6 phosphate buffer that was sparged with Argon for 30 minutes. The peaks at 7.23 and 7.11 ppm are from $^{15}\text{NH}_3$ and the peak at 6.25 ppm is from the maleic acid internal standard. The small triplet interspaced with the $^{15}\text{NH}_3$ doublet is due the presence of trace amounts of $^{14}\text{NH}_4$ 184

Figure S5.17 Representative H-NMR of the electrolyte solution obtained after a 2-hour controlled potential electrolysis (CPE) at -0.65 V vs RHE and 250 RPM of isotopically labeled NO_3^- on a glassy carbon electrode modified with a p-TPTCrCl₃ film. The electrolysis was conducted in a sealed cell containing 100 mM Na¹⁵NO₃ dissolved in 0.1 M pH 6 phosphate buffer that was sparged with Argon for 30 minutes. The peaks at 7.23 and 7.11 ppm are from ¹⁵NH₃ and the peak at 6.25 ppm is from the maleic acid internal standard. The small triplet interspaced with the ¹⁵NH₃ doublet is due the presence of trace amounts of ¹⁴NH₄. 185

Figure S5.18 Representative H-NMR of the electrolyte solution obtained after a 2-hour controlled potential electrolysis (CPE) at -0.75 V vs RHE and 250 RPM of isotopically labeled NO_3^- on a glassy carbon electrode modified with a p-TPTCrCl₃ film. The electrolysis was conducted in a sealed cell containing 100 mM Na¹⁵NO₃ dissolved in 0.1 M pH 6 phosphate buffer that was sparged with Argon for 30 minutes. The peaks at 7.23 and 7.11 ppm are from ¹⁵NH₃ and the peak at 6.25 ppm is from the maleic acid internal standard. The small triplet interspaced with the ¹⁵NH₃ doublet is due the presence of trace amounts of ¹⁴NH₄. 186

Figure S5.19 Representative H-NMR of the electrolyte solution obtained after a 2-hour controlled potential electrolysis (CPE) at -0.85 V vs RHE and 250 RPM of isotopically labeled NO_3^- on a glassy carbon electrode modified with a p-TPTCrCl₃ film. The electrolysis was conducted in a sealed cell containing 100 mM Na¹⁵NO₃ dissolved in 0.1 M pH 6 phosphate buffer that was sparged with Argon for 30 minutes. The peaks at 7.23 and 7.11 ppm are from ¹⁵NH₃ and the peak at 6.25 ppm is from the maleic acid internal standard. The small triplet interspaced with the ¹⁵NH₃ doublet is due the presence of trace amounts of ¹⁴NH₄. 187

Figure S5.20 Representative H-NMR of the electrolyte solution obtained after a 2-hour controlled potential electrolysis (CPE) at -0.95 V vs RHE and 250 RPM of isotopically labeled NO_3^- on a glassy carbon electrode modified with a p-TPTCrCl₃ film. The electrolysis was conducted in a sealed cell containing 100 mM Na¹⁵NO₃ dissolved in 0.1 M pH 6 phosphate buffer that was sparged with Argon for 30 minutes. The peaks at 7.23 and 7.11 ppm are from ¹⁵NH₃ and the peak at 6.25 ppm is from the maleic acid internal standard. The small triplet interspaced with the ¹⁵NH₃ doublet is due the presence of trace amounts of ¹⁴NH₄. 188

Figure S5.21 Representative H-NMR of the electrolyte solution obtained after a 2-hour controlled potential electrolysis (CPE) at -0.75 V vs RHE and 100 RPM of isotopically labeled NO_3^- on a glassy carbon electrode modified with a p-TPTCrCl₃ film. The electrolysis was conducted in a sealed cell containing 100 mM Na¹⁵NO₃ dissolved in 0.1 M pH 6 phosphate buffer that was sparged with Argon for 30 minutes. The peaks at 7.23 and 7.11 ppm are from ¹⁵NH₃ and the peak at 6.25 ppm is from the maleic acid internal standard. The small triplet interspaced with the ¹⁵NH₃ doublet is due the presence of trace amounts of ¹⁴NH₄. 189

Figure S5.22 Representative H-NMR of the electrolyte solution obtained after a 2-hour controlled potential electrolysis (CPE) at -0.75 V vs RHE and 500 RPM of isotopically labeled NO_3^- on a glassy carbon electrode modified with a p-TPTCrCl₃ film. The electrolysis was conducted in a sealed cell containing 100 mM Na¹⁵NO₃ dissolved in 0.1 M pH 6 phosphate buffer that was sparged with Argon for 30 minutes. The peaks at 7.23 and 7.11 ppm are from ¹⁵NH₃ and the peak at 6.25 ppm is from the maleic acid internal standard. The small triplet interspaced with the ¹⁵NH₃ doublet is due the presence of trace amounts of ¹⁴NH₄. 190

Figure S5.23 Representative H-NMR of the electrolyte solution obtained after a 2-hour controlled potential electrolysis (CPE) at -0.75 V vs RHE and 750 RPM of isotopically labeled NO_3^- on a glassy carbon electrode modified with a p-TPTCrCl₃ film. The electrolysis was conducted in a sealed cell containing 100 mM Na¹⁵NO₃ dissolved in 0.1 M pH 6 phosphate buffer that was sparged with Argon for 30 minutes. The peaks at 7.23 and 7.11 ppm are from ¹⁵NH₃ and the peak at 6.25 ppm is from the maleic acid internal standard. The small triplet interspaced with the ¹⁵NH₃ doublet is due the presence of trace amounts of ¹⁴NH₄. 191

Figure S5.24 Representative H-NMR of the electrolyte solution obtained after a 2-hour controlled potential electrolysis (CPE) at -0.75 V vs RHE and 250 RPM of isotopically labeled NO_2^- on a glassy carbon electrode modified with a p-TPTCrCl₃ film. The electrolysis was conducted in a sealed cell containing 100 mM Na¹⁵NO₂ dissolved in 0.1 M pH 6 phosphate buffer that was sparged with Argon for 30 minutes. The peaks at 7.23 and 7.11 ppm are from ¹⁵NH₃ and the peak at 6.25 ppm is from the maleic acid internal standard. The small triplet interspaced with the ¹⁵NH₃ doublet is due the presence of trace amounts of ¹⁴NH₄. 192

Figure S5.25 Representative H-NMR of an electrolyte solution obtained after a 1-hour controlled potential electrolysis (CPE) at -0.75 V vs RHE and 250 RPM of isotopically labeled ¹⁵NH₂OH on a glassy carbon electrode modified with a p-TPTCrCl₃ film. The electrolysis was conducted in a sealed cell containing 100 mM Na¹⁵NH₂OH•HCl dissolved in 0.1 M pH 6 phosphate buffer that was sparged with Argon for 30 minutes. The resulting electrolyte was diluted 1:4 with 100 mM pH 6 phosphate buffer prior to analysis. The peaks at 7.23 and 7.11 ppm are from ¹⁵NH₃ and the peak at 6.25 ppm is from the maleic acid internal standard. The small triplet interspaced with the ¹⁵NH₃ doublet is due the presence of trace amounts of ¹⁴NH₄. 193

Figure S5.26 Faradaic efficiencies (a) and partial current densities (b) obtained from 2-hour controlled potential electrolyses (CPE) at -0.75 V vs RHE of isotopically labeled NO_3^- on bare glassy carbon electrodes. Electrolyses were conducted in a sealed cell containing 100 mM Na¹⁵NO₃ dissolved in 0.1 M pH 6 phosphate buffer that was sparged with Argon for 30 minutes. All reported values are averages of 3 independently conducted measurements, and all errors are standard deviations..... 194

Figure S5.27 Representative H-NMR of the electrolyte solution obtained after a 2-hour controlled potential electrolysis (CPE) at -0.75 V vs RHE and 250 RPM of isotopically labeled NO_3^- on a bare glassy carbon electrode. The electrolysis was conducted in a sealed cell containing 100 mM Na¹⁵NO₃ dissolved in 0.1 M pH 6 phosphate buffer that was sparged with Argon for 30 minutes. The peaks at 7.23 and 7.11 ppm are from ¹⁵NH₃ and the peak at 6.25 ppm is from the maleic acid internal standard. The small triplet interspaced with the ¹⁵NH₃ doublet is due the presence of trace amounts of ¹⁴NH₄. 195

Figure S5.28 Faradaic efficiencies (a) and partial current densities (b) obtained from 2-hour controlled potential electrolyses (CPE) at -0.75 V vs RHE of isotopically labeled NO_3^- on glassy carbon coated with p-TPT (poly-4'-(4-([2,2':5',2''-terthiophen]-3'-yl)phenyl)-2,2':6',2''-terpyridine) . Electrolyses were conducted in a sealed cell containing 100 mM Na¹⁵NO₃ dissolved in 100 mM pH 6 phosphate buffer that was sparged with Argon for 30 minutes. All reported values are averages of 3 independently conducted measurements, and all errors are

standard deviations. The very low currents seen during the electrolysis suggest that the TPT film is not catalytically active..... 196

Figure S5.29 Representative H-NMR of an electrolyte solution obtained after a 2-hour controlled potential electrolysis (CPE) at -0.75 V vs RHE and 250 RPM of isotopically labeled $^{15}\text{NO}_3^-$ on a glassy carbon electrode modified with an unmetalled TPT film. The electrolysis was conducted in a sealed cell containing 100 mM $\text{Na}^{15}\text{NO}_3$ dissolved in 0.1 M pH 6 phosphate buffer that was sparged with Argon for 30 minutes. The peaks at 7.23 and 7.11 ppm are from $^{15}\text{NH}_3$ and the peak at 6.25 ppm is from the maleic acid internal standard. The small triplet interspaced with the $^{15}\text{NH}_3$ doublet is due the presence of trace amounts of $^{14}\text{NH}_4$ 197

Figure S5.30 Representative H-NMR of the electrolyte solution obtained after a 2-hour controlled potential electrolysis (CPE) at -0.75 V vs RHE and 250 RPM in nitrate-free electrolyte on a glassy carbon electrode modified with a p-TPTCrCl₃ film. The electrolysis was conducted in a sealed cell containing 0.1 M pH 6 phosphate buffer that was sparged with Argon for 30 minutes. No $^{15}\text{NH}_4$ was detected. The small triplet present at ~ 7.17 ppm is due the presence of trace amounts of $^{14}\text{NH}_4$ 198

Figure S5.31 Representative current density of a 2-hour controlled potential electrolysis (CPE) at -0.75 V vs RHE and 250 RPM of isotopically labeled NO_3^- on a glassy carbon electrode modified with a p-TPTCrCl₃ film. The electrolysis was conducted in a sealed cell containing 100 mM $\text{Na}^{15}\text{NO}_3$ dissolved in 0.1 M pH 6 phosphate buffer that was sparged with Argon for 30 minutes. 199

Figure S5.32 Representative XPS of (left) a freshly synthesized p-TPTCrCl₃ film on a glassy carbon electrode and (right) a p-TPTCrCl₃ film on a glassy carbon electrode after a 2-hour controlled-potential electrolysis (CPE) at -0.75 V vs RHE and 250 RPM of isotopically labeled $^{15}\text{NO}_3^-$. The electrolysis was conducted in a sealed cell containing 100 mM $\text{Na}^{15}\text{NO}_3$ dissolved in 0.1 M pH 6 phosphate buffer that was sparged with Argon for 30 minutes. The XPS supports the presence of some degradation over the course of the electrolysis but also demonstrates that a large part of the film remains intact. Additionally, the loss of chlorine is also clearly shown. This suggests that chlorine loss is part of the catalytic cycle and is necessary to free up active sites for NO_3RR 200

Figure S5.33 Representative data showing the relative stability of the p-TPTCrCl₃ post 2-hour controlled potential electrolysis (CPE) at -0.75 vs RHE in 100 mM pH 6 phosphate buffer containing 100 mM $\text{Na}^{15}\text{NO}_3$. All CVs were conducted in 100 mM pH 6 phosphate buffer that was sparged with N_2 for at least 10 minutes. The blue CVs are of a freshly prepared glassy carbon electrode coated with p-TPTCrCl₃ and the red CVs are of an identically prepared electrode after a CPE. The results suggest that some degradation of the film occurred, but that it was still catalytically active post-electrolysis. 201

Figure 6.1 Representative XPS of p-TPTCrCl₃ films on a glassy carbon electrode post-electrolysis under varying applied potentials and substrate concentration. All controlled-potential electrolyses (CPE) were conducted for 2-hours with a stir rate of 250 RPM in a sealed cell with 0.1 M pH 6 phosphate buffer that was sparged with Argon for 30 minutes. The substrate was 100

mM Na ¹⁵ NO ₃ unless otherwise noted. XPS of a freshly prepared film is also included for comparison.....	212
Figure 6.2 Proposed synthetic scheme for 4'-(4-vinylphenyl)-2,2':6',2"-terpyridine.....	214
Figure 6.3 Rhenium Bipyridine Complex.....	216
Figure 6.4 Representative XPS of a glassy carbon electrode covalently modified with a diethynyl rhenium bipyridine complex.....	216
Figure 6.5 Representative Cyclic Voltammogram of a glassy carbon electrode covalently modified with a rhenium diethynylbipyridine complex. The electrolyte is 100 mM tetrabutylammonium hexafluorophosphate in acetonitrile with 5% H ₂ O added as a proton source.	217
Figure 6.6 Representative Cyclic Voltammogram of bis-chromium terpyridine PF ₆ complex encapsulated in poly-4-vinylpyridine and dropcast onto a glassy carbon electrode. The electrolyte is 0.1 M pH 7 phosphate buffer sparged with either N ₂ or CO ₂ for 10 minutes.	218

Abstract

The use of molecular electrochemical catalysts for small molecule transformations is a quickly growing and challenging field with numerous environmental, industrial, and agricultural applications. Molecular catalysts, while prized for their selectivity and tunability, are often hindered by issues of solubility, relative activity, and post-electrolysis separation and reconstitution. One method for alleviating some of the drawbacks of molecular catalysts without compromising their benefits is to attach them to solid-state surfaces, a process also known as heterogenization. In this dissertation I will share the results of several methods for heterogenization of molecular electrocatalysts for environmentally relevant small molecule transformations, culminating in the discovery of a novel polymeric chromium catalyst capable of the direct reduction of nitrate, and other NO_x species, to ammonia with activity and selectivity comparable to state-of-the-art solid-state electrocatalysts.

Chapters 1 and 2 provide background information for this thesis. **Chapter 1** includes an in-depth discussion of the research motivation along with a discussion of current methods for molecular electrocatalyst heterogenization. This is followed, in **Chapter 2**, by descriptions and backgrounds for the main analytical methods employed throughout this work. In **Chapter 3** I present my work on layer-by-layer growth of multilayer films of discrete molecular catalysts using sequential Cu-Catalyzed Azide–Alkyne Cycloaddition or ‘Click’ reactions for the electrocatalytic reduction of oxygen. The resulting multi-layer films of Copper Diethynylphenanthroline were capable of the oxygen reduction reaction and showed an increase in both activity and selectivity for the 4-electron reduction of oxygen to water. However, as

discussed in more detail in the chapter, the films were limited to two layers due to steric hindrance preventing the formation of additional layers.

In **Chapter 4**, I discuss the use of the same ‘Click’ reaction to modify glassy carbon electrodes with (2,2,6,6-Tetramethylpiperidin-1-yl)oxyl (TEMPO) for alcohol oxidation. I present the synthesis and heterogenization of several different TEMPO analogues. I determined that while TEMPO can be readily covalently attached to glassy carbon electrodes and the resulting electrodes are active for alcohol oxidation, the TEMPO complexes are highly unstable and rapidly degrade under catalytic conditions. These results suggest that further work into this area should focus on either TEMPO stability, generating a large excess of catalyst on the surface, or rapid replacement/regeneration of the catalytic surface.

Chapter 5 focuses on my work in using electropolymerization to overcome the limitations of the ‘Click’ reaction for forming multi-layer films. I present my work on using molecular electrocatalysts modified with a terthiophene backbone in order to form catalyst-containing conductive electropolymerized films on glassy carbon electrodes. This method is capable of forming much higher surface coverages than the aforementioned ‘Click’ method, albeit at the cost of less control over the film due to the radical polymerization process. Using a novel chromium terpyridine terthiophene complex as the monomer I form electrode surfaces that are capable for the reduction of nitrate, and other NO_x species, to ammonia with activity and selectivity comparable to those of state-of-the-art solid-state systems. To our knowledge this is the first example of a molecular electrocatalyst capable of this reaction at high selectivity and activity and also one of the first examples of a highly active polythiophene based electrocatalytic system. It has many implications for environmental remediation of nitrate with the added benefit of nutrient recovery. Finally, in **Chapter 6**, I provide a brief summary of my work, descriptions

of the future directions I believe this work should take, and some preliminary data for the
aforementioned directions.

Chapter 1 : Research Motivation and Introduction to Electrode Modification with Molecular Catalysts

1.1 Introduction

The use of electrocatalysis for small molecules transformations has been a rapidly expanding field with applications in renewable energy and organic synthesis. With the deleterious effects of anthropogenic emissions becoming an increasingly pressing issue, technologies capable of helping to combat global climate change and pollution and make use of solar fuels are crucially important. Electrocatalysts can be used to convert renewable energy sources like solar or wind into chemical bonds for energy storage through reactions like the CO₂ reduction reaction (CO₂RR). They are also an important part of chemical fuel cells where the opposite reaction occurs, and the potential energy stored in chemical bonds is converted directly to energy. In other words, electrocatalysts are capable of lowering the kinetic barrier between electrical and chemical potential energy. In theory, the energy obtained from this process is larger than that obtained through combustion of the same material.¹ More recently, electrocatalysis has shown promise for organic transformations as well.²⁻⁴ Electrocatalysts have been used for alcohol oxidations to form precursors to industrially and pharmaceutically relevant molecules with high yield and without the use of toxic or environmentally harmful oxidants.⁵

Electrocatalysts can be broadly divided into two categories: solid-state and molecular. With solid-state catalysts, such as copper for the CO₂RR, the reactions take place at a high concentration of poorly defined surface-sites.⁶⁻¹⁰ These surface sites can vary as a function of location on the surface, applied potential, and time over the course of an experiment.¹¹ This is a key difference

between solid-state and molecular electrocatalysts where the reactions take place at singular well-defined active sites. It is important to note that a molecular electrocatalyst does not necessarily mean a homogenous catalyst as well. Molecular electrocatalysts attached to surfaces, while heterogenous in nature, would still be considered a molecular, not solid-state, electrocatalyst. This is why we define our electrocatalyst types as molecular and solid-state rather than hetero- and homogenous.

Solid-state electrocatalysts generally have the advantage in overall activity for a given reaction. A large concentration of surface-sites which can be enhanced with nano-structuring and/or porous surfaces results in high electrochemical activity. State-of-the-art nano-structured copper catalysts, for example, can obtain CO₂RR activities upwards of 10 mA cm⁻².^{12, 13} However, because the reactions take place at a variety of surface-sites there are limits in terms of selectivity and mechanistic evaluations. While copper is capable of reducing CO₂ with high activity and to highly reduced C₁ and C₂ containing products including methane and ethanol, the overall selectivity is quite low. At least 16 different carbon containing products have been detected from CO₂RR on polycrystalline copper in aqueous electrolyte (Figure 1.1).¹⁴ In addition, the product selectivity is highly potential dependent and specific products may only be obtainable within a narrow potential window. Changing the applied potential to increase activity may result in different, less desirable products, including competitive H₂ formation from the hydrogen evolution reaction (HER).

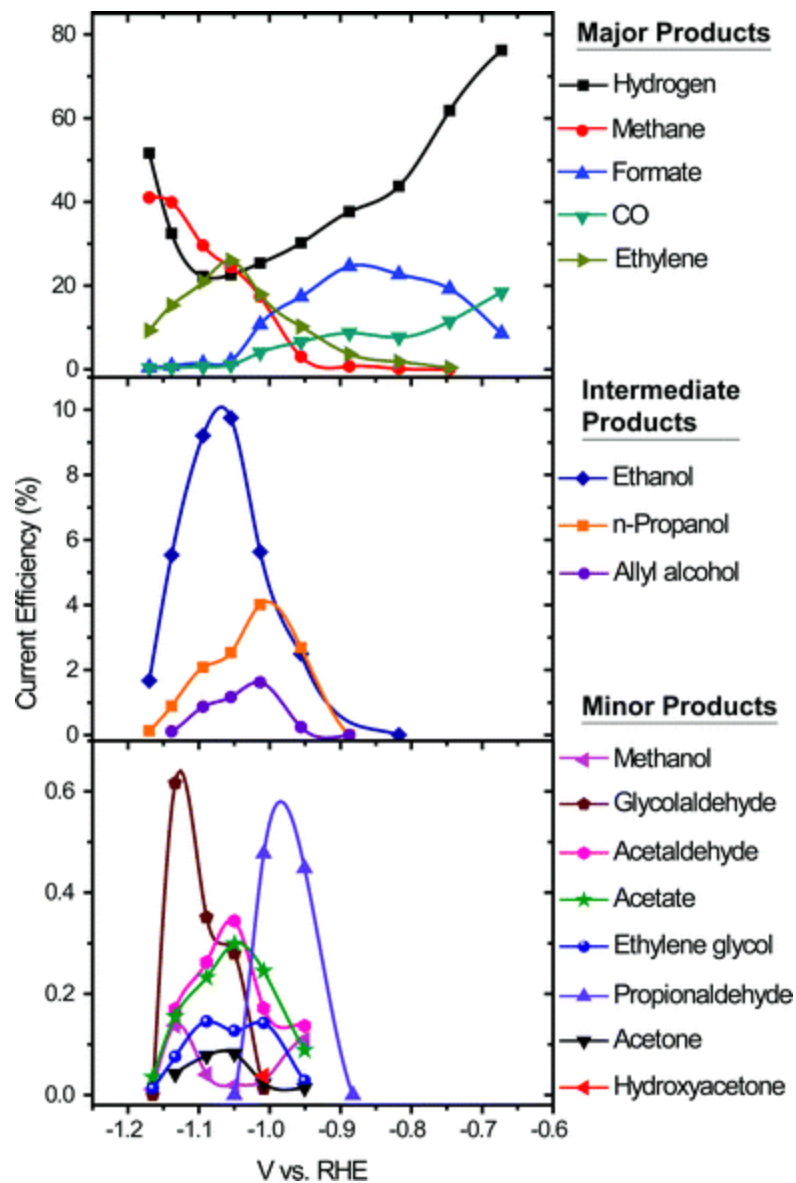


Figure 1.1 Potential dependent product distribution for CO₂RR on polycrystalline copper in aqueous electrolyte.¹⁴ Reproduced from *Energy Environ. Sci.*, **2012**, 5, 7050-7059. with permission from the Royal Society of Chemistry.

Other metals, such as silver and gold, only produce a single carbon containing product, CO. However, like copper, the selectivity varies drastically with the applied potential and high selectivity for CO versus competitive HER only occurs in a very narrow potential window. As seen in Figure 1.2 silver is only highly selective for the CO₂RR between -1.0 and -1.1 V vs RHE.¹⁵ Because the surface sites are hard to define and can change over the course of an experiment it is difficult to rationally tune a solid-state catalyst. Efforts to do so generally focus on nano-structuring the material either to increase surface area,^{16, 17} enhance the concentration of a specific surface structure such as step sites,^{13, 18} or control the local pH environment around the catalyst surface.^{19,}²⁰ While all of these methods are capable of changing the activity and selectivity to an extent, they lack the degree of control that a molecular catalyst can provide.

Unlike solid-state catalysts, molecular catalysts have the advantage of a single, well-defined active site at which the reaction occurs. In addition, the environment around the active site can be rationally tuned through ligand alterations²¹⁻²⁹ and/or outer sphere effects such as polymer encapsulation.³⁰⁻³³ This degree of control over the active site is not found in solid-state catalysts. Because of the singular nature of the active site molecular catalysts generally operate with higher selectivity than their solid-state counterparts. The selectivity is also much less potential dependent so activity can be modulated through potential changes with reduced risk of generating side products.

However, molecular catalysts have their own set of drawbacks, many of which stem from the fact that molecular catalysts are often used as homogenous solutions. This means that the electrolyte solution must be one in which the catalyst is soluble and often precludes the use of greener solvents. In addition, solubility issues may arise over the course of an experiment resulting in precipitation or decomposition of the catalyst onto the electrode surface.³⁴ Catalyst deactivation

can also be enhanced by intramolecular interactions between multiple catalyst complexes in solution. For example fac-Re(bpy-R)(CO)₃X complexes, capable of CO₂RR, can form inactive dimers in solution.³⁵

It is also important to note that as with all electrochemical processes the reactions only take place at the surface of the electrode. The majority of the catalyst in the solution will not be active at any given time during an experiment. This has implications in terms of both resources, as a large amount of catalyst will be superfluous, but also in terms of activity measurements. Because only catalyst within the diffusion layer of the electrode is capable of undergoing redox processes determining the actual number of active complexes over the course of an experiment can at best only be estimated.^{34, 36, 37} As an alternative, the activity can be based on the total amount of catalyst in solution but this will greatly underestimate the TOF. While both methods have their benefits, they still make benchmarking different catalysts difficult as the TOFs will always be approximations.

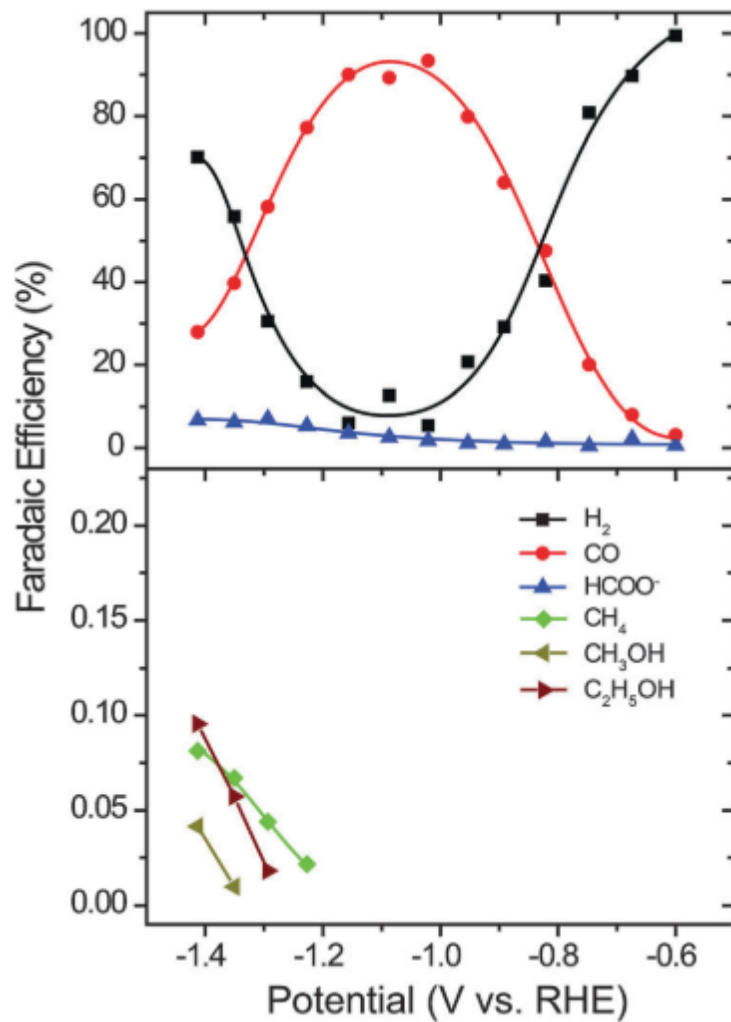


Figure 1.2 Potential dependence product distribution of the CO₂RR on silver in aqueous electrolyte.¹⁵ Reproduced from *Phys. Chem. Chem. Phys.*, 2014, 16, 13814-13819. with permission from the Royal Society of Chemistry.

Finally, the overall activity of molecular electrocatalysts is generally lower than those of their solid-state counterparts. Because molecular catalysts are limited to a monolayer on the electrode surface the overall concentration of active sites is lower than nano-structured state-of-the-art solid-state systems. While the maximum coverage of a monolayer will be somewhat species and surface roughness dependent, theoretical calculations of a monolayer of ferrocene idealized as cylinders, on graphitic carbon result in a monolayer coverage on the order of 10^{14} molecules cm^{-2} .³⁸ These coverages have also been experimentally confirmed³⁸ and this is consistent with our results as well where we have found that a monolayer of copper diethynylphenanthroline covalently attached to carbon surfaces is also on the order of 10^{14} (see Chapter 3).³⁹ However, with these coverages, to reach current densities common to solid-state catalysts, either a highly active catalyst ($\text{TOF} \sim 300 \text{ s}^{-1}$) would need to be found, or surface coverage would need to be increased.

Many of the issues associated with the use of molecular catalysts can be alleviated by attaching them to a surface rather than using them in a homogenous solution. By employing this method solubility is no longer a concern and the best, or greenest solvent, can be used for the electrolyte without worrying about catalyst precipitation. In addition, as long as the complexes are not mobile on the surface, intermolecular interactions can be drastically reduced or eliminated, thereby also eliminating one pathway towards catalyst deactivation. The attachment strategy also reduces the amount of catalyst needed for an electrochemical reaction. Only enough catalyst to cover the surface of the electrode is required and no catalyst is wasted in solution. This also makes calculating the activity of the catalyst much simpler. Because all the catalyst is contained on the electrode surface it is much easier to determine the number of active sites and from that information

determine the TOF. There exist many strategies for surface immobilization including both covalent and non-covalent methodologies and they will be described in the following sections.

1.2 Non-Covalent Attachment Methods

The simplest method of attaching molecular electrocatalysts to a surface is likely through non-covalent interactions. Inorganic and organometallic complexes can be physisorbed onto certain carbon surfaces. This works best on high surface area substrates such as edge-plane graphite, carbon felt, or HOPG (highly ordered pyrolytic carbon). Graphite powder can also be used to increase the effective surface area but is susceptible to delamination. It is important to note that the catalysts must be capable of strong interactions with the substrate and therefore aromatic complexes or complexes with aromatic substituents are desired to induce pi-stacking. When using non-covalent attachment it is important to use an electrolyte in which your catalyst is not soluble as solvent-catalyst interactions will be capable of displacing the catalyst from the surface. Aqueous electrolytes are commonly used to avoid this issue.

1.2.1 Physisorption

Anson and co-workers found that copper complexes of 1,10-phenanthroline when adsorbed to edge plane graphite were capable of reducing both oxygen and hydrogen peroxide.⁴⁰⁻
⁴³ The polished edge plane graphite electrodes were loaded either by submerging them in a solution of ligand-metal complex, or by first adsorbing the ligand then chelating copper in a similar manner. Because the complexes used were molecular, the activity and redox potentials could be modified through ligand alterations. This was examined in detail by Chidsey and co-workers where they examined a series of 1,10-phenanthroline copper complexes adsorbed onto edge plane graphite for ORR (Table 1.1).⁴⁴ They determined that the redox potential of the metal center, and the potential

of the oxygen reduction peak, could be shifted positive by the addition of electron withdrawing groups or bulky ligands in the 1 and 9 positions. However, this positive shift was also generally associated with a decrease in the overall kinetic rate for the ORR due to a lower energy active state of the catalyst.

TABLE 1: Ligands Adsorbed onto EPG and Complexed with Cu^{II} ^a

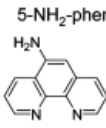
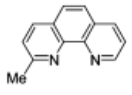
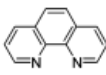
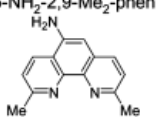
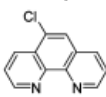
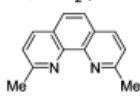
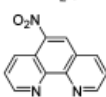
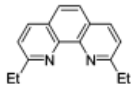
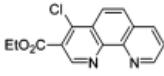
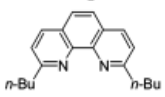
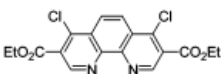
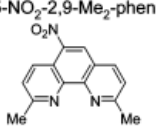
e ⁻ Donating / Withdrawing Substituents Remote to Cu-Binding Site	E_{cat}^0 mV vs. NHE	E_{O_2} mV vs. NHE	$\frac{i_K(E_{\text{cat}}^0)}{q_{\text{cat}}}$ s ⁻¹	Substituents Adjacent to Cu- Binding Site	E_{cat}^0 mV vs. NHE	E_{O_2} mV vs. NHE	$\frac{i_K(E_{\text{cat}}^0)}{q_{\text{cat}}}$ s ⁻¹
5-NH ₂ -phen 	20	10	—	2-Me-phen 	215	205	7 ± 2
phen 	25	10	16 ± 3	5-NH ₂ -2,9-Me ₂ -phen 	285	275	—
5-Cl-phen 	50	40	—	2,9-Me ₂ -phen 	310	290	1.6 ± 0.5
5-NO ₂ -phen 	75	40	—	2,9-Et ₂ -phen 	335	305	0.4 ± 0.2
3-CO ₂ Et-4-Cl-phen 	90	65	6 ± 2	2,9-nBu ₂ -phen 	340	260	—
3,8-(CO ₂ Et) ₂ -4,7-Cl ₂ -phen 	150	130	1.9 ± 0.5	5-NO ₂ -2,9-Me ₂ -phen 	390	80	—

Table 1.1 Redox potential (E_{cat}^0), oxygen reduction peak potential (E_{O_2}), and measured kinetic current ($\frac{i_K(E_{\text{cat}}^0)}{q_{\text{cat}}}$) of a series of 1,10-phenanthroline copper complexes adsorbed on edge plane graphite.⁴⁴ Reproduced from J. Phys. Chem. A., **2007**, 111, 12641-12650. with permission from the American Chemistry Society.

Cobalt phthalocyanine is well-studied CO₂RR and ORR catalyst that has been incorporated onto graphite electrodes using non-covalent pi stacking interactions.⁴⁵⁻⁵⁰ However, it suffers from significant competitive HER while under the standard aqueous electrolyte conditions. Kaneko and co-workers found that both the activity and selectivity of the catalyst could be improved through incorporation in poly-4-vinyl pyridine.^{30, 33} Additional mechanistic studies by McCrory and co-workers suggest that this effect is due to both inner sphere interactions between the pyridine and cobalt but also outer sphere effects based on proton relays through the polymer (Figure 1.3).^{31, 32} Films formed in these studies were generally done through drop casting, an alternative method for forming non-covalent catalyst layers on graphite.

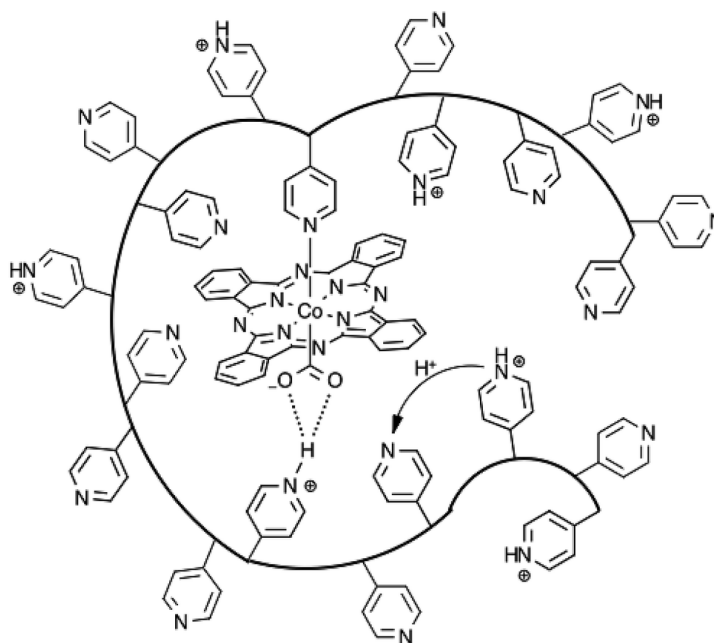


Figure 1.3 Figure demonstrating proposed effects of the poly-4-vinyl pyridine on CO₂RR by CoPc including 1) pyridine coordination to the cobalt center, 2) H-bonding stabilization of the CO₂RR intermediates and 3) proton relay through the polymer film.³¹ Reproduced from *Chem. Sci.*, 2016, 7, 2506-2515. with permission from the American Chemistry Society.

1.2.2 Pyrene Attachment

As an alternative for direct interaction of the catalyst and the electrode, the catalyst can be modified with a pyrene substituent in order to facilitate binding.^{5, 51-57} Carbon nanotubes are often used as the substrate in order to improve binding interactions. Stahl and co-workers modified a TEMPO complex with a pyrene moiety and attached it to multi-walled carbon nanotubes (MWCNT) on both glassy carbon and carbon cloth using a dipping method (Figure 1.4).⁵ The TEMPO-modified electrodes were capable of alcohol oxidation on multiple substrates including a hydroxymethylpyrimidine precursor to rosuvastatin (Crestor™).

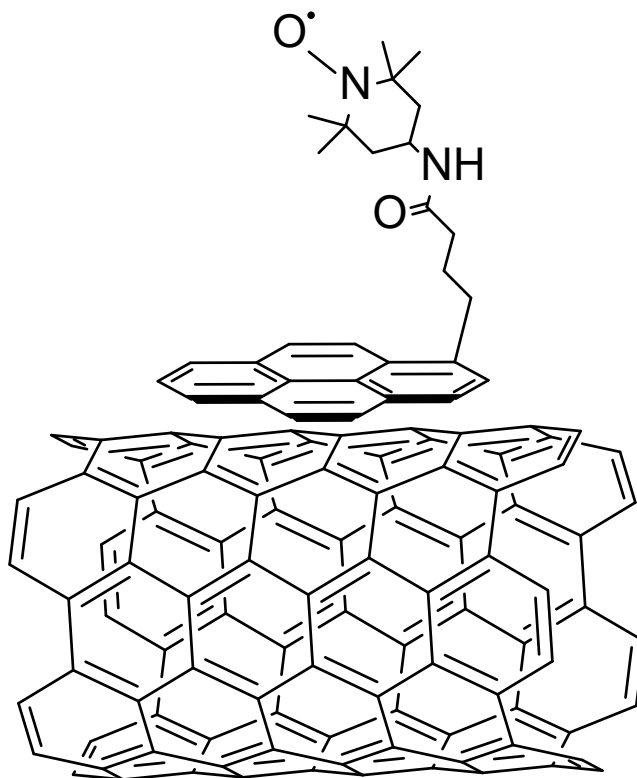


Figure 1.4 Noncovalent attachment of a pyrene modified TEMPO complex to a MWCNT.

Organometallic complexes can also be attached to electrodes using this method. Robert and co-workers modified an iron porphyrin complex with pyrene for the electrochemical reduction of CO₂ to CO (Figure 1.5).⁵⁷ Glassy carbon electrodes of the complex were made by drop casting MWCNTs onto the surface followed by the iron catalyst. The resulting electrodes were highly selective for CO₂RR over HER and were stable over a 3-hour electrolysis.

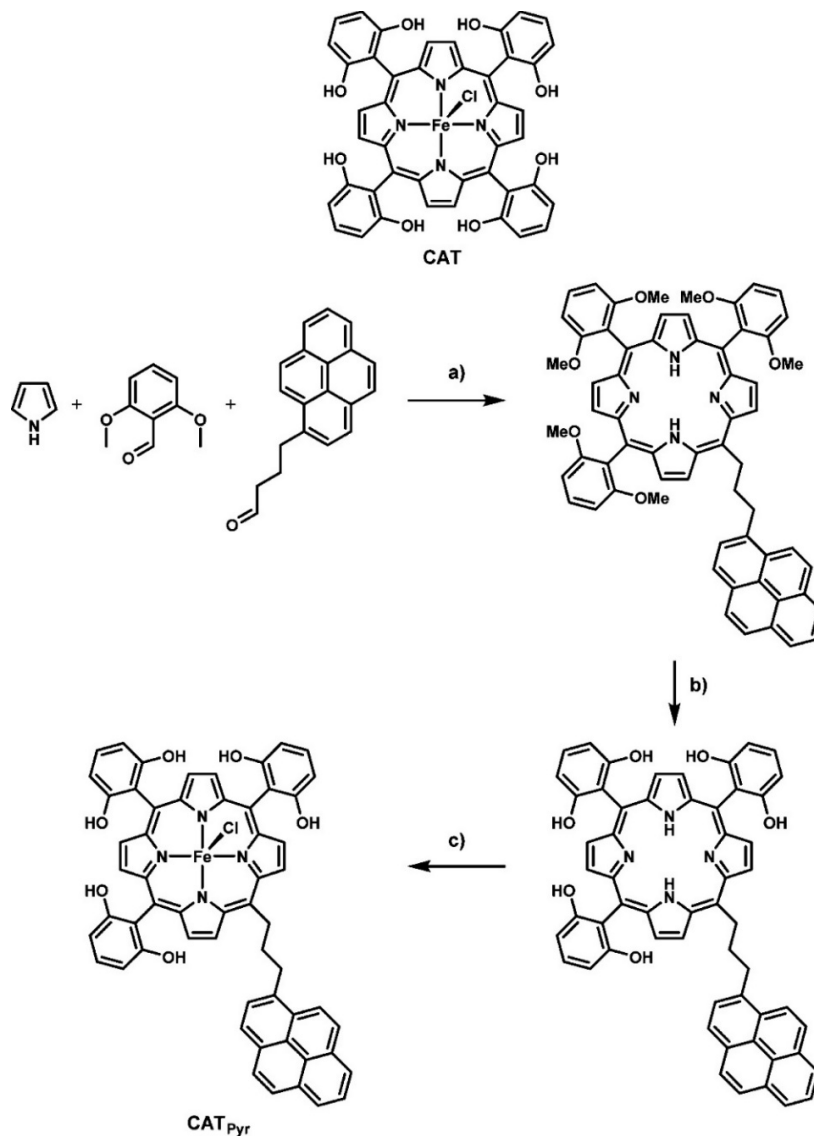


Figure 1.5 Synthetic scheme for the pyrene modified iron porphyrin used by Robert and co-workers for the CO₂RR in aqueous electrolyte.⁵⁷ Reproduced from *J. Am. Chem. Soc.*, **2016**, 138, 2492-2495., with permission from the American Chemistry Society.

1.3 Covalent Attachment Methods

As an alternative to non-covalent interactions, covalent attachment strategies can be used to form direct bonds between a carbon electrode and a molecular catalyst. Systems created by this method are often more robust than non-covalent systems and can be used in any solvent without risking displacement of the catalyst. This strategy also prevents films delamination due to bubble formation during an electrolysis. Many synthetic methods exist for covalently attaching molecular catalysts, but most require specific functional groups to be present on either the carbon electrode, the catalyst, or both.

1.3.1 Pyrazine Bond Formation

Surendranath and co-workers reported a novel method of attaching molecular catalysts to graphitic carbon surfaces. Their method takes advantage of the inherent *o*-quinone moieties present at edge planes and step-edge defects on the graphitic carbon. Complexes modified to contain an *o*-phenylenediamine functionality can irreversibly condense with the *o*-quinone moiety on the electrode to form conjugated pyrazine linkers. Using this method they attached both a ruthenium and rhodium catalyst to glassy carbon surfaces (Figure 1.6).⁵⁸ Interestingly, CVs of the material did not display the expected redox couples of the attached catalyst. Instead, their data suggests that the coupling of the catalyst to the electrode through the pyrazine link is so strong that the metal center remains in electronic equilibrium with the electrode itself. This result holds great promise for future heterogenization of molecular electrocatalysts.

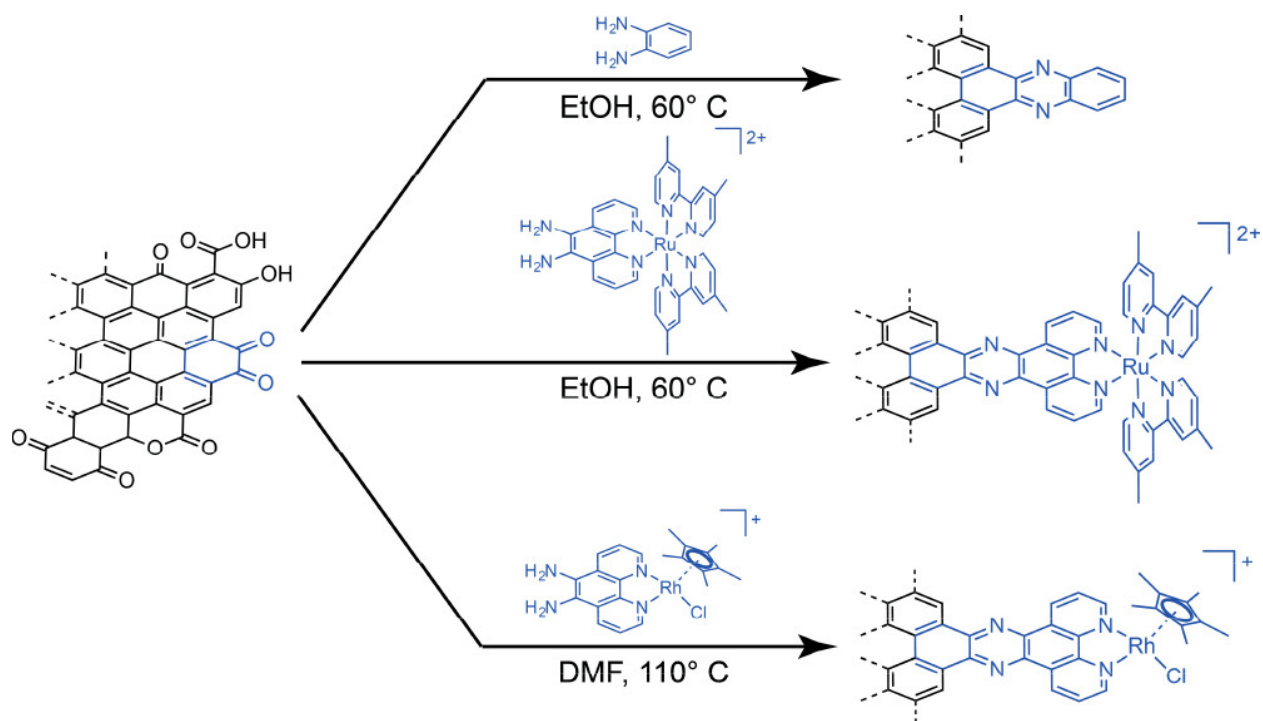


Figure 1.6 Pyrazine conjugation between a glassy carbon electrode and a molecular catalyst containing an o-diamine moiety.⁵⁸ Reproduced from *J. Am. Chem. Soc.*, **2018**, 140, 1004-1010., with permission from the American Chemistry Society.

1.3.2 Amide Bond Formation

Shaw and co-workers used amide-bond formation to attach both a molecular catalyst and a hydrogenase enzyme to glassy carbon electrodes in order to compare them for the hydrogen oxidation reaction (HOR).⁵⁹ They attached them by reacting carboxylic acid moieties on the complexes with amine-functionalized glassy carbon electrodes (Figure 1.7). This method can be used in aqueous solution which makes it much more compatible with enzymes. They found that the molecular catalyst showed a similar response to the enzyme with the enzyme being more active at pH 7 and the catalyst more active at pH 3. Interestingly, the enzyme also demonstrated improved stability when compared to the catalyst. This work highlights how surface attachment can be used to enhance the study of molecular electrocatalysts. Here it directly enabled the comparison of a

molecular catalyst with a bio-enzyme, something that would be much harder in homogenous solution. As an additional note, the functionalization of the glassy carbon electrodes with amines used a second surface modification technique called diazonium coupling. This will be discussed directly below.

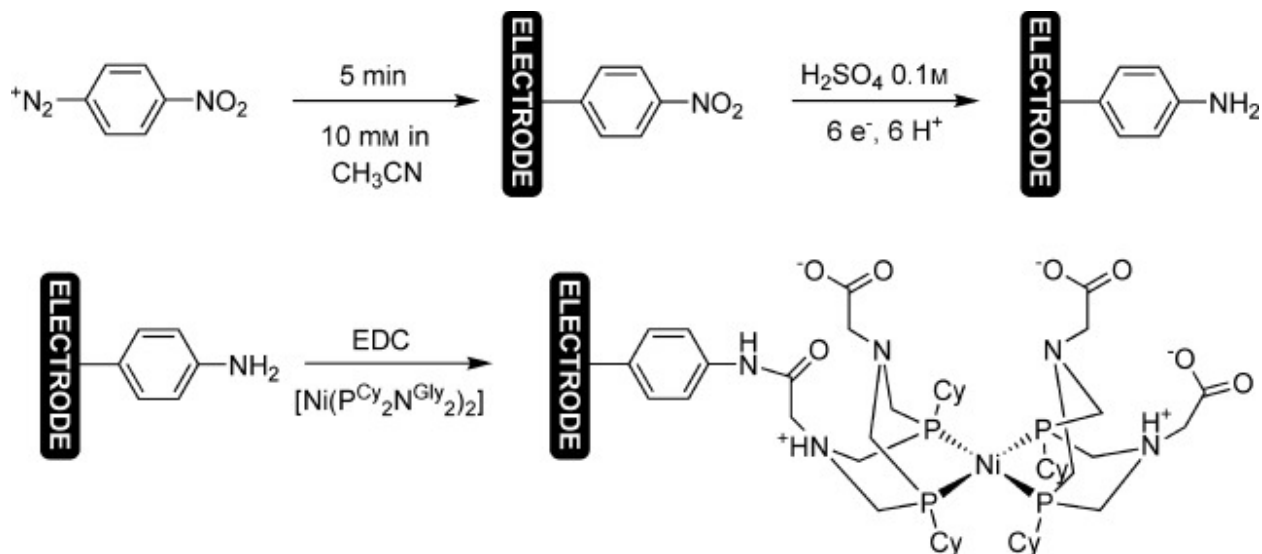


Figure 1.7 Amide bond formation between an amine-functionalized glassy carbon electrode and a carboxylic acid containing nickel catalyst.⁵⁹ EDC stands for 1-Ethyl-3-(3-dimethylaminopropyl)carbodiimide which is used to activate the carboxylic acid. Note that this reaction is performed in water. Reproduced from *Angew. Chem. Int. Ed.*, **2015**, 54, 12303-12307., with permission from John Wiley & Sons.

1.3.3 Diazonium Coupling

Diazonium coupling is a radical-based surface modification technique that only requires the molecular complex to contain an aryl diazonium salt. The salt can be synthesized in advance or generated *in situ* from a parent aniline.⁶⁰ The diazonium salt is then reduced, usually electrochemically although molecular reducing agents can also be used. This results in the evolution of dinitrogen and the formation of an aryl radical which can react with the glassy carbon substrate to form a covalent bond (Figure 1.8). It is important to note that because this method uses a radical complex to form the bond, there is minimal control over the surface structure. The generated radicals can react with complexes already on the surface to form branched multi-layer films.

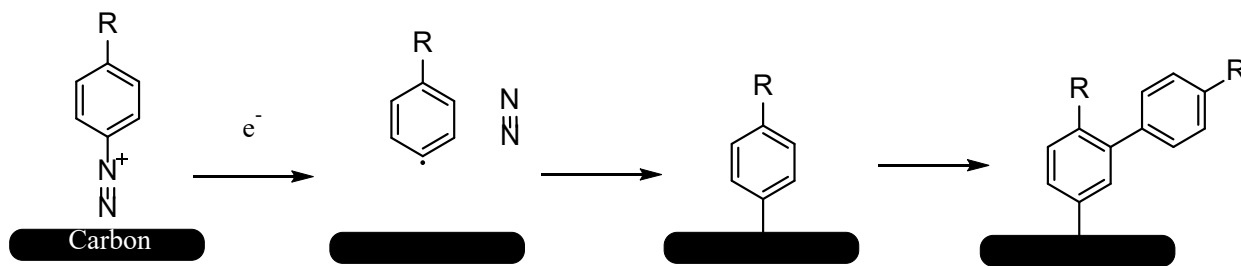


Figure 1.8 Mechanism of diazonium salt grafting of molecular complexes to glassy carbon. Note that because it is a radical based mechanism there is minimal control over the surface structure and multi-layer grafting can occur.

Diazonium coupling is generally used to modify surfaces in two ways. The first, as shown by Shaw and co-workers in Figure 1.7, is to modify a carbon electrode with an aryl diazonium salt containing a functional group that will selectively form a bond with another functional group on the desired catalyst. Shaw and co-workers, for example, modified glassy carbon electrodes with aryl amines that they could use to form amide bonds with carboxylic acid containing complexes.⁶¹

Carbon electrodes can also be modified with azide or ethynyl groups which can be used to attach molecular complexes using the Cu(I) catalyzed Azide Alkyne Cycloaddition (CuAAC) or “click” reaction (Figure 1.9).^{62, 63}

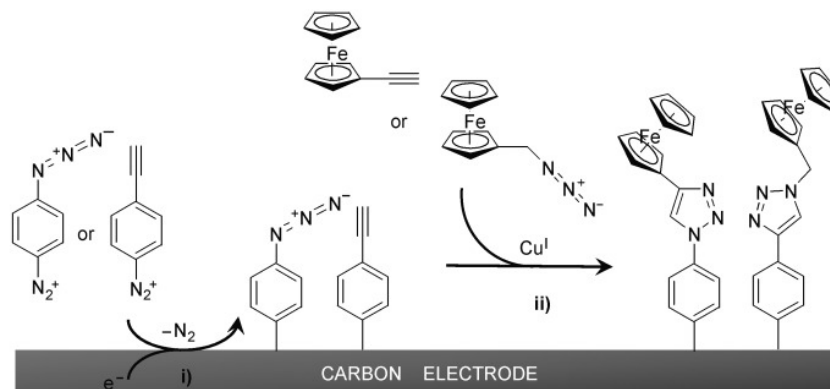


Figure 1.9 Diazonium salt modification of a carbon electrode with azide and ethynyl functional groups. These groups can then be used to attach complexes to the electrode using the Cu(I) Catalyzed Azide Alkyne Cycloaddition (CuAAC).⁶² Reproduced from *Chem. Eur. J.*, 2008, 14, 9286-9291., with permission from John Wiley & Sons.

Alternatively, diazonium coupling can be used to directly attach a catalyst to an electrode surface. Lin and co-workers used diazonium coupling to directly graft both rhenium and manganese bipyridine complexes to a carbon electrode (Figure 1.10).⁶⁴ Surface attachment of the rhenium complex is especially beneficial because it helps to prevent the complex from undergoing intermolecular deactivation. Lin and co-workers were able to use the modified electrodes to generate CO from the CO_2RR and H_2 from the HER. The H_2 was generated from bare glassy carbon, and they found that the CO/H_2 ratio could be modulated by controlling the CO_2 diffusion rate or by changing the surface coverage of the catalyst. This makes the electrodes a promising candidate for production of syngas in a one-pot electrochemical setup.

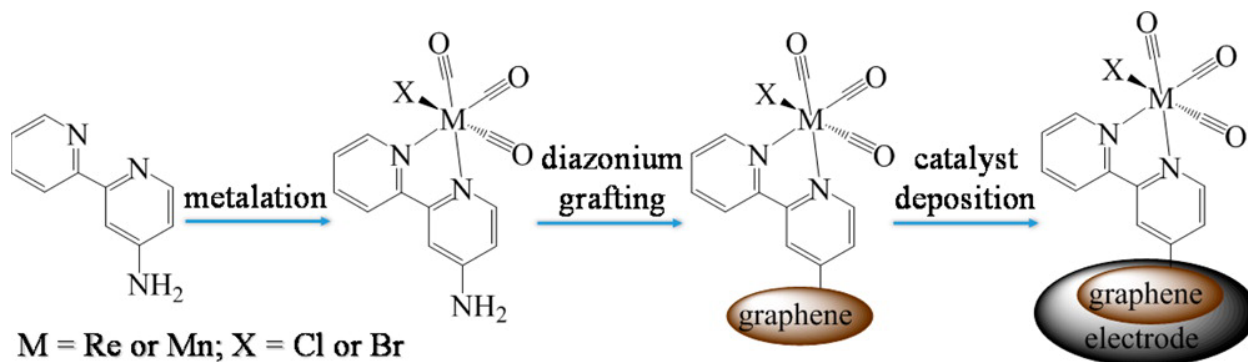


Figure 1.10 Synthesis procedure for attaching Re and Mn bipyridine catalysts to glassy carbon using diazonium salt grafting. Note how the diazonium salt is formed from the parent amine prior to surface attachment.⁶⁴ Reproduced from *ACS Appl. Mater. Interfaces.*, **2016**, 14, 4192-4198., with permission from the American Chemistry Society.

1.3.4 Copper(I) Catalyzed Azide Alkyne Cycloaddition

As noted earlier, the Cu(I) Catalyzed Azide Alkyne Cycloaddition (CuAAC) or “click” chemistry is a highly robust surface modification technique which can be used to attach a wide variety of complexes to an electrode surface^{61, 63, 65-70} (Figure 1.11). Due to its use in later chapters of this thesis, a more in-depth profile of the “click” reaction will be presented here. The reaction requires both a terminal azide and a terminal alkyne which, when reacted in the presence of a Cu(I) catalyst, will form a triazole linker. Because it is relatively simple to modify a carbon surface with azide groups, the alkyne is generally attached to the catalyst, usually through a Sonogashira coupling. There are two commonly used methods for modifying the electrode surface with azides. The first is by reacting a carbon electrode with iodine azide (generated *in situ*) to generate an azide monolayer directly on the electrode surface, and the second is through diazonium coupling with an azide-modified diazonium complex. For the first method the carbon surface must be initially treated to remove any surface oxidation prior to the azidification step. This is done either by heating the electrode in a reducing atmosphere^{38, 70} (forming gas which is 5% H₂ in N₂ is commonly

used here) or by polishing the electrode in an oxygen free environment like a glovebox.^{61, 69} The oxygen free surface is then exposed to iodine azide, which can be generated *in situ* by combining an azide source (e.g. NaN_3 or Bu_4N_3) with ICl in an organic solvent such as acetonitrile or hexanes. It is important that these reactions be carried out in the dark to avoid UV-activated decomposition of the azides. The azidified surface can then be used in CuAACs to attach molecular complexes covalently to the electrode surface. The resulting triazole linker has been previously shown to be very stable in strongly acidic and alkaline conditions,^{38, 68} and is robust to exposure to 1 M HClO_4 and 1 M NaOH at 100 °C for at least 12 h.

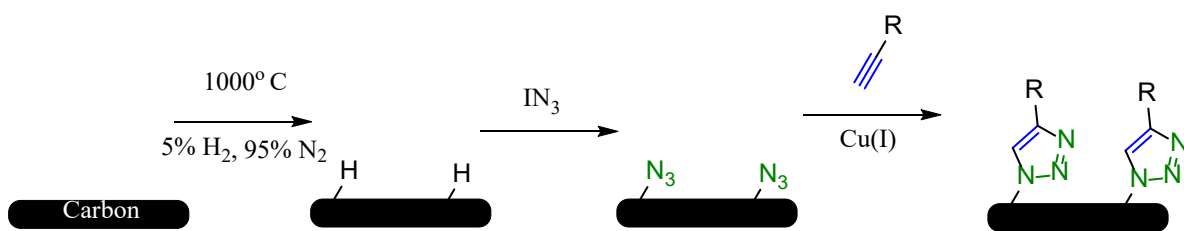


Figure 1.11 A generalized reaction scheme for modification of an azide modified carbon electrode with the CuAAC “click” reaction.

There are several important points to be made about this procedure. Generally a copper chelating ligand such as TBTA (Tris(benzyltriazolylmethyl)amine) will be added to help stabilize the Cu(I) catalyst. In addition, it is possible to use either Cu(II) and a reducing agent such as ascorbic acid, or to employ only a Cu(I) catalyst such as copper iodide. The choice largely depends on the molecule that is to be attached to the surface. Cu(II) and ascorbic acid is easier to work with as the use of excess ascorbic acid can keep the solution oxygen free over the course of the reaction. However, if you are attempting to attach an organometallic complex, such as rhenium bipyridine, there is the possibility that the copper used as the catalyst will displace the metal center of the complex. In these cases, it is better to use a Cu(I) catalyst and no reducing agent. The Cu(I) should have a lower binding affinity than the metal center, which will remain in a more oxidized form

due to the lack of any reducing agent. However, when using Cu(I) it is more important to ensure that your CuAAC solution is air free as once the Cu(I) is oxidized to Cu(II), it is no longer able to catalyze the reaction and is more likely to displace the metal center of your complex.

The second option for modifying a carbon surface with azides is to use diazonium coupling. As shown in Figure 1.9, an aryl azide can be electrografted to a carbon electrode. The steps following the azidification are analogous to those described for a surface modified with iodine azide. It is also possible to use this method to attach a terminal aryl alkyne. However, because it is generally easier to attach an ethynyl moiety to a molecular complex it is recommended to modify the carbon surface with an azide.

Chidsey and co-workers used the CuAAC to attach copper ethynyl phenanthroline complexes to glassy carbon electrodes and study their activity for the ORR.⁷⁰ The covalent attachment of the catalyst to the electrode surface revealed that there are two mechanisms for the ORR by copper phenanthroline. The first is a mononuclear $2 e^-$ reduction of O_2 to H_2O_2 while the second is a binuclear $4 e^-$ reduction of O_2 to H_2O that involves two metal centers (See Figure 1.12). This was determined by looking at the activity of the modified electrodes compared to the surface coverage of copper. There was a 2nd order dependence of the activity on the copper surface coverage. Previous studies of copper phenanthroline physisorbed onto edge plane graphite had only a 1st order dependence on the surface coverage of the catalyst.⁴³ The 1st order coverage seen on edge plane graphite is due to the catalysts mobility on the surface. Once O_2 is bound by a single copper phenanthroline a second can quickly combine with it to form a binuclear complex. It was only by constraining the copper phenanthrolines to the surface through “click” chemistry that the binuclear mechanism was revealed.

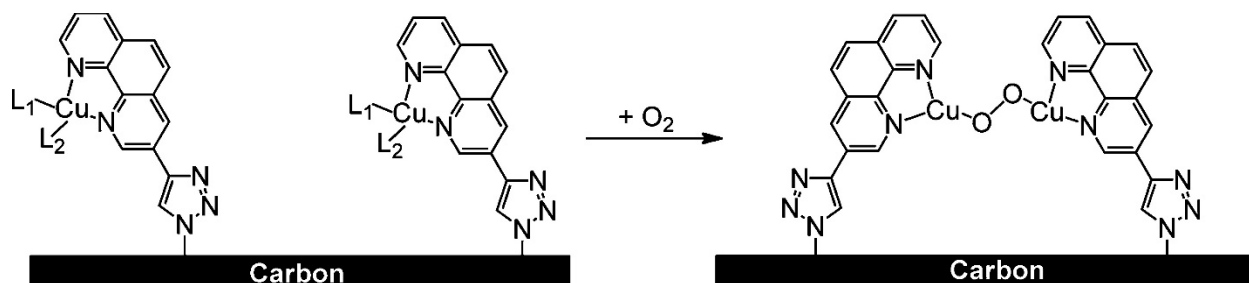


Figure 1.12 The proposed binuclear intermediate in the 4 e⁻ reduction of O₂ to H₂O by copper phenanthroline.⁷⁰ Reproduced from *J. Am. Chem. Soc.*, **2011**, 133, 3696-3699., with permission from the American Chemistry Society.

1.3.5 Electropolymerization

One more alternative method for catalyst immobilization is electropolymerization. Electropolymerization can be used to form electrocatalyst layers on multiple electrode surfaces, including carbon making it relatively versatile. However, due to the radical nature of these reactions the resulting surfaces are generally less well defined and amorphous surface-bound polymers are difficult to characterize. The resulting polymers can be conductive or non-conductive depending on the monomers used. Abruna and co-workers were able to synthesize electropolymerized films of vinyl terpyridine chelated to multiple metals including cobalt, chromium, and iron (Figure 1.13).^{71, 72} The resulting chromium-based films were active for the reduction of CO₂ to formate and formaldehyde in organic and aqueous solutions respectively. Increasing the loading of the catalyst on the surface resulted in lower activity per active site which they attribute to sluggish electron transport through the non-conductive film.

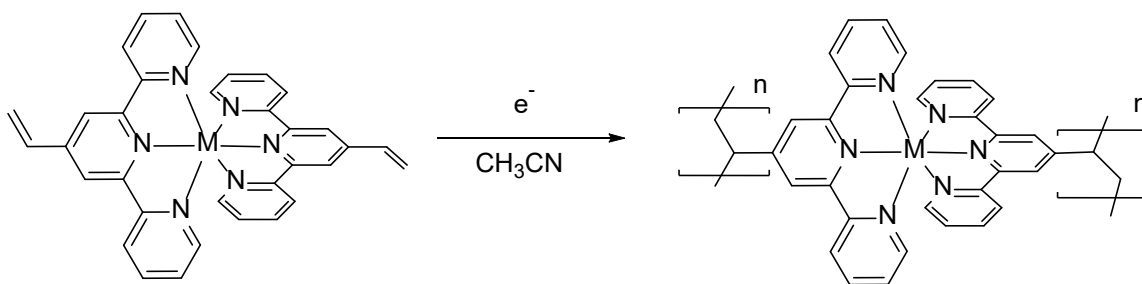


Figure 1.13 Electropolymerization of vinyl terpyridine metal complexes.

To generate conductive electropolymerized films a different monomer must be used. Polythiophene is a commonly used conductive polymer that can be synthesized by electropolymerization from thiophene based monomers. By attaching a catalyst to the thiophene monomer catalytically active and conductive films can be formed. Pilo and co-workers synthesized a thiophene based polymer containing ruthenium terthiophene complexes (See Figure 1.14).^{73, 74} Of note here is that they used a terthiophene based monomer for their electropolymerization. This is likely because thiophene monomers with substituents, especially bulky ones, can be exceedingly difficult to polymerize.⁷⁵ Switching to a terthiophene monomer can drastically increase the polymerization of molecule by both lowering the steric inhibition and decreasing the oxidation potential to a more negative value.

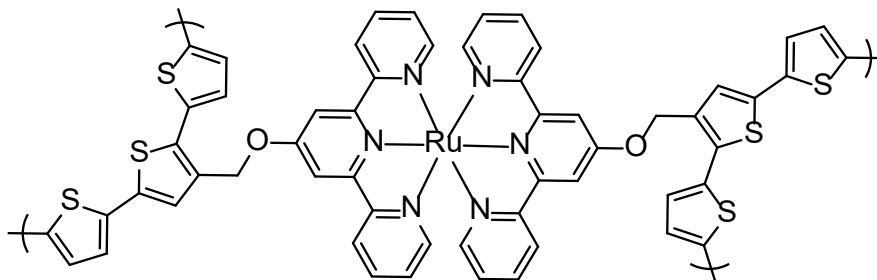


Figure 1.14 Polyterthiophene containing a ruthenium terpyridine catalyst.

1.3.6 Multi-Layer Approach

Despite the many advantages of heterogenization of molecular catalysts, the overall activity is still generally lower than those of their solid-state counterparts. This is largely due to the smaller number of active sites present on an electrode modified with a molecular catalyst compared to state-of-the-art nanostructured solid-state materials. For the vast majority of surface attachment methods presented in this Chapter there is an inherent limitation of a single layer of molecular catalysts on the electrode surface. This generally results in a surface coverage of around 10^{14} molecules cm^{-2} .^{39, 70} In order to reach activities comparable to state-of-the-art solid state catalytic systems either catalysts with extremely rapid TOFs would need to be designed or discovered, or the surface coverage of already known catalysts would need to be increased. One of the more straight-forward methods for increasing the surface coverage would be to add multiple layers of catalyst to the electrode. This increase in active sites per geometric surface area would increase the activity of the electrode,⁷⁶ while still maintaining the selectivity and tunability of the molecular catalyst. This highlights one of the major goals of my work presented in this thesis, which is the design and testing of systems that use multiple layers of molecular catalysts to obtain electrodes which operate with the *activity* of solid-state systems while maintaining the *selectivity* and *tunability* of molecular electrocatalysts. The following Chapters contains my work on two different methods for increasing surface coverage of molecular electrocatalysts on electrode surfaces. The first is a layer-by-layer approach using sequential Cu(I)-Catalyzed Azide-Alkyne Cycloadditions (Chapter 3) and the second is an oxidative electropolymerization of terthiophene modified with a molecular electrocatalyst (Chapter 5).

1.4 References

1. Electrocatalysis for the generation and consumption of fuels. *Nature Reviews Chemistry* **2018**, *2* (4), 0125.
2. Inagi, S.; Sawamura, T.; Fuchigami, T., Effects of additives on anodic fluorination in ionic liquid hydrogen fluoride salts. *Electrochemistry Communications* **2008**, *10* (8), 1158-1160.
3. Wiebe, A.; Gieshoff, T.; Möhle, S.; Rodrigo, E.; Zirbes, M.; Waldvogel, S. R., Electrifying Organic Synthesis. *Angewandte Chemie International Edition* **2018**, *57* (20), 5594-5619.
4. Vasilopoulos, A.; Zultanski, S. L.; Stahl, S. S., Feedstocks to Pharmacophores: Cu-Catalyzed Oxidative Arylation of Inexpensive Alkylarenes Enabling Direct Access to Diarylalkanes. *Journal of the American Chemical Society* **2017**, *139* (23), 7705-7708.
5. Das, A.; Stahl, S. S., Noncovalent Immobilization of Molecular Electrocatalysts for Chemical Synthesis: Efficient Electrochemical Alcohol Oxidation with a Pyrene-TEMPO Conjugate. *Angewandte Chemie International Edition* **2017**, *56* (30), 8892-8897.
6. Kortlever, R.; Shen, J.; Schouten, K. J. P.; Calle-Vallejo, F.; Koper, M. T. M., Catalysts and Reaction Pathways for the Electrochemical Reduction of Carbon Dioxide. *The Journal of Physical Chemistry Letters* **2015**, *6* (20), 4073-4082.
7. Jackson, M. N.; Surendranath, Y., Molecular Control of Heterogeneous Electrocatalysis through Graphite Conjugation. *Accounts of Chemical Research* **2019**.
8. Garlyyev, B.; Fichtner, J.; Piqué, O.; Schneider, O.; Bandarenka, A. S.; Calle-Vallejo, F., Revealing the nature of active sites in electrocatalysis. *Chemical Science* **2019**, *10* (35), 8060-8075.
9. Ma, L.; Hu, W.; Mei, B.; Liu, H.; Yuan, B.; Zang, J.; Chen, T.; Zou, L.; Zou, Z.; Yang, B.; Yu, Y.; Ma, J.; Jiang, Z.; Wen, K.; Yang, H., Covalent Triazine Framework Confined Copper Catalysts for Selective Electrochemical CO₂ Reduction: Operando Diagnosis of Active Sites. *ACS Catalysis* **2020**, 4534-4542.
10. Huang, J.; Hörmann, N.; Oveisi, E.; Loiudice, A.; De Gregorio, G. L.; Andreussi, O.; Marzari, N.; Buonsanti, R., Potential-induced nanoclustering of metallic catalysts during electrochemical CO₂ reduction. *Nature Communications* **2018**, *9* (1), 3117.
11. Grosse, P.; Gao, D.; Scholten, F.; Sinev, I.; Mistry, H.; Roldan Cuenya, B., Dynamic Changes in the Structure, Chemical State and Catalytic Selectivity of Cu Nanocubes during CO₂ Electroreduction: Size and Support Effects. *Angewandte Chemie International Edition* **2018**, *57* (21), 6192-6197.
12. Jeong, H. M.; Kwon, Y.; Won, J. H.; Lum, Y.; Cheng, M.-J.; Kim, K. H.; Head-Gordon, M.; Kang, J. K., Atomic-Scale Spacing between Copper Facets for the Electrochemical Reduction of Carbon Dioxide. *Advanced Energy Materials* **2020**, *10* (10), 1903423.
13. Shen, S.; He, J.; Peng, X.; Xi, W.; Zhang, L.; Xi, D.; Wang, L.; Liu, X.; Luo, J., Stepped surface-rich copper fiber felt as an efficient electrocatalyst for the CO₂RR to formate. *Journal of Materials Chemistry A* **2018**, *6* (39), 18960-18966.
14. Kuhl, K. P.; Cave, E. R.; Abram, D. N.; Jaramillo, T. F., New insights into the electrochemical reduction of carbon dioxide on metallic copper surfaces. *Energy & Environmental Science* **2012**, *5* (5), 7050-7059.
15. Hatsukade, T.; Kuhl, K. P.; Cave, E. R.; Abram, D. N.; Jaramillo, T. F., Insights into the electrocatalytic reduction of CO₂ on metallic silver surfaces. *Physical Chemistry Chemical Physics* **2014**, *16* (27), 13814-13819.

16. Hall, A. S.; Yoon, Y.; Wuttig, A.; Surendranath, Y., Mesostructure-Induced Selectivity in CO₂ Reduction Catalysis. *Journal of the American Chemical Society* **2015**, *137* (47), 14834-14837.
17. Reske, R.; Mistry, H.; Behafarid, F.; Roldan Cuenya, B.; Strasser, P., Particle Size Effects in the Catalytic Electroreduction of CO₂ on Cu Nanoparticles. *Journal of the American Chemical Society* **2014**, *136* (19), 6978-6986.
18. Feng, X.; Jiang, K.; Fan, S.; Kanan, M. W., A Direct Grain-Boundary-Activity Correlation for CO Electroreduction on Cu Nanoparticles. *ACS Central Science* **2016**, *2* (3), 169-174.
19. Kim, D.; Kley, C. S.; Li, Y.; Yang, P., Copper nanoparticle ensembles for selective electroreduction of CO₂ to C₂-C₃ products. *Proceedings of the National Academy of Sciences* **2017**, *114* (40), 10560-10565.
20. Liu, Y.; Leung, K. Y.; Michaud, S. E.; Soucy, T. L.; McCrory, C. C. L., Controlled Substrate Transport to Electrocatalyst Active Sites for Enhanced Selectivity in the Carbon Dioxide Reduction Reaction. *Comments on Inorganic Chemistry* **2019**, *39* (5), 242-269.
21. Agarwal, J.; Shaw, T. W.; Schaefer, H. F.; Bocarsly, A. B., Design of a Catalytic Active Site for Electrochemical CO₂ Reduction with Mn(I)-Tricarbonyl Species. *Inorganic Chemistry* **2015**, *54* (11), 5285-5294.
22. Bullock, R. M.; Das, A. K.; Appel, A. M., Surface Immobilization of Molecular Electrocatalysts for Energy Conversion. *Chemistry – A European Journal* **2017**, *23* (32), 7626-7641.
23. Costentin, C.; Savéant, J.-M., Towards an intelligent design of molecular electrocatalysts. *Nature Reviews Chemistry* **2017**, *1* (11), 0087.
24. Gonell, S.; Massey, M. D.; Moseley, I. P.; Schauer, C. K.; Muckerman, J. T.; Miller, A. J. M., The Trans Effect in Electrocatalytic CO₂ Reduction: Mechanistic Studies of Asymmetric Ruthenium Pyridyl-Carbene Catalysts. *Journal of the American Chemical Society* **2019**, *141* (16), 6658-6671.
25. Hellman, A. N.; Haiges, R.; Marinescu, S. C., Rhenium bipyridine catalysts with hydrogen bonding pendant amines for CO₂ reduction. *Dalton Transactions* **2019**, *48* (38), 14251-14255.
26. McCrory, C. C. L.; Ottenwaelder, X.; Stack, T. D. P.; Chidsey, C. E. D., Kinetic and Mechanistic Studies of the Electrocatalytic Reduction of O₂ to H₂O with Mononuclear Cu Complexes of Substituted 1,10-Phenanthrolines *The Journal of Physical Chemistry A* **2007**, *111* (49), 12641-12650.
27. Ngo, K. T.; McKinnon, M.; Mahanti, B.; Narayanan, R.; Grills, D. C.; Ertem, M. Z.; Rochford, J., Turning on the Protonation-First Pathway for Electrocatalytic CO₂ Reduction by Manganese Bipyridyl Tricarbonyl Complexes. *Journal of the American Chemical Society* **2017**, *139* (7), 2604-2618.
28. Smieja, J. M.; Kubiak, C. P., Re(bipy-tBu)(CO)₃Cl-improved Catalytic Activity for Reduction of Carbon Dioxide: IR-Spectroelectrochemical and Mechanistic Studies. *Inorganic Chemistry* **2010**, *49* (20), 9283-9289.
29. Nie, W.; Wang, Y.; Zheng, T.; Ibrahim, A.; Xu, Z.; McCrory, C. C. L., Electrocatalytic CO₂ Reduction by Cobalt Bis(pyridylmonoimine) Complexes: Effect of Ligand Flexibility on Catalytic Activity. *ACS Catalysis* **2020**.
30. Abe, T.; Yoshida, T.; Tokita, S.; Taguchi, F.; Imai, H.; Kaneko, M., Factors affecting selective electrocatalytic CO₂ reduction with cobalt phthalocyanine incorporated in a

- polyvinylpyridine membrane coated on a graphite electrode. *Journal of Electroanalytical Chemistry* **1996**, *412* (1), 125-132.
31. Kramer, W. W.; McCrory, C. C. L., Polymer coordination promotes selective CO₂ reduction by cobalt phthalocyanine. *Chemical Science* **2016**, *7* (4), 2506-2515.
 32. Liu, Y.; McCrory, C. C. L., Modulating the mechanism of electrocatalytic CO₂ reduction by cobalt phthalocyanine through polymer coordination and encapsulation. *Nature Communications* **2019**, *10* (1), 1683.
 33. Yoshida, T.; Kamato, K.; Tsukamoto, M.; Iida, T.; Schlettwein, D.; Wöhrle, D.; Kaneko, M., Selective electrocatalysis for CO₂ reduction in the aqueous phase using cobalt phthalocyanine/poly-4-vinylpyridine modified electrodes. *Journal of Electroanalytical Chemistry* **1995**, *385* (2), 209-225.
 34. Nie, W.; McCrory, C. C. L., Electrocatalytic CO₂ reduction by a cobalt bis(pyridylmonoimine) complex: effect of acid concentration on catalyst activity and stability. *Chemical Communications* **2018**, *54* (13), 1579-1582.
 35. Riplinger, C.; Sampson, M. D.; Ritzmann, A. M.; Kubiak, C. P.; Carter, E. A., Mechanistic Contrasts between Manganese and Rhenium Bipyridine Electrocatalysts for the Reduction of Carbon Dioxide. *Journal of the American Chemical Society* **2014**, *136* (46), 16285-16298.
 36. Costentin, C.; Drouet, S.; Robert, M.; Savéant, J.-M., A Local Proton Source Enhances CO₂ Electroreduction to CO by a Molecular Fe Catalyst. *Science* **2012**, *338* (6103), 90-94.
 37. Costentin, C.; Robert, M.; Savéant, J.-M., Catalysis of the electrochemical reduction of carbon dioxide. *Chemical Society Reviews* **2013**, *42* (6), 2423-2436.
 38. Devadoss, A.; Chidsey, C. E. D., Azide-Modified Graphitic Surfaces for Covalent Attachment of Alkyne-Terminated Molecules by “Click” Chemistry. *Journal of the American Chemical Society* **2007**, *129* (17), 5370-5371.
 39. Kallick, J. D.; Feng, W.-J.; McCrory, C. C. L., Controlled Formation of Multilayer Films of Discrete Molecular Catalysts for the Oxygen Reduction Reaction Using a Layer-by-Layer Growth Mechanism Based on Sequential Click Chemistry. *ACS Applied Energy Materials* **2020**, *3* (7), 6222-6231.
 40. Zhang, J.; Anson, F. C., Complexes of Cu(II) with electroactive chelating ligands adsorbed on graphite electrodes: Surface coordination chemistry and electrocatalysis. *Journal of Electroanalytical Chemistry* **1993**, *348* (1), 81-97.
 41. Zhang, J.; Anson, F. C., Electrocatalysts for the reduction of O₂ and H₂O₂ based on complexes of Cu(II) with the strongly adsorbing 2,9-dimethyl-1,10-phenanthroline ligand. *Electrochimica Acta* **1993**, *38* (16), 2423-2429.
 42. Zhang, J.; Anson, F. C., Electrochemistry of the Cu(II) complex of 4,7-diphenyl-1,10-phenanthroline disulfonate adsorbed on graphite electrodes and its behavior as an electrocatalyst for the reduction of O₂ and H₂O₂. *Journal of Electroanalytical Chemistry* **1992**, *341* (1), 323-341.
 43. Lei, Y.; Anson, F. C., Mechanistic aspects of the electroreduction of dioxygen as catalyzed by copper-phenanthroline complexes adsorbed on graphite electrodes. *Inorganic Chemistry* **1994**, *33* (22), 5003-5009.
 44. McCrory, C. C. L.; Ottenwaelde, X.; Stack, T. D. P.; Chidsey, C. E. D., Kinetic and Mechanistic Studies of the Electrocatalytic Reduction of O₂ to H₂O with Mononuclear Cu

Complexes of Substituted 1,10-Phenanthrolines. *The Journal of Physical Chemistry A* **2007**, *111* (49), 12641-12650.

45. Aga, H.; Aramata, A.; Hisaeda, Y., The electroreduction of carbon dioxide by macrocyclic cobalt complexes chemically modified on a glassy carbon electrode. *Journal of Electroanalytical Chemistry* **1997**, *437* (1), 111-118.
46. Isaacs, M.; Armijo, F.; Ramírez, G.; Trollund, E.; Biaggio, S. R.; Costamagna, J.; Aguirre, M. J., Electrochemical reduction of CO₂ mediated by poly-M-aminophthalocyanines (M=Co, Ni, Fe): poly-Co-tetraaminophthalocyanine, a selective catalyst. *Journal of Molecular Catalysis A: Chemical* **2005**, *229* (1), 249-257.
47. Scheffler, M.; Smykalla, L.; Baumann, D.; Schlegel, R.; Hänke, T.; Toader, M.; Büchner, B.; Hietschold, M.; Hess, C., Structural study of monolayer cobalt phthalocyanine adsorbed on graphite. *Surface Science* **2013**, *608*, 55-60.
48. Schlettwein, D.; Yoshida, T., Electrochemical reduction of substituted cobalt phthalocyanines adsorbed on graphite. *Journal of Electroanalytical Chemistry* **1998**, *441* (1), 139-146.
49. Zagal, J.; Páez, M.; Tanaka, A. A.; dos Santos, J. R.; Linkous, C. A., Electrocatalytic activity of metal phthalocyanines for oxygen reduction. *Journal of Electroanalytical Chemistry* **1992**, *339* (1), 13-30.
50. Zagal, J. H., Metallophthalocyanines as catalysts in electrochemical reactions. *Coordination Chemistry Reviews* **1992**, *119*, 89-136.
51. Li, F.; Zhang, B.; Li, X.; Jiang, Y.; Chen, L.; Li, Y.; Sun, L., Highly Efficient Oxidation of Water by a Molecular Catalyst Immobilized on Carbon Nanotubes. *Angewandte Chemie International Edition* **2011**, *50* (51), 12276-12279.
52. Tran, P. D.; Le Goff, A.; Heidkamp, J.; Jusselme, B.; Guillet, N.; Palacin, S.; Dau, H.; Fontecave, M.; Artero, V., Noncovalent Modification of Carbon Nanotubes with Pyrene-Functionalized Nickel Complexes: Carbon Monoxide Tolerant Catalysts for Hydrogen Evolution and Uptake. *Angewandte Chemie International Edition* **2011**, *50* (6), 1371-1374.
53. Blakemore, J. D.; Gupta, A.; Warren, J. J.; Brunschwigg, B. S.; Gray, H. B., Noncovalent Immobilization of Electrocatalysts on Carbon Electrodes for Fuel Production. *Journal of the American Chemical Society* **2013**, *135* (49), 18288-18291.
54. Gentil, S.; Serre, D.; Philouze, C.; Holzinger, M.; Thomas, F.; Le Goff, A., Electrocatalytic O₂ Reduction at a Bio-inspired Mononuclear Copper Phenolato Complex Immobilized on a Carbon Nanotube Electrode. *Angewandte Chemie International Edition* **2016**, *55* (7), 2517-2520.
55. Lalaoui, N.; Means, N.; Walgama, C.; Le Goff, A.; Holzinger, M.; Krishnan, S.; Cosnier, S., Enzymatic versus Electrocatalytic Oxidation of NADH at Carbon-Nanotube Electrodes Modified with Glucose Dehydrogenases: Application in a Bucky-Paper-Based Glucose Enzymatic Fuel Cell. *ChemElectroChem* **2016**, *3* (12), 2058-2062.
56. Lalaoui, N.; Reuillard, B.; Philouze, C.; Holzinger, M.; Cosnier, S.; Le Goff, A., Osmium(II) Complexes Bearing Chelating N-Heterocyclic Carbene and Pyrene-Modified Ligands: Surface Electrochemistry and Electron Transfer Mediation of Oxygen Reduction by Multicopper Enzymes. *Organometallics* **2016**, *35* (17), 2987-2992.
57. Maurin, A.; Robert, M., Noncovalent Immobilization of a Molecular Iron-Based Electrocatalyst on Carbon Electrodes for Selective, Efficient CO₂-to-CO Conversion in Water. *Journal of the American Chemical Society* **2016**, *138* (8), 2492-2495.

58. Jackson, M. N.; Oh, S.; Kaminsky, C. J.; Chu, S. B.; Zhang, G.; Miller, J. T.; Surendranath, Y., Strong Electronic Coupling of Molecular Sites to Graphitic Electrodes via Pyrazine Conjugation. *Journal of the American Chemical Society* **2018**, *140* (3), 1004-1010.
59. Rodriguez-Maciá, P.; Dutta, A.; Lubitz, W.; Shaw, W. J.; Rüdiger, O., Direct Comparison of the Performance of a Bio-inspired Synthetic Nickel Catalyst and a [NiFe]-Hydrogenase, Both Covalently Attached to Electrodes. *Angewandte Chemie International Edition* **2015**, *54* (42), 12303-12307.
60. Mahouche-Chergui, S.; Gam-Derouich, S.; Mangeney, C.; Chehimi, M. M., Aryl diazonium salts: a new class of coupling agents for bonding polymers, biomacromolecules and nanoparticles to surfaces. *Chemical Society Reviews* **2011**, *40* (7), 4143-4166.
61. Das, A. K.; Engelhard, M. H.; Bullock, R. M.; Roberts, J. A. S., A Hydrogen-Evolving Ni(P2N2)2 Electrocatalyst Covalently Attached to a Glassy Carbon Electrode: Preparation, Characterization, and Catalysis. Comparisons with the Homogeneous Analogue. *Inorganic Chemistry* **2014**, *53* (13), 6875-6885.
62. Evrard, D.; Lambert, F.; Policar, C.; Balland, V.; Limoges, B., Electrochemical Functionalization of Carbon Surfaces by Aromatic Azide or Alkyne Molecules: A Versatile Platform for Click Chemistry. *Chemistry – A European Journal* **2008**, *14* (30), 9286-9291.
63. Zhanaidarova, A.; Ostericher, A. L.; Miller, C. J.; Jones, S. C.; Kubiak, C. P., Selective Reduction of CO₂ to CO by a Molecular Re(ethynyl-bpy)(CO)₃Cl Catalyst and Attachment to Carbon Electrode Surfaces. *Organometallics* **2019**, *38* (6), 1204-1207.
64. Zhou, X.; Micheroni, D.; Lin, Z.; Poon, C.; Li, Z.; Lin, W., Graphene-Immobilized fac-Re(bipy)(CO)₃Cl for Syngas Generation from Carbon Dioxide. *ACS Applied Materials & Interfaces* **2016**, *8* (6), 4192-4198.
65. Raicopol, M. D.; Chira, N. A.; Pandele, A. M.; Hanganu, A.; Ivanov, A. A.; Tecuceanu, V.; Bugean, I. G.; Buica, G.-O., Electrodes modified with clickable thiosemicarbazone ligands for sensitive voltammetric detection of Hg(II) ions. *Sensors and Actuators B: Chemical* **2020**, *313*, 128030.
66. Mpetta, L. S.; Sen, P.; Nyokong, T., Investigation of electrocatalytic behaviour of low symmetry cobalt phthalocyanines when clicked to azide grafted carbon electrodes. *Journal of Electroanalytical Chemistry* **2020**, *860*, 113896.
67. Cluff, D. B.; Arnold, A.; Fettinger, J. C.; Berben, L. A., Electrocatalytic Reduction of CO₂ into Formate with Glassy Carbon Modified by [Fe₄N(CO)₁₁(PPh₂Ph-linker)]⁻. *Organometallics* **2019**, *38* (6), 1230-1235.
68. Stenehjem, E. D.; Ziatdinov, V. R.; Stack, T. D. P.; Chidsey, C. E. D., Gas-Phase Azide Functionalization of Carbon. *Journal of the American Chemical Society* **2013**, *135* (3), 1110-1116.
69. Das, A. K.; Engelhard, M. H.; Liu, F.; Bullock, R. M.; Roberts, J. A. S., The Electrode as Organolithium Reagent: Catalyst-Free Covalent Attachment of Electrochemically Active Species to an Azide-Terminated Glassy Carbon Electrode Surface. *Inorganic Chemistry* **2013**, *52* (23), 13674-13684.
70. McCrory, C. C. L.; Devadoss, A.; Ottenwaelder, X.; Lowe, R. D.; Stack, T. D. P.; Chidsey, C. E. D., Electrocatalytic O₂ Reduction by Covalently Immobilized Mononuclear Copper(I) Complexes: Evidence for a Binuclear Cu₂O₂ Intermediate. *Journal of the American Chemical Society* **2011**, *133* (11), 3696-3699.
71. Potts, K. T.; Usifer, D. A.; Guadalupe, A.; Abruna, H. D., 4-Vinyl-, 6-vinyl-, and 4'-vinyl-2,2':6',2''-terpyridinyl ligands: their synthesis and the electrochemistry of their transition-

- metal coordination complexes. *Journal of the American Chemical Society* **1987**, *109* (13), 3961-3967.
72. Ramos Sende, J. A.; Arana, C. R.; Hernandez, L.; Potts, K. T.; Keshevarz-K, M.; Abruna, H. D., Electrocatalysis of CO₂ Reduction in Aqueous Media at Electrodes Modified with Electropolymerized Films of Vinylterpyridine Complexes of Transition Metals. *Inorganic Chemistry* **1995**, *34* (12), 3339-3348.
73. Scanu, R.; Manca, P.; Zucca, A.; Sanna, G.; Spano, N.; Seeber, R.; Zanardi, C.; Pilo, M. I., Homoleptic Ru(II) complex with terpyridine ligands appended with terthiophene moieties: Synthesis, characterization and electropolymerization. *Polyhedron* **2013**, *49* (1), 24-28.
74. Manca, P.; Scanu, R.; Zucca, A.; Sanna, G.; Spano, N.; Pilo, M. I., Electropolymerization of a Ru(II)-terpyridine complex ethynyl-terthiophene functionalized originating different metallopolymers. *Polymer* **2013**, *54* (14), 3504-3509.
75. Roncali, J.; Garreau, R.; Yassar, A.; Marque, P.; Garnier, F.; Lemaire, M., Effects of steric factors on the electrosynthesis and properties of conducting poly(3-alkylthiophenes). *The Journal of Physical Chemistry* **1987**, *91* (27), 6706-6714.
76. Sathrum, A. J.; Kubiak, C. P., Kinetics and Limiting Current Densities of Homogeneous and Heterogeneous Electrocatalysts. *The Journal of Physical Chemistry Letters* **2011**, *2* (18), 2372-2379.

Chapter 2 Major Electrochemical and Surface Techniques

The following sections will offer a mini-review of the major analytical and electrochemical techniques used throughout this Thesis. For those for whom these techniques are novel this this Chapter should offer a useful introduction, but readers are encouraged to explore other sources of information if they want a more in-depth explanation than can be found in a single Thesis Chapter. The final section of this Chapter is a list of sources readers may be interested in reading. Those already familiar with certain techniques may still find the refresher useful.

2.1 X-Ray Photoelectron Spectroscopy

This overview is intended to give a background into the basic scientific principles behind XPS and give a brief practical guide to interpreting XPS data.

2.1.1 Introduction

X-Ray Photoelectron Spectroscopy (XPS) is a highly valuable technique for gathering information about a materials surface composition.¹⁻³ What makes it unique among other surface techniques such as SEM/EDX is that XPS is incredibly surface sensitive. Unlike SEM/EDX which can penetrate into the μm , XPS only penetrates to about 8-10 nm making it highly valuable for examining surface modification.^{4, 5} XPS is also relatively simple to use and requires minimal sample preparation. It can give information about the surface composition, speciation, and bonding of elements making up the sample surface.⁶⁻¹⁰ It is important to note however, that while XPS can give relative ratios between different elements of a sample, it *cannot* give any quantitative values

of surface coverage. In other words, it is unable to tell you how much of an element there is, just how much there is compared to other elements within your sample. XPS is also a very useful tool for postmortem analysis of electrocatalyst surfaces. While it can't give quantitative changes it is extremely good at showing qualitative changes in both surface speciation and coverage, which can lead to valuable information about catalyst durability.^{11, 12}

2.1.2 XPS Principles

XPS in its most basic form is an application of the photoelectric effect.^{13, 14} The sample to be analyzed is bombarded with photons in the form of X-rays which results in the ejection of inner core electrons. The interaction between the photons and the electrons is completely lossless meaning that there is a complete transfer of energy from the photon to the electron. If the energy is high enough, the bombarded electron will be ejected from both the atom/ion it was bound to and from whatever solid it was a part of. It is any leftover kinetic energy (KE) of the electron that is measured by the XPS. From the KE the binding energy (BE) of the electron can be extrapolated (see Equation 2.1). Because the BE of an electron is element and environment specific it is a fairly straightforward process to determine the electron's source. It is important to note that if an electron ejected from its orbital interacts with the solid prior to be fully ejected from the solid it can lose part of its energy and become part of the spectral background. The likelihood of this happening increases *substantially* the deeper in the sample the electron is ejected from. This is why, even though the X-rays can penetrate micrometers in the sample, electrons can only be collected from the top ~10 nanometers.

$$(2.1) \quad K.E.e^- = E_{ph} - \phi_{XPS} - B.E.e^-$$

In this equation $K.E_{e^-}$ is the kinetic energy of an electron ejected from a solid hit by a photon of energy E_{ph} . The binding energy of that electron ($B.E_{e^-}$) is element and environment specific and is the main source of information gathered during XPS analysis. The ϕ_{XPS} represents the work function of the instrument. This is the minimum energy required to remove an electron from the instrument and will be instrument specific. Note that this assumes that the sample is conductive and in contact with the instrument. For non-conductive samples, a charge buildup will occur, although most XPS instruments will have functions to help compensate for that charge.

2.1.3 Basic XPS Instrumentation

A basic diagram of an XPS instrument can be seen in Figure 2.1 (For a more in depth look at modern XPS instrumentation please refer to the following section). Note that depending on their construction the energy analyzer of the XPS may be different. The diagram used here depicts a Concentric Hemispherical Analyzer (CHA) although other types exist as well.¹⁵ As seen in the Figure, after an electron is ejected from the sample it first travels through a transfer lens. The transfer lens improves the transmission of electrons from the sample to the analyzer and can also be used in certain modes to alter the energy of the electrons passing through it. The lens is also used to redirect the ejected photoelectrons towards the analyzer such that the sample can be optimally positioned to interact with the incident X-ray beam and other XPS components. The electrons then enter the analyzer. The CHA displayed in Figure 2.1 works by applying a potential to both the outer and inner spheres such that only electrons of a certain energy will be able to pass through the analyzer and make it to the detector without colliding with the CHA walls. There are two main methods of operation for a CHA:

- 1) Constant Retard Ratio (CRR). In this mode of operation the potentials of the inner and outer spheres are scanned across a range of electron energies. The resolution in this mode decreases with increasing electron energy.
- 2) Constant Analyzer Energy (CAE). This mode of operation works by holding the potentials of the CHA constant such that electrons of only a specific energy (known as the pass energy) can make it through. Then the transfer lens is used to accelerate/deaccelerate electrons from the sample to that energy. The main difference is that because the pass energy remains constant, the resolution is independent of the energy of the ejected electrons. Instead, lower pass energy values offer high resolution but at the cost of decreased sensitivity.

Then, upon exiting the analyzer electrons are collected at the detector. Generally, there will be an electron multiplier to enhance the signal prior to detection.

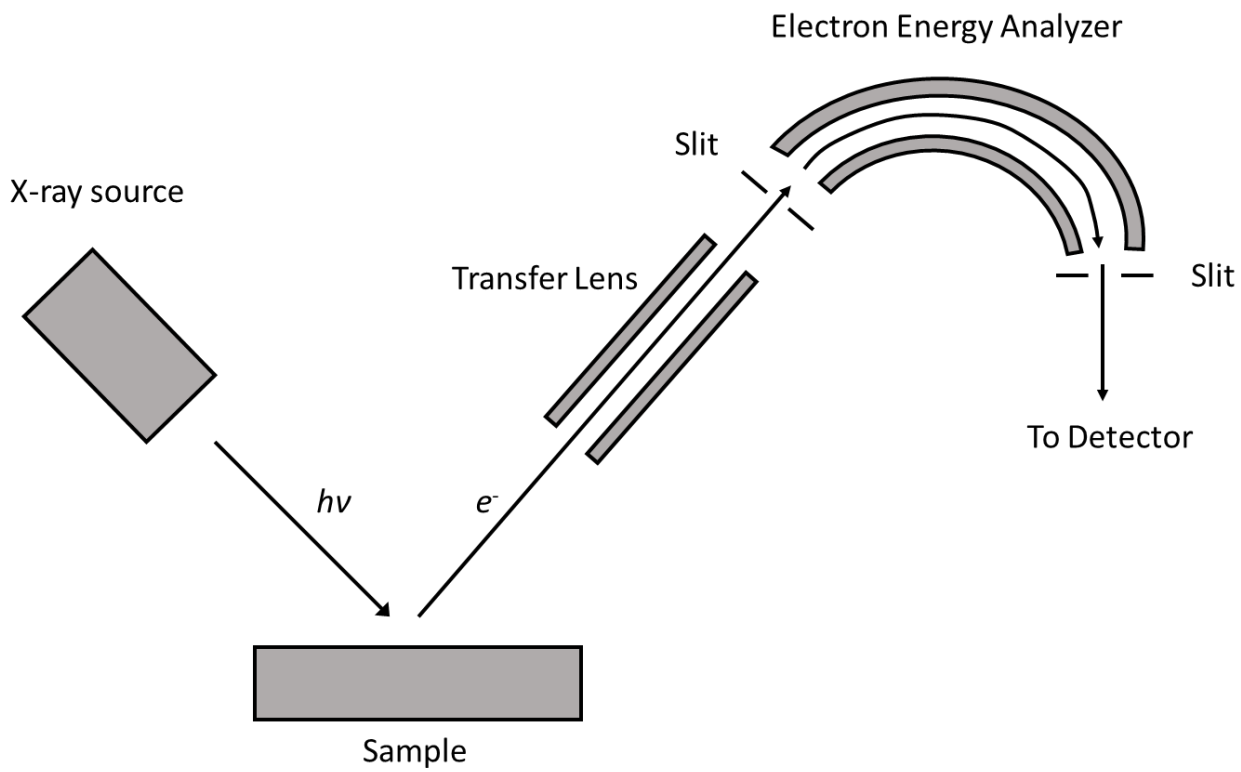


Figure 2.1 Basic XPS instrumentation

2.1.4 Modern XPS Instrumentation

Modern XPS built upon the basic design shown in Figure 2.1. A schematic of a more modernized instrument can be seen in Figure 2.2 and some of the additions will be discussed here.

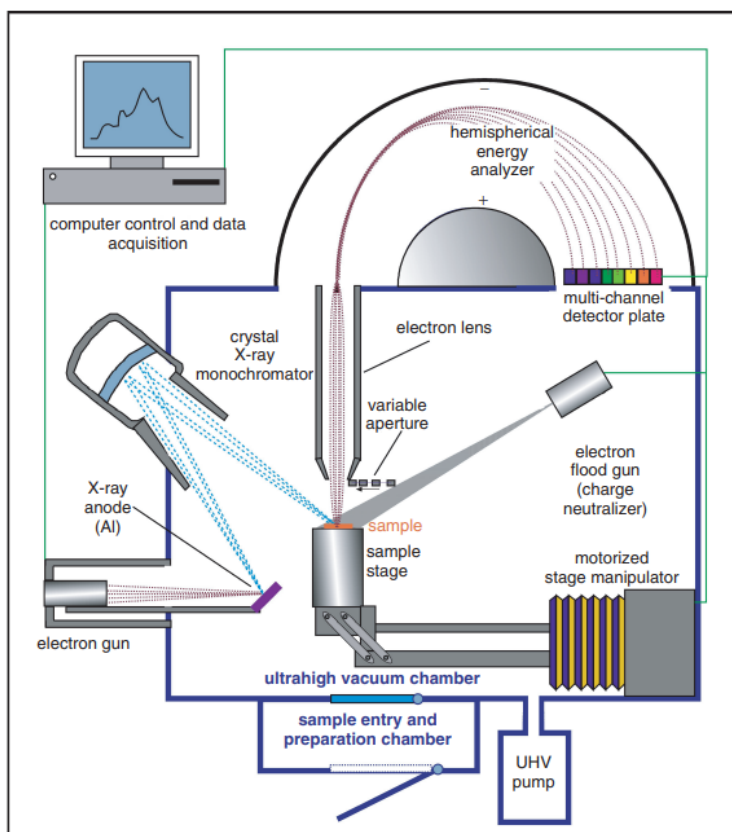


Figure 2.2 A modern XPS Instrument. Reproduced from "Electron Spectroscopy for Chemical Analysis," In *Surface Analysis – The Principal Techniques 2009*, p 47-112. with permission from John Wiley and Sons.¹⁶

X-rays for XPS measurements are generally obtained by blasting a target material or anode with electrons (Al and Mg are two of the most common materials). This results in the formation of core electron holes within the target material and the subsequent emission of fluorescent photons and electrons (also known as Auger electrons) as higher energy electrons

drop down to fill the now vacant core hole. The emission from the anode can be allowed to directly strike the sample but this is no longer the preferred method. While the direct application of X-rays results in higher X-ray flux it also results in the increased flux of other energy sources including high energy electrons, Bremsstrahlung (secondary radiation produced from the deceleration of charged particles), and heat. Most modern XPS instruments will make use of a quartz crystal monochromator to isolate the X-ray source from the sample and narrow the bandwidth of the incident X-ray beam. This does however result in lower X-ray flux and therefore lower sensitivity but other modern advancements in collection efficiency can help compensate for the loss. Additionally, the monochromator decreases the sample area illuminated by X-rays allowing for much smaller areas ($< 50 \mu\text{m}$ in diameter) to be analyzed, compared to direct sample illumination (typically a few mm).^{17, 18}

Improvements in electron lens design have resulted in an increase in the collection solid angle for ejected photoelectrons. A higher collection solid angle means that a higher percentage of photoelectrons ejected from the sample are collected by the instrument and can help offset the decreased sensitivity of the monochromatized incident X-ray beam. For the rare experiment where a higher collection solid angle is a disadvantage (e.g. non-destructive depth profiling) a variable aperture is employed to reduce the angle.¹⁹

The CHA has also benefited from modern advancements. CHAs are dispersive analyzers which means that there is a spread of electron energies that can make it through the analyzer without hitting the walls. Older XPS instruments used slits to limit the spread of electrons that made it through the analyzer and strike the detector, but this decreases the instrument sensitivity and results in longer acquisition times. Newer instruments take advantage of multi-channel detector plates to simultaneously detect the entire range of electron energies that make it through

the CHA resulting in much faster experiments. Other advancements include the use of an electrode flood gun to keep non-conductive samples from charging over time²⁰ and motorized sample holders for easy manipulation of sample position.

2.1.5 XPS Data Analysis

XPS data can be generally broken down into two pieces of information. The peak position gives information about chemical identity and environment while the peak intensity gives information about how much of it is on the sample's surface compared to other elements. However, analyzing XPS data is not an entirely straightforward process and there are some important points that any user should be aware of.

2.1.6 XPS Relative Sensitivity Factors

The first of these is the Relative Sensitivity Factor (RSF).²¹ The intensities of photoelectrons produced during XPS analysis are going to be inherently different based on which element is the source. Part of this is due to the *photoelectron cross section* which is the probability that a photon striking an atom/ion will cause a photoelectron to be ejected. These values are dependent on both the element and orbital in question but are independent of the element's ionization. In addition, photoelectron intensities are also dependent on the geometry and setup of the XPS instrument. These are related to the detection probability for a photoelectron leaving a sample's surface within a specific instrument. The RSF values are used to correct for differences in inherent photoelectron intensity. In order to accurately calculate relative concentrations of elements on a sample's surface the RSF for each element must be known. Tabulated RSF values should be available for each instrument. It is of *paramount* importance to ensure that you are using the correct RSF values for your instrument. To do otherwise would render your analysis unusable.

Using RSF values, however, is a simple process of dividing the raw calculated area of a peak by the corresponding RSF value.

2.1.7 Spin Orbit Splitting

The second effect to pay attention to is known as spin orbit splitting.²²⁻²⁴ Spin orbit splitting can be found on electrons originating from orbitals that have a non-zero l quantum number. Because a spinning charged body will always produce a magnetic field, a magnetic field will arise from an electron spinning around its own axis. By that same effect, a second magnetic field will arise from an electron orbiting a nucleus. These two magnetic fields can interact, and the resulting coupling produces the effect known as spin orbit splitting. Note that this only occurs for electrons in orbits with non-zero angular momentum, hence the requirement that l have a non-zero value. In an XPS spectrum, this effect is observed as a slight splitting of the peaks arising from these electrons. The difference in BE for the split peaks is much smaller than BE differences between different elements and is therefore considered to be part of the fine structure of a spectrum. In addition, the magnitude of the splitting is element and orbital specific, and a larger nuclear charge (Z) will induce a larger spin orbit splitting. The ratio for the area of the split peaks will also be dependent on the orbital from which the electrons were ejected. A table showing the splittings and peak areas for the different orbitals can be seen in Table 2.1.

Orbital	l	m_s	$J (l + m_s)$	Area Ratio ($2J + 1$)
p	1	+1/2, -1/2	3/2, 1/2	2:1
d	2	+1/2, -1/2	5/2, 3/2	3:2
f	3	+1/2, -1/2	7/2, 5/2	4:3

Table 2.1 Spin Orbit Splitting

The area ratio is important when calculating actual intensity values for your peaks. For example, the RSF value for the Cu_{2p} peak for a Kratos Axis Ultra XPS is 5.321. It is important to note that this value is for the combination of the $\text{Cu}_{2p(3/2)}$ and $\text{Cu}_{2p(1/2)}$ peaks. Therefore to use this value one would have to first determine the area of both the peaks and then divide that value by the RSF of 5.321. If one wanted to only use a single peak, either the 3/2 or the 1/2 peak, a different RSF would be required. Determining the new RSF however is trivial and can be accomplished easily by using the ratios in Table 2.1. As seen in Table 2.1 the area ratio for split peaks arising from a p orbital is 2:1 for the 3/2 to 1/2 peak. Therefore, the RSF values for the two peaks should also be 2:1 and should add up to the total RSF value for both peaks combined. For Cu_{2p} on a Kratos Axis Ultra XPS the total RSF of the two peaks should add up to 5.321. With this knowledge it is easy to see that the RSF for the $\text{Cu}_{2p(3/2)}$ is 3.547 ($\frac{2}{3} * 5.321$) and the RSF for the $\text{Cu}_{2p(1/2)}$ is 1.77 ($\frac{1}{3} * 5.321$). RSFs for other peaks can be calculated in a similar manner. An example of spin orbit coupling can be seen in Figure 2.2. Note that because s orbitals have no angular momentum there will only be a single peak for any s electrons.

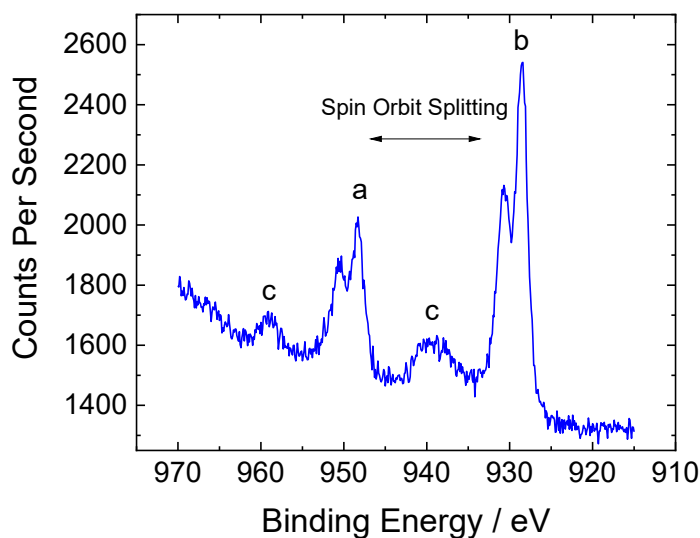


Figure 2.3 A representative XPS spectrum from Cu_{2p} . Within this spectrum can be seen the following: a) the peaks arising from $\text{Cu}_{2p(1/2)}$ energy state; b) the peaks arising from the $\text{Cu}_{2p(3/2)}$ energy state; and c) the ‘shakeup’ satellite peaks due to the presence of Cu(II) . The splitting of the peaks designated a and b are due to the presence of both Cu(I) and Cu(II) within the sample which have slightly different binding energies. The satellite peaks are a unique feature of Cu(II) and are discussed further in section 2.1.8. Note that the ratio of a to b is approximately 1:2.

2.1.8 ‘Shakeup’ Satellite Peaks

The last effect that will be discussed here is ‘shakeup’ satellite peaks.^{24, 25} These peaks also fall into the fine structure of a spectrum, or peaks arising from effects much smaller than nuclear charge. A ‘shakeup’ peak arises from an interaction between an ejected photoelectron and the remaining ionized species. When a photoelectron is ejected there is a finite probability that the resulting ion will be left in a slightly excited state. The energy for that excited state comes directly from the ejected photoelectron. As a result, the photoelectron will have slightly less kinetic energy due to some of it going towards the excited state of the ion. As seen in Equation 1.1 if the KE of the photoelectron is reduced, but the energy of the incident photon and the work function remain the same, the BE must increase. Note that the actual binding energy of the electron remains unchanged but because the BE is determined from the measured KE, the BE will be calculated as

having a higher value. Therefore, satellite peaks arising from a 'shakeup' event will have a slightly higher BE. An example of this can be seen in Figure 2.3 where a satellite peak due to the presence of Cu(II) can be seen. *An important aspect of 'shakeup' satellite peaks is that they arise from inner core electrons of the analyzed element and should be included in any data workup.* Not including the area of the satellite peaks will underestimate the concentration of the element (in this case copper) on the sample's surface. Note that there are other sources of satellite peaks (such as plasmon peaks) which are not covered here.

2.1.9 Determining the Baseline

One of the more important aspects of working up XPS data is the background subtraction. The background, which arises from multiple sources, is mainly made up of lower KE (higher BE) electrons from inelastic scattering. There are three main methods used for fitting and subtracting the background radiation which will be covered here. Examples of each fitting type can be seen in Figure 2.4.

1. Linear Method: Linear fitting is the most simplistic method for background subtraction. It is the simple generation of a linear line between two points outlining the XPS peak. This method has greatly fallen out of favor as the accessibility of more robust computational methods has improved.
2. Shirley Method: The Shirley algorithm generates an S-shaped curve for each peak. The background calculation is based on the peak intensity and the background trends to either side of the peak. This method is fairly subjective depending on parameters used but is quite popular due to its relative simplicity and accuracy.
3. Tougaard Method: This is the most complicative method covered here. The Tougaard method attempts to calculate the background based on a simulation of inelastic scattering

events. Proper use of a Tougaard function would have to incorporate any effects of the instrument itself on the background radiation. In order to reduce the complexity of the method several universal functions have been derived. However, because these functions do not take into account the specifics of the XPS instrument it is doubtful that they are any more accurate than the Shirley method. This is part of the reason that the popularity of the Shirley method has not decreased even with the Tougaard option available.

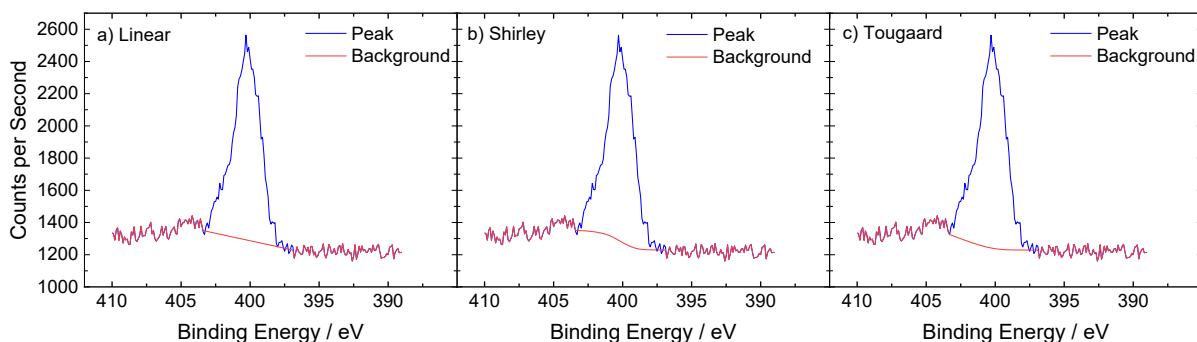


Figure 2.4 Background fitting for a Nitrogen 1s peak using three different methods: a) Linear, b) Shirley, and c) Tougaard.

2.1.10 Peak Fitting

The most popular method of peak fitting for routine XPS analysis is based on the combination of Gaussian and Lorentzian functions. Both functions give symmetric peaks with slightly different shapes. As seen in Figure 2.5, the Lorentzian function has a wider base, and narrower peak than the Gaussian. These functions can be combined in different ratios to best approximate a given XPS peak. For example, the Nitrogen 1s peak is often fit with a 70% Gaussian and 30% Lorentzian function, while the Copper 2p peak is better fit with a 10% Gaussian and 90% Lorentzian function.²⁶ Readers are encouraged to experiment with their XPS software and use the literature to determine the best fitting method for the element they are examining.

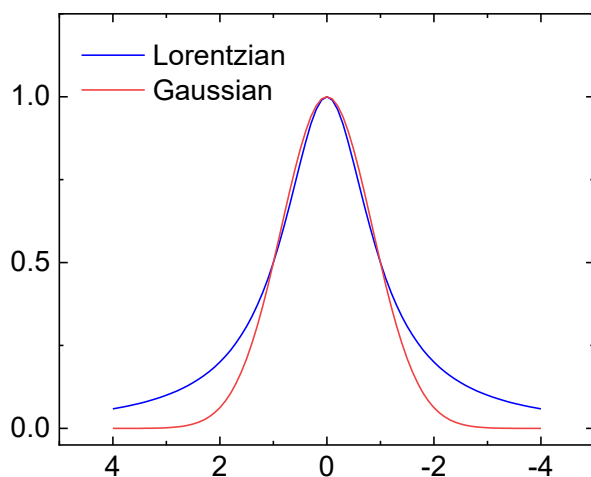


Figure 2.5 Comparison of Gaussian and Lorentzian standardized line shapes.

In conclusion, XPS is a highly useful method for characterizing relative concentrations of most species on a samples surface. However, analyzing the data is non-trivial and care must be taken when determining peak areas and origins. Readers are encouraged to seek out more in-depth literature if they intend to make XPS a cornerstone of their experiments.

2.2 Rotating Disk Electrode Voltammetry

This section will give a brief overview of rotating disk electrode voltammetry or RDEV and will focus on the chemistry behind its use. A small section on data workup will also be included here. Note that a basic understanding of electrochemistry is suggested before reading this section.

Rotating disk electrode voltammetry is a type of electrochemical experiment that falls under the broader umbrella of forced convection or hydrodynamic methods.²⁷ These are experiments that involve an external convective force and includes methods in which the electrode moves with respect to the solution such as RDEV and streaming mercury electrodes, as well as

methods in which the solution is forced past an electrode like with an impinging jet electrode. The benefits of these methods are that steady-state is achieved more quickly and as a result, double layer charging does not enter into the equation. In addition, because of the increased mass transfer at high convection rates, diffusion plays a much smaller role in the kinetics of a measured reaction.

Rotating disk electrode voltammetry is fairly simple to set up and conduct experiments with, which makes it a very popular method for hydrodynamic studies.²⁸⁻³³ The basic RDEV design is a shaft, made out of some inert material such as Teflon or PEEK, that acts as the electrode holder. The shaft contains a conductive core and is attached to a motor which can rotate the shaft at some user defined rate. A diagram of the setup can be seen in Figure 2.6.

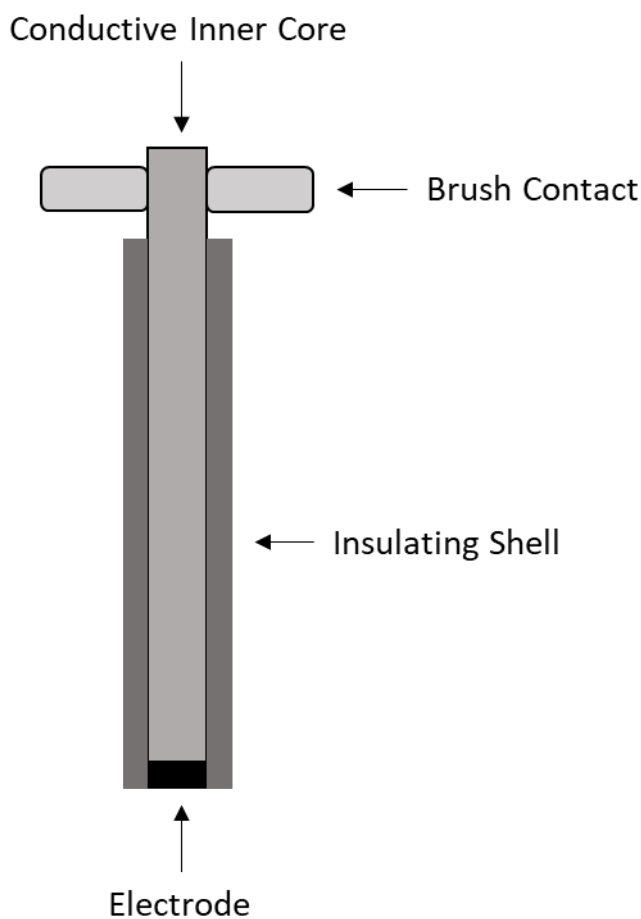


Figure 2.6 Basic construction of a rotating disk electrode.

To conduct a typical RDEV experiment a slow (< 50 mV/s) linear sweep or cyclic voltammogram will be collected under multiple rotation rates. Rates should be selected that will give a wide range of rotation speeds without going fast enough to produce turbulent flow. For the majority of RDEV experiments in this thesis rotation rates of 400, 800, 1600, and 3000 RPM were used. An example of RDEV data collected for O_2 reduction by Copper Diethynylphenanthroline covalently immobilized on a glassy carbon surface can be seen in Figure 2.7.²⁶ Note that the current increases as a function of the rotation rate. This is due to increased mass transport of the substrate, in this case O_2 , to the electrode surface as the rotation rate increases.

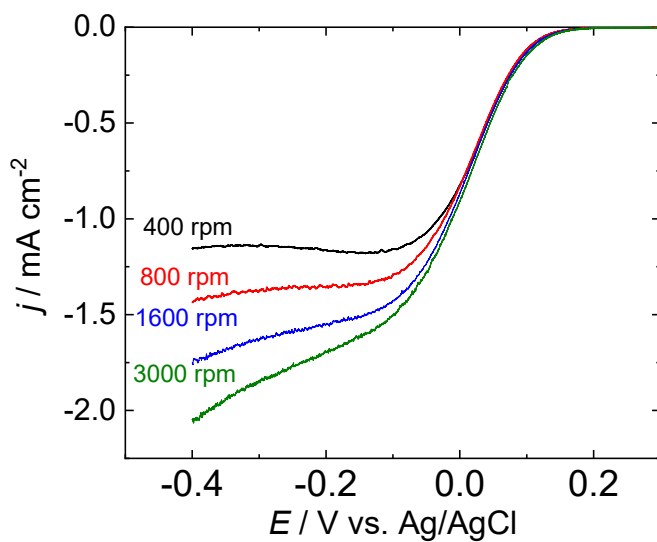


Figure 2.7 Representative rotating disk electrode voltammogram showing O_2 reduction by copper diethynylphenanthroline covalently attached to a glassy carbon electrode in pH 4.8 0.1 M acetate buffer with 1.0 M sodium perchlorate as a supporting electrolyte.

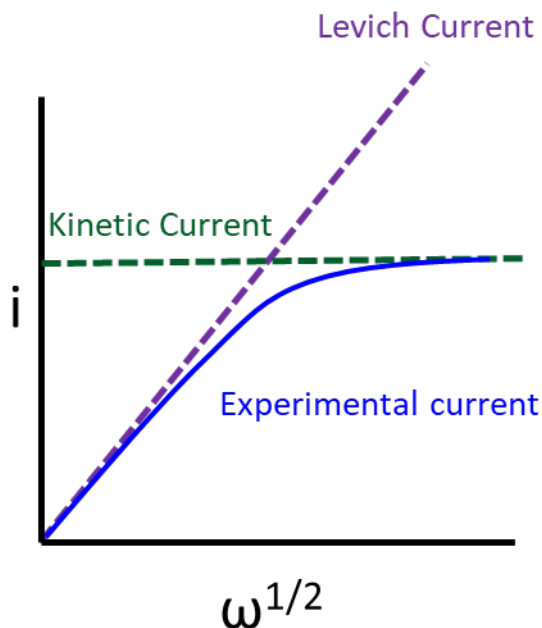


Figure 2.8 Diagram showing the change in measured current as a function of the applied rotation rate for a theoretical electrochemical reaction with a slow kinetic rate.

What is particularly useful about the data collected from an RDEV experiment is that it can be used to estimate the kinetic current for an electrochemical reaction. This means that activities of different species can be compared in the absence of any effects due to diffusion or mass transport. In order to understand this process consider the graph shown in Figure 2.8. In this graph two theoretical currents are shown with dashed lines versus the root of the rotation rate. The kinetic current, in green, is the current that would be measured if mass transport were fast enough that the concentration of substrate at the surface of the electrode was always equal to the bulk concentration within the solution. In other words, substrate is being replenished as soon as it is consumed and there is no dependence on the rotation rate. The current, in this case, is entirely due to the kinetics of electron transport at the electrode surface. The Levich current, shown in purple, is the theoretical current due solely to mass transport. This supposes that the electron transport kinetics are

instantaneous, such that as soon as substrate reaches the electrode surface it is immediately consumed. This theoretical current would scale linearly with the square root of the rotation rate. What actually occurs when conducting an RDEV experiment lies somewhere in between the kinetic and Levich currents. As shown in blue, as the rotation rate increases the measured current will increase until it flattens out at a maximum defined by the kinetic current. This is because no matter how fast the rotation rate, a reaction will always be limited by the kinetics of electron transport. In practice, achieving a rotation rate fast enough to measure the kinetic current will be very difficult due to turbulent flow at higher rotation rates. However, we can model the measured current and rotation rate relationship using the Koutecký-Levich equation (Equation 2.2) and use it to predict the kinetic current.²⁷

$$(2.2) \quad \frac{1}{i} = \frac{1}{i_k} + \frac{1}{i_l} = \frac{1}{i_k} + \frac{1}{0.62nFAD_o^{\frac{2}{3}}\omega^{\frac{1}{2}}\nu^{-\frac{1}{6}}[S]}$$

In the Koutecký -Levich equation shown above i is the measured current, i_k is the kinetic current and i_l is the Levich current. The Levich term can be expanded as shown on the far right. In the expansion n is the number of electrons transferred, F is Faraday's constant, A is the area of the electrode, D_o is the diffusion coefficient of the substrate, ω is the rotation rate of the electrode, ν is the kinematic viscosity of the electrolyte, and $[S]$ is the concentration of the substrate. From this relationship it becomes clear that by plotting the reciprocal of the measured current (i^{-1}) versus the reciprocal of the root of the rotation rate ($\omega^{-1/2}$) the plot will take on a $y = mx + b$ form where the y intercept is the inverse of the kinetic current (i_k^{-1}). An example of this process for a single potential along the RDEV measurement shown in Figure 2.7 is shown in Figure 2.9. By completing

this process for each potential of the RDEV measurement the potential dependent kinetic current can be calculated. The results of this calculation can be seen in Figure 2.10.

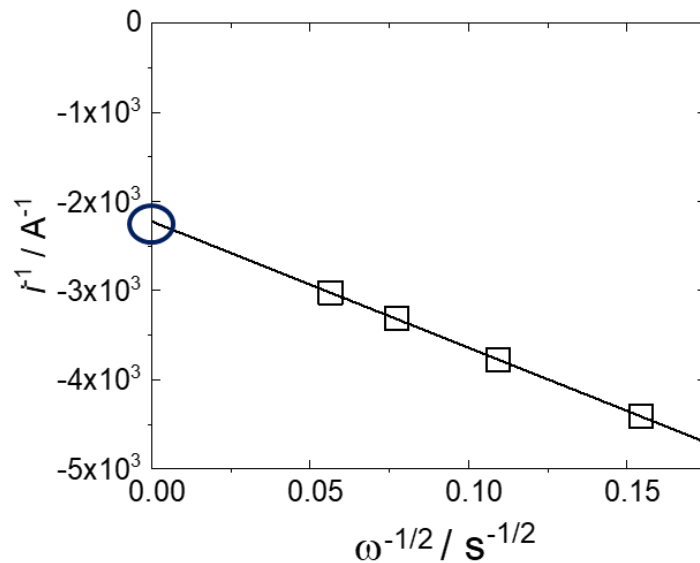


Figure 2.9 Example of Koutecký-Levich analysis of a single potential of the RDEV measurement shown in Figure 2.6. Each square represents the current at a single rotation rate. The y-intercept of the best fit line is circled in blue and is the inverse of the kinetic current.

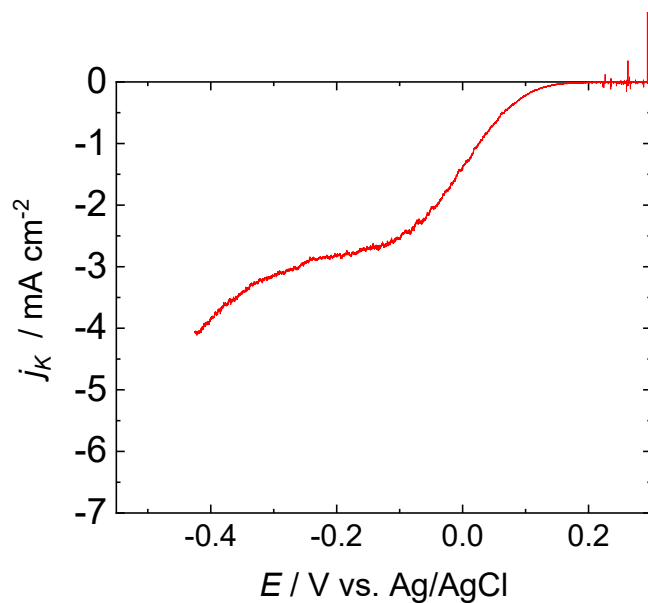


Figure 2.10 Potential dependent kinetic current obtained from Koutecký-Levich analysis of the RDEV measurement shown in Figure 2.6.

2.3 Rotating Ring Disk Electrode Voltammetry

While RDEV measurements are incredibly useful for predicting kinetic currents, they give no direct information about any products that might be formed during the experiment. Rotating ring disk electrode voltammetry (RRDEV) is a subset of RDEV that can be used to determine the amount of charge being passed that goes towards the formation of a specific product.^{29, 34-38} The main difference between RDEV and RRDEV is the presence of an independently controlled second ring electrode surrounding the central electrode that can be held at a separate potential (See Figure 2.11). The ring is typically made of a fairly inert metal with fast electron transfer kinetics such as platinum or gold. In an RRDEV experiment, the ring is held at a potential such that a product produced at the central working will be swept across the ring where it is ‘collected’ or re-oxidized/re-reduced. By comparing the current at the ring electrode with the current at the disk electrode a Faradaic efficiency for the collected product can be calculated.

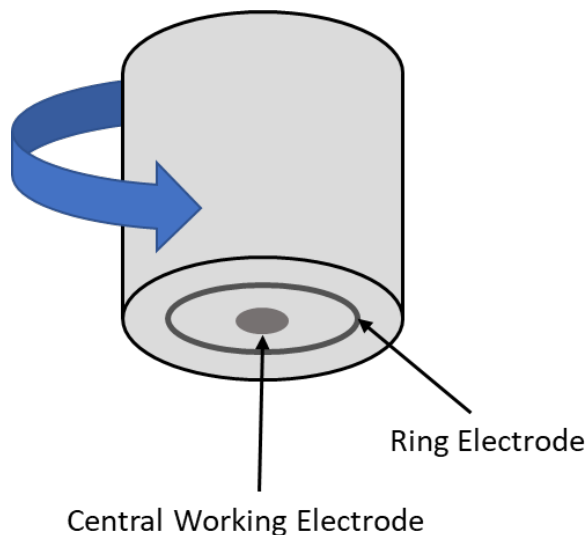


Figure 2.11 A typical rotating ring disk electrode setup showing the additional ring electrode surrounding the central disk working electrode.

There are a couple of important caveats to this method. The first is that the product must be capable of undergoing a reaction at the ring. For example, in the case of oxygen reduction in aqueous electrolyte, the two main products are hydrogen peroxide and water. Because water is both the product and the solvent, it cannot be detected at the ring. Therefore, only the Faradaic efficiency for hydrogen peroxide can be determined with RRDEV. The second aspect of RRDEV to pay close attention to is the collection efficiency. The collection efficiency is defined as the fraction of product produced at the central disk electrode that reacts or is ‘collected’ at the outer ring electrode. This value can be determined theoretically from the following equation first reported by Albery and Bruckenstein, and based on the diameter of the disk (d_1), the inner diameter of the ring (d_2), and the outer diameter of the ring (d_3) (Equation 2.9).³⁹ To understand this equation the following variables and the complex function $G(X)$ are also defined (Equations 2.3-2.8).

$$(2.3) \quad \sigma_{OD} = \frac{d_3}{d_1}$$

$$(2.4) \quad \sigma_{ID} = \frac{d_2}{d_1}$$

$$(2.5) \quad \sigma_A = \sigma_{ID}^3 - 1$$

$$(2.6) \quad \sigma_B = \sigma_{OD}^3 - \sigma_{ID}^3$$

$$(2.7) \quad \sigma_C = \frac{\sigma_A}{\sigma_B}$$

$$(2.8) \quad G(x) = \frac{1}{4} + \frac{\sqrt{3}}{4\pi} \ln \left[\frac{\left(x^{\frac{1}{3}} + 1\right)^3}{x + 1} \right] + \left(\frac{3}{2\pi}\right) \arctan \left[\frac{2x^{\frac{1}{3}} - 1}{\sqrt{3}} \right]$$

$$(2.9) \quad N_{theoretical} = 1 - \sigma_{OD}^2 - \sigma_B^{\frac{2}{3}} - G(\sigma_C) - \sigma_B^{\frac{2}{3}} G(\sigma_A) + \sigma_{OD}^2 G(\sigma_C \sigma_{OD}^3)$$

Theoretical collection efficiencies are often supplied by the manufacturer of a RRDE. However, in practice, the best way to determine collection efficiencies is by far to do so experimentally. This is because the theoretical efficiencies do not consider any manufacturing defects, or the effects of turbulent flow caused by the electrode rotation. A classic experiment to empirically determine the collection efficiency of a RRDE setup is to collect RRDEV data for the ferricyanide/ferrocyanide half-reaction under your planned experimental conditions (Equation 2.10). This is a simple one electron process with only a single product.



To perform this experiment, a small concentration of potassium ferricyanide (~0.01 M) should be added to your electrolyte and then, under a constant rotation rate, the working electrode should be slowly (<50 mV/s) swept more negative. The ring should be held at an oxidizing potential so it can ‘collect’ or reoxidize the reduced ferrocyanide. From this data, the empirical collection efficiency can be determined from Equation 2.11.

$$(2.11) \quad N_{empirical} = \left| \left(\frac{i_{ring}}{i_{disk}} \right) \left(\frac{n_{disk}}{n_{ring}} \right) \right|$$

In this equation i_{ring} is the measured ring current, i_{disk} is the measured disk current, n_{disk} is the number of electrons transferred at the disk, and n_{ring} is the number of electrons transferred at the ring (these last two values are very often the same). Note that the correct potential to hold the ring at is also best determined experimentally by testing different ring potentials until the one that produces the best collection efficiency is found. These values will need to be determined for each product collected. In addition, while the collection efficiency is theoretically independent of the rotation rate, experimentally this is generally not the case, so collection efficiencies should

be determined for each rotation rate used. Slower rotation and scan rates are best when performing RRDEV experiments. Once the collection efficiency has been determined the Faradaic efficiency can be calculated from the following equation (Equation 2.12).

$$(2.12) \quad \epsilon = \frac{i_{ring}}{i_{disk}N}$$

In this equation ϵ is the Faradaic efficiency, i_{ring} is the measured ring current, i_{disk} is the measured disk current, and N is the collection efficiency. As a final note, consideration should be given to if collection efficiency can be determined for a product that your catalyst is expected to make. For example, in Chapter 3 of this thesis RRDEV data is collected for the reduction of oxygen to hydrogen peroxide by copper diethynylphenanthroline covalently attached to glassy carbon electrodes. In order to determine the collection efficiency for our RRDEV setup, we measured empirical collection efficiencies for oxygen reduction on glassy carbon. Because glassy carbon can only do the two-electron reduction of oxygen to hydrogen peroxide we were able to obtain collection efficiencies under conditions as close to our planned experiments as possible. While this method is not always feasible, it is the best way to determine collection efficiencies. An Example of an RRDEV measurement can be seen in Figure 2.12.

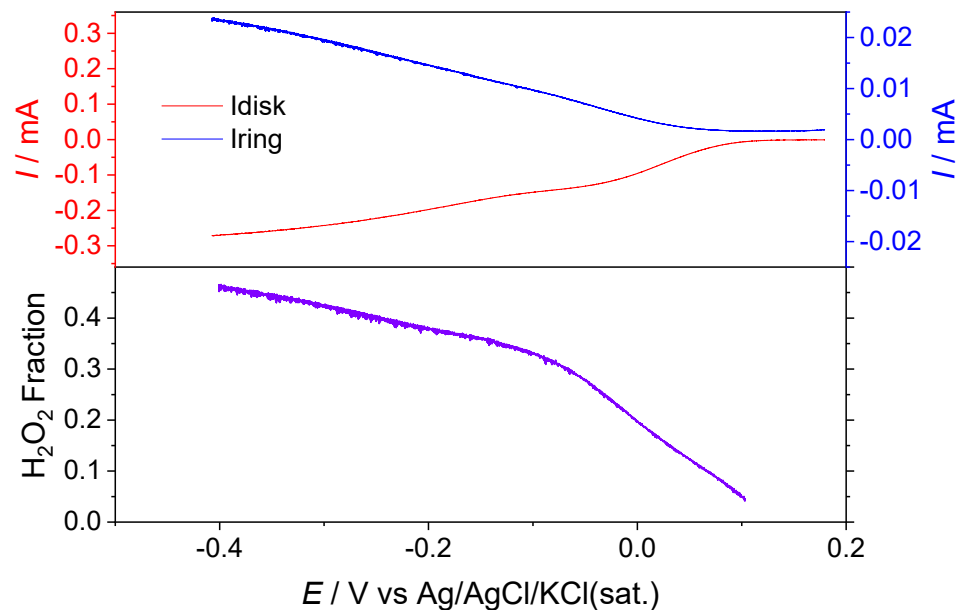


Figure 2.12 An example RRDEV measurement for ORR by copper diethynylphenanthroline covalently attached to glassy carbon in a 100 mM acetate buffer (50 mM NaOAc•3H₂O and 50 mM HOAc) at pH 4.8 containing 1 M NaClO₄ supporting electrolyte under an O₂ atmosphere. The rotation rate was 400 RPM and the platinum ring was held at 0.73 V vs Ag/AgCl/KCl(sat.). The scan rate of 10 mV/s. The ring current is not corrected for collection efficiency ($N = 0.175$).

2.4.1 Resources for XPS

Van der Heide, Paul. *X-Ray Photoelectron Spectroscopy: An Introduction to Principles and Practices*. John Wiley & Sons, 2011.

Vickerman, John C., and Ian S. Gilmore, eds. *Surface Analysis: The Principal Techniques*. John Wiley & Sons, 2011.

Hofmann, Siegfried. *Auger- and X-ray Photoelectron Spectroscopy in Materials Science: A User-Oriented Guide*. Vol. 49. Springer Science & Business Media, 2012.

Crist, B. Vincent. *Handbooks of Monochromatic XPS Spectra, Volumes 1-5*, XPS International LLC, 2004.

2.4.2 Resources for Electrochemistry

Bard, Allen J., and Faulkner, Larry R. *Electrochemical Methods : Fundamentals and Applications*. Wiley, 1980.

Sawyer, Donald T., Sobkowiak, Andrzej, Roberts, Julian L., and Sawyer, Donald T. *Electrochemistry for Chemists*. Wiley, 1995.

Harris, Daniel C. *Quantitative Chemical Analysis*. W.H. Freeman and Co., 2010.

Heineman, William R. *Laboratory Techniques in Electroanalytical Chemistry*. CRC Press, 2018.

2.5 References

1. Hofmann, S., *Auger- and X-Ray Photoelectron Spectroscopy in Materials Science A User-Oriented Guide*. 1st ed. 2013. ed.; Springer: 2013.
2. Van der Heide, P., *X-ray photoelectron spectroscopy: an introduction to principles and practices*. John Wiley & Sons: 2011.
3. Vickerman, J. C.; Gilmore, I. S., *Surface analysis: the principal techniques*. John Wiley & Sons: 2011.
4. Jablonski, A.; Powell, C. J., Electron effective attenuation lengths in electron spectroscopies. *Journal of Alloys and Compounds* **2004**, *362* (1), 26-32.
5. Tilinin, I. S.; Jablonski, A.; Zemek, J.; Hucek, S., Escape probability of signal photoelectrons from non-crystalline solids: influence of anisotropy of photoemission. *Journal of Electron Spectroscopy and Related Phenomena* **1997**, *87* (2), 127-140.
6. McArthur, S. L., Applications of XPS in bioengineering. *Surface and Interface Analysis* **2006**, *38* (11), 1380-1385.
7. Paul Pijpers, A.; J. Meier, R., Core level photoelectron spectroscopy for polymer and catalyst characterisation. *Chemical Society Reviews* **1999**, *28* (4), 233-238.
8. Pijpers, A. P.; Donners, W. A. B., Quantitative determination of the surface composition of acrylate copolymer latex films by XPS (ESCA). *Journal of Polymer Science: Polymer Chemistry Edition* **1985**, *23* (2), 453-462.
9. Kim, J.; Jung, D.; Park, Y.; Kim, Y.; Moon, D. W.; Lee, T. G., Quantitative analysis of surface amine groups on plasma-polymerized ethylenediamine films using UV-visible spectroscopy compared to chemical derivatization with FT-IR spectroscopy, XPS and TOF-SIMS. *Applied Surface Science* **2007**, *253* (9), 4112-4118.
10. Corcoran, C. J.; Tavassol, H.; Rigsby, M. A.; Bagus, P. S.; Wieckowski, A., Application of XPS to study electrocatalysts for fuel cells. *Journal of Power Sources* **2010**, *195* (24), 7856-7879.
11. Calvillo, L.; Carraro, F.; Vozniuk, O.; Celorrio, V.; Nodari, L.; Russell, A. E.; Debellis, D.; Fermin, D.; Cavani, F.; Agnoli, S.; Granozzi, G., Insights into the durability of Co-Fe spinel oxygen evolution electrocatalysts via operando studies of the catalyst structure. *Journal of Materials Chemistry A* **2018**, *6* (16), 7034-7041.
12. Michaud, S. E.; Riehs, M. T.; Feng, W.-J.; Lin, C.-C.; McCrory, C. C. L., A CoV₂O₄ precatalyst for the oxygen evolution reaction: highlighting the importance of postmortem electrocatalyst characterization. *Chemical Communications* **2021**, *57* (7), 883-886.
13. Berkowitz, J., *Photoabsorption, photoionization, and photoelectron spectroscopy*. Academic Press: New York ;, 1979; Vol. New York :.
14. Feldman, L. C.; Mayer, J. W., *Fundamentals of surface and thin film analysis*. North-Holland: New York ;, 1986; Vol. New York :.
15. Briggs, D.; Seah, M. P., *Practical surface analysis*. 2nd ed. ed.; Wiley ; Salle + Sauerländer: Chichester ; New York : Aarau ;, 1990; Vol. Chichester ; New York : Aarau :.
16. Ratner, B. D.; Castner, D. G., Electron Spectroscopy for Chemical Analysis. In *Surface Analysis – The Principal Techniques*, 2009; pp 47-112.
17. Baer, D. R.; Engelhard, M. H., Approach for determining area selectivity in small-area XPS analysis. *Surface and Interface Analysis* **2000**, *29* (11), 766-772.
18. Chaney, R. L., Recent developments in spatially resolved ESCA. *Surface and Interface Analysis* **1987**, *10* (1), 36-47.

19. Tyler, B. J.; Castner, D. G.; Ratner, B. D., Determining depth profiles from angle dependent x-ray photoelectron spectroscopy: The effects of analyzer lens aperture size and geometry. *Journal of Vacuum Science & Technology A* **1989**, 7 (3), 1646-1654.
20. Barth, G.; Linder, R.; Bryson, C., Advances in charge neutralization for XPS measurements of nonconducting materials. *Surface and Interface Analysis* **1988**, 11 (6-7), 307-311.
21. Wagner, C. D., Sensitivity factors for XPS analysis of surface atoms. *Journal of Electron Spectroscopy and Related Phenomena* **1983**, 32 (2), 99-102.
22. Svensson, S.; Naves de Brito, A.; Keane, M. P.; Correia, N.; Karlsson, L., Observation of an energy shift in the S_{2p_{3/2}} – S_{2p_{1/2}} spin-orbit splitting between x-ray photoelectron and Auger-electron spectra for the H₂S molecule. *Physical Review A* **1991**, 43 (11), 6441-6443.
23. Grosvenor, A. P.; Kobe, B. A.; Biesinger, M. C.; McIntyre, N. S., Investigation of multiplet splitting of Fe 2p XPS spectra and bonding in iron compounds. *Surface and Interface Analysis* **2004**, 36 (12), 1564-1574.
24. Van der Heide, P., *X-ray photoelectron spectroscopy an introduction to principles and practices*. Wiley: Hoboken, N.J. :, 2012; Vol. Hoboken, N.J. :.
25. Ertl, G.; Hierl, R.; Knözinger, H.; Thiele, N.; Urbach, H. P., XPS study of copper aluminate catalysts. *Applications of Surface Science* **1980**, 5 (1), 49-64.
26. Kallick, J. D.; Feng, W.-J.; McCrory, C. C. L., Controlled Formation of Multilayer Films of Discrete Molecular Catalysts for the Oxygen Reduction Reaction Using a Layer-by-Layer Growth Mechanism Based on Sequential Click Chemistry. *ACS Applied Energy Materials* **2020**, 3 (7), 6222-6231.
27. Bard, A. J.; Faulkner, L. R., *Electrochemical methods : fundamentals and applications*. Wiley: New York :, 1980; Vol. New York :.
28. Bartlett, P. N.; Pratt, K. F. E., A study of the kinetics of the reaction between ferrocene monocarboxylic acid and glucose oxidase using the rotating-disc electrode. *Journal of Electroanalytical Chemistry* **1995**, 397 (1), 53-60.
29. Paulus, U. A.; Schmidt, T. J.; Gasteiger, H. A.; Behm, R. J., Oxygen reduction on a high-surface area Pt/Vulcan carbon catalyst: a thin-film rotating ring-disk electrode study. *Journal of Electroanalytical Chemistry* **2001**, 495 (2), 134-145.
30. Schmidt, T. J.; Gasteiger, H. A.; Stäb, G. D.; Urban, P. M.; Kolb, D. M.; Behm, R. J., Characterization of High-Surface-Area Electrocatalysts Using a Rotating Disk Electrode Configuration. *Journal of The Electrochemical Society* **1998**, 145 (7), 2354-2358.
31. Shinozaki, K.; Zack, J. W.; Richards, R. M.; Pivovar, B. S.; Kocha, S. S., Oxygen Reduction Reaction Measurements on Platinum Electrocatalysts Utilizing Rotating Disk Electrode Technique. *Journal of The Electrochemical Society* **2015**, 162 (10), F1144-F1158.
32. Suntivich, J.; Gasteiger, H. A.; Yabuuchi, N.; Shao-Horn, Y., Electrocatalytic Measurement Methodology of Oxide Catalysts Using a Thin-Film Rotating Disk Electrode. *Journal of The Electrochemical Society* **2010**, 157 (8), B1263.
33. Wiberg, G. K. H.; Mayrhofer, K. J. J.; Arenz, M., Investigation of the Oxygen Reduction Activity on Silver – A Rotating Disc Electrode Study. *Fuel Cells* **2010**, 10 (4), 575-581.
34. Dalton, F., ECS Classics: Historical Origins of the Rotating Ring-Disk Electrode. *Interface magazine* **2016**, 25 (3), 50-59.
35. Bonakdarpour, A.; Delacote, C.; Yang, R.; Wieckowski, A.; Dahn, J. R., Loading of Se/Ru/C electrocatalyst on a rotating ring-disk electrode and the loading impact on a H₂O₂

- release during oxygen reduction reaction. *Electrochemistry Communications* **2008**, *10* (4), 611-615.
36. Jaouen, F., O₂ Reduction Mechanism on Non-Noble Metal Catalysts for PEM Fuel Cells. Part II: A Porous-Electrode Model To Predict the Quantity of H₂O₂ Detected by Rotating Ring-Disk Electrode. *The Journal of Physical Chemistry C* **2009**, *113* (34), 15433-15443.
37. Kamin, R. A.; Wilson, G. S., Rotating ring-disk enzyme electrode for biocatalysis kinetic studies and characterization of the immobilized enzyme layer. *Analytical Chemistry* **1980**, *52* (8), 1198-1205.
38. Zimer, A. M.; Medina da Silva, M.; Machado, E. G.; Varela, H.; Mascaro, L. H.; Pereira, E. C., Development of a versatile rotating ring-disc electrode for in situ pH measurements. *Analytica Chimica Acta* **2015**, *897*, 17-23.
39. Albery, W. J.; Bruckenstein, S., Ring-disc electrodes. Part 2.—Theoretical and experimental collection efficiencies. *Transactions of the Faraday Society* **1966**, *62* (0), 1920-1931.

Chapter 3 Controlled Formation of Multilayer Films of Discrete Molecular Catalysts for the Oxygen Reduction Reaction using a Layer-by-Layer Growth Mechanism Based on Sequential Click Chemistry

3.1 Preface

This chapter of my dissertation is derived from a manuscript which was published in ACS Applied Energy Materials¹ and presents the synthesis and study of multi-layer films of Copper Diethynylphenanthroline for the oxygen reduction reaction. Our results suggest that while single- and double-layer films can be reproducibly synthesized the formation of triple layer films is prevented by steric hinderance. The double-layer films show an increase in activity and an increase in selectivity for the 4-electron reduction of oxygen to water. I am the primary author on the manuscript, responsible for material synthesis, electrochemical measurements, electrochemical and physical analysis, and preparation and revision of the manuscript. Weijie Feng provided significant insight into XPS analysis. My advisor, Dr. Charles C. L. McCrory, provided significant insight and expertise in electrochemical measurements and analysis and provided help with writing and revising the manuscript. Reprinted with permission from ACS *Appl. Energy Mater.* 2020, 3, 7, 6222-6231. Copyright 2020 American Chemical Society.

3.2 Abstract

Molecular electrocatalysts show promise for energy-relevant multi-electron transformations due to their rationally-tunable activity and selectivity from systematic ligand modifications. However, surface-immobilized molecular electrocatalytic systems are typically limited by low activity per geometric surface area compared to traditional solid-state analogues because of their lower active site surface coverage. Many existing methods for increasing surface coverage through the formation of multilayer films are based on radical-coupling or electropolymerization strategies that often result in dense, poorly defined films that may inhibit charge or substrate transport and complicate mechanistic studies. We report an alternative controlled layer-by-layer deposition strategy for the formation of multilayer catalyst films on carbon electrodes surfaces based on sequential Cu(I) catalyzed azide-alkyne cycloaddition reactions. As a proof-of-concept, we explore the growth of multilayer films of 3,8-diethynylphenanthroline for the oxygen reduction reaction. Double-layer catalyst films operate with increased activity and selectivity for the reduction of O₂ to H₂O compared to single-layer catalyst films. We attribute this increased activity and selectivity to the increased coverage of the double-layer films which both increases the number of active sites and facilitates the 4 e⁻ reduction to H₂O, rather than the 2 e⁻ to H₂O₂. Unfortunately, growth of triple-layer catalyst films in this system were unsuccessful, possibly due to steric congestion in the double-layer films.

3.3 Introduction

Molecular electrocatalysts show significant promise for *selective* electrochemical conversion of small molecules to single products in energy-relevant multi-electron reactions such as the oxygen reduction reaction (ORR) and the CO₂ reduction reaction (CO₂RR). In particular, with molecular electrocatalysts, reactions occur at single active sites and the environment surrounding these active sites can be rationally tuned via ligand alterations to induce beneficial primary- and secondary-coordination sphere effects.²⁻⁶ In contrast, with traditional solid-state electrocatalysts, reactions occur at a variety of surface sites that may undergo changes throughout the experiment or as a function of location on the electrode surfaces.⁷⁻⁹ The increased site specificity and tunability of activity through ligand modifications makes molecular catalysts a particularly promising class of catalysts for selective electrocatalytic transformations.

Even though molecular electrocatalysts often show high selectivity compared to their solid-state analogues, solid-state heterogeneous electrocatalysts typically operate with significantly higher activity per geometric area.¹⁰ This is because the most active solid-state heterogeneous systems are nanostructured films with 3D architectures that have a dramatically increased number of active sites per geometric area compared to molecular electrocatalysts.¹¹⁻¹⁴ One of the outstanding challenges in molecular electrocatalysis is designing new methods to attach molecular catalysts to electrode supports using novel architectures that allow the new heterogenized systems to operate with the *activity* of traditional solid-state systems while maintaining the *selectivity* of discrete molecular catalysts.

Existing strategies for multilayer film formation have typically relied on radical-coupling chemistry such as reductive deposition of diazonium salts¹⁵ or electropolymerization reactions.¹⁶⁻

¹⁸ These deposition strategies often result in multilayer films that are not well defined,¹⁹

complicating mechanistic and kinetic studies, and often form dense layers that may inhibit charge, electrolyte, and reactant transport to interior active sites.^{17, 20} We note recent studies show that controlled growth of catalyst species for select systems is possible via diazonium coupling through careful control of the charge passed during deposition.²¹

In this study, we report an alternative strategy for the controlled, layer-by-layer polymerization of molecular catalysts directly onto electrode surfaces using sequential Cu(I) catalyzed Azide-Alkyne Cycloaddition (CuAAC) reactions (Figure 3.1). This approach provides for explicit control of film thickness and composition through the deposition mechanism. A similar layer-by-layer CuAAC-deposition strategy²² has been previously used for the formation of multilayer structures of porphyrins,²³⁻²⁶ chromophores,²⁷ and molecular wires,²⁸ but has not been studied for formation of electrocatalytic films. As a proof of concept, we have developed a synthesis strategy for the formation of multilayer films of Cu(3,8-diethynyl-1,10-phenanthroline) (Cu(DEphen)) on carbon surfaces and studied the resulting films for the oxygen reduction reaction (ORR). We chose this as a starting system because the activity of surface-immobilized single-layers of Cu(1,10-phenanthroline)-based catalysts for the ORR has been previously reported for both physisorbed^{3, 29-31} and covalently-immobilized systems.³² We show that as we increase the catalyst film thickness from a single layer to a double layer of Cu(DEphen), there is roughly a doubling of catalytic activity for the ORR. In addition, we observe increased production of the 4- e^- product H_2O , as compared to the 2- e^- product H_2O_2 , for the double-layer Cu(DEphen) compared to the single-layer films. However, attempts to synthesize triple-layer films of Cu(DEphen) resulted in films that were nearly indistinguishable from the double-layer films. We propose that formation of TL-Cu(DEphen) films was unsuccessful likely due to steric constraints during synthesis.

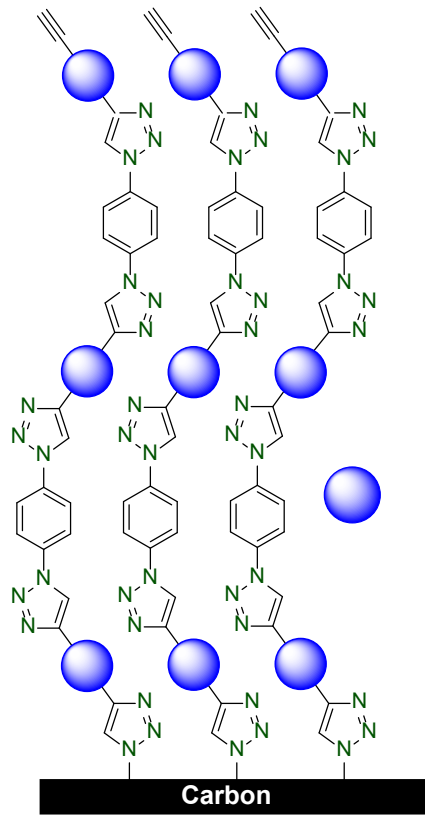


Figure 3.1 Multilayer catalyst films on electrode surfaces grown from sequential Cu(I) catalyzed Azide-Alkyne Cycloaddition (CuACC) reactions.

3.4 Experimental

3.4.1 Materials and General Instrumentation

Aldrich. Tetrahydrofuran (THF, ACS Grade), Chloroform, (CHCl_3 , ACS Grade) Methanol (MeOH, ACS Grade), Diethyl Ether (Anhydrous, BHT Stabilized, ACS grade, 99%), Petroleum Ether (ACS Grade), Dichloromethane (DCM, ACS Grade, 99.5%), Potassium Chloride (KCl, ACS Grade, 99%), and Sodium Diethyldithiocarbamate Trihydrate (ACS Grade) were purchased from **Fisher Scientific**. Copper(II) Sulfate (CuSO_4 , Anhydrous, 98%), and Copper (II) Sulfate Pentahydrate ($\text{CuSO}_4 \cdot 5\text{H}_2\text{O}$, 99%) were purchased from **Acros Organics**. 3,8-Dibromophenanthroline (96%) was purchased from **TCI America**. Iodine Monochloride (ICl, ACS Grade), 1,4-Diiodobenzene (98%), Sodium Carbonate (Na_2CO_3 , Anhydrous, ACS Grade), L-proline (99%), Tris[(1-benzyl-1H-1,2,3-triazol-4-yl)methyl]amine (TBTA, 97%), and Silica Gel 60 (230-450 Mesh) were purchased from **Alfa Aesar**. Sodium Perchlorate Monohydrate ($\text{NaClO}_4 \cdot \text{H}_2\text{O}$, ACS grade) was purchased from **EMD Millipore**. Perchloric Acid (ACS Grade, 70%) was purchased from **VWR**. Deuterated Chloroform (CDCl_3 , 99.8%), Deuterated Tetrahydrofuran (d_8 -THF, $\text{C}_4\text{D}_8\text{O}$, 99.5 %), and D_2O (99 %) were purchased from **Cambridge Isotope Laboratories**. Forming Gas (5% H_2 , balance N_2) and Oxygen (O_2 , industrial grade) were purchased from **Cryogenic Gases**. Nitrogen gas (N_2) was boil-off gas from a liquid nitrogen source. All water used in this study was purified to 18.2 $\text{M}\Omega \cdot \text{cm}$ resistivity in house using a Thermo Scientific GenPure UV-TOC/UF xCAD-plus water purification system. Glassy carbon disks (Sigradur-G grade, 5 mm diameter, 4 mm tall, 0.195 cm^2 disk surface area) were purchased from HTW Hochtemperatur-Werkstoffe GmbH. Pt wire (99.99% 0.5 mm diameter) purchased from Surepure Chemetals L.L.C. Boron-Doped Diamond plates (10 mm x 10 mm x 0.6 mm) were purchased from Element Six.

NMR spectra were collected on a Varian MR400 (400 Mhz) spectrometer and all chemical shifts are reported in ppm relative to TMS standards. All electrochemistry was performed using a

Bio-Logic SP-300 bipotentiostat and data was recorded using the Bio-Logic EC-Lab v10.44 software package. Electrochemical data analysis and figure preparation was done in Origin 2019 (OriginLab Corporation). X-ray Photoelectron Spectroscopy (XPS) measurements were conducted using a Kratos Axis Ultra XPS with a monochromatic Al K α X-ray source operating at 8 mA and 14 kV. All XPS data analysis was done using the CasaXPS version 2.3.17 software package (Casa Software Ltd). Some synthetic steps were carried out under a dry N₂ atmosphere using an mBraun Labstar 4-glove inert atmosphere glovebox.

3.4.2 Synthetic Procedures

3,8-bis(trimethylsilyl)ethynyl-1,10-phenanthroline. A 50 ml thick-walled pressure vessel was charged with 3,8-dibromophenanthroline (500 mg, 1.5 mmol), PdCl₂(PPh₃)₂ (62.5 mg, 0.09 mmol), CuI (34 mg, 0.18 mmol), and a stir bar. The pressure vessel was brought into a N₂-purged glovebox. Inside the glovebox the following reagents were added to the pressure vessel in order: tetrahydrofuron (10 ml), ethynyltrimethylsilane (820 μ l, 6 mmol), and diisopropylamine (3 ml). The pressure vessel was then sealed and removed from the glovebox. The reaction was heated to 60 °C for 72 hours with stirring. The reaction turned black shortly after heating began. After 72 hours the reaction was cooled down to room temperature and solvent was removed under reduced pressure. Residue was dissolved in 40 ml of dichloromethane. An additional 40 ml of 2% aqueous KCN was added and the mixture was stirred vigorously for 1-2 hours to remove the copper. The solution turned a lighter orange color during this process. The organic phase was removed using a separatory funnel then washed two times with H₂O and once with saturated aqueous NaCl. The organic phase was then dried over Na₂SO₄ and the solvent was removed under reduced pressure. The crude material was purified with flash chromatography on a silica column

using DCM as the eluent. The product was obtained as an off-white solid (494 mg, 88% yield). ^1H NMR (CD_3Cl , 400 MHz): δ 9.20 (2H, d), δ 8.33 (2H, d), δ 7.76 (2H, s), δ 0.32 (18 H, s).

3,8-diethynyl-1,10-phenanthroline (DEphen). 3,8-bis((trimethylsilyl)ethynyl)-1,10-phenanthroline (494 mg, 1.3 mmol) was dissolved in 14 ml of 1:1 MeOH:THF. 7 ml of 1 M aqueous KOH was added with stirring resulting in the immediate precipitation of a white solid. Solution was then stirred overnight at room temperature. The solid was collected via vacuum filtration and washed with copious amounts of water followed by small amounts of chilled methanol and diethyl ether. The white solid was then dried overnight under vacuum to give 242 mg (80% yield) of product as a white solid. ^1H NMR (CD_3Cl , 400 MHz): δ 9.25 (2H, d), δ 8.38 (2H, d), δ 7.81 (2H, s), δ 3.40 (2 H, s).

1,4-diazidobenzene (DAB). 1,4-diazidobenzene was synthesized based on literature methods.³³ A 150 ml round bottom flask with a stir bar was charged with 1,4-diiodobenzene (1g, 3.3 mmol), sodium azide (427 mg, 7.3 mmol), copper sulfate (48.5 mg, 0.3 mmol), ascorbic acid (106 mg, 0.60 mmol), sodium carbonate (63 mg, 0.60 mmol), l-proline (70 mg, 0.60 mmol), DMSO (5.5 ml), and H_2O (0.6 ml). The round bottom flask was capped with a rubber septum and heated to 65 °C for 24 hours in the dark. The workup was also completed in the dark to avoid photodecomposition of the product. Product was added to a separatory funnel with ethyl acetate and washed three times with H_2O followed by washing with saturated aqueous NaCl. The organic phase was dried over MgSO_4 and subsequently the solvent was removed under reduced pressure. The product was purified using flash chromatography on silica with petroleum ether as the eluent giving 114 mg (23 % yield) of light-yellow crystals. Crystals were stored in the dark in a freezer at -4 °C to avoid decomposition. Product will be stable for at least 6 months under these conditions. ^1H NMR (CD_3Cl , 400 MHz): δ 7.02 (s). **CAUTION:** 1,4-diazidobenzene is a potentially explosive

substance and extreme caution should be used in their preparation and manipulation. To minimize risk to lab personnel, 1,4-diazidobenzene was always synthesized in small (≤ 200 mg) amounts, stored in a freezer at -4 °C, and used in small amounts (≤ 2 mg) for each CuAAC experiment. Synthesis and drying of 1,4-diazidobenzene was always done behind a blast shield and appropriate PPE was used during handling including face shields and blast-resistant leather gloves.

3.4.3 General Procedure for Preparation of Modified Glassy Carbon Electrodes with Multilayer Films

Iodine Azide (IN₃) Solution Preparation. 100 mg of NaN₃ and 10 ml of hexanes was added to a 20 ml scintillation vial. Note that NaN₃ will not dissolve in the hexanes solution. ICl, stored in freezer at -4 °C, was heated at ~ 30 °C in a water bath until a small portion had melted. Immediately prior to use, 10 μ l of ICl was added to the scintillation vial and it was capped, briefly shaken, and wrapped with aluminum foil. The resulting suspension was used immediately after preparation. **CAUTION:** IN₃ is a potentially explosive substances and extreme caution should be used in its preparation and use. To minimize risk to lab personnel, IN₃ was only prepared in solution in small amounts (≤ 2 mg), and used immediately after preparation.

Glassy Carbon Electrode Azide Modification. Glassy carbon disks were hand-polished on 240 grit SiC sandpaper, sonicated for 20 minutes in water, rinsed with water, and then dried under an N₂ stream. Polished disks were then heated in a fused silica-lined furnace at 1000 °C for 90 minutes under a 5 L min⁻¹ forming gas (5% H₂ balance N₂) purge. After 90 minutes, the tube furnace was cooled to approximately 65 °C under the forming gas purge and the electrodes were removed and immediately added to a freshly-prepared IN₃ solution. Electrodes were kept in the solution in the dark for 1 hour.

Step 1: Deposition of Single-Layer Cu(DEphen) Films (SL-Cu(DEphen)). The Cu(DEphen)-click solution was prepared as follows: TBTA (5.3 mg, 0.01 mmol) and DEphen (1.1 mg, 0.0048 mmol) were added to a 20 ml scintillation vial along with 5 ml of DMSO. In a separate 20 ml scintillation vial, CuSO₄•5H₂O (2.7 mg 0.0108 mmol) and 5 ml of water was added. Both vials were vortexed until all solids were dissolved, and then both solutions are combined in a single vial resulting in a light blue solution which was stored in a freezer at -4°C. Immediately prior to use, the solution was removed from the freezer, ascorbic acid (18 mg, 0.102 mmol) was added, and the vial shaken resulting in a deep red solution. In the dark, azide-modified electrodes were removed from the azidification solution, briefly dipped in a cold 1:1 solution of DMSO:H₂O and placed polished-side up in the click solution. Electrodes were stored in the click solution at room temperature for 14 hours in the dark. The resulting SL-Cu(DEphen)-modified electrodes were either cleaned for analysis as described below or immediately used for further click reactions. Characterization of the SL-Cu(DEphen)-modified electrodes is described in the Results and Discussion section.

Step 2: Formation of DAB-terminated SL-Cu(DEphen) films. The DAB-click solution was prepared in a similar manner to above and was done immediately prior to use. TBTA (5.3 mg, 0.01 mmol) was dissolved in 5 ml THF in a 20 mL scintillation vial. CuSO₄•5H₂O (2.7 mg 0.0108 mmol) was dissolved in 5 ml of H₂O in a separate 20 mL scintillation vial. Next, 1,4-diazidobenzene (1.3 mg 0.008 mmol) and ascorbic acid (18 mg, 0.102 mmol) were added to the solution. The vial was briefly shaken to dissolve the solids and the solution changed from light blue to clear. In the dark, SL-Cu(DEphen)-modified electrodes were removed from the DEphen click solution from Step 1, rinsed by dipping in THF, and immediately placed face up in the DAB-click solution. The vial was then sealed and stored in the dark for 14 hours. The resulting DAB-

terminated SL-Cu(DEphen)-modified-electrodes were used immediately for further click reactions. Characterization of the DAB-terminated SL-Cu(DEphen)-modified electrodes is described in the Results and Discussion section.

Step 3: Formation of Double-layer Cu(DEphen) Films (DL-Cu(DEphen)). The Cu(DEphen)-click solution was prepared as described above: TBTA (5.3 mg, 0.01 mmol) and DEphen (1.1 mg, 0.0048 mmol) were added to a 20 ml scintillation vial along with 5 ml of DMSO. In a separate 20 ml scintillation vial, CuSO₄•5H₂O (2.7 mg 0.0108 mmol) and 5 ml of water was added. Both vials were vortexed until all solids were dissolved, and then both solutions are combined in a single vial resulting in a light blue solution which was stored in a freezer at -4 °C. Immediately prior to use, the solution was removed from the freezer, ascorbic acid (18 mg, 0.102 mmol) was added, and the vial shaken resulting in a deep red solution. In the dark, DAB-terminated SL-Cu(DEphen)-modified electrodes were removed from the DAB-click solution from Step 2, rinsed by dipping in THF, and immediately placed face up in the Cu(DEphen)-click solution. The vial was then sealed and stored in the dark for 14 hours. The resulting DL-Cu(DEphen)-modified electrodes were either cleaned for analysis as described below or immediately used for further click reactions. Characterization of the DL-Cu(DEphen)-modified electrodes is described in the Results and Discussion section.

Attempted Formation of Triple-layer Cu(DEphen) Films (TL-Cu(DEphen)). In attempts to form larger multilayer films, Steps 2 and 3 were repeated on the DL-Cu(DEphen)-modified electrodes. Characterization of the resulting attempted TL-Cu(DEphen)-modified electrodes is described in the Results and Discussion section.

Cleaning Procedure for Analysis of Modified Electrodes. After reaction completion, electrodes were removed from the click solution and sonicated for 2 min each in DMSO and

CHCl₃. The electrodes were then rinsed with EtOH followed by a further 2-minute sonication in H₂O. After the final sonication the electrodes were rinsed again with EtOH and dried under an N₂ stream.

Procedure for Stripping Cu from Multilayer Films. Cu was stripped by rotating each electrode at 3000 RPM in a saturated solution of sodium diethyldithiocarbamate trihydrate in methanol for ca. 10 minutes. Afterwards, each electrode was sonicated for 2 minutes in DMSO and then rinsed with copious amounts of water before further analysis. Note that after Cu stripping, Cu could be reinserted into films by soaking them in aqueous solutions of 1 M solution of CuSO₄ for 1 h. After Cu reinsertion, each electrode was rinsed with water, sonicated for 3 minutes in water, and again rinsed in water. Electrodes with the reinserted Cu were then dried under an N₂ stream prior to further analysis.

3.4.4 XPS Measurements

Peak positions of the XPS spectra were referenced to the advantageous carbon peak occurring at 284.8 eV. High-resolution spectra were collected with a pass energy of 20 eV and a step size of 0.1 eV. To quantify elemental ratios, peaks in the XPS high-resolution spectra were first fit to symmetric Voigt lines shapes comprised of 70% Gaussian and 30% Lorentzian functions with a Shirley background for Nitrogen and 10% Gaussian and 90% Lorentzian functions with a Shirley background for Copper. Elemental ratios were calculated by quantifying the total peak area in the N 1s region and the Cu 2p^{3/2} peak and associated shake-up peak, and then dividing by their respective relative sensitivity factors (as tabulated for the Kratos Ultra XPS instrument).

3.4.5 Electrochemical Methods

All electrochemical measurements were done using a standard three electrode electrochemical setup in a one-chamber electrochemical cell. The electrolyte was a 100 mM acetate buffer (50 mM NaOAc•3H₂O and 50 mM HOAc) at pH 4.8 containing 1 M NaClO₄ supporting electrolyte. The pH 4.8 acetate buffer conditions were chosen to be consistent with previous studies of ORR by Cu(phen)-based systems.^{3, 29-32} The surface 1,2,3-triazole linkage tethered to carbon surfaces has been previously shown to be very stable in strongly acidic and alkaline conditions,^{34, 35} and is robust to exposure to 1 M HClO₄ and 1 M NaOH at 100 °C for at least 12 h.³⁴ The working electrodes were the chemically-modified 0.195 cm² glassy carbon disk electrodes. Unless otherwise noted, the auxiliary electrode used was a Pt wire. ORR activity measurements for the single layer and double layer catalyst films were reproduced using a 1 cm² boron doped diamond (BDD) plate, and ORR activity data collected using both the Pt and BDD auxiliary electrodes are essentially equivalent (Figure S3.31 in the SI). The reference was a homemade single-junction Ag/AgCl/KCl(sat.) separated from the electrolyte solution by a CoralPor porous glass frit (Bioanalytical Systems, Inc.) prepared as previously described.³⁶ Ag/AgCl/KCl(sat.) reference electrodes were externally referenced to ferrocenecarboxylic acid in 0.2 M phosphate buffer at pH 7 (0.329 V vs. Ag/AgCl/KCl(sat.)).³⁷

Cyclic Voltammetry (CV) and Rotating Disk Electrode Voltammetry (RDEV) Measurements. Working electrodes were used in combination with a Pine Research Instrumentation E6-series change-disk rotating disk electrode (RDE) assembly attached to a Pine Research Instrumentation MSR rotator. Before each cyclic voltammetry measurement, the electrochemical cells were sparged with either N₂ or O₂ for a minimum of 10 minutes prior to use, and the solution was blanketed with N₂ or O₂ during each measurement. Unless otherwise noted,

the scan rate was 0.1 V s^{-1} for each CV measurement, and 0.025 V s^{-1} for each RDEV measurement.

Rotating Ring Disk Electrode Voltammetry (RRDEV) Measurements. Working electrodes were used in combination with a Pine Research Instrumentation E6-series change-disk rotating-ring disk Pt-ring electrode assembly (RRDE) attached a Pine Research Instrumentation MSR rotator. The Pt ring in the RRDE tip was cleaned prior to each measurement by hand polishing with a $1 \mu\text{m}$ MetaDi diamond slurry (Buehler) first on a Nylon polishing cloth (Buehler), and then on a MicroCloth polishing cloth (Buehler). The RRDE tip was then sonicated in water for 2 minutes, followed by insertion of the working electrode disk. The scan rate for RRDE measurements was 2 mV s^{-1} and the rotation rate was 400 RPM. The optimal ring potential of 0.73 V vs Ag/AgCl/KCl(sat.) and experimentally-determined collection efficiency of 0.175 were determined by detecting H_2O_2 from the 2 e^- reduction of O_2 to H_2O_2 on unmodified glassy carbon disk electrodes. The peroxide fraction was calculated using the follow equation:

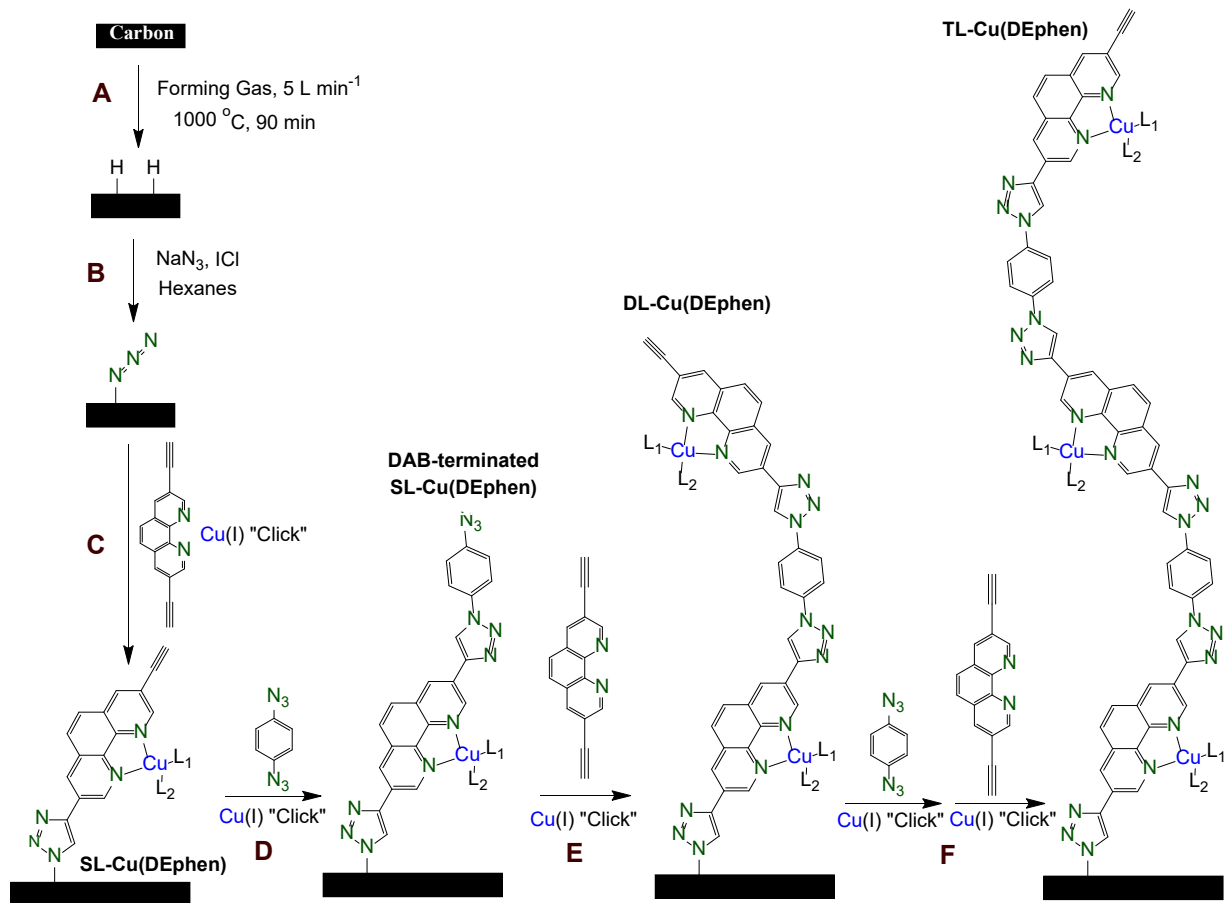
$$\epsilon = \frac{i_r}{i_d N}$$

ϵ is the peroxide fraction, i_r is the ring current, i_d is the disc current, and N is the collection efficiency.

3.5 Results and Discussion

The synthesis strategy for the formation of putative multilayer films of Cu(DEphen) is shown in Scheme 1. The general synthesis strategy is based on a previously-reported preparation for single-layer coverage of Cu(3-ethynyl-1,10-phenanthroline) on glassy carbon surfaces,³² but has been optimized for layer-by-layer film growth (see Figures S3.1 – S3.11 and related discussion in the SI regarding synthesis optimization). First, rough-polished glassy carbon electrodes were

H-terminated by heating in forming gas (5% H₂, balance N₂) for 90 min at 1000 °C (Scheme 1A). The H-terminated carbon surface was then reacted with IN₃ made *in situ* from a suspension of NaN₃ and dissolved ICl in hexanes (Scheme 1B). The resulting N₃-terminated carbon surface was then reacted for 14 h with 3,8-diethynyl-1,10-phenanthroline (DEphen) in the CuAAC with Cu(I) formed *in situ* from dissolved CuSO₄•5H₂O and an excess of ascorbic acid (Scheme 1C). This resulted in a single-layer coverage of Cu(DEphen) covalently tethered to the glassy carbon surface via a robust 1,2,3-triazole linkage. This was followed by sequential 14-h CuAAC reactions with 1,4-diazidobenzene (DAB) (Scheme 1D) and Cu(DEphen) (Scheme 1E) to form a double-layer Cu(DEphen) system. The sequential CuAAC reactions were repeated once more for the attempted synthesis of the triple-layer Cu(DEphen) system (Scheme 1F). Single-layer, double-layer, and triple-layer films of Cu(DEphen) are denoted SL-Cu(DEphen), DL-Cu(DEphen), and TL-Cu(DEphen), respectively. Note that the 14-h CuAAC reaction time is based on time-dependent CuAAC studies that showed 12-14 h was required to fully react the N₃-terminated GC surface with Cu(DEphen) to form SL-Cu(DEphen) films, and to fully react the SL-Cu(DEphen) surface with DAB to form DAB-terminated SL-Cu(DEphen) films (Figures S3.5 and S3.10 in the SI). The optimized 14-h CuAAC reaction time used in this study is consistent with those previously reported for clicking redox probes to N₃-terminated glassy carbon surfaces^{32, 34} and clicking DAB to ethynyl-terminated monolayers.²⁸



Scheme 3.1 Layer-by-layer growth strategy for formation of putative multilayer films of Cu(DEphen) on electrode surfaces using sequential Cu(I) catalyzed Azide-Alkyne Cycloaddition (CuAAC) reactions.

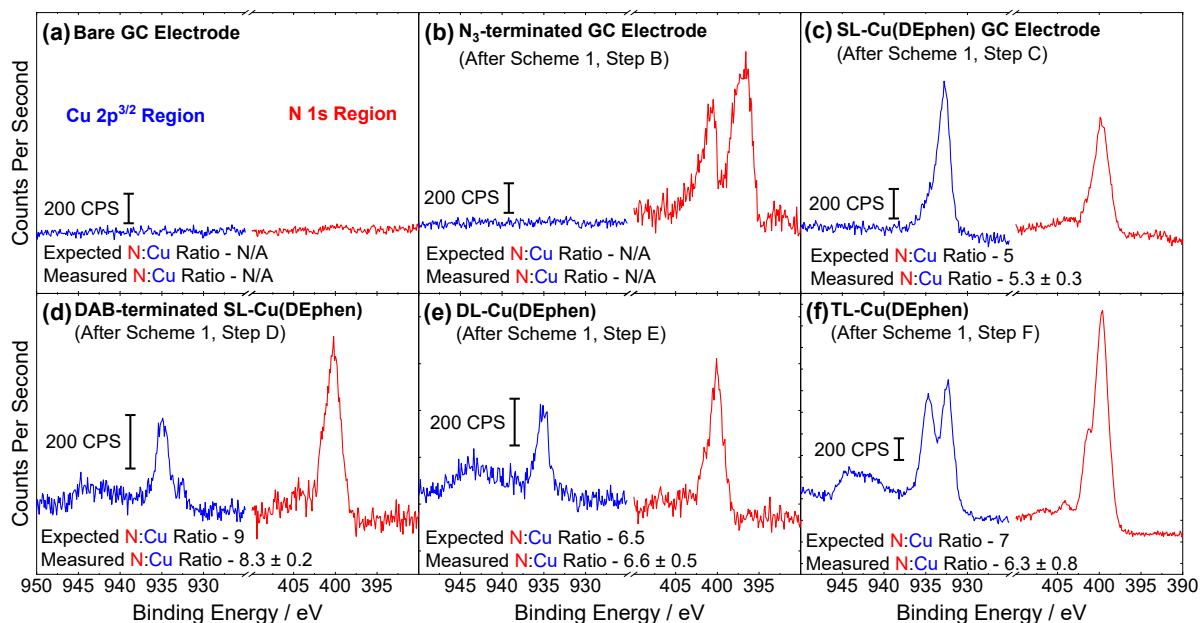


Figure 3.2 Representative high-resolution XPS in the Cu 2p^{3/2} and N 1s regions for independently-prepared multilayer film samples stopped after various steps in the synthesis outlined in Scheme 1. Calculated N:Cu ratios based on the expected structures are listed along with the actual average measured N:Cu ratios from XPS collected from at least 3 independent samples. Note that for (d), the expected N:Cu ratio = 9 assumes the X-ray promoted photodecomposition of the terminal aromatic azide to a terminal aromatic amine.^{38, 39} Reported errors are standard deviations. The broad peak between 940-945 eV in (d)-(f) is a Cu shake-up structure consistent with the presence of Cu(II) in the sample.^{40, 41} The presence of two distinct Cu 2p^{3/2} peaks at 932.5 and 934.7 eV in (f) is consistent of the presence of both Cu(I) and larger amounts of Cu(II) compared to (d) and (e).

Each step of the multilayer film synthesis was confirmed by XPS, and representative spectra from independently synthesized films stopped at different steps in the synthetic process are shown in Figure 2. Starting with a bare GC surface (Figure 3.2a), upon heat-treatment and subsequent treatment with IN₃ solution (Scheme 3.1B) we observe two N 1s peaks at ~397 and ~401 eV in a 2 to 1 ratio consistent with an azide-terminated carbon surface (Figure 3.2b).^{32, 35} Exposure to DEphen under CuAAC conditions (Scheme 3.1C) leads to an XPS spectra consistent with formation of a SL-Cu(DEphen) as indicated by the coalescence of the azide N peaks into a single N 1s feature at 399 eV and the appearance of a Cu 2p^{3/2} peak at 933 eV (Figure 3.2c). The ratio of the integrated peak areas, corrected for their respective relative sensitivity factors,

corresponds to a N:Cu ratio of 5.3:1, close to the expected 5:1 ratio. After exposure to DAB under CuAAC conditions (Scheme 3.1D), the N:Cu ratio from XPS shifts to 8.3:1, smaller than but close to the 9:1 ratio expected for a DAB-terminated surface in which the terminal N₃ has photodecomposed to a terminal aromatic amine (Figure 3.2d).^{38, 39} Subsequent exposure to DEphen under CuAAC conditions (Scheme 3.1E) leads to an XPS spectra with a N:Cu ratio of 6.6:1 consistent with formation of a DL-Cu(DEphen) (Figure 3.2e). Finally, further sequential exposure to DAB followed by DEphen both under CuAAC conditions (Scheme 3.1F) leads to an XPS spectra with a total N:Cu ratio of 6.3:1 (Figure 3.2f). This ratio is closer to the expected N:Cu ratio of the DL-Cu(DEphen), but still within error of the N:Cu ratio of 7:1 expected for the TL-Cu(DEphen).

Surface coverages of Cu in the SL-Cu(DEphen), DL-Cu(DEphen), and TL-Cu(DEphen) were estimated by integrating the peak area from the Cu^{II/I} couples in cyclic voltammograms (CVs). Representative CVs are shown in Figure 3.3a, and a box-and-whisker plot showing the measured coverages from CV data is shown in Figure 3.3b. The peak current increases linearly with scan rate for each system (Figures S3.12 – S3.14 in the SI) confirming that the species are surface-immobilized. There is roughly a doubling of the estimated Cu coverage moving from SL-Cu(DEphen) with $\Gamma_{\text{SL}} = 0.94 \pm 0.26 \times 10^{15}$ molecules cm⁻² to DL-Cu(DEphen) with $\Gamma_{\text{DL}} = 1.93 \pm 0.54 \times 10^{15}$ molecules cm⁻² consistent with a double layer film. The average coverage Cu in TL-Cu(DEphen) at $\Gamma_{\text{TL}} = 2.08 \pm 0.73 \times 10^{15}$ molecules cm⁻² is roughly the same as the double layer suggesting that the triple layer formation was unsuccessful.

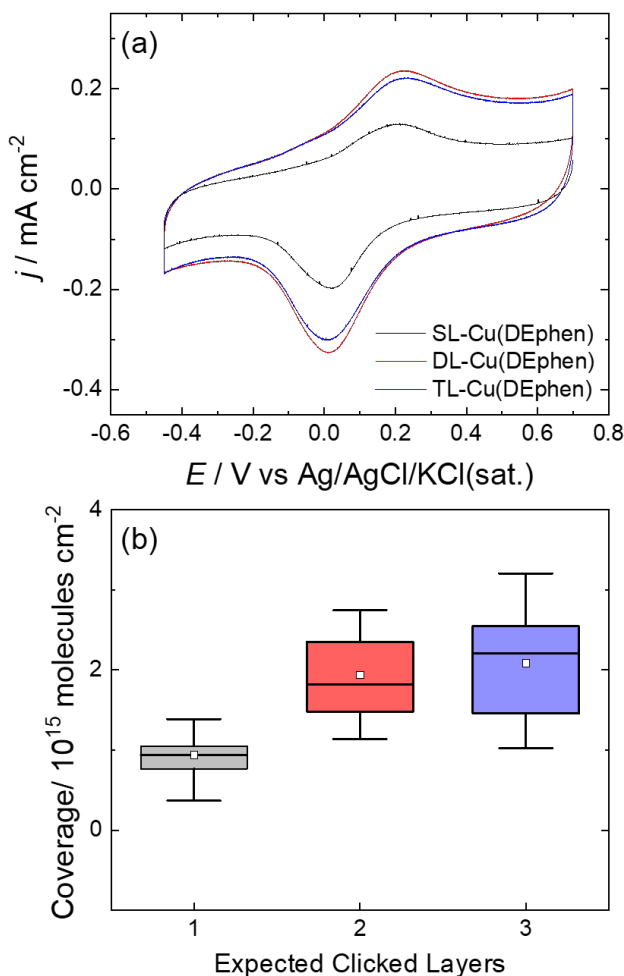


Figure 3.3 (a) Representative CVs of SL-Cu(DEphen), DL-Cu(DEphen), and TL-Cu(DEphen) film samples. The coverage of each surface was estimated by integrating the charge under the $\text{Cu}^{\text{II/I}}$ redox features. (b) A box and whisker plot of coverages of the SL-Cu(DEphen), DL-Cu(DEphen), and TL-Cu(DEphen) estimated from integrated charges from cyclic voltammograms. The small white box represents the average (mean) coverage while the horizontal line represents the median value. The larger shaded box represents the coverage range in which 50% of the measurements occur, and the error bars represent the 1.5 IQR range. N is the number of coverage measurements from independently-prepared electrodes. The estimated coverage of the DL-Cu(DEphen) system is roughly double that of the SL-Cu(DEphen). However, the average coverage of the TL-Cu(DEphen) is roughly equivalent to that of the DL-Cu(DEphen).

Note that the lack of an observed increase in surface coverage and activity for the TL-Cu(DEphen) films compared to the DL-Cu(DEphen) could be a result of either an unsuccessful final CuAAC reaction resulting in no attachment of the third DEphen layer, or a successful final CuAAC reaction but without Cu insertion resulting in a third layer of unmetallated DEphen. To

distinguish between these two possibilities, we exposed TL-Cu(DEphen) films to aqueous solutions of 1 M $\text{Cu}(\text{NO}_3)_2$ for 1 hr. The post-synthesis exposure of the TL-Cu(DEphen) surface to Cu did not result in an increase in the Cu coverage as determined from CV measurements (Figure S15 in the SI). This suggests that the CuAAC reaction was unsuccessful in attaching a third DEphen unit to the surface.

The irreversibility of the redox couple under N_2 is likely due to a structural reorganization of the Cu(DEphen) complex upon reduction, presumably from a square planar Cu(II) complex to a tetrahedral Cu(I) complex.³ We observe an increased peak-to-peak splitting as a function of increasing scan rate in the CVs that is consistent with a large structural reorganization associated with the redox event (Figure S3.16 in the SI). Note that both the SL-Cu(DEphen) and the DL-Cu(DEphen) show similar peak-to-peak splitting at each scan rate. However, the full-width-at-half-max (FWHM) of the DL-Cu(DEphen) is up to 30% larger than that of the SL-Cu(DEphen) (Figure S3.17 in the SI). This suggests that the Cu(DEphen) sites in the DL-Cu(DEphen) film experience a larger variance in their chemical environments compared to the SL-Cu(DEphen), leading to an effective peak broadening. This larger variance in chemical environment for the DL-Cu(DEphen) could be due to the slightly slower electron transfer rates to the exterior sites compared to the interior sites in the double layer film, or different effective electrolyte exposure to the interior and exterior Cu(DEphen) sites.

To confirm that the increased coverage measured for DL-Cu(DEphen) and TL-Cu(DEphen) compared to SL-Cu(DEphen) lead to a corresponding increase in catalytic activity, we measured CVs of each deposited film in the presence of O_2 , and representative CVs are shown in Figure 3.4a-c. Note that there is a qualitative increase in the catalytic peak current in O_2 -saturated solution when going from SL-Cu(DEphen) in Figure 3.4a to DL-Cu(DEphen) in Figure

3.4b, but there is no additional appreciable increase in the catalytic peak current when going from DL-Cu(DEphen) in Figure 3.4b to TL-Cu(DEphen) in Figure 3.4c. To better quantify the catalytic activity, we conducted rotating-disk voltammetry measurements at multiple rotation rates for each film (Figures S3.18 – S3.20 in the SI), and conducted Koutecky-Levich analysis as previously reported to estimate the kinetic current densities, j_K , at which the current is limited only by the underlying kinetics of the system and not mass transport.^{3, 32, 42, 43} The resulting potential-dependent kinetic currents are shown in Figures 3.4d-3.4f, and a table of j_K average values and standard deviations at selected potentials is shown in Table S3.2. The SL-Cu(DEphen) films operate with similar activities for the ORR compared to previously-reported single-layer films of clicked Cu(3-ethynyl-1,10-phenanthroline) onto glassy carbon electrodes with similarly high loadings.³² In general, the DL-Cu(DEphen) film operates with approximately twice the activity of the SL-Cu(DEphen) film at every potential negative of the catalytic onset at $E \approx 0$ V vs Ag/AgCl/KCl(sat.), consistent with a doubling of the number of the active sites. However, TL-Cu(DEphen) films show essentially no difference in activity compared to the DL-Cu(DEphen) films.

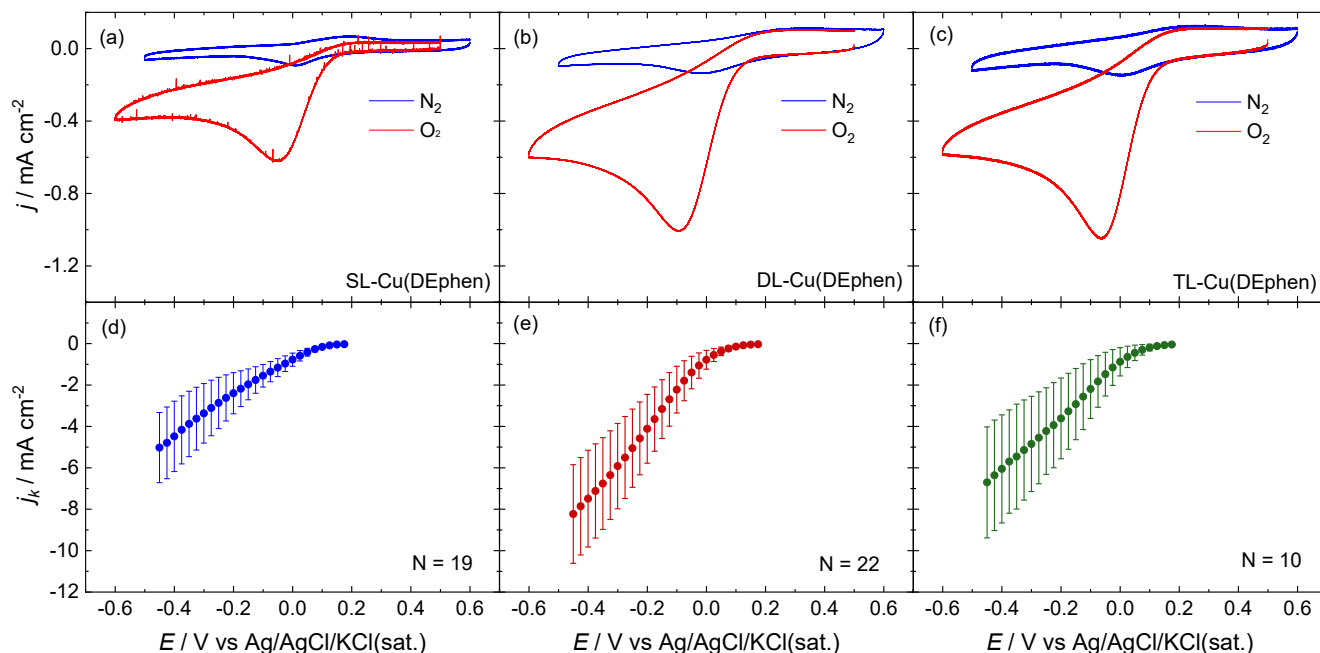


Figure 3.4 Representative CVs of (a) SL-Cu(DEphen), (b) DL-Cu(DEphen), and (c) TL-Cu(DEphen) film samples under N_2 (blue line) and O_2 (red line). The large increase in the magnitude of the reductive current in the presence of O_2 is indicative of catalytic turnover. Kinetic current densities (j_K) estimated from Koutecky-Levich analysis of rotating disk voltammetry data are shown in (d) for SL-Cu(DEphen), (e) for DL-Cu(DEphen), and (f) for TL-Cu(DEphen). The central data points in each plot are the average potential-dependent j_K values, and the exterior error bars are the standard deviations at each potential. The area within the error bars is the $\sim 68\%$ confidence interval of the measurement set, and N is the number of j_K estimates from independently prepared electrodes in each measurement set including data collected using both Pt and BDD auxiliary electrodes.

To ensure that Cu was not leaching from the catalyst films during the RDE experiments, we measured the surface coverage before-and-after the catalytic RDE experiments for 3 independently-synthesized SL-Cu(DEphen) and 3 independently-synthesized DL-Cu(DEphen) films. Representative CVs of the SL-Cu(DEphen) and DL-Cu(DEphen) under N_2 are shown in Figures S3.21 and S3.22 in the SI. The measured coverages based on CV data for the SL-Cu(DEphen) and DL-Cu(DEphen) films after the catalytic RDE experiments were within $84 \pm 10\%$ and $97 \pm 4\%$ of the initial values, respectively. In addition, to measure for possible loss of

catalytic activity over the course of the RDE experiments, we included an initial and final catalytic RDE voltammograms at 400 RPM in O₂-saturated solution into each set of experiments as seen in the representative RDE voltammograms in Figures S3.18-S3.20 in the SI. The final RDE voltammograms at 400 RPM were within 10% of the initial measurements (Figure S3.23), confirming no appreciable loss of activity during the catalytic ORR measurements.

To confirm that the molecular Cu(DEphen) catalyst in the films are responsible for the observed ORR activity, as opposed to a trace contaminant, we performed a series of control experiments. First, we measured the ORR activity of an N₃-terminated glassy carbon surface not exposed to click conditions. The resulting surface shows essentially no activity for the ORR at potentials positive of -0.15 V vs Ag/AgCl/KCl(sat.) which is consistent with previous reports of background ORR activity on N₃-terminated glassy carbon surfaces (Figure S3.24 in the SI).³² Next, we measured the ORR activity of glassy carbon electrodes exposed to CuACC *minus* one critical component for successful surface attachment: 1) without a surface azide (Figure S3.25 in the SI), 2) without the CuSO₄·5 H₂O click catalyst (Figure S3.26 in the SI), or 3) without the DEphen (Figure S3.27 in the SI). In all three cases, the ORR activity was qualitatively analogous to the N₃-terminated glassy carbon backgrounds, with no evidence of surface-immobilized Cu(DEphen) via CV and no appreciable ORR current at potentials positive of -0.15 V vs Ag/AgCl/KCl(sat.). We also measured the ORR activity of SL-Cu(DEphen) and DL-Cu(DEphen) that were stripped of their Cu using diethyldithiocarbamate (Figures S3.28-S3.29 in the SI). Copper stripping was confirmed by loss of the Cu^{II/I} redox couple via CV under N₂. The resulting films also showed similar activity to the N₃-terminated glassy carbon backgrounds with essentially no ORR activity at potentials positive of -0.15 V vs Ag/AgCl/KCl(sat.). These control experiments confirm that both Cu and DEphen are necessary for the ORR activity observed in Figure 3.4. Note

that SL-Cu(DEphen) electrodes stripped of Cu could be regenerated by soaking them in a solution of 1 M CuSO₄ for 1 hour. We were able to obtain regenerated surface coverages equivalent to $67 \pm 10\%$ of the original loading (See Figure S3.30 in the SI). We suspect the incomplete regeneration may be related to the film sterics preventing complete insertion of Cu and that the higher original loading is due to copper insertion into the DEphen complex during film synthesis.

In addition, to verify that trace Pt contamination from the auxiliary electrode does not contribute to the observed ORR activity, we repeated the ORR activity measurements for SL-Cu(DEphen) and DL-Cu(DEphen) using a boron-doped diamond (BDD) auxiliary electrode (Figure S3.31). The resulting ORR measurements are essentially identical to those measured using a Pt auxiliary electrode, confirming that trace Pt contamination is not responsible for the measured ORR activity for the SL-Cu(DEphen) and DL-Cu(DEphen) systems.

The cumulative XPS, electrochemical coverage, and ORR activity data suggest that the DL-Cu(DEphen) film is, in fact, a double-layer film containing approximately twice the Cu(DEphen) components each operating at equivalent turnover frequencies compared to the SL-Cu(DEphen) film. In contrast, based on our measurements we propose that synthesis of the TL-Cu(DEphen) film was largely unsuccessful using our layer-by-layer synthesis strategy—the average coverage and ORR activity measured for the TL-Cu(DEphen) film are similar to those of the DL-Cu(DEphen) films. We postulate that steric limitations may prevent the growth of triple layer films. Specifically, the rotational flexibility between the DEphen ligands and the 1,4-ditriazolylbenzene linkages and the high roughness of our actual carbon surfaces may introduce steric interactions between adjacent multilayer Cu(DEphen) strands and inhibit triple-layer formation due to resulting steric constraints. Due to the relatively high ORR background activity for the ORR, it is likely that moving to the order-of-magnitude lower catalyst loadings on GC

electrodes necessary to alleviate the steric limitations to further film growth will result in catalyst films that do not have measurable ORR activity above the GC background activity. We are currently exploring layer-by-layer growth of more dilute films on alternative electrode surfaces that show lower background activity for the electrocatalytic reactions being investigated.

In addition to the increased activity observed for the ORR by DL-Cu(DEphen) compared to SL-Cu(DEphen), we also observed a change in the potential-dependent product distribution. In particular, we measured the fractional current going to H₂O₂ production using rotating ring-disk electrode (RRDE) voltammetry at 400 rpm. Representative RRDE voltammograms are shown in Figures S3.32-S3.34 in the SI, and the average fractional of current going to H₂O₂ production at various potentials for SL-Cu(DEphen) and DL-Cu(DEphen) are shown in Figure 3.5a-b. In the case of SL-Cu(DEphen), there is an increase in the fractional H₂O₂ production at more negative potentials, from 0.16 ± 0.06 at 0 V vs Ag/AgCl/KCl(sat.) to 0.45 ± 0.13 at -0.4 V vs Ag/AgCl/KCl(sat.). This trend is consistent with previous studies of the ORR by clicked Cu(3-ethynyl-1,10-phenanthroline) which suggest two different mechanisms for oxygen reduction: a lower overpotential bimetallic mechanism in which O₂ is activated by two adjacent clicked Cu complexes and reduced by 4 e⁻ to H₂O, and a higher overpotential monomolecular mechanism in which O₂ is activated by a single Cu complex and reduced by 2 e⁻ to H₂O₂.³²

In the case of DL-Cu(DEphen), there is no discernable potential dependence of the fractional H₂O₂ production which remains low at $\leq 20\%$ at every potential. We suggest two different mechanisms that may be responsible for the decreased potential-independent H₂O₂ production observed for DL-Cu(DEphen). First, entanglement of the DL-Cu(DEphen) strands could force Cu centers closer together in the exterior layer, leading to an increased number of bimetallic active sites that can coordinate and reduce O₂ by 4 e⁻ to H₂O as illustrated in Figure

3.5c. Alternatively, because Cu complexes with 1,10-phenanthroline-based ligands are known to reduce H_2O_2 by $2 e^-$ to H_2O ,^{29, 31, 44-46} an equally-valid explanation might be a cascade (or tandem) catalysis mechanism in which O_2 is first reduced to H_2O_2 at the exterior Cu site, and then the H_2O_2 is subsequently reduced to H_2O at a second Cu site as illustrated in Figure 3.5d. We cannot distinguish between the two different possible explanations in the present study, but the important point is that the DL-Cu(DEphen) shows dramatically decreased H_2O_2 production compared to the single-layer analogue. Note that the TL-Cu(DEphen) shows analogous product distribution compared to the DL-Cu(DEphen) (see Figure S3.35).

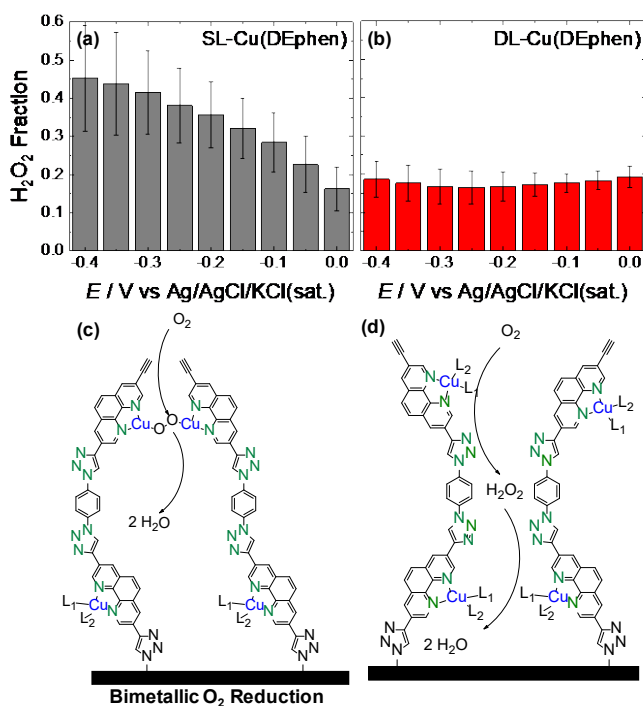


Figure 3.5 (a-b) Fraction of the ORR current going to H_2O_2 production as a function of potential based on RRDE measurements at 400 rpm for (a) SL-Cu(DEphen) and (b) DL-Cu(DEphen). (c-d) Postulated mechanisms explaining the decreased H_2O_2 production observed for DL-Cu(DEphen) due to (c) increased likelihood of bimetallic activation of O_2 or (d) possibility of cascade (or tandem) catalysis involving sequential reduction of O_2 to H_2O_2 to H_2O .

3.6 Conclusions

In this study, we have reported a layer-by-layer synthesis strategy for the controlled growth of electrocatalytic films on carbon surfaces and showed that this method is effective for the formation of single-layer and double-layer films of Cu(DEphen). The double-layer DL-Cu(DEphen) films showed roughly twice the coverage and activity for the ORR compared to the single-layer SL-Cu(DEphen), and significantly increased selectivity for the $4 e^-$ reduction of O_2 to H_2O over the $2 e^-$ reduction of O_2 to H_2O_2 . Triple layer formation was not achieved using this synthesis procedure likely due to steric interactions between adjacent multilayer Cu(DEphen) strands on the high-coverage surfaces. However, these same postulated steric interactions between adjacent Cu(DEphen) strands that may prevent triple-layer formation may also lead to an increased number of bimetallic active sites in the DL-Cu(DEphen) resulting in the increased product selectivity for the ORR to H_2O , although we cannot distinguish this from possible cascade catalysis of O_2 to H_2O_2 to H_2O along the tethered double layers. This study serves as a proof-of-principle that highlights the benefits and limitations of layer-by-layer growth by sequential CuACC. We showed that we can increase activity in predictable ways by forming multilayer films, but steric congestion can prevent formation of larger film thicknesses. One strategy to prevent this steric limitation to thicker film synthesis may be increasing the spacing between covalently linked strands on the electrode surfaces, thereby decreasing the probability of entanglement and facilitating the growth of further layers.

3.7 Supplementary Information

3.7.1 Optimization of Layer-by-Layer Synthesis: SL-Cu(DEphen)

Initial syntheses based on previously published methods³² resulted in highly variable films that showed no clear trends. Activity and surface coverage demonstrated only a small increase for the double-layer. In addition N:Cu ratios were often far from the ideal value of 5:1 for the single-layer and 6.5:1 for the double-layer. These results suggested that the conditions we were using were not optimal for multilayer film formation. In order to optimize the conditions we performed multiple sets of syntheses during which we varied one condition while holding the others constant. The initial set of optimizations were performed for SL-Cu(DEphen) electrodes using the N:Cu ratio as a marker for successful film synthesis. This allowed us to detect successful formation of mono-ligated Cu(DEphen) complexes.

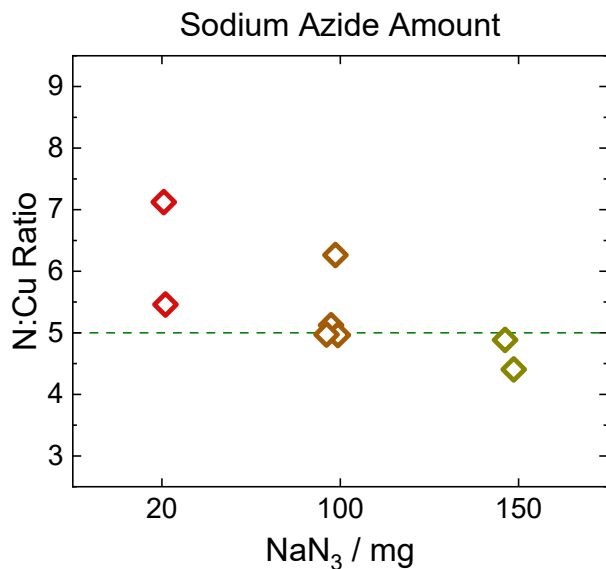


Figure S3.1 N:Cu ratio for SL-Cu(DEphen) electrodes synthesized with varying amounts of NaN₃ in the azidification solution used for the initial preparation of the N₃-terminated glassy carbon electrode. The ideal ratio of 5:1 is denoted by the dashed line. Based on the results 100 mg of NaN₃ was used for the optimized synthesis conditions.

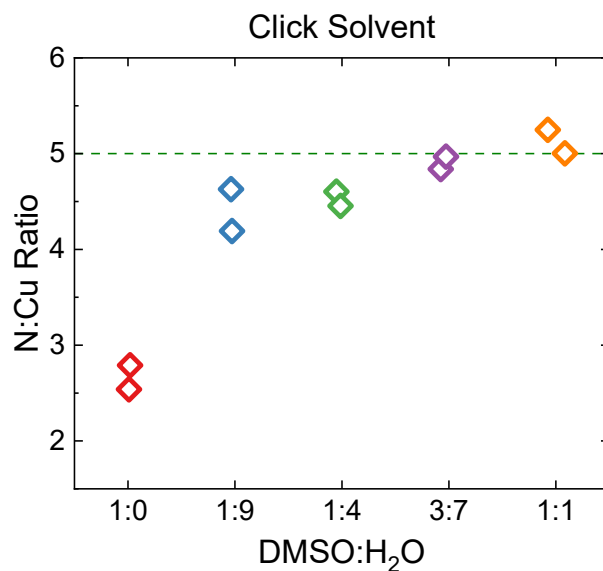


Figure S3.2 N:Cu ratios for SL-Cu(DEphen) synthesized with varying DMSO:H₂O ratios in the CuACC click solution. Increasing the amount of H₂O beyond a 1:1 ratio resulted in precipitation of reagents. Based on these results a DMSO:H₂O ratio of 1:1 was used in the optimized conditions.

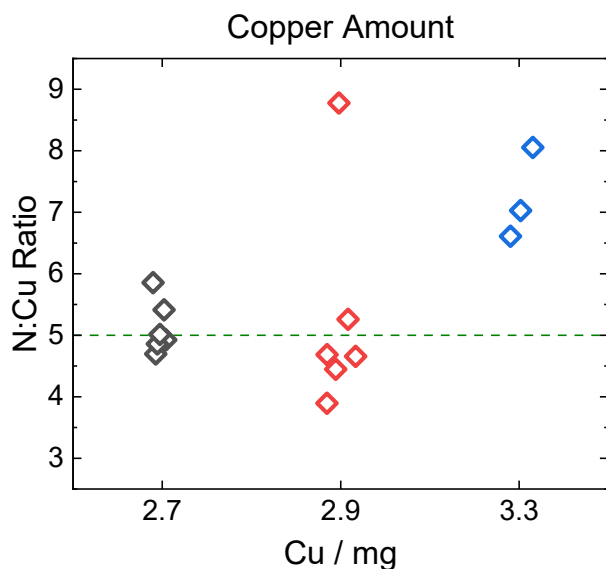


Figure S3.3 N:Cu ratios for SL-Cu(DEphen) synthesized with varying copper amounts in the CuACC click solution. The concentration of copper plays a critical role in the synthesis because of the high stability of the bis $\text{Cu}(\text{DEphen})_2$ complex. To promote formation of the mono complex an excess of Cu must be used. Based on these results 2.7 mg of Cu was used for the optimized conditions.

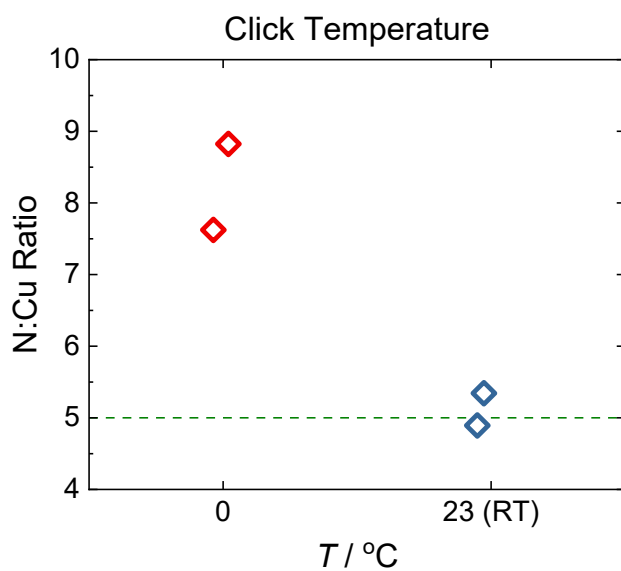


Figure S3.4 N:Cu ratios for SL-Cu(DEphen) synthesized using CuAAC solutions at either 0 °C or room temperature (RT). Elevated temperatures (not shown) resulted in decomposition of the azide. Based on these results room temperature was used for subsequent reactions.

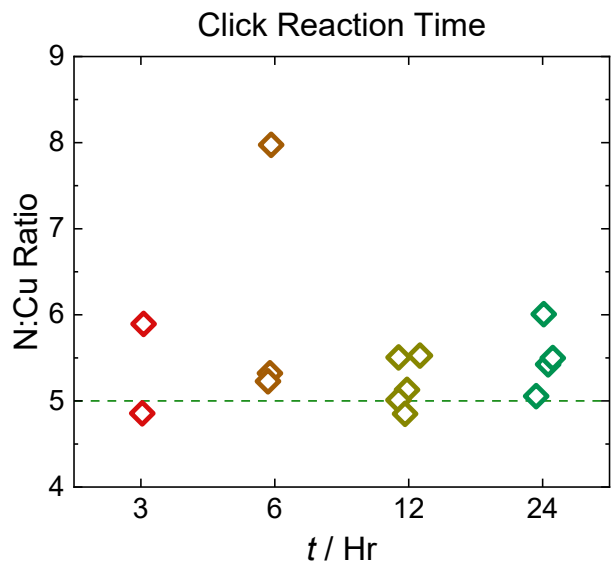


Figure S3.5 N:Cu ratios for SL-Cu(DEphen) synthesized with varying reaction times (e.g. times of exposure to the CuAAC click solution). Each CuAAC reaction was done in a separate vial to avoid contamination when removing electrodes for cleaning. Although 12 hours shows the appropriate N:Cu ratio, we used 14 hours in the optimized synthesis conditions to remain consistent with the optimized double-layer film synthesis procedure as described in Figure S3.10.

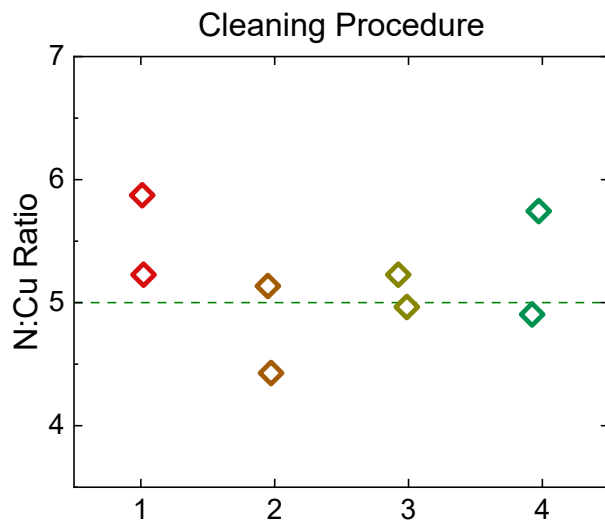


Figure S3.6 N:Cu ratios for SL-Cu(DEphen) synthesized with varying cleaning procedures. The four cleaning procedures 1-4 are outlined in **Table S1**. There are two points in the synthesis that require cleaning. First, after the azidification step used to prepare the N₃-terminated glassy carbon surfaces, a cleaning step is required to remove hexanes and unreacted sodium azide. Failure to clean the electrode after the azidification step resulted in the formation of precipitates in the CuAAC click solution. Second, after the CuAAC click reaction is completed, a cleaning step is required to remove any unclicked physisorbed species from the electrode surface. Based on these results cleaning procedure 3 was used in the optimized procedure.

Table S3.1 Cleaning Procedures

Cleaning Procedure	After Azidification	Final Cleaning
1	Rinsed with EtOH	2 minute sonication in DMSO, DCM, EtOH, and H ₂ O
2	Rinsed with EtOH	2 minute sonication in DMSO and DCM. Rinse with EtOH. 2 minute sonication in EtOH
3	Dipped in Cold 1:1 DMSO:H ₂ O	2 minute sonication in DMSO and DCM. Rinse with EtOH. 2 minute sonication in EtOH
4	Dipped in Cold 1:1 DMSO:H ₂ O	2 minute sonication in DMSO, DCM, EtOH, and H ₂ O

3.7.2 Optimization of Layer-by-Layer Synthesis: DL-Cu(DEphen)

Using the optimized conditions outlined in Figures S1-S6, we were able to reproducibly synthesize SL-Cu(DEphen) films. However, when we attempted to use the conditions to form the DL-Cu(DEphen) films, we found that the DAB linker was decomposing to 1,4-diaminobenzene in the click solution (Figure S8-S9). We postulate that this decomposition is due to the heat released by the exergonic mixing of DMSO and H₂O. Attempts to add the DAB to the pre-mixed 1:1 DMSO:H₂O solutions was unsuccessful due to the low solubility of DAB in the mixture. We determined that 1:1 THF:H₂O could be used as an alternative solution in which the DAB was more soluble and stable (Figure S10). Using the new click solution we were able to successfully synthesize the DAB-terminated SL-Cu(DEphen) and the DL-Cu(DEphen) as described below.

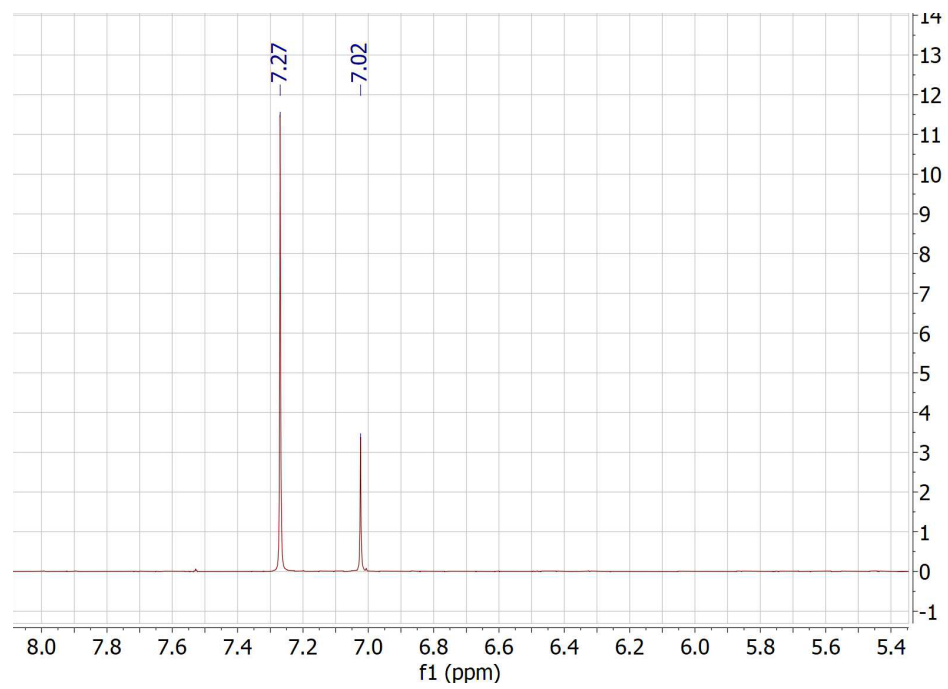


Figure S3.7 NMR spectrum of 1,4-diazidobenzene in CDCl_3 showing characteristic peak at 7.02 ppm.

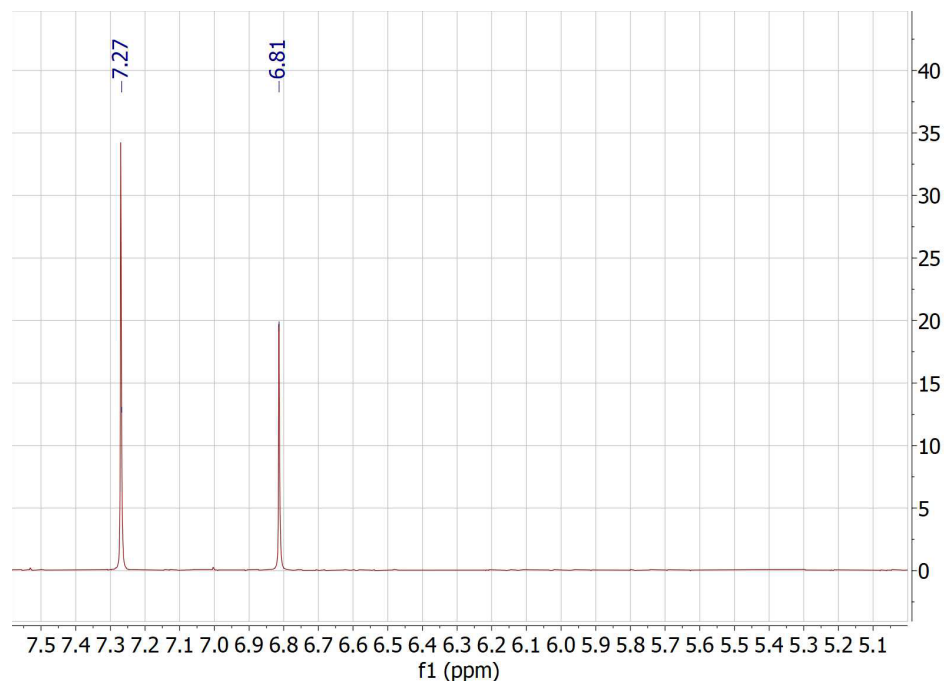


Figure S3.8 NMR depicting decomposition of 1,4-diazidobenzene to 1,4-diaminobenzene in DMSO:H₂O mixture. 1.3 mg of 1,4-diazidobenzene was first dissolved into 5 mL of DMSO, and then the resulting solution was added to 5 mL of H₂O. There was a noticeable heating of the solution upon mixing the DMSO and H₂O. The resulting 1,4-diaminobenzene was then extracted into CDCl₃. The resulting NMR shows a peak at 6.81 ppm consistent with the formation of 1,4-diaminobenzene. The peak at 7.27 is due to CDCl₃.

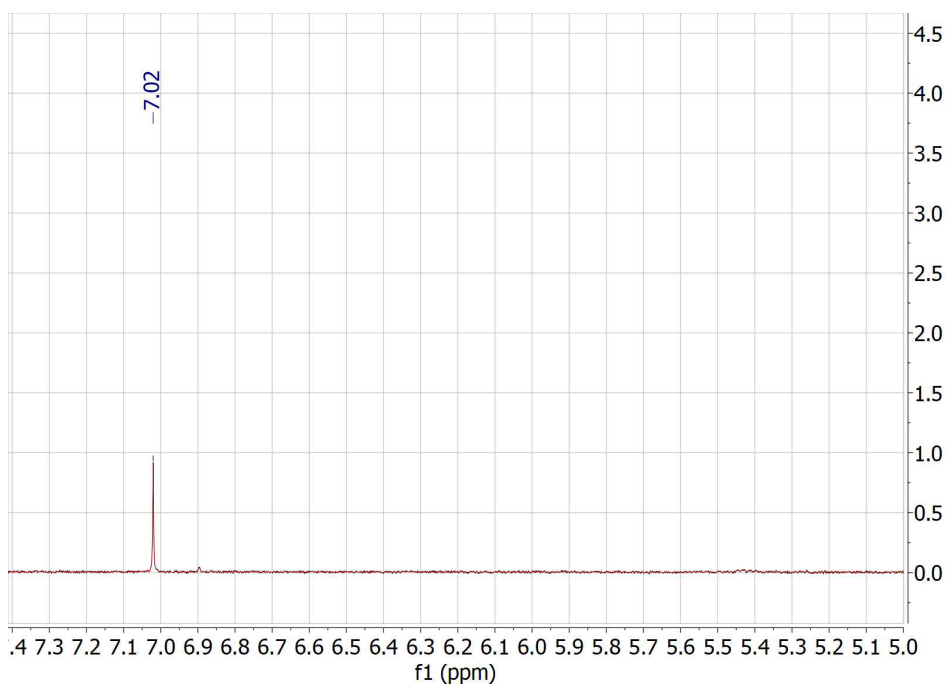


Figure S3.9 1.3 mg of 1,4-diazidobenzene was first dissolved into 5 mL of d8-THF, and then the resulting solution was added to 5 mL of D₂O. There was no noticeable heating of the solution upon mixing the d8-THF and D₂O. An NMR of the resulting 1:1 d8-THF:D₂O solution shows a peak at 7.02 ppm consistent with 1,4-diazidobenzene, confirming the reactant does not decompose during mixing of these solvents.

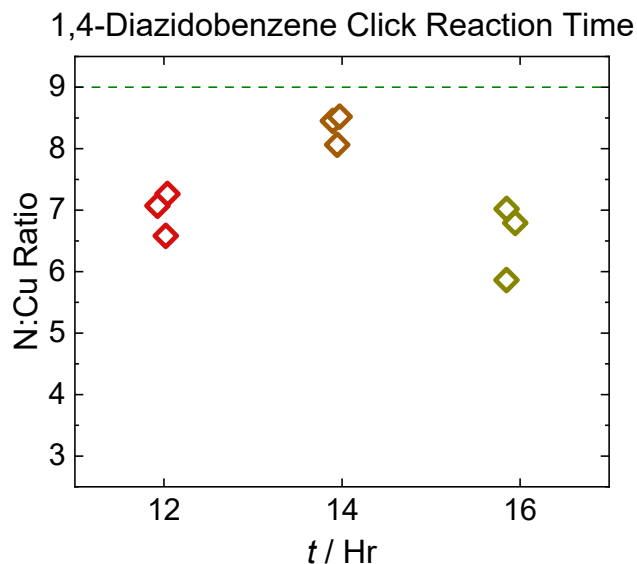


Figure S3.10 N:Cu ratios for DAB terminated SL-Cu(DEphen) synthesized with varying reaction times (e.g. times of exposure to the DAB CuAAC click solution). The ideal N:Cu ratio of 9 assumes X-ray promoted photodecomposition of the terminal azide to a terminal amine.^{38, 39} Based on these results 14 hours was used for the reaction time.

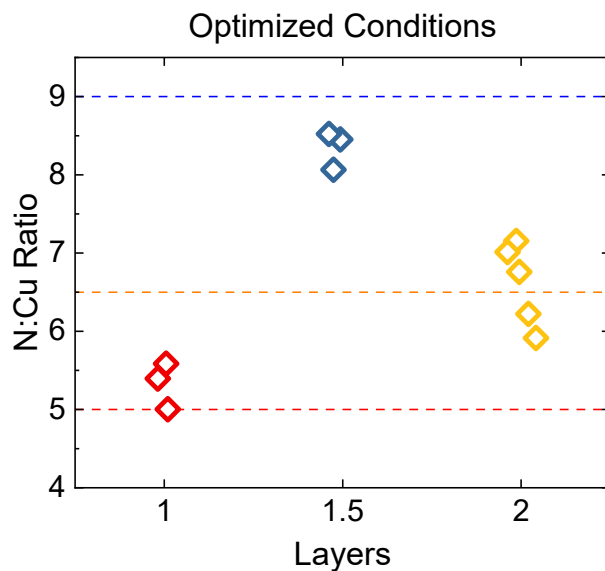


Figure S3.11 N:Cu ratios for SL-Cu(DEphen), DAB terminated SL-Cu(DEphen), and DL-Cu(DEphen) using the optimized conditions outlined in the experimental section of the main text as derived from the experiments in Figures S1-S10. The ideal ratios for each are denoted with a dashed line.

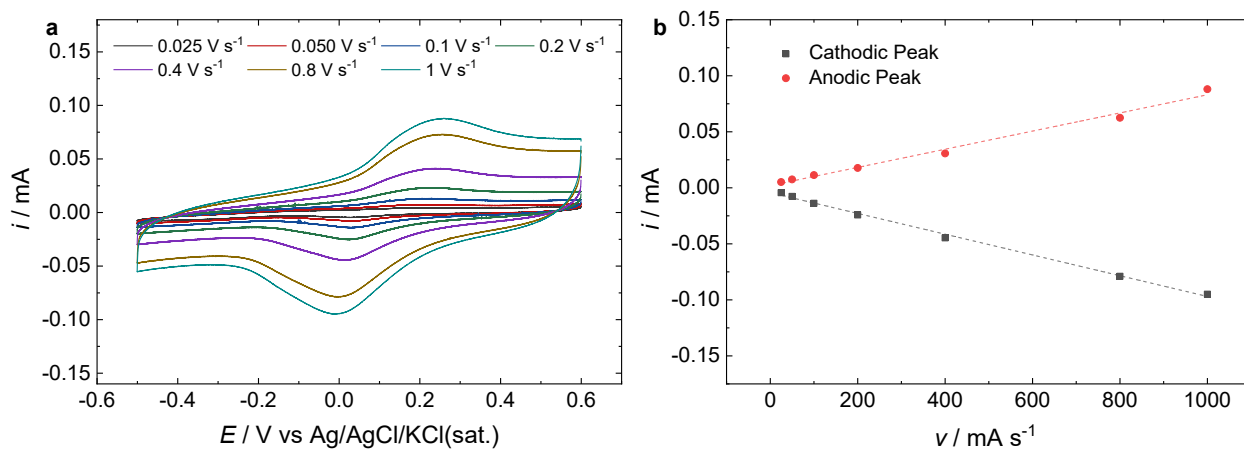


Figure S3.12 Representative scan rate dependence of a SL-Cu(DEphen) film.

a. Representative cyclic voltammograms of the phenanthroline-free surface in a 100 mM acetate buffer (50 mM NaOAc•3H₂O and 50 mM HOAc) at pH 4.8 containing 1 M NaClO₄ supporting electrolyte under an N₂ and O₂ atmosphere.

b. Representative kinetic current in the same buffer under an O₂ atmosphere as derived from RRDE measurements and Koutecky-Levich analysis.

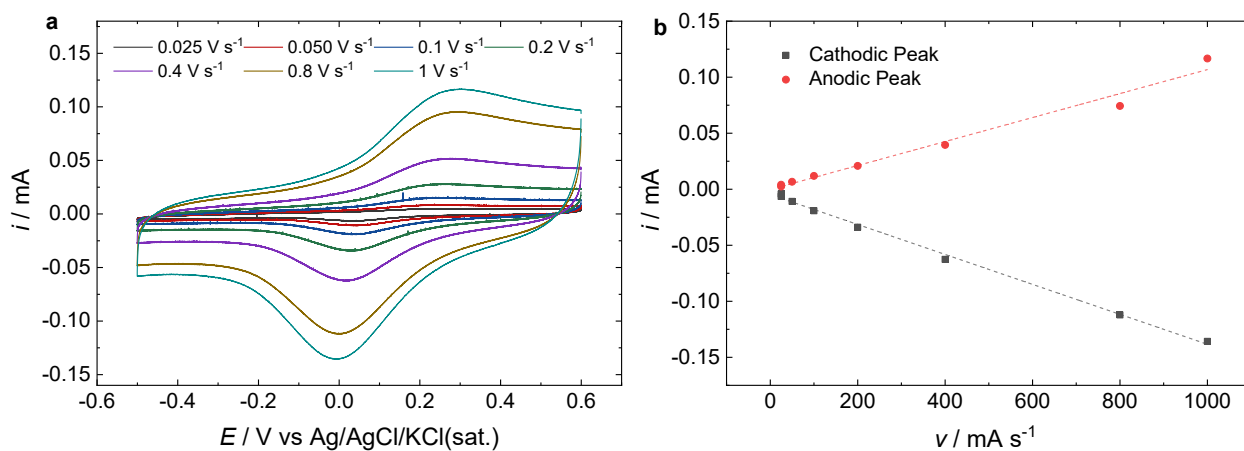


Figure S3.13 Representative scan rate dependence of a DL-Cu(DEphen) film.

a. Cyclic voltammograms of a DL-Cu(DEphen) film in a 100 mM acetate buffer (50 mM NaOAc•3H₂O and 50 mM HOAc) at pH 4.8 containing 1 M NaClO₄ supporting electrolyte under an N₂ atmosphere at multiple scan rates.

b. Linear dependence of peak current versus scan rate. The linear relationship is indicative of a surface-immobilized species.

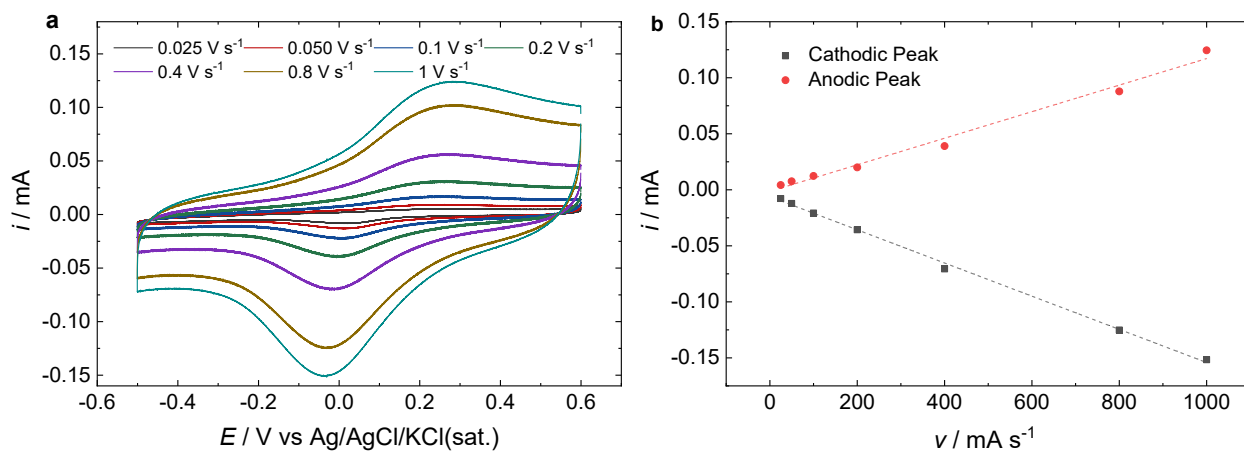


Figure S3.14 Representative scan rate dependence of a TL-Cu(DEphen) film.

a. Cyclic voltammograms of a TL-Cu(DEphen) film in a 100 mM acetate buffer (50 mM $\text{NaOAc} \cdot 3\text{H}_2\text{O}$ and 50 mM HOAc) at pH 4.8 containing 1 M NaClO_4 supporting electrolyte under an N_2 atmosphere at multiple scan rates.

b. Linear dependence of peak current versus scan rate. The linear relationship is indicative of a surface-immobilized species.

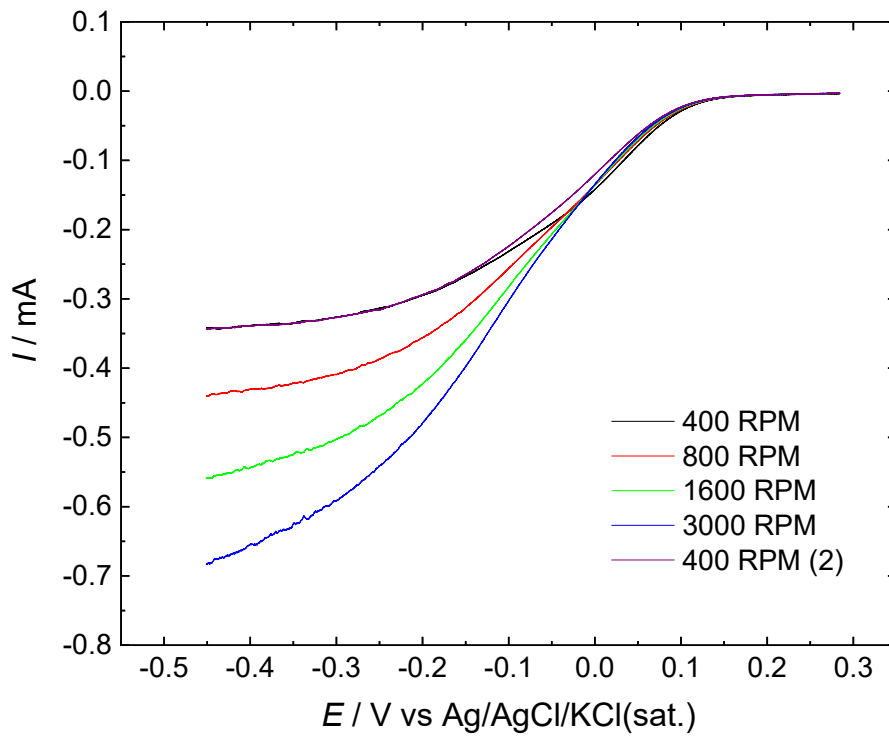


Figure S3.15 Representative rotating disk electrode voltammogram of a SL-Cu(DEphen) film in a 100 mM acetate buffer (50 mM NaOAc \cdot 3H₂O and 50 mM HOAc) at pH 4.8 containing 1 M NaClO₄ supporting electrolyte under an O₂ atmosphere. A 400 RPM scan is performed at the beginning and end of the experiment to ensure stability of the film.

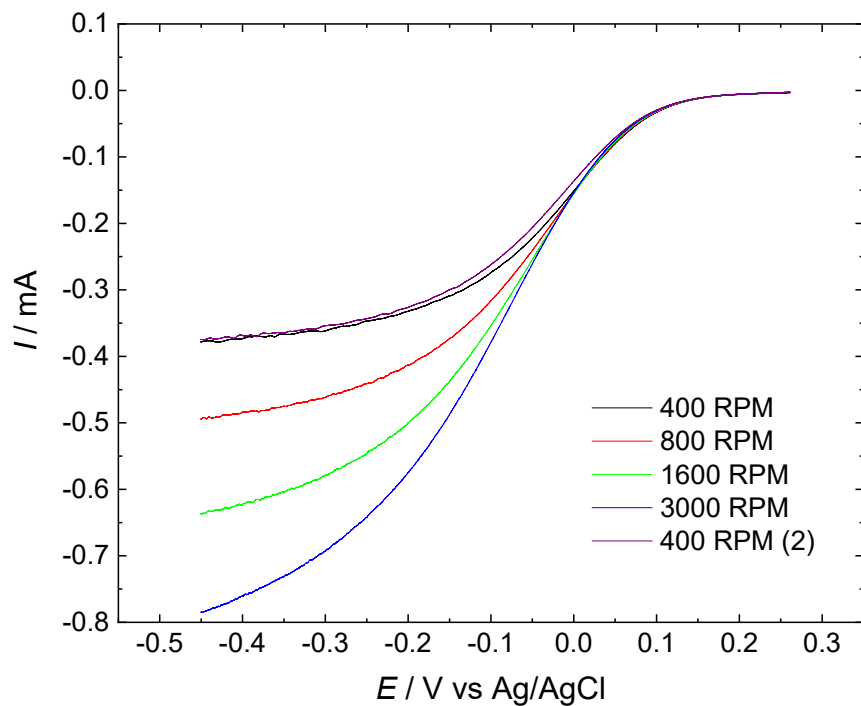


Figure S3.16 Representative rotating disk electrode voltammogram of a DL-Cu(DEphen) film in a 100 mM acetate buffer (50 mM NaOAc \cdot 3H₂O and 50 mM HOAc) at pH 4.8 containing 1 M NaClO₄ supporting electrolyte under an O₂ atmosphere. A 400 RPM scan is performed at the beginning and end of the experiment to ensure stability of the film.

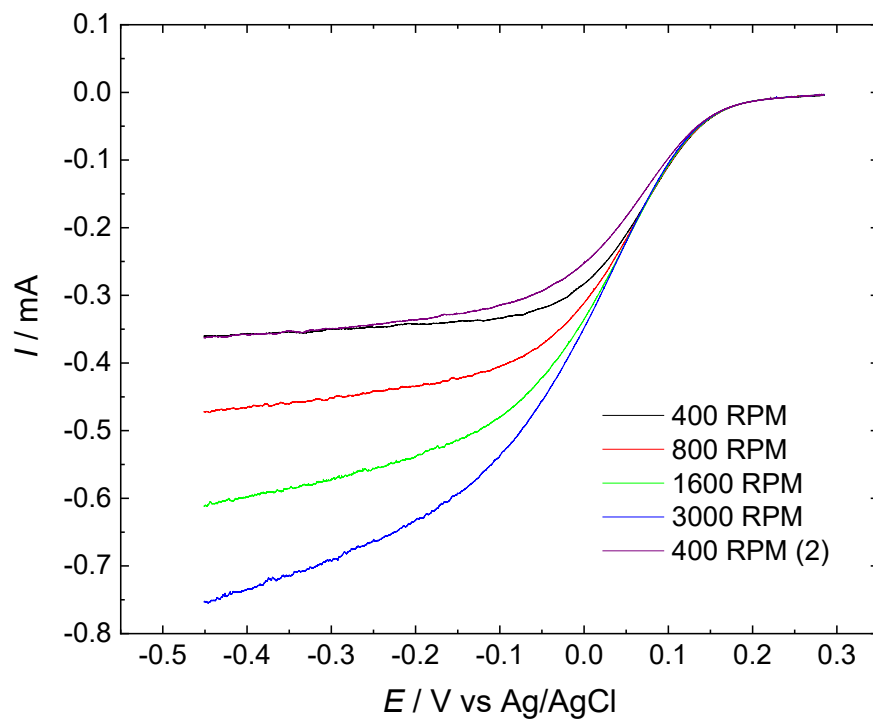


Figure S3.17 Representative rotating disk electrode voltammogram of a TL-Cu(DEphen) film in a 100 mM acetate buffer (50 mM NaOAc \cdot 3H₂O and 50 mM HOAc) at pH 4.8 containing 1 M NaClO₄ supporting electrolyte under an O₂ atmosphere. A 400 RPM scan is performed at the beginning and end of the experiment to ensure stability of the film.

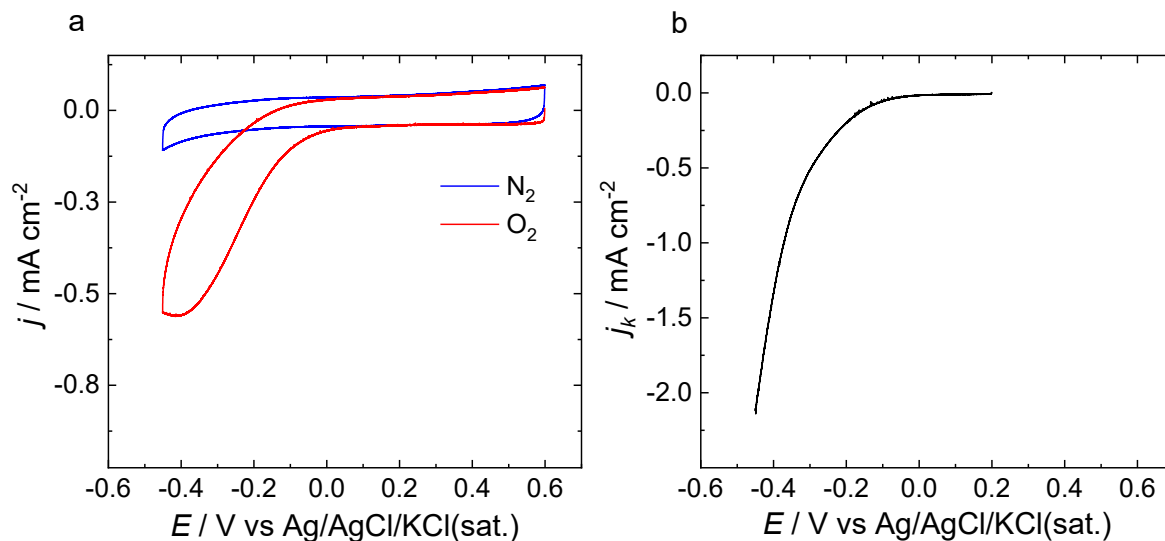


Figure S3.18 Control experiment in which the synthesis was stopped after the azidification step resulting in an azide terminated surface. The sonication steps in combination with exposure to light during cleaning likely resulted in the decomposition of the azides to amines prior to analysis.

a. Representative cyclic voltammograms of the azide-terminated surface in a 100 mM acetate buffer (50 mM NaOAc•3H₂O and 50 mM HOAc) at pH 4.8 containing 1 M NaClO₄ supporting electrolyte under an N₂ and O₂ atmosphere.

b. Representative kinetic current in the same buffer under an O₂ atmosphere as derived from RRDE measurements and Koutecky-Levich analysis.

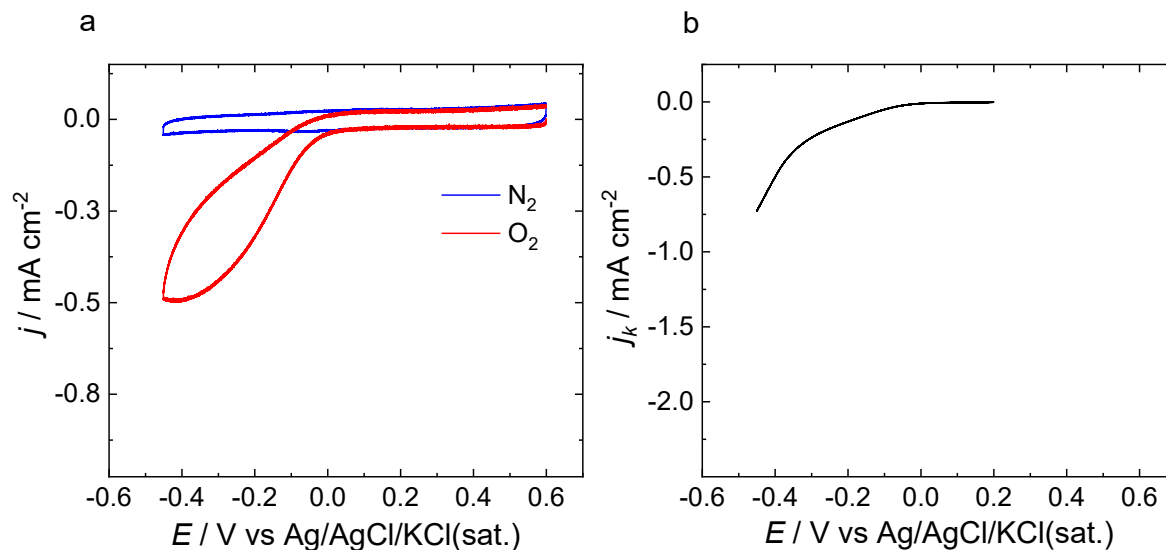


Figure S3.19 Control experiment in which a heat-treated glassy carbon disk electrode was exposed to optimized click conditions without the azidification step. Without the azide present the click reaction cannot occur.

a. Representative cyclic voltammograms of the stripped surface in a 100 mM acetate buffer (50 mM NaOAc•3H₂O and 50 mM HOAc) at pH 4.8 containing 1 M NaClO₄ supporting electrolyte under an N₂ and O₂ atmosphere.

b. Representative kinetic current in the same buffer under an O₂ atmosphere as derived from RRDE measurements and Koutecky-Levich analysis.

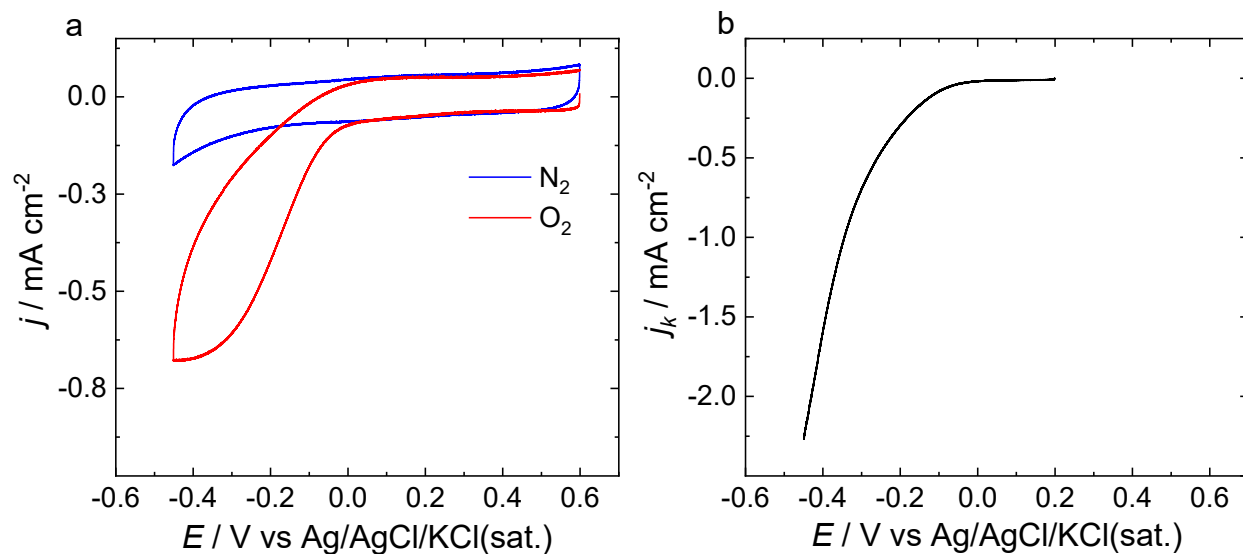


Figure S 3.20 Control experiment in which $\text{CuSO}_4 \cdot 5\text{H}_2\text{O}$ was not added to the click solution. All other steps were not changed from optimized conditions. Note that a large amount of precipitate formed when the DMSO solution and H_2O were mixed due to the decreased stability of the ligands in the absence of copper.

a. Representative cyclic voltammograms of the copper-free surface in a 100 mM acetate buffer (50 mM $\text{NaOAc} \cdot 3\text{H}_2\text{O}$ and 50 mM HOAc) at pH 4.8 containing 1 M NaClO_4 supporting electrolyte under an N_2 and O_2 atmosphere.

b. Representative kinetic current in the same buffer under an O_2 atmosphere as derived from RRDE measurements and Koutecky-Levich analysis.

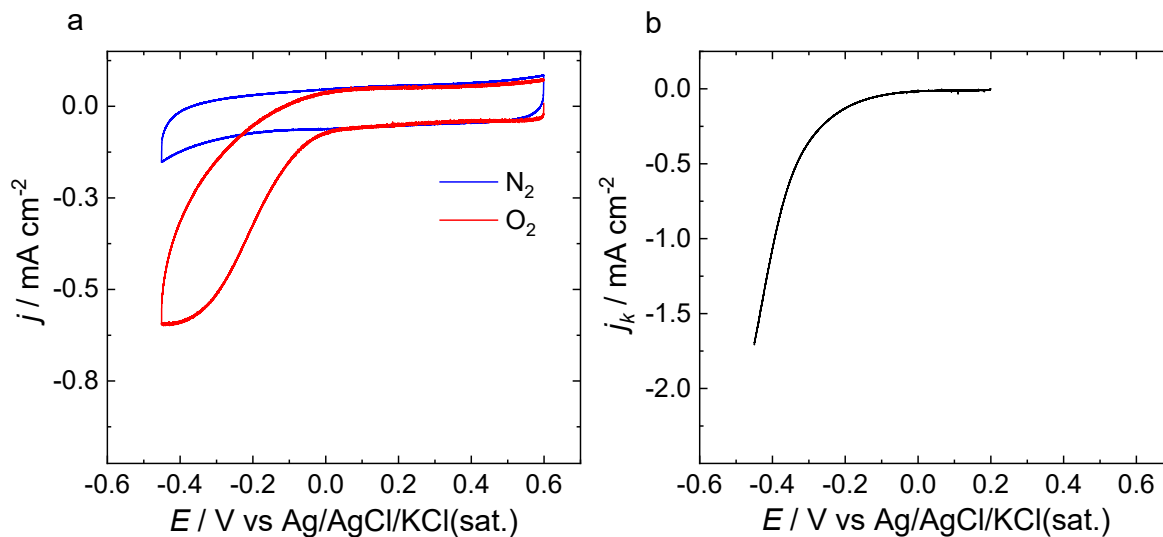


Figure S3.21 Control experiment in which 3,8-diethynyl-1,10-phenanthroline was not added to the click solution. All other steps were not changed from optimized conditions. Note that the solution was clear upon the addition of ascorbic acid due to the absence of the reduced Cu(DEphen).

a. Representative cyclic voltammograms of the phenanthroline-free surface in a 100 mM acetate buffer (50 mM NaOAc•3H₂O and 50 mM HOAc) at pH 4.8 containing 1 M NaClO₄ supporting electrolyte under an N₂ and O₂ atmosphere.

b. Representative kinetic current in the same buffer under an O₂ atmosphere as derived from RRDE measurements and Koutecky-Levich analysis.

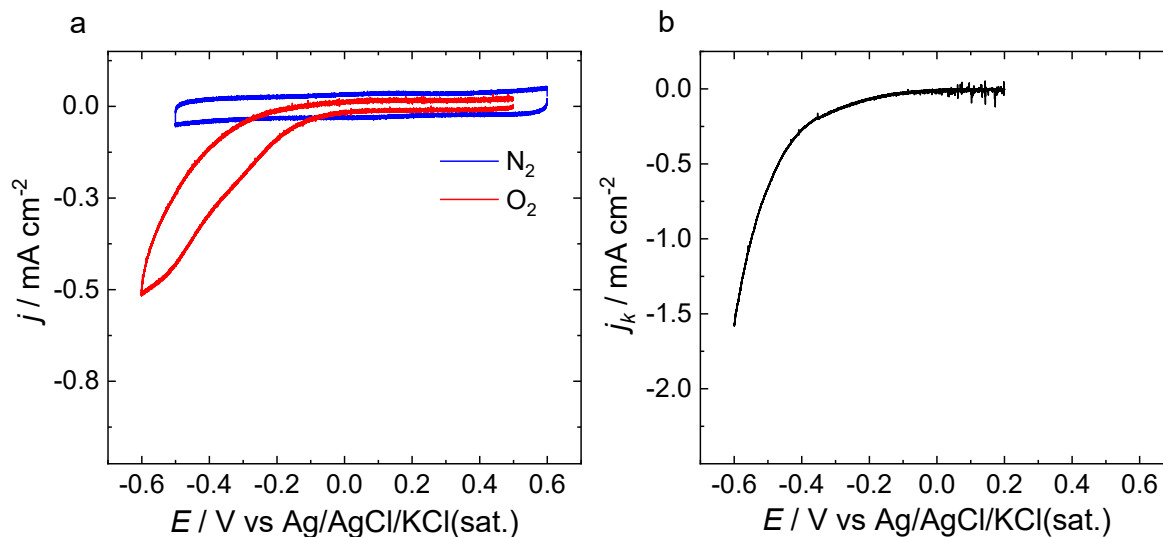


Figure S3.22 Single Layer Cu(DEphen) which has been stripped of copper using sodium diethyldithiocarbamate as described in the experimental section of the main paper.

a. Representative cyclic voltammograms of the phenanthroline-free surface in a 100 mM acetate buffer (50 mM NaOAc•3H₂O and 50 mM HOAc) at pH 4.8 containing 1 M NaClO₄ supporting electrolyte under an N₂ and O₂ atmosphere.

b. Representative kinetic current in the same buffer under an O₂ atmosphere as derived from RRDE measurements and Koutecky-Levich analysis.

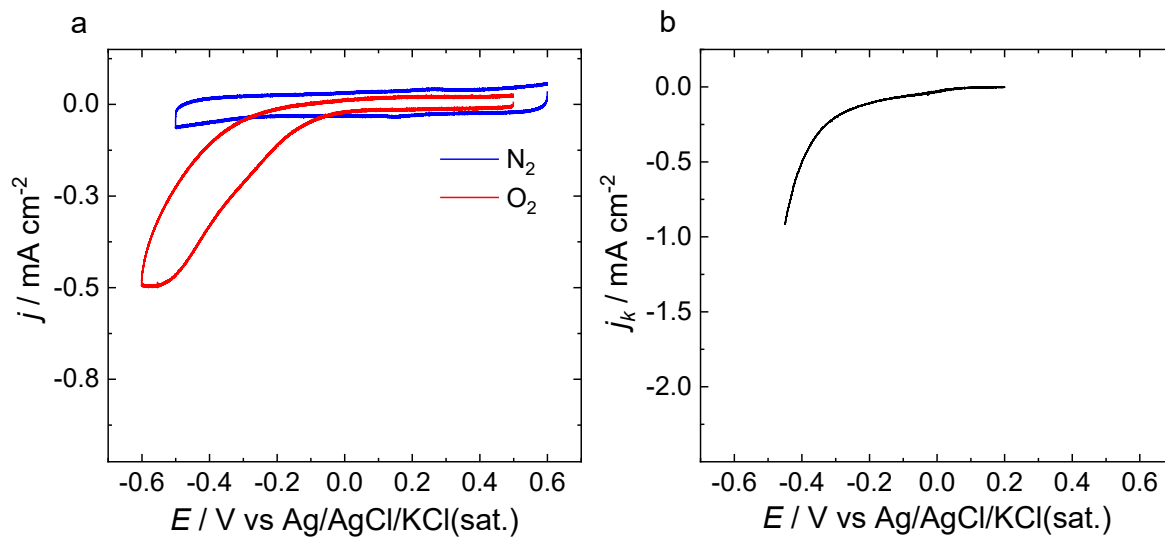


Figure S3.23 Double Layer Cu(DEphen) which has been stripped of copper using sodium diethyldithiocarbamate as described in the experimental section of the main paper.

- Representative cyclic voltammograms of the stripped surface in a 100 mM acetate buffer (50 mM NaOAc•3H₂O and 50 mM HOAc) at pH 4.8 containing 1 M NaClO₄ supporting electrolyte under an N₂ and O₂ atmosphere.
- Representative kinetic current in the same buffer under an O₂ atmosphere as derived from RRDE measurements and Koutecky-Levich analysis.

Table S3.2 Catalyst loading and ORR activities at selected potentials for multilayer Cu(DEphen) films and representative activities for control experiments

Electrode	Loading (10^{15} molecules cm^{-2})	J_k (0 V) (mA cm^{-2})	J_k (-0.1 V) (mA cm^{-2})	J_k (-0.2 V) (mA cm^{-2})	J_k (-0.3 V) (mA cm^{-2})	J_k (-0.4 V) (mA cm^{-2})
SL-Cu(DEphen)	0.94 ± 0.26	- 0.77 \pm 0.31	- 1.54 \pm 0.51	- 2.41 \pm 1.03	- 3.38 \pm 1.44	- 4.46 \pm 1.69
DL-Cu(DEphen)	1.93 ± 0.54	- 0.77 \pm 0.46	- 2.21 \pm 1.13	- 4.10 \pm 1.64	- 5.89 \pm 2.05	- 7.49 \pm 2.31
TL-Cu(DEphen)	2.08 ± 0.73	- 0.87 \pm 0.67	- 2.21 \pm 1.44	- 3.64 \pm 1.94	- 4.87 \pm 2.3	- 6.05 \pm 2.62
Background of N ₃ -Terminated GC	N/A	- 0.005	- 0.01	- 0.38	- 0.1	- 0.25
Control 1: CuAAC on bare GC (no N ₃)	N/A	- 0.003	- 0.007	- 0.025	- 0.045	- 0.01
Control 2: CuAAC without Cu catalyst	N/A	- 0.004	- 0.015	- 0.056	- 0.13	- 0.31
Control 3: CuAAC without DEphen	N/A	- 0.003	- 0.01	- 0.025	- 0.072	- 0.20
SL-Cu(DEphen) after Cu stripping	N/A	- 0.003	- 0.004	- 0.015	- 0.031	- 0.052
DL-Cu(CEphen) After Cu Stripping	N/A	- 0.006	- 0.013	- 0.023	- 0.041	- 0.010

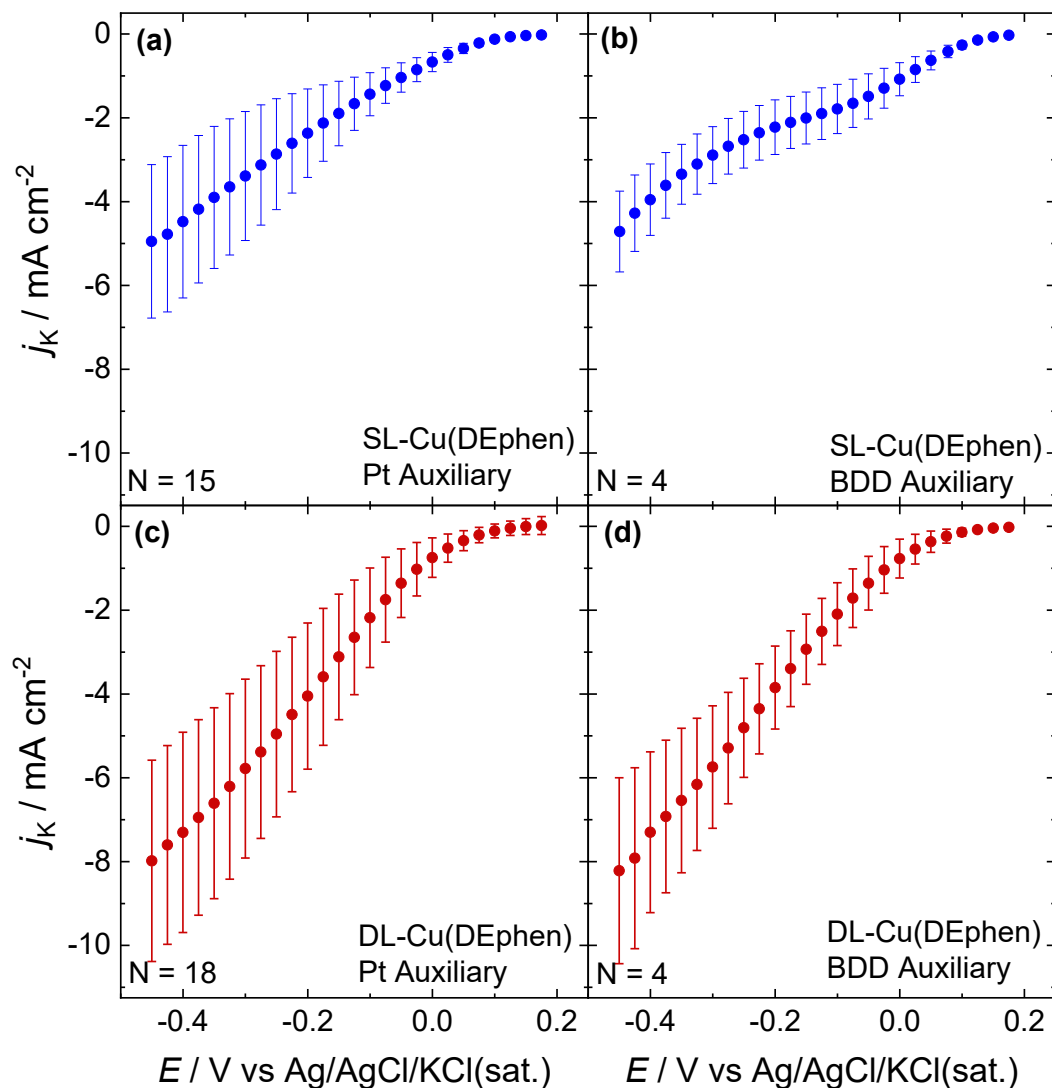


Figure S3.24 Kinetic current densities (j_k) estimated from Koutecky-Levich analysis of rotating disk voltammetry data for (a) a SL-Cu(DEphen) film measured using a Pt auxiliary electrode, (b) a SL-Cu(DEphen) film measured using a BDD auxiliary electrode, (c) a DL-Cu(DEphen) film measured using a Pt auxiliary electrode and (d) a DL-Cu(DEphen) film measured using a BDD auxiliary electrode. The central data points in each plot are the average potential-dependent j_k values, and the exterior error bars are the standard deviations at each potential. N is the number of measurement sets of independently-prepared electrodes that went towards determining each j_k value. Importantly, there is no observed dependence of ORR activity based on choice of auxiliary electrode (Pt or BDD), suggesting the ORR activity is not a result of trace Pt contamination.

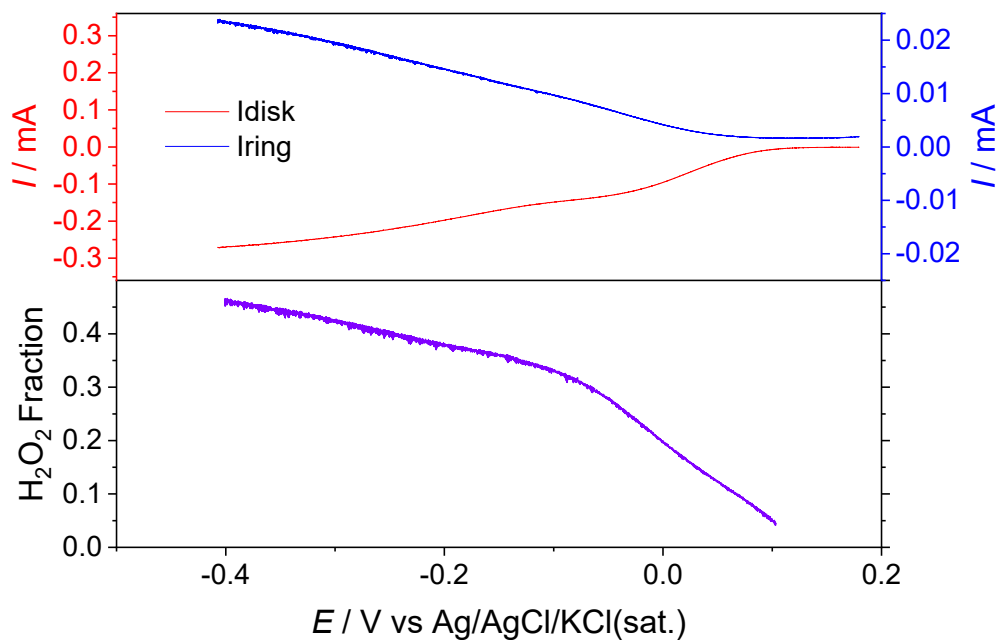


Figure S3.25 Representative rotating ring disk electrode voltammogram of a SL-Cu(DEphen) film in a 100 mM acetate buffer (50 mM NaOAc \cdot 3H₂O and 50 mM HOAc) at pH 4.8 containing 1 M NaClO₄ supporting electrolyte under an O₂ atmosphere. The rotation rate was 400 RPM and the platinum ring was held at 0.73 V vs Ag/AgCl/KCl(sat.)

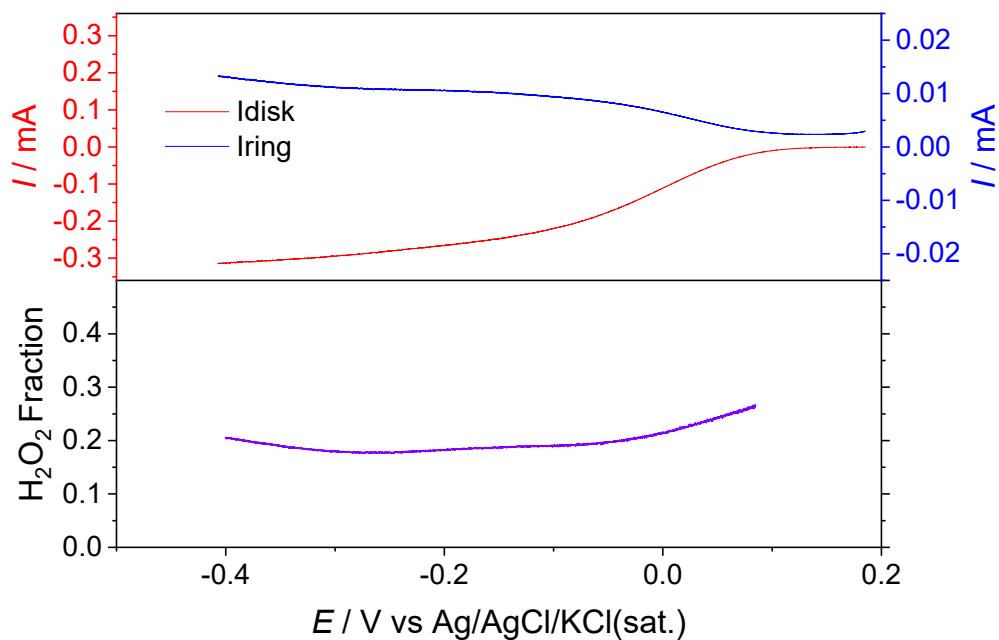


Figure S3.26 Representative rotating ring disk electrode voltammogram of a DL-Cu(DEphen) film in a 100 mM acetate buffer (50 mM NaOAc•3H₂O and 50 mM HOAc) at pH 4.8 containing 1 M NaClO₄ supporting electrolyte under an O₂ atmosphere. The rotation rate was 400 RPM and the platinum ring was held at 0.73 V vs Ag/AgCl/KCl(sat.)

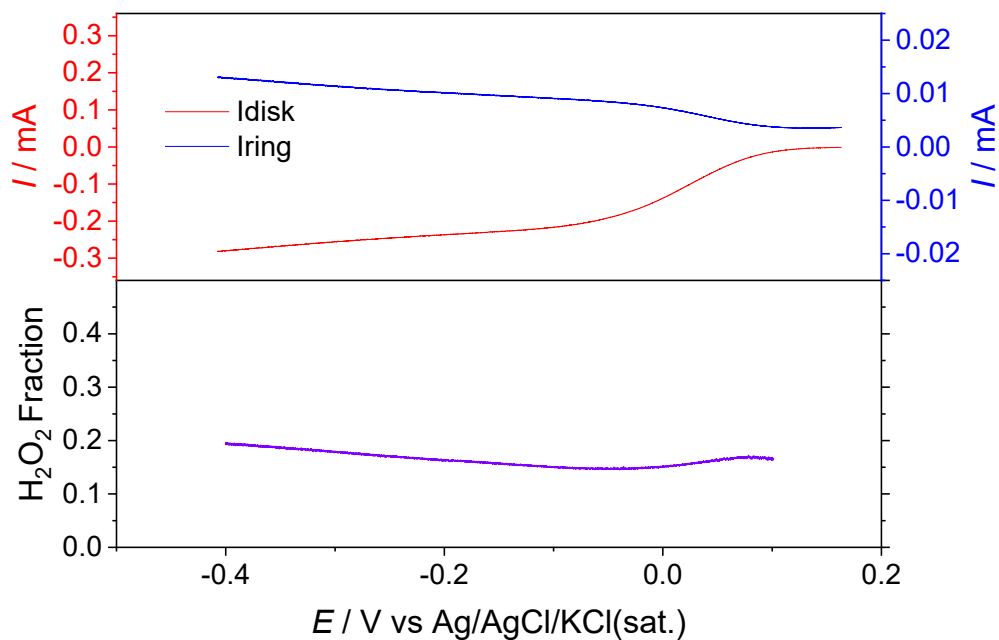


Figure S3.27 Representative rotating ring disk electrode voltammogram of a TL-Cu(DEphen) film in a 100 mM acetate buffer (50 mM NaOAc \cdot 3H₂O and 50 mM HOAc) at pH 4.8 containing 1 M NaClO₄ supporting electrolyte under an O₂ atmosphere. The rotation rate was 400 RPM and the platinum ring was held at 0.73 V vs Ag/AgCl/KCl(sat.)

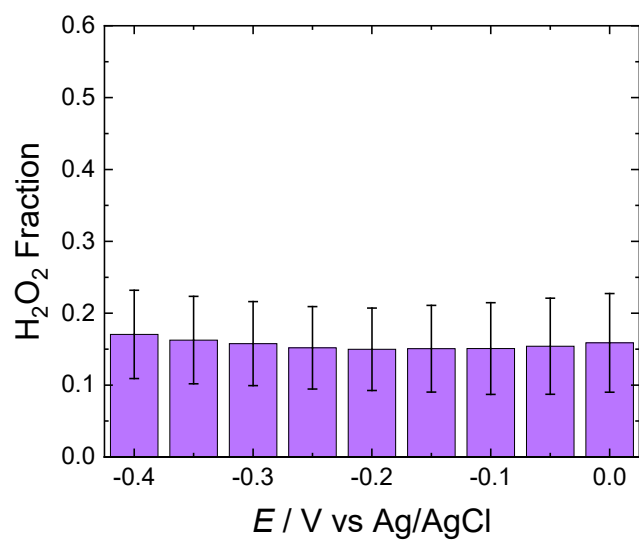


Figure S3.28 Fraction of the ORR current going to H₂O₂ production as a function of potential based on RRDE measurements at 400 RPM for the TL-Cu(DEphen) films.

3.8 References

1. Kallick, J. D.; Feng, W.-J.; McCrory, C. C. L., Controlled Formation of Multilayer Films of Discrete Molecular Catalysts for the Oxygen Reduction Reaction Using a Layer-by-Layer Growth Mechanism Based on Sequential Click Chemistry. *ACS Applied Energy Materials* **2020**, *3* (7), 6222-6231.
2. Costentin, C.; Savéant, J.-M., Towards an intelligent design of molecular electrocatalysts. *Nature Reviews Chemistry* **2017**, *1* (11), 0087.
3. McCrory, C. C. L.; Ottenwaelder, X.; Stack, T. D. P.; Chidsey, C. E. D., Kinetic and Mechanistic Studies of the Electrocatalytic Reduction of O₂ to H₂O with Mononuclear Cu Complexes of Substituted 1,10-Phenanthrolines *J. Phys. Chem. A* **2007**, *111* (49), 12641-12650.
4. Smieja, J. M.; Kubiak, C. P., Re(bipy-tBu)(CO)₃Cl-improved Catalytic Activity for Reduction of Carbon Dioxide: IR-Spectroelectrochemical and Mechanistic Studies. *Inorg. Chem.* **2010**, *49* (20), 9283-9289.
5. Gonell, S.; Massey, M. D.; Moseley, I. P.; Schauer, C. K.; Muckerman, J. T.; Miller, A. J. M., The Trans Effect in Electrocatalytic CO₂ Reduction: Mechanistic Studies of Asymmetric Ruthenium Pyridyl-Carbene Catalysts. *J. Am. Chem. Soc.* **2019**, *141* (16), 6658-6671.
6. Bullock, R. M.; Das, A. K.; Appel, A. M., Surface Immobilization of Molecular Electrocatalysts for Energy Conversion. *Chem. Eur. J.* **2017**, *23* (32), 7626-7641.
7. Kortlever, R.; Shen, J.; Schouten, K. J. P.; Calle-Vallejo, F.; Koper, M. T. M., Catalysts and Reaction Pathways for the Electrochemical Reduction of Carbon Dioxide. *J. Phys. Chem. Lett.* **2015**, *6* (20), 4073-4082.
8. Jackson, M. N.; Surendranath, Y., Molecular Control of Heterogeneous Electrocatalysis through Graphite Conjugation. *Acc. Chem. Res.* **2019**.
9. Garlyyev, B.; Fichtner, J.; Piqué, O.; Schneider, O.; Bandarenka, A. S.; Calle-Vallejo, F., Revealing the nature of active sites in electrocatalysis. *Chem. Sci.* **2019**, *10* (35), 8060-8075.
10. Sathrum, A. J.; Kubiak, C. P., Kinetics and Limiting Current Densities of Homogeneous and Heterogeneous Electrocatalysts. *J. Phys. Chem. Lett.* **2011**, *2* (18), 2372-2379.
11. Peng, L.; Wang, Y.; Masood, I.; Zhou, B.; Wang, Y.; Lin, J.; Qiao, J.; Zhang, F.-Y., Self-growing Cu/Sn bimetallic electrocatalysts on nitrogen-doped porous carbon cloth with 3D-hierarchical honeycomb structure for highly active carbon dioxide reduction. *Applied Catalysis B: Environmental* **2020**, *264*, 118447.
12. Lv, M.; Zhou, Y.; Rasaki, S. A.; Shen, H.; Wang, C.; Song, W.; Thomas, T.; Yang, M.; Wang, J., Gold Nanocluster-Decorated Nickel Nitride as Stable Electrocatalyst for Oxygen Evolution Reaction in Alkaline Media. *ChemElectroChem* **2019**, *6* (22), 5744-5749.
13. Liu, Y.; Ju, S.; Wang, C.; Li, M.; Zhu, W.; Chen, D.; Yuan, A.; Zhu, G., In Situ Derived Electrocatalysts from Fe-Co Sulfides with Enhanced Activity toward Oxygen Evolution. *Industrial & Engineering Chemistry Research* **2019**, *58* (41), 18976-18985.
14. Hod, I.; Sampson, M. D.; Deria, P.; Kubiak, C. P.; Farha, O. K.; Hupp, J. T., Fe-Porphyrin-Based Metal-Organic Framework Films as High-Surface Concentration, Heterogeneous Catalysts for Electrochemical Reduction of CO₂. *ACS Catalysis* **2015**, *5* (11), 6302-6309.
15. Mahouche-Chergui, S.; Gam-Derouich, S.; Mangeney, C.; Chehimi, M. M., Aryl diazonium salts: a new class of coupling agents for bonding polymers, biomacromolecules and nanoparticles to surfaces. *Chem. Soc. Rev.* **2011**, *40* (7), 4143-4166.

16. Potts, K. T.; Usifer, D. A.; Guadalupe, A.; Abruna, H. D., 4-Vinyl-, 6-vinyl-, and 4'-vinyl-2,2':6',2''-terpyridinyl ligands: their synthesis and the electrochemistry of their transition-metal coordination complexes. *J. Am. Chem. Soc.* **1987**, *109* (13), 3961-3967.
17. Ramos Sende, J. A.; Arana, C. R.; Hernandez, L.; Potts, K. T.; Keshevarz-K, M.; Abruna, H. D., Electrocatalysis of CO₂ Reduction in Aqueous Media at Electrodes Modified with Electropolymerized Films of Vinylterpyridine Complexes of Transition Metals. *Inorg. Chem.* **1995**, *34* (12), 3339-3348.
18. Kingsborough, R. P.; Swager, T. M., Electrocatalytic Conducting Polymers: Oxygen Reduction by a Polythiophene–Cobalt Salen Hybrid. *Chemistry of Materials* **2000**, *12* (4), 872-874.
19. Sadki, S.; Schottland, P.; Brodie, N.; Sabouraud, G., The mechanisms of pyrrole electropolymerization. *Chemical Society Reviews* **2000**, *29* (5), 283-293.
20. Orchanian, N. M.; Hong, L. E.; Marinescu, S. C., Immobilized Molecular Wires on Carbon-Cloth Electrodes Facilitate CO₂ Electrolysis. *ACS Catalysis* **2019**, *9* (10), 9393-9397.
21. Orchanian, N. M.; Hong, L. E.; Skrainka, J. A.; Esterhuizen, J. A.; Popov, D. A.; Marinescu, S. C., Surface-Immobilized Conjugated Polymers Incorporating Rhenium Bipyridine Motifs for Electrocatalytic and Photocatalytic CO₂ Reduction. *ACS Applied Energy Materials* **2019**, *2* (1), 110-123.
22. Such, G. K.; Quinn, J. F.; Quinn, A.; Tjijto, E.; Caruso, F., Assembly of Ultrathin Polymer Multilayer Films by Click Chemistry. *Journal of the American Chemical Society* **2006**, *128* (29), 9318-9319.
23. Palomaki, P. K. B.; Dinolfo, P. H., A Versatile Molecular Layer-by-Layer Thin Film Fabrication Technique Utilizing Copper(I)-Catalyzed Azide–Alkyne Cycloaddition. *Langmuir* **2010**, *26* (12), 9677-9685.
24. Krawicz, A.; Palazzo, J.; Wang, G.-C.; Dinolfo, P. H., Layer-by-layer assembly of Zn(ii) and Ni(ii) 5,10,15,20-tetra(4-ethynylphenyl)porphyrin multilayers on Au using copper catalyzed azide-alkyne cycloaddition. *RSC Advances* **2012**, *2* (19), 7513-7522.
25. Palomaki, P. K. B.; Krawicz, A.; Dinolfo, P. H., Thickness, Surface Morphology, and Optical Properties of Porphyrin Multilayer Thin Films Assembled on Si(100) Using Copper(I)-Catalyzed Azide–Alkyne Cycloaddition. *Langmuir* **2011**, *27* (8), 4613-4622.
26. Palomaki, P. K. B.; Dinolfo, P. H., Structural Analysis of Porphyrin Multilayer Films on ITO Assembled Using Copper(I)-Catalyzed Azide–Alkyne Cycloaddition by ATR IR. *ACS Applied Materials & Interfaces* **2011**, *3* (12), 4703-4713.
27. Beauvilliers, E. E.; Topka, M. R.; Dinolfo, P. H., Synthesis and characterization of perylene diimide based molecular multilayers using CuAAC: towards panchromatic assemblies. *RSC Advances* **2014**, *4* (62), 32866-32875.
28. Luo, L.; Frisbie, C. D., Length-Dependent Conductance of Conjugated Molecular Wires Synthesized by Stepwise “Click” Chemistry. *Journal of the American Chemical Society* **2010**, *132* (26), 8854-8855.
29. Zhang, J.; Anson, F. C., Electrochemistry of the Cu(II) complex of 4,7-diphenyl-1,10-phenanthrolinedisulfonate adsorbed on graphite electrodes and its behavior as an electrocatalyst for the reduction of O₂ and H₂O₂. *Journal of Electroanalytical Chemistry* **1992**, *341* (1), 323-341.
30. Lei, Y.; Anson, F. C., Mechanistic aspects of the electroreduction of dioxygen as catalyzed by copper-phenanthroline complexes adsorbed on graphite electrodes. *Inorg. Chem.* **1994**, *33* (22), 5003-5009.

31. Marques, A. L. B.; Zhang, J.; Lever, A. B. P.; Pietro, W. J., Poisoning effect of SCN⁻, H₂S and HCN on the reduction of O₂ and H₂O₂ catalyzed by a 1:1 surface complex of Cu: 1,10-phenanthroline adsorbed on graphite electrodes, and its possible application in chemical analysis. *Journal of Electroanalytical Chemistry* **1995**, 392 (1), 43-53.
32. McCrory, C. C. L.; Devadoss, A.; Ottenwaelder, X.; Lowe, R. D.; Stack, T. D. P.; Chidsey, C. E. D., Electrocatalytic O₂ Reduction by Covalently Immobilized Mononuclear Copper(I) Complexes: Evidence for a Binuclear Cu₂O₂ Intermediate. *J. Am. Chem. Soc.* **2011**, 133 (11), 3696-3699.
33. Wang, Y.; Wang, D.; Han, J.; Feng, S., Facile synthesis of σ - π conjugated organosilicon polymers via Click polymerization. *Journal of Organometallic Chemistry* **2011**, 696 (9), 1874-1878.
34. Stenehjem, E. D.; Ziatdinov, V. R.; Stack, T. D. P.; Chidsey, C. E. D., Gas-Phase Azide Functionalization of Carbon. *J. Am. Chem. Soc.* **2013**, 135 (3), 1110-1116.
35. Devadoss, A.; Chidsey, C. E. D., Azide-Modified Graphitic Surfaces for Covalent Attachment of Alkyne-Terminated Molecules by "Click" Chemistry. *J. Am. Chem. Soc.* **2007**, 129 (17), 5370-5371.
36. Leung, K. Y.; McCrory, C. C. L., Effect and Prevention of Trace Ag⁺ Contamination from Ag/AgCl Reference Electrodes on CO₂ Reduction Product Distributions at Polycrystalline Copper Electrodes. *ACS Applied Energy Materials* **2019**, 2 (11), 8283-8293.
37. Liaudet, E.; Battaglini, F.; Calvo, E. J., Electrochemical study of sulphonated ferrocenes as redox mediators in enzyme electrodes. *Journal of Electroanalytical Chemistry and Interfacial Electrochemistry* **1990**, 293 (1), 55-68.
38. Heinrich, T.; Traulsen, C. H. H.; Darlatt, E.; Richter, S.; Poppenberg, J.; Traulsen, N. L.; Linder, I.; Lippitz, A.; Dietrich, P. M.; Dib, B.; Unger, W. E. S.; Schalley, C. A., The versatility of "click" reactions: molecular recognition at interfaces. *RSC Advances* **2014**, 4 (34), 17694-17702.
39. Heal, H. G., The Decomposition of Crystalline Sodium Oxide by X Rays. *Canadian Journal of Chemistry* **1953**, 31 (12), 1153-1163.
40. Li, B.; Luo, X.; Zhu, Y.; Wang, X., Immobilization of Cu(II) in KIT-6 supported Co₃O₄ and catalytic performance for epoxidation of styrene. *Applied Surface Science* **2015**, 359, 609-620.
41. Hu, L.; Shi, L.; Hong, H.; Li, M.; Bao, Q.; Tang, J.; Ge, J.; Lu, J.; Cao, X.; Gu, H., Catalytic epoxidation of stilbene with FePt@Cu nanowires and molecular oxygen. *Chemical Communications* **2010**, 46 (45), 8591-8593.
42. Bard, A. J.; Faulkner, L. R., Fundamentals and applications. *Electrochemical Methods* **2001**, 2, 482.
43. Lee, K.; Zhang, L.; Lui, H.; Hui, R.; Shi, Z.; Zhang, J., Oxygen reduction reaction (ORR) catalyzed by carbon-supported cobalt polypyrrole (Co-PPy/C) electrocatalysts. *Electrochimica Acta* **2009**, 54 (20), 4704-4711.
44. Sugiyama, K.; Aoki, K., Catalytic reactions of bis(1,10-phenanthroline) cuprous complex with hydrogen peroxide at glassy carbon and pyrolytic graphite electrodes. *Journal of Electroanalytical Chemistry and Interfacial Electrochemistry* **1989**, 262 (1), 211-219.
45. Zhang, J.; Anson, F. C., Electrocatalysts for the reduction of O₂ and H₂O₂ based on complexes of Cu(II) with the strongly adsorbing 2,9-dimethyl-1,10-phenanthroline ligand. *Electrochimica Acta* **1993**, 38 (16), 2423-2429.

46. Gayathri, P.; Senthil Kumar, A., Electrochemical Behavior of the 1,10-Phenanthroline Ligand on a Multiwalled Carbon Nanotube Surface and Its Relevant Electrochemistry for Selective Recognition of Copper Ion and Hydrogen Peroxide Sensing. *Langmuir* **2014**, *30* (34), 10513-10521.

Chapter 4 Heterogenization of TEMPO for Electrocatalytic Alcohol Oxidation

4.1 Preface

This chapter presents the synthesis and study of monolayer films of multiple TEMPO derivatives for electrochemical alcohol oxidation. My results show that while TEMPO can be covalently attached to glassy carbon electrodes through the Cu(I)-Catalyzed Azide-Alkyne Cycloaddition or ‘Click’ reaction, their inherent instability prevents the modified electrodes from being used for catalysis. I was responsible for material synthesis, electrochemical measurements, analysis, and preparation and revision of the Chapter. My advisor, Dr. Charles C. L. McCrory, provided significant insight and expertise in electrochemical measurements and provided help with writing and revising the Chapter.

4.2 Abstract

Heterogenization or the attachment of molecular electrocatalysts to solid-state surfaces is a quickly growing field with many applications in energy storage and small molecule transformations. Electrochemical alcohol oxidation is one such application where the usage of electrochemical catalysts can be used as alternatives to toxic or hazardous oxidants. TEMPO or 2,2,6,6-Tetramethylpiperidin-1-yl)oxyl is a known molecular electrocatalyst for alcohol oxidation that has been previously attached to electrode surfaces using polymer encapsulation, electropolymerization, and other mainly non-covalent interactions. In this thesis chapter, multiple TEMPO complexes are covalently attached to glassy carbon surfaces as an alternative to non-covalent methods. Unfortunately, we found that while the surfaces were catalytically active for the desired reaction, the instability of the catalyst coupled with the relatively low surface coverage resulted in surfaces that degraded rapidly under catalytic conditions.

4.3 Introduction

Heterogenization or the attachment of molecular electrocatalysts to solid-state surfaces is a quickly growing field with many applications in energy storage and small molecule transformations.¹ New research is also finding uses for electrocatalysts in electroorganic synthetic chemistry.^{2, 3} TEMPO or (2,2,6,6-Tetramethylpiperidin-1-yl)oxyl is a molecular electrocatalyst widely known for its ability to catalyze the selective oxidation of alcohols to aldehydes and carboxylic acids.⁴ Selective alcohol oxidations are an important synthetic step in many industrial and pharmaceutical synthetic schemes. However, they often use toxic or hazardous oxidants such as organic peroxides, permanganates, and chromates which can have poor environmental impacts and difficulty with selective oxidations. These reactions can also require environmentally hazardous organic solvents. The use of a selective electrocatalyst can open up greener routes for these reactions that can remove or add electrons directly from an electrode and can operate in more aqueous conditions.

These methods, however, are not without their own difficulties. The solubility of the catalyst can make using aqueous solvents more difficult, the stability of the molecular catalyst is sometimes low resulting in decomposition of the catalyst over time,⁴ only catalyst at the surface of the electrode is active and so any catalyst in the solution but not at the electrode surface is not being used,⁵ and separation of the catalyst from the product can increase time required and costs. Heterogenization seeks to alleviate some of these issues. By attaching an electrocatalyst to a surface the solubility requirement is removed, there is no longer excess catalyst in the solution, and separation is much easier. Furthermore, heterogenization can sometimes help to stabilize the catalyst.⁶

Several methods for surface attachment of TEMPO to electrode surfaces have been previously achieved including polymer encapsulation,^{7, 8} electropolymerization of complexes containing TEMPO moieties,⁹ and the non-covalent interaction of TEMPO modified pyrenes with carbon paper.¹⁰ Interestingly, nobody thus far has attempted to directly attach TEMPO covalently to an electrode surface. The benefit of this method would be a stronger bond to the electrode that would prevent solvent interactions from displacing the catalyst as can occur with non-covalent attachment methods. Additionally, the lack of a surrounding polymeric film could help improve substrate diffusion to the electrocatalyst.¹¹

Our lab has previous experience with the covalent attachment of molecular electrocatalysts to glassy carbon surfaces using the Cu(I) Catalyzed Azide-Alkyne Cycloaddition (CuAAC) or “Click” reaction.^{12, 13} By modifying a glassy carbon surface with azide groups we can then react it with a molecular electrocatalyst that has been modified with an ethynyl moiety to form a covalent triazole linker between the two. This method has already been used to attach multiple complexes to glassy carbon electrodes. In this study, I will discuss my work on the synthesis and covalent surface attachment of several ethynyl-modified TEMPO complexes (Figure 4.1), their catalytic activity for alcohol oxidation, and the drawbacks of this methodology.

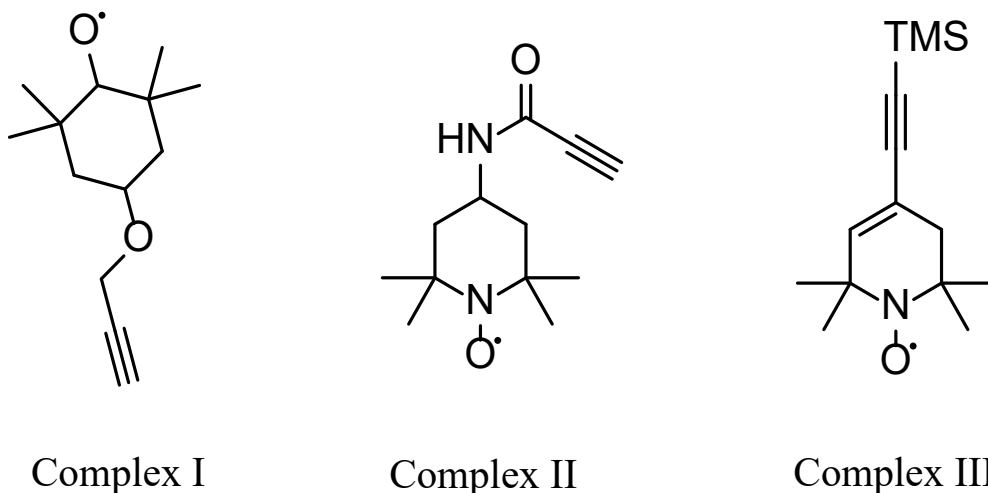


Figure 4.1 Ethynyl-modified TEMPO complexes used for covalent attachment to glassy carbon surfaces via the Cu(I)-Catalyzed Azide-Alkyne Cycloaddition.

4.4 Experimental Methods

4.4.1 Materials and General Instrumentation

All solvents and compounds, including Complex I, were purchased from **Sigma Aldrich** and **Fisher Scientific** and used as received. NMR spectra for organic compounds were collected on a Varian MR400 (400 MHz) spectrometer and all chemical shifts are reported in ppm relative to TMS standards. A small amount of phenylhydrazine was added to the NMR tube with TEMPO complexes in order to prevent the free radical of TEMPO from interfering. All NMR data analysis was done using MestReNova version 14.1.2 (Mestrelab Research). All electrochemistry was performed using a Bio-Logic SP-300 bipotentiostat and Bio-Logic SP-200 potentiostat and data was recorded using the Bio-Logic EC-Lab v10.44 software package. Electrochemical data analysis and figure preparation was done in Origin 2020 (OriginLab Corporation).

4.4.2 Synthetic Procedures

2,2,6,6-tetramethyl-4-[(1-oxo-2-propyn-1-yl)amino]-1-Piperidinyloxy (Complex II). A two or three neck RBF was first charged with 4-amino-2,2,6,6-tetramethyl-1-Piperidinyloxy (0.250 g, 1.5 mmol) and 30 ml of DCM and a stir bar. The mixture was then sparged with N₂ for 15 minutes. 2-propynoic acid (0.105 g, 1.5 mmol) was then pulled into a syringe and the syringe was then inserted into the RBF still under nitrogen pressure. The plunger of the syringe was removed and the 2-propynoic acid was sparged for several minutes within the syringe barrel before the plunger was reinserted and the acid added to the reaction. The solution was left to stir at RT for 30 minutes. Afterwards N-N'-dicyclohexylcarbodiimide (0.309 g, 1.5 mmol) and 4-dimethylaminopyridine (0.020 g, 0.15 mmol) was added under N₂ pressure and the solution stirred for an additional 20 hours. After 20 hours the reaction solution was filtered, and the solvent removed under reduced pressure. Purification was achieved with column chromatography on silica gel using 80:20 DCM:MeOH as the eluent. Product was confirmed with mass spectroscopy.

3,6-dihydro-4-iodo-2,2,6,6-tetramethyl-1(2H)-Pyridinyloxy. 3,6-dihydro-4-iodo-2,2,6,6-tetramethyl-1(2H)-Pyridinyloxy was synthesized based on previously reported methods.¹⁴ 2,2,6,6-tetramethyl-4-oxo-1-Piperidinyloxy (8.5g, 50 mmol) was first dissolved in EtOH (30 ml). The solution was then added dropwise over 3 hours to a solution of hydrazine hydrate (0.3 mol, 15 ml). After which the solutions were combined the resulting mixture was refluxed for 1 hour during which time the solution color lightened. The solvent was then removed under reduced pressure and the residue redissolved in 50 ml of a 9:1 mixture of DCM and MeOH. The resulting solution was added to a separatory funnel and washed with saturated NaCl (brine, 10 ml) before being dried over MgSO₄ and filtered. Then PbO₂ (1.19 g, 5.0 mmol) was added, and the solution was sparged with O₂ for 30 minutes. The orange solution was then filtered and dried under reduced

pressure resulting in a thick orange oil (hydrazone). The orange oil was then dissolved in diethyl ether (30 ml) and added dropwise to a stirring solution of I₂ (27.9 g, 0.11 mol) and tetramethyl guanidine (20.12 g, 0.175 mol) also in diethyl ether (50 ml). The solution should produce gas at this point. After all the hydrazone was added, the mixture was left to stir for 60 minutes at RT. After stirring the solution was diluted with diethyl ether (40 ml), added to a separatory funnel, and washed first with water (30 ml) and then with 5% aqueous H₂SO₄ (60 ml). The organic phase was then collected, dried over MgSO₄, filtered, and the solvent removed under reduced pressure. The resulting dark brown residue was purified with column chromatography on silica gel with hexane:Et₂O (2:1) as the eluent. The product was in the second band which was orange/pink in color. The first band (green) can be discarded. ¹H NMR (CDCl₃, 400 MHz, phenylhydrazine): δ 6.10 (1H, s), δ 2.58 (2H, s), δ 1.26 (6H, s), δ 1.23 (6H, s).

3,6-dihydro-2,2,6,6-tetramethyl-4-[2-(trimethylsilyl)ethynyl]-1(2H)-Pyridinyloxy. 3,6-dihydro-2,2,6,6-tetramethyl-4-[2-(trimethylsilyl)ethynyl]-1(2H)-Pyridinyloxy was synthesized based on previously reported methods.¹⁵ In 2 neck RBF 3,6-dihydro-4-iodo-2,2,6,6-tetramethyl-1(2H)-Pyridinyloxy (0.5 g, 1.78 mmol) was dissolved in THF (4 ml) and triethylamine (1 ml) with a stir bar. The solution was degassed with N₂ sparge for 10 minutes and then CuI (0.010 g, 0.048 mmol) and Bis(triphenylphosphine)palladium(II) dichloride (0.034 g, 0.048 mmol) was added under N₂ pressure followed by TMS-acetylene (0.200 g, 2 mmol). The reaction was stirred at RT overnight. The following day the reaction was filtered and added to a separatory funnel where saturated aqueous ammonium chloride (15 ml) was added. The aqueous layer was then extracted 3x with ethyl acetate (15 ml). The organic phases were then combined and washed with saturated sodium chloride (brine), dried over Na₂SO₄, filtered, and then dried under reduced

pressure. The product was used as is for deprotection. H NMR (CDCl₃, 400 MHz, phenylhydrazine): δ 5.94 (1H, s), δ 2.24 (2H, s), δ 1.26 (6H, s), δ 1.20 (6H, s), δ 0.21 (9H, s).

4-ethynyl-3,6-dihydro-2,2,6,6-tetramethyl-1(2H)-Pyridinyloxy (Complex III). A single neck RBF was charged with 3,6-dihydro-2,2,6,6-tetramethyl-4-[2-(trimethylsilyl)ethynyl]-1(2H)-Pyridinyloxy (0.250 g, 1 mmol), 1 M TBAF in THF (4 ml), THF (4 ml), and a stir bar. The solution was then stirred at RT for 3 hours during which time the solution turned black. After 3 hours brine (10 ml) was added, and the mixture poured into a separatory funnel where it was extracted 3x with DCM (15 ml). The organic phases were then combined, dried over MgSO₄, filtered, and the solvent removed under reduced pressure. The crude material was purified using column chromatography on silica gel with hexane:ethyl acetate (5:1) as the eluent resulting in 120 mg (67% yield) of an orange oil. H NMR (CDCl₃, 400 MHz, phenylhydrazine): δ 5.97 (1H, s), δ 2.87 (1H, s), δ 2.28 (2H, s), δ 1.30 (6H, s), δ 1.23 (6H, s).

4.4.3 General Procedure for Glassy Carbon Electrodes Modified with Monolayer TEMPO Films.

Iodine Azide (IN₃) Solution Preparation. 100 mg of NaN₃ and 10 mL of hexanes were added to a 20 mL scintillation vial. Note that NaN₃ will not dissolve in the hexanes solution. ICl₃, stored in freezer at -4 °C, was heated at ~30 °C in a water bath until a small portion had melted. Immediately prior to use, 10 μ L of ICl₃ was added to the scintillation vial, and it was capped, briefly shaken, and wrapped with aluminum foil. The resulting suspension was used immediately after preparation. Caution: IN₃ is a potentially explosive substances, and extreme caution should be used in its preparation and use. To minimize risk to lab personnel, IN₃ was only prepared in solution in small amounts (\leq 2 mg) and used immediately after preparation.

Glassy Carbon Electrode Azide Modification. Glassy carbon disks were hand-polished on 240 grit SiC sandpaper, sonicated for 20 min in water, rinsed with water, and then dried under an N₂ stream. Polished disks were then heated in a fused silica-lined furnace at 1000 °C for 90 min under a 5 L min⁻¹ forming gas (5% H balance N₂) purge. After 90 min, the tube furnace was cooled to ~65 °C under the forming gas purge, and the electrodes were removed and immediately added to a freshly prepared IN₃ solution. Electrodes were kept in the solution in the dark for 1 h. Step 1: Deposition of Single-Layer Cu(DEphen) Films (SLCu(DEphen)). The Cu(DEphen) click solution was prepared as follows: TBTA (5.3 mg, 0.01 mmol) and TEMPO Complex (0.0048 mmol) were added to a 20 mL scintillation vial along with 7 mL of DMSO. In a separate 20 mL scintillation vial, CuSO₄·5H₂O (2.7 mg, 0.0108 mmol) and 3 mL of water were added. Both vials were vortexed until all solids were dissolved, and then both solutions were combined in a single vial, resulting in a light blue solution which was stored in a freezer at -4 °C. Immediately prior to use, the solution was removed from the freezer, ascorbic acid (18 mg, 0.102 mmol) was added, and the vial was shaken, resulting in a colorless solution. In the dark, azide-modified electrodes were removed from the azidification solution, briefly dipped in a cold 7:3 solution of DMSO:H₂O, and placed polished-side up in the click solution. Electrodes were stored in the click solution at room temperature for 14 h in the dark. The resulting TEMPO-modified electrodes were either cleaned for analysis as described below.

Cleaning Procedure for Analysis of Modified Electrodes. After reaction completion, electrodes were removed from the click solution and sonicated for 2 min each in DMSO and CHCl₃. The electrodes were then rinsed with EtOH followed by a further 2 min sonication in H₂O. After the final sonication, the electrodes were rinsed again with EtOH and dried under an N₂ stream.

4.4.4 Electrochemical Methods

All electrochemical measurements were done using a standard three electrode electrochemical setup in a single cell. The working electrodes were 0.195 cm² glassy carbon disk electrodes. The auxiliary electrode was a graphite rod. The reference for organic electrolyte was a homemade single-junction Ag/AgNO₃ (1.0 mM in MeCN with 0.1 M nBu₄NPF₆) nonaqueous reference electrode separated from the solution by a CoralPor glass frit (Bioanalytical Systems, Inc.) and externally referenced to the ferrocenium/ferrocene redox couple (Fc⁺⁰). The reference for aqueous solutions was a homemade single-junction Ag/AgCl/KCl(sat.) separated from the electrolyte solution by a CoralPor porous glass frit (Bioanalytical Systems, Inc.) Ag/AgCl/KCl(sat.) reference electrodes were externally referenced to ferrocenecarboxylic acid in 0.2 M phosphate buffer at pH 7 (0.329 V vs. Ag/AgCl/KCl(sat.)). Organic electrolyte consisted of acetonitrile with 0.1 M tetrabutylammonium hexafluorophosphate. The aqueous electrolyte was 0.1 M pH 10 sodium carbonate buffer.

Cyclic Voltammetry (CV) Measurements. Working electrodes were used in combination with a Pine Research Instrumentation E6-series change-disk rotating disk electrode (RDE) assembly attached to a Pine Research Instrumentation MSR rotator. Cyclic voltammograms of the TEMPO complex showing the redox peak were always done in organic electrolyte. Aqueous measurements were done solely to show the instability of the TEMPO monolayers.

4.5 Results and Discussion

We initially attempted to attach 2,2,6,6-Tetramethyl-4-(2-propynyloxy)piperidine 1-Oxyl (Complex I - See Figure 4.1) to a glassy carbon electrode. We chose this TEMPO derivative due to its commercial availability making it a relatively simple test compound for both surface attachment and alcohol oxidation. The complex was attached to a glassy carbon surface using the

conditions based on our previous work on attaching copper complexes of diethynylphenanthroline to glassy carbon electrodes^{12, 13} (Figure 4.2).

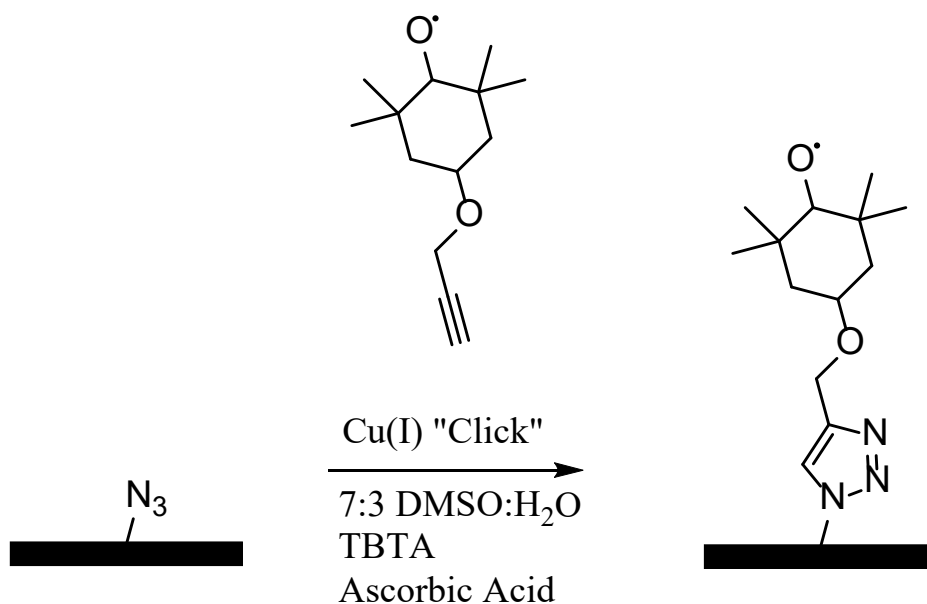


Figure 4.2 Surface modification of a glassy carbon electrode with Complex I using the Cu(I)-Catalyzed Azide-Alkyne Cycloaddition reaction.

Cyclic Voltammetry experiments demonstrated successful surface attachment of the TEMPO complex to the electrode. As seen in Figure 4.3 the TEMPO redox peak is clearly defined. Using background subtraction we estimated the surface coverage to be $7.95 \times 10^{14} \pm 7.07 \times 10^{12}$ molecules cm^{-2} a value very similar to those achieved previously for the diethynylphenanthroline complexes. We then screened for alcohol oxidation and for the sacrificial base necessary for the reaction to proceed catalytically. The base here is used as a proton acceptor during the oxidation process. A good base will have a minimal effect on the system in the absence of an alcohol but greatly increase the activity of alcohol oxidation. Previous work by Stahl et al¹⁰ on alcohol oxidation by TEMPO complexes non-covalently linked to carbon paper found that n-methyl imidazole (NMI) was a good base for this purpose and we used it as a baseline for our screening.

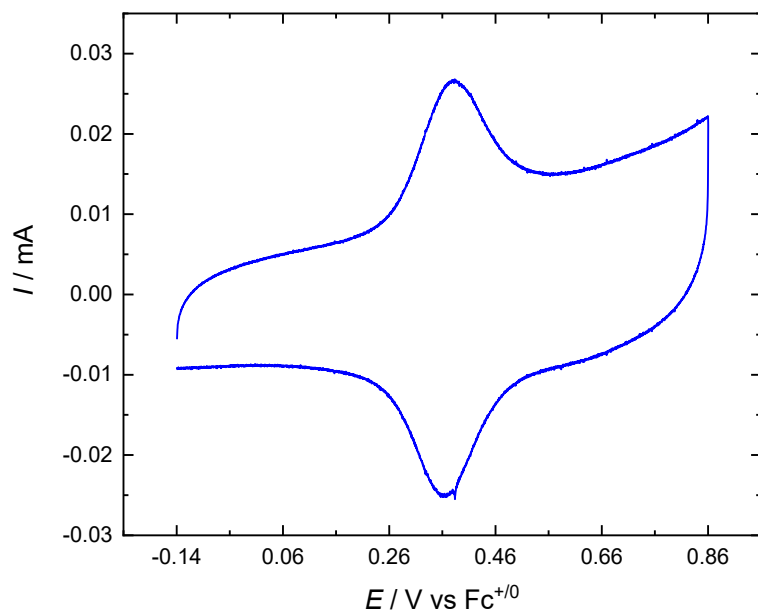


Figure 4.3 Representative Cyclic Voltammogram of a glassy carbon electrode covalently modified with TEMPO complex (I)

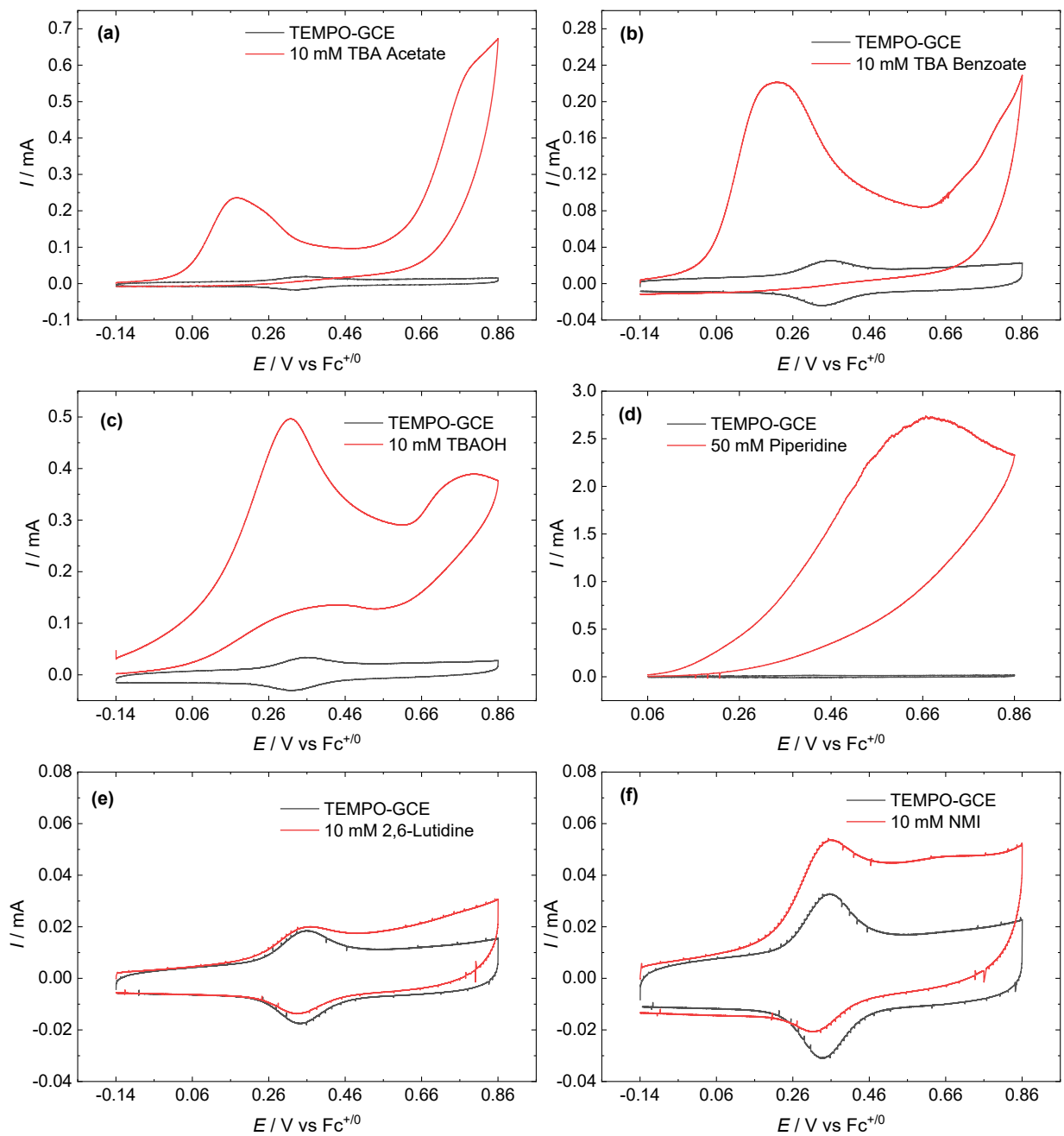


Figure 4.4 Representative cyclic voltammograms of all bases tested for background effects when cycled with a TEMPO complex (I) modified glassy carbon electrode. The bases tested were (a) Tetrabutylammonium Acetate, (b) Tetrabutylammonium Benzoate, (c) Tetrabutylammonium Hydroxide, (d) Piperidine, (e) 2,6-Lutidine, and (f) N-methyl Imidazole.

The results of the screening can be seen in Figure 4.4. As seen in the Figure, tetrabutylammonium acetate (Figure 4.4a), tetrabutylammonium benzoate (Figure 4.4b), tetrabutylammonium hydroxide (Figure 4.4c), and piperidine (Figure 4.4d) were all poor base choices due to high background activity under more positive potentials. The two successful bases were 2,6-lutidine (Figure 4.4e) and NMI (Figure 4.4f) due to their relatively low background activity. Alcohol oxidation experiments were then carried out by doping in benzyl alcohol as a substrate (Figure 4.5). Both bases promoted TEMPO-catalyzed alcohol oxidation, but the NMI was significantly more active. These experiments demonstrated that the TEMPO modified classy carbon electrode was active for alcohol oxidation.

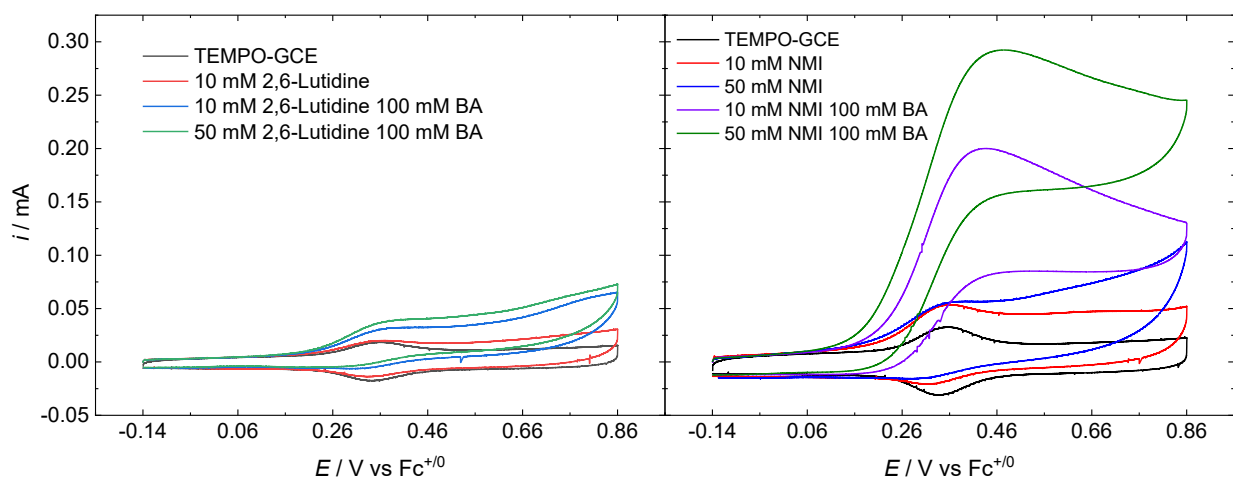


Figure 4.5 Representative Cyclic Voltammograms of alcohol oxidation with glassy carbon electrodes modified with TEMPO complex I using either 2,6-Lutidine (left) or N-methyl Imidazole (right), as the sacrificial base.

Our initial screening also revealed that the electrode was very unstable. As seen in Figure 4.6 exposing the surface to a positive potential in basic aqueous solution resulting in a significant decrease in coverage after only a single sweep. In addition, the oxidation of benzyl alcohol in dry acetonitrile also resulted in a rapid decrease in activity within minutes. This result was most prominent when the catalyst was used for alcohol oxidation rotating disk electrode voltammetry

(RDEV) experiments in which the working electrode is rotated at increasing rates during a potential sweep. Nominally, the current or activity should increase with the increasing rotating rate as more substrate is swept across the electrode surface. We found the opposite in that regardless of increasing rotation rate, the activity decreased with each subsequent potential sweep. Furthermore, a second sweep at the same rotation rate as the initial sweep (400 RPM) showed a drastically attenuated response (Figure 4.7).

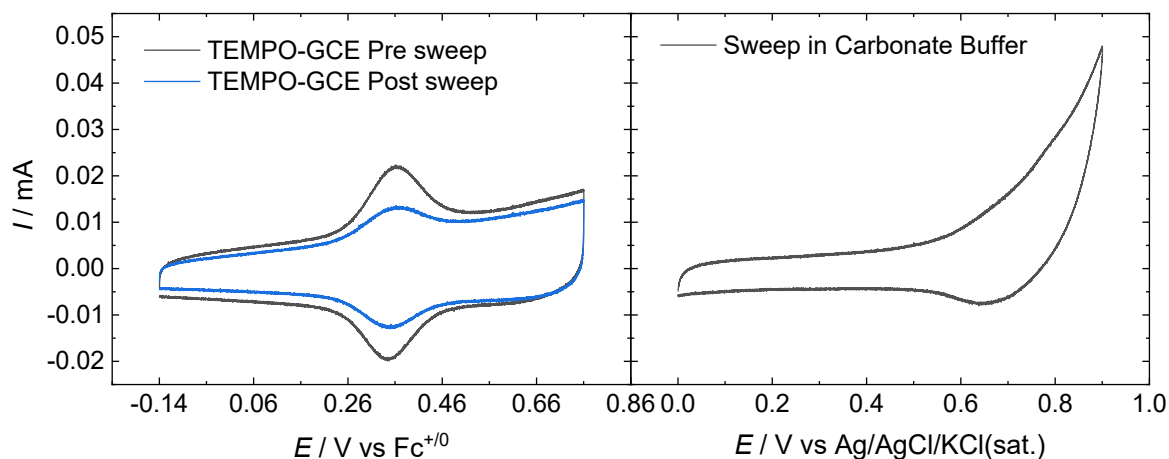


Figure 4.6 Representative CVs demonstrating instability of the TEMPO complex I under oxidative aqueous conditions. The CVs on the left are of the complex in acetonitrile where the redox peak is visible both before and after a single positive sweep in pH 10 carbonate buffer (right).

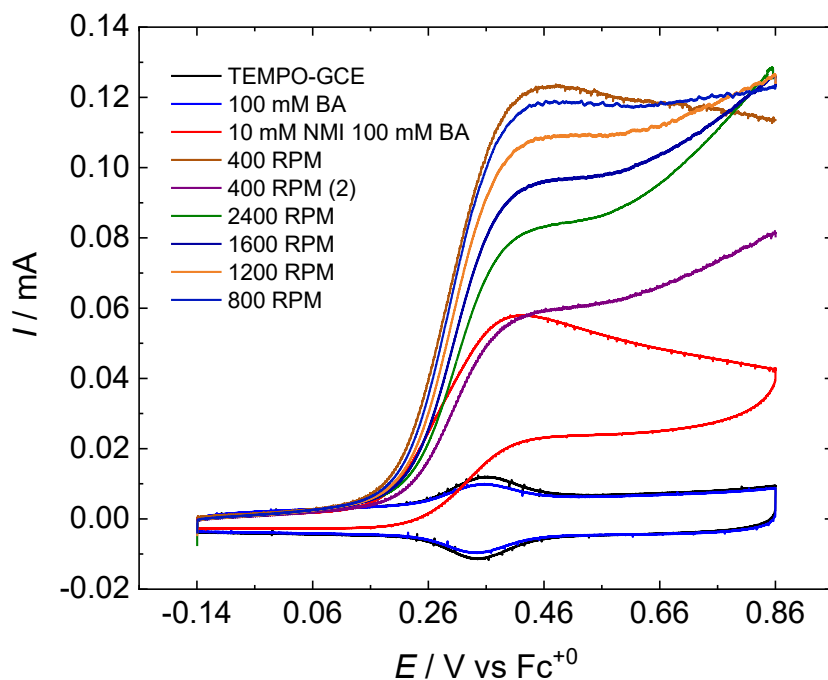


Figure 4.7 Representative Rotating Disk Electrode Voltammograms (RDEV) of a glassy carbon electrode covalently modified with TEMPO complex I used for alcohol oxidation in acetonitrile with 0.1 M tetrabutylammonium hexafluorophosphate as the electrolyte and N-methyl Imidazole as the sacrificial base.

These results suggested that either the TEMPO complex was decomposing, or the linker was degrading. Due to the stability of the triazole bond it seemed unlikely that the triazole linker itself was being broken. However, TEMPO itself is capable of cleaving an ether bond in the presence of water.¹⁶ Whether this process can occur electrochemically is unknown, but to rule out the possibility we synthesized two alternative TEMPO complexes; one that attaches through an amide bond (Figure 4.1 complex II) and one that is bound directly through the triazole linker (Figure 4.1 Complex III). Both cases were first tested for monolayer formation using the same procedure as complex I. As seen in Figures 4.8 and 4.9 both complexes were capable of attachment to a glassy carbon electrode suggesting that it is in fact the TEMPO complex that is decomposing rather than the linker degrading.

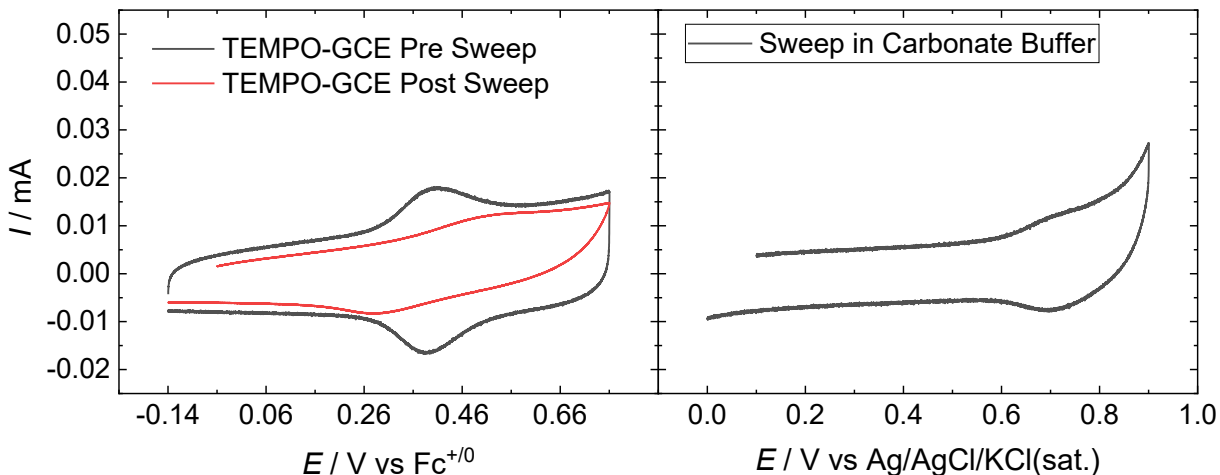


Figure 4.8 Representative CVs demonstrating instability of the TEMPO complex II under oxidative aqueous conditions. The CVs on the left are of the complex in acetonitrile where the redox peak is visible both before and after a single positive sweep in pH 10 carbonate buffer (right).

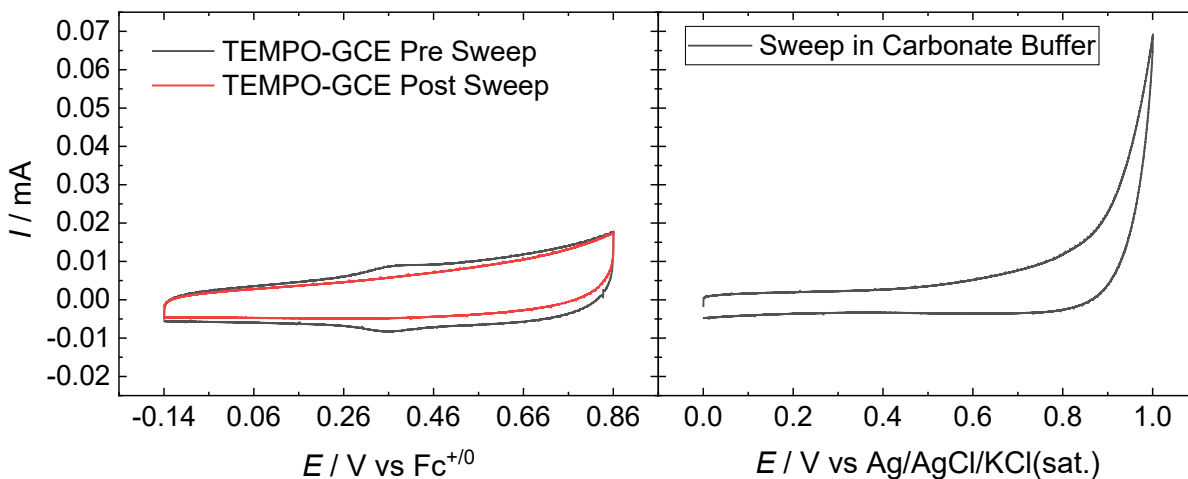


Figure 4.9 Representative CVs demonstrating instability of the TEMPO complex III under oxidative aqueous conditions. The CVs on the left are of the complex in acetonitrile where the redox peak is visible both before and after a single positive sweep in pH 10 carbonate buffer (right).

4.6 Conclusions

While this work was a good example of the versatility of the CuAAC method for glassy carbon surface modification it ultimately was not a successful method for alcohol oxidation. We believe that this is mainly due to the relative instability of the TEMPO catalyst. Such stability issues have also been seen before in the literature and the covalent bonding to glassy carbon does not appear to help stabilize the complex in any way. If TEMPO is to be used a catalyst for electrochemical alcohol oxidation the focus should be on either attempting to stabilize the complex or designing methods with a large excess of TEMPO that can be easily replaced or regenerated. A good example of this can be found in the previously mentioned work by Stahl et al where they used TEMPO non-covalently bound to high surface area carbon cloth in order to achieve an excess of TEMPO.¹⁰ Unfortunately, surface coverages of TEMPO on glassy carbon using our method are hindered by the maximum monolayer coverage even when using a roughly polished surface and as a result the majority of the catalyst decomposes too rapidly for any kind of bulk electrolysis to be achieved.

4.7 References

1. Bullock, R. M.; Das, A. K.; Appel, A. M., Surface Immobilization of Molecular Electrocatalysts for Energy Conversion. *Chemistry – A European Journal* **2017**, *23* (32), 7626-7641.
2. Vasilopoulos, A.; Zultanski, S. L.; Stahl, S. S., Feedstocks to Pharmacophores: Cu-Catalyzed Oxidative Arylation of Inexpensive Alkylarenes Enabling Direct Access to Diarylalkanes. *Journal of the American Chemical Society* **2017**, *139* (23), 7705-7708.
3. Wiebe, A.; Gieshoff, T.; Möhle, S.; Rodrigo, E.; Zirbes, M.; Waldvogel, S. R., Electrifying Organic Synthesis. *Angewandte Chemie International Edition* **2018**, *57* (20), 5594-5619.
4. Hoover, J. M.; Ryland, B. L.; Stahl, S. S., Mechanism of Copper(I)/TEMPO-Catalyzed Aerobic Alcohol Oxidation. *Journal of the American Chemical Society* **2013**, *135* (6), 2357-2367.
5. Savéant, J.-M., Molecular Catalysis of Electrochemical Reactions. Mechanistic Aspects. *Chemical Reviews* **2008**, *108* (7), 2348-2378.
6. Bairagya, M. D.; Bujol, R. J.; Elgrishi, N., Fighting Deactivation: Classical and Emerging Strategies for Efficient Stabilization of Molecular Electrocatalysts. *Chemistry – A European Journal* **2020**, *26* (18), 3991-4000.
7. Belgsir, E. M.; Schäfer, H. J., Selective oxidation of carbohydrates on Nafion®–TEMPO-modified graphite felt electrodes. *Electrochemistry Communications* **2001**, *3* (1), 32-35.
8. Palmisano, G.; Ciriminna, R.; Pagliaro, M., Waste-Free Electrochemical Oxidation of Alcohols in Water. *Advanced Synthesis & Catalysis* **2006**, *348* (15), 2033-2037.
9. Deronzier, A.; Limosin, D.; Moutet, J.-C., Electrochemical oxidation of carbinols mediated by nitroxyl radicals in solution or bonded to polypyrrolic coatings on platinum and carbon electrodes. *Electrochimica Acta* **1987**, *32* (11), 1643-1647.
10. Das, A.; Stahl, S. S., Noncovalent Immobilization of Molecular Electrocatalysts for Chemical Synthesis: Efficient Electrochemical Alcohol Oxidation with a Pyrene–TEMPO Conjugate. *Angewandte Chemie International Edition* **2017**, *56* (30), 8892-8897.
11. Andrieux, C. P.; Saveant, J. M., Heterogeneous (chemically modified electrodes, polymer electrodes) vs. homogeneous catalysis of electrochemical reactions. *Journal of Electroanalytical Chemistry and Interfacial Electrochemistry* **1978**, *93* (2), 163-168.
12. McCrory, C. C. L.; Devadoss, A.; Ottenwaelder, X.; Lowe, R. D.; Stack, T. D. P.; Chidsey, C. E. D., Electrocatalytic O₂ Reduction by Covalently Immobilized Mononuclear Copper(I) Complexes: Evidence for a Binuclear Cu₂O₂ Intermediate. *Journal of the American Chemical Society* **2011**, *133* (11), 3696-3699.
13. Kallick, J. D.; Feng, W.-J.; McCrory, C. C. L., Controlled Formation of Multilayer Films of Discrete Molecular Catalysts for the Oxygen Reduction Reaction Using a Layer-by-Layer Growth Mechanism Based on Sequential Click Chemistry. *ACS Applied Energy Materials* **2020**, *3* (7), 6222-6231.
14. Kálai, T.; Jekő, J.; Berente, Z.; Hideg, K., Palladium-Catalyzed Cross-Coupling Reactions of Paramagnetic Vinyl Bromides and Paramagnetic Boronic Acids. *Synthesis* **2006**, *2006* (03), 439-446.

15. Arai, S.; Koike, Y.; Hada, H.; Nishida, A., Catalytic Dicyanative [4+2] Cycloaddition Triggered by Cyanopalladation of Conjugated Enynes under Aerobic Conditions. *Journal of the American Chemical Society* **2010**, *132* (13), 4522-4523.
16. Pradhan, P. P.; Bobbitt, J. M.; Bailey, W. F., Oxidative Cleavage of Benzylic and Related Ethers, Using an Oxoammonium Salt. *The Journal of Organic Chemistry* **2009**, *74* (24), 9524-9527.

Chapter 5 Selective Reduction of Aqueous Nitrate to Ammonia with an Electropolymerized Chromium Molecular Catalyst

5.1 Preface

This chapter of my dissertation is in preparation for submission as a manuscript and presents the synthesis and study of electropolymerized films of terthiophene modified with a chromium terpyridine moiety for the Nitrate Reduction Reaction (NO_3RR). This work highlights, to our knowledge, the first example of a molecular system capable of reducing nitrate to ammonia with activity and selectivity comparable to those of state-of-the-art solid-state systems. Additionally, I show how the reaction proceeds through a cascade-catalysis type mechanism with nitrite and hydroxylamine identified as key intermediates. I am the primary author on the manuscript, responsible for material synthesis, electrochemical measurements, electrochemical and other analysis, and preparation and revision of the manuscript. My advisor, Dr. Charles C. L. McCrory, provided significant insight and expertise in electrochemical measurements and provided help with writing and revising the manuscript.

5.2 Abstract

Excessive use of anthropogenic nitrogen compounds has significantly disturbed the natural nitrogen cycle and detrimentally impacted local and global ecosystems.¹⁻³ In particular, nitrate (NO_3^-) is a common nitrogen-containing contaminant in agricultural,⁴ industrial,⁵ and low-level nuclear wastewater⁶ that causes significant environmental damage including eutrophication when introduced into groundwater.⁷ Standard nitrate remediation techniques often involve separation that lead to highly-concentrated nitrate brines that require further remediation. An alternate strategy is direct electrochemical nitrate remediation. In this work, we report a bio-inspired Cr-based molecular catalyst incorporated into a redox polymer that selectively and efficiently reduces aqueous NO_3^- to NH_3 , a desirable value-added fertilizer component, at rates of $\sim 0.29 \text{ mmol NH}_3 \text{ g}_{\text{cat}}^{-1} \text{ h}^{-1}$ with $>90\%$ Faradaic efficiency for NH_3 . The NO_3^- reduction occurs via a cascade catalysis mechanism involving the stepwise reduction of NO_3^- to NH_3 via observed NO_2^- and NH_2OH intermediates. To our knowledge, this is one of the first examples of a molecular catalyst, homogeneous or heterogenized, that reduces NO_3^- to NH_3 at rates and efficiencies rivaling those of state-of-the-art solid-state electrocatalysts. This work highlights a promising and previously unexplored area of electrocatalyst research using polymer-catalyst composites containing early transition-metal complexes for electrochemical nitrate remediation with nutrient recovery.

5.3 Introduction

Nitrogen is a key element essential to known life. As a result, the nitrogen cycle, which regulates nitrogen speciation and concentration in terrestrial and marine ecosystems, is one of the most important biogeochemical cycles on the planet. However, the advent of anthropogenic nitrogen species and their agricultural and industrial uses have drastically altered the nitrogen cycle and detrimentally impacted local and global ecosystems.¹⁻³ NO_x species, and especially NO_3^- , are particularly damaging to marine ecosystems,⁸ and are common contaminants found in concentrated streams from nuclear wastewater and industrial processes,⁵ or more dilute streams from agricultural runoff.⁴ NO_3^- contamination in groundwater results in eutrophication,⁹ or “dead zones,” in which hypoxic or anoxic conditions result in mass deaths of many pelagic species and the selective overgrowth of those which can survive the harsh conditions.^{7, 8} Microbial denitrification in contaminated groundwater results in the conversion of NO_x to N_2O , a potent greenhouse gas.¹⁰⁻¹² Furthermore, the US Environmental Protection Agency and the World Health Organization have determined that NO_3^- is a drinking water pollutant, and have established safe drinking water limits of less than $50 \text{ mg}_{\text{NO}_3^-} \text{ L}^{-1}$.¹³ These various detrimental effects of NO_3^- contamination on the environment and human health underscore the need for efficient nitrate remediation technologies.

Existing NO_3^- remediation technologies largely focus on either separation and concentration of NO_3^- and other NO_x species¹⁴ or bioremediation with nitrate-consuming bacteria.^{15, 16} The former, while often used for wastewater treatment, results in highly concentrated brines that require further treatment to achieve true remediation.¹⁶ Bioremediation can achieve true remediation but is hindered by its requirements for a viable bacterial environment, additional chemical substrates (usually either carbon or an electron donor), and the possibility of growing

pathogenic bacteria.¹⁷ A promising alternative strategy is the direct reduction of NO_3^- to other value-added products in the electrochemical NO_3 reduction reaction (e- NO_3RR).^{1, 18-20} Sustainable bioremediation is possible by coupling efficient e- NO_3RR with renewable energy sources. In addition, the electrochemical reduction of NO_3^- all the way to NH_3 is particularly desirable as it couples NO_3^- remediation with nutrient recovery.²¹

We have identified a $\text{Cr}(2,2';6',2'')\text{-terpyridine})\text{Cl}_3$ complex with an appended 2,2':5',2''-terthiophene (TPTCrCl₃) that, when electropolymerized onto a glassy carbon electrode, forms a conductive p-TPTCrCl₃ redox polymer film that is active and selective for the electrochemical reduction of NO_3^- to NH_3 via a cascade catalysis mechanism (Figure 5.1). Our catalyst is inspired by the nitrate reductase molybdoenzymes that reduce NO_3^- to NO_2^- via a mechanism that is thought to involve an oxo-transfer from NO_3^- to the Mo-containing active site buried within the enzyme scaffold with controlled substrate and proton transfer.²²⁻²⁴ Similarly, our p-TPTCrCl₃ system incorporates Cr active sites, with similar oxophilicity as Mo,²⁵ inside of a polymeric structure that should control substrate transport for enhanced reaction selectivity²⁶ as we have demonstrated previously in other polymer-electrocatalyst composite materials.^{27, 28}

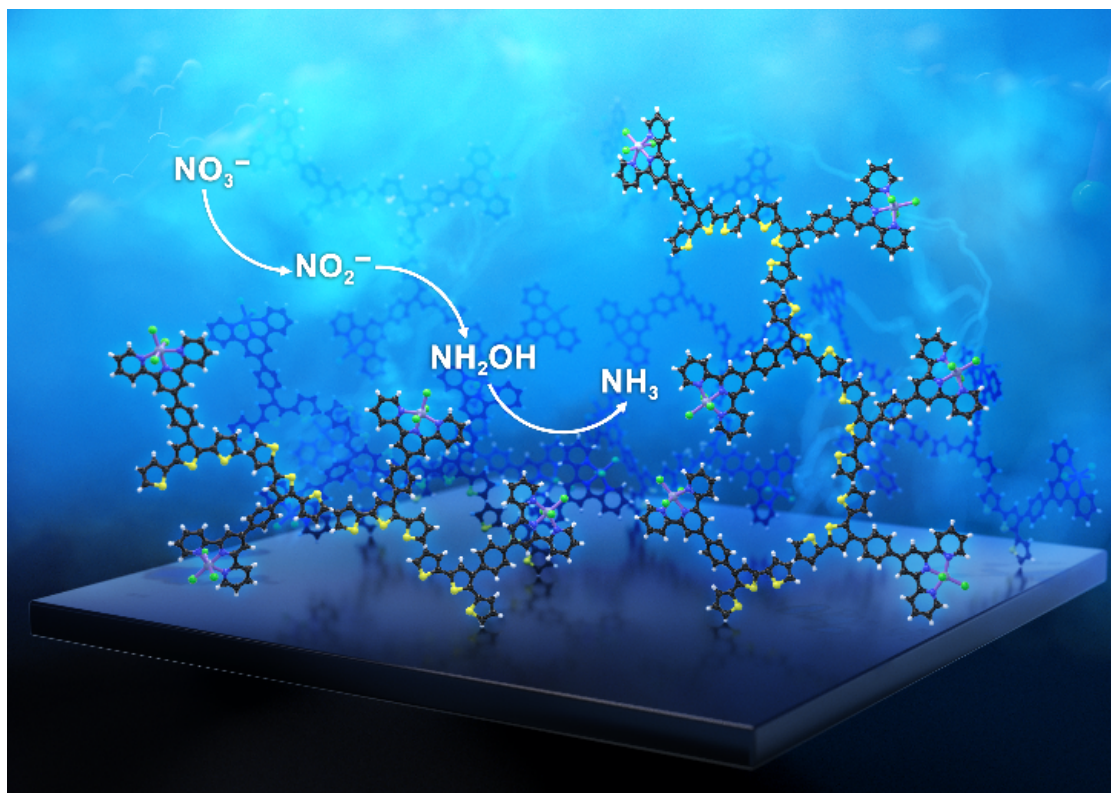


Figure 5.1 Electropolymerized terthiophene films with appended chromium terpyridine moieties (p-TPTCrCl₃) are selective for the electrochemical reduction of NO₃⁻ to NH₃ via a stepwise mechanism with an overall rate of 0.29 ± 0.053 mol NH₃ g_{cat}⁻¹ h⁻¹.

5.4 Experimental

5.4.1 Materials and General Instrumentation

All purchased chemicals were used as received with the exception of tetrabutylammonium hexafluorophosphate which was recrystallized from EtOH/H₂O. Ferrocenecarboxylic acid (97%), Ferrocene (98%), Sodium Hydroxide (Anhydrous, BioUltra, ≥ 98%), Sodium Phosphate Monobasic Dihydrate (BioUltra, ≥ 99.0%), Sodium Phosphate dibasic Dihydrate (BioUltra, ≥ 99.0%), Maleic Acid (ReagentPlus, ≥ 99 %), Sodium Nitrate (NaNO₃, 99.999% Trace Metals Basis), Sodium Nitrite (NaNO₂, BioUltra, ≥ 99.0%), Phosphoric Acid (85% wt in H₂O, 99.99% Trace Metals Basis), Sodium Carbonate (anhydrous, ACS Reagent, 99.6%), Sodium Bicarbonate (BioXtra, 99.5-100.5%), Potassium Carbonate (Anhydrous, ACS Reagent, 99+%) Isopropanol (ACS Grade, 95%+), Potassium Hydroxide (ACS Grade, 85%+), Tetrakis(triphenylphosphine)palladium(0) (99%), Magnesium Sulfate (ReagentPlus, ≥ 99.5%), Silver Nitrate (ReagentPlus, ≥ 99.0%), 8-hydroxyquinoline, Chromium(III) chloride tetrahydrofuran complex (1:3) (97%), N¹⁵ Sodium Nitrate (≥98 atom % N¹⁵, ≥99%), N¹⁵ Sodium Nitrite ((≥ 98 atom % N¹⁵, ≥ 95%), and N¹⁵ Hydroxylamine Hydrochloride (≥98 atom % N¹⁵, ≥95%), were purchased from **Sigma Aldrich**. Diethyl Ether (Anhydrous, BHT Stabilized, ACS grade, 99%), Petroleum Ether (ACS Grade, 36°-86° C BP), Dichloromethane (DCM, ACS Grade, 99.5%), Tetrahydrofuran (THF, ACS Grade), Ethanol (ACS Grade, 190 Proof), Dimethylsulfoxide (DMSO, ACS Grade, 99.8%) Potassium Chloride (KCl, ACS Grade, 99%), Ammonium Hydroxide Solution (28-30%, ACS Grade), Hydrogen Peroxide (30%, ACS Grade), and Sulfuric Acid (Optima Grade) were purchased from **Fisher Scientific**. 1,2-Dimethoxyethane (99%), 2,3,5-Tribromothiophene (98%), 2-acetylpyridine (99%), and TetrabutylAmmonium Hexafluorophosphate (98%) were purchased from **Oakwood Chemical**. N-(1-

Naphthyl)ethylenediamine dihydrochloride (98%+) was purchased from **TCI America**. 2-thienylboronic acid (97%) and 4-Formylphenylboronic acid (97%) were purchased from **Matrix Scientific**. Sulfanilamide (98%) and Hydroxylamine Hydrochloride (99%) were purchased from Alfa Aesar. Nafion 117 membrane was purchased from **Fuel Cell Store**. Carbon Rods (99.999%) were purchased from **Strem**. Deuterated Chloroform (CDCl_3 , 99.8%) and Deuterated Dimethylsulfoxide ($\text{C}_2\text{D}_6\text{SO}$, 99.9%) was purchased from **Cambridge Isotopic Laboratories**. Argon (UHP) was purchased from Cryogenic Gases. Nitrogen gas (N_2) was boil-off gas from a liquid nitrogen source. All water used in this study was purified to 18.2 $\text{M}\Omega\cdot\text{cm}$ resistivity in house using a Thermo Scientific GenPure UV-TOC/UF xCAD-plus water purification system. Glassy carbon disks (Sigradur-G grade, 5 mm diameter, 4 mm tall, 0.195 cm^2 disk surface area) were purchased from **HTW Hochtemperatur-Werkstoffe GmbH**.

NMR spectra for organic compounds were collected on a Varian MR400 (400 Mhz) spectrometer and all chemical shifts are reported in ppm relative to TMS standards. NMR spectra for N^{15} ammonia quantification were collected on a Bruker 600 MHz spectrometer with a liquid nitrogen cooled Prodigy broadband probe. All NMR data analysis was done using MestReNova version 14.1.2 (Mestrelab Research). Elemental analysis was performed by Midwest Microlabs. All electrochemistry was performed using a Bio-Logic SP-300 bipotentiostat and Bio-Logic SP-200 potentiostat and data was recorded using the Bio-Logic EC-Lab v10.44 software package. Electrochemical data analysis and figure preparation was done in Origin 2020 (OriginLab Corporation). X-ray Photoelectron Spectroscopy (XPS) measurements were conducted using a Kratos Axis Ultra XPS with a monochromatic Al $\text{K}\alpha$ X-ray source operating at 10 mA and 14 kV. All XPS data analysis was done using the CasaXPS version 2.3.17 software package (Casa Software Ltd). All SEM/EDX imaging was conducted using a JEOL JSM-7800FLV Scanning

Electron Microscope. UV-vis measurements were collected on a PerkinElmer Lambda 265 UV-Vis Spectrophotometer with fast mode. GC measurements were conducted on a Thermo Scientific Trace 1310 GC system. Some synthetic steps were carried out under a dry N₂ atmosphere using an mBraun Labstar 4-glove inert atmosphere glovebox. All electrodes were polished on a Struers LaboPol-5 polisher with a LaboForce-1 specimen mover. The disks were held in the LaboForce-1 specimen mover with 5 psi of applied pressure per disk, and during polishing the rotation speed was held at 200 rpm.

5.4.2 Synthetic Procedures

3'-bromo-2,2':5',2''-terthiophene 3'-bromo-2,2':5',2''-terthiophene was synthesized based on previously reported methods.²⁹ A three neck RBF was first charged with 2,3,5-tribromothiophene (0.2 g , 0.623 mmol), 2-thienylboronic acid (0.159 g, 1.240 mmol), 1,2-dimethoxyethane (6 ml), 1 M NaHCO₃ solution (2.2 mL), and a stir bar. Then a reflux condenser was added, and the mixture was sparged with nitrogen for 10 minutes. Under constant nitrogen pressure tetrakis-(triphenylphosphine)palladium(0) (0.0416 g , 0.036 mmol) was added and the solution sparged for an additional 5 minutes. The solution was then refluxed overnight. After the first reflux the solution was then cooled to RT and under constant nitrogen pressure additional 2-thienylboronic acid (0.0952 g, 0.744 mmol) and tetrakis-(triphenylphosphine)palladium(0) (0.0416 g , 0.036 mmol) was added and the solution was again refluxed overnight. After disappearance of the 2-thienylboronic acid peak via TLC was confirmed the reaction was cooled down to RT. The reaction mixture was first filtered, then the 1,2-dimethoxyethane was removed via reduced pressure. Afterwards, 15 ml of water was added to the residue and it was poured into a separatory funnel. The product was then extracted 3 times with diethyl ether (30 ml). The combined organic phase was then washed once with a saturated NaCl solution (brine), dried over

MgSO₄, and filtered. The organic solvent was then removed via reduced pressure to yield a dark brown oil. The crude product was purified via column chromatography on silica gel using petroleum ether/DCM as the eluent (9:1) to give a yellow oil (95.8 mg, 47% yield) that solidified upon cooling in the freezer where it was stored. Note that this reaction can be easily scaled up to 20 times. ¹H NMR (CDCl₃, 400 MHz): δ 7.44 (1H, dd), δ 7.38 (1H, dd), δ 7.29 (1H, dd), δ 7.20 (1H, dd), δ 7.10 (2H, m), δ 7.05 (1H, dd)

(4-([2,2':6',2''-terpyridin]-4'-yl)phenyl)boronic acid A single necked RBF was charged with the following: 100 ml EtOH, 2-acetylpyridine (4.5 ml, 40 mmol), 4-formylphenyl boronic acid (3 g, 20 mmol), and a stir bar. The mixture was then stirred until everything was fully dissolved. Afterwards ammonium hydroxide solution (28%-30%, 58 ml) and KOH (3 g, 55 mmol) was added. The RBF was then capped with a septum and the solution stirred for 72 hours at RT during which an off-white precipitate formed. The resulting precipitate was then collected via vacuum filtration and washed with copious amounts of isopropanol until the run-off was no longer basic. It was then washed with chloroform. The solid was then collected and dried under vacuum to yield 1.5 g (21.23% yield) of an off-white solid. ¹H NMR (CD₃OD, 400 MHz): δ 8.72 (2H, m), δ 8.68 (2H, s), δ 8.66 (2H, d), δ 8.01 (2H, td), δ 7.76 (4H, q), δ 7.49 (2H, qd).

4'-(4-([2,2':5',2''-terthiophen]-3'-yl)phenyl)-2,2':6',2''-terpyridine (TPT) A three-neck RBF was first charged with 3'-bromo-2,2':5',2''-terthiophene (400 mg, 1.2 mmol), (4-([2,2':6',2''-terpyridin]-4'-yl)phenyl)boronic acid (474 mg, 1.34 mmol), 1,2 dimethoxyethane (50 ml), and a stir bar. A reflux condenser was then added and the solution sparged with N₂ for 15 minutes. Separately, K₂CO₃ (500 mg, 36 mmol) was dissolved in minimal H₂O in a Schlenk tube and sparged with N₂ for 10 minutes. Under constant N₂ pressure tetrakis-(triphenylphosphine)palladium(0) (0.100 g, 0.0865 mmol) was added and the solution sparged

for an additional 5 minutes. The K_2CO_3 solution was then added via cannula transfer and the solution refluxed overnight. Progress was checked via TLC and once the 3'-bromo-2,2':5',2''-terthiophene was consumed the reaction was stopped. After the reaction was completed the 1,2-dimethoxyethane was removed via reduced pressure and the crude residue added to a separatory funnel with additional water (20 ml). The product was then extracted with DCM (20 ml) three times. The combined organic phases were washed with a saturated NaCl solution (brine), dried over $MgSO_4$, and then the solvent was removed with reduced pressure. The crude material was purified with column chromatography on basic alumina using ethyl acetate/petroleum ether (1:9 to 4:6). The crude material was loaded dry using DCM to initially load the material on alumina gel. Product was collected as a yellow oil that solidified into yellow crystals (0.345 g, 51.73%). The product was stored in the freezer until further use. 1H NMR ($CDCl_3$, 400 MHz): δ 8.79 (2H, s), δ 8.75 (2H, dd), δ 8.70 (2H, d), δ 7.91 (4H, m), δ 7.55 (3H, m), δ 7.38 (2H, qd), 7.34 (3H, m), δ 7.07 (1H, q), δ 7.04 (1H, dd), 6.98 (1H, q).

4'-(4-([2,2':5',2''-terthiophen]-3'-yl)phenyl)-2,2':6',2''-terpyridine chromium trichloride (TPTCrCl₃) In a nitrogen glovebox a single neck RBF was charged with 4'-(4-([2,2':5',2''-terthiophen]-3'-yl)phenyl)-2,2':6',2''-terpyridine (0.0498 g, 0.09 mmol) and a stir bar. In a separate vial, also within the glovebox, chromium(III) chloride tetrahydrofuran complex (1:3) (0.040, 0.109 mmol) was dissolved in THF (10 ml). The THF solution was then transferred to the RBF via pipette which was sealed with a reflux condenser and gas adapter. The reaction set up was then removed from the glovebox, hooked up to a Schlenk line, and refluxed overnight under nitrogen (~24 hr) resulting in the precipitation of a brown solid. The reaction was then cooled, and the precipitate collected via vacuum filtration. The product was then rinsed with THF and diethyl ether before being dried under vacuum resulting in 25 mg (38.9%) of light brown solid. **Anal.**

Calcd (found) TPTCrCl₃•2H₂O, (C₃₃H₂₅ON₃S₃CrCl₃): %C 52.84, (53.29); %H 3.36, (2.94); %N 5.6, (5.71); %S 12.82 (12.95). Crystals suitable for X-Ray Diffraction were grown by dissolving a small amount of the compound in CH₃CN in a test tube followed by layering with a small amount of hexanes as a buffer and a large amount of diethyl ether.

5.4.3 XPS Measurements

Peak positions of the XPS spectra were referenced to the advantageous carbon peak occurring at 284.8 eV. High-resolution spectra were collected with a pass energy of 20 eV and a step size of 0.1 eV. To quantify elemental ratios, peaks in the XPS high-resolution spectra were first fit to symmetric Voigt lines shapes comprised of 70% Gaussian and 30% Lorentzian functions with a Shirley background for Nitrogen and Chlorine, and 30% Gaussian and 70% Lorentzian functions with a Shirley background for Chromium and Sulfur. Elemental ratios were calculated by quantifying the total peak area in the N 1s region, the Cr 2p^{3/2} peak, the S 2p region, and the Cl 2p region, and then dividing by their respective relative sensitivity factors (as tabulated for the Kratos Ultra XPS instrument).

5.4.4 Electrochemical Methods

All electrochemical measurements were done using a standard three electrode electrochemical setup. Electropolymerization was done in a single 50 ml beaker. All electrolyses were performed in a custom-built cell consisting of a sealed main chamber containing the working and reference electrodes and a stir bar along with an unsealed auxiliary chamber separated by a Nafion membrane containing the counter electrode. The electrolyte for depositions was a 100 mM tetrabutyl ammonium hexafluorophosphate solution in dichloromethane. The electrolyte for electrolyses was a 100 mM phosphate buffer (0.094 M NaH₂PO₄ : 0.006 M Na₂HPO₄) titrated to

pH 6 with NaOH (see Hydroxylamine Quantification for a discussion on pH). The working electrodes were the 0.195 cm² glassy carbon disk electrodes. The auxiliary electrode was a graphite rod. The reference for electropolymerizations was a homemade single-junction Ag/AgNO₃ (1.0 mM in MeCN with 0.1 M nBu₄NPF₆) nonaqueous reference electrode separated from the solution by a CoralPor glass frit (Bioanalytical Systems, Inc.) and externally referenced to the ferrocenium/ferrocene redox couple (Fc⁺⁰). The reference for aqueous experiments including all electrolyses was a homemade single-junction Ag/AgCl/KCl(sat.) separated from the electrolyte solution by a CoralPor porous glass frit (Bioanalytical Systems, Inc.) prepared as previously described. Ag/AgCl/KCl(sat.) reference electrodes were externally referenced to ferrocenecarboxylic acid in 0.2 M phosphate buffer at pH 7 (0.329 V vs. Ag/AgCl/KCl(sat.)). All potentials obtained from the Ag/AgCl/KCl(sat.) reference were then converted to RHE (Real Hydrogen Electrode) using the following equation:³⁰

$$E_{RHE} = E_{exp} + E_{ref} + 0.059V * pH$$

Where E_{RHE} is the potential vs RHE, E_{exp} is the measured potential, E_{ref} is the potential of the reference vs SHE (Standard Hydrogen Electrode), and pH is the pH of the electrolyte. The potential of an Ag/AgCl/KCl(sat.) reference vs SHE is 0.197 mV.³¹

General Procedure for Film Polymerization. Glassy carbon disks were first mechanically polished on silicon carbide abrasive papers (CarbiMet 2, 600/P1200, Buehler) for 30 seconds followed by sequential polishing on synthetic nap polishing pads (MD Floc, Struers) with alumina abrasive slurries (Struers) in an order of 1 μm, 0.3 μm, 0.1 μm, and 0.05 μm for 1 minute each. The electrodes and electrode holder were thoroughly rinsed with nanopure water after each polishing. After the final polishing step the electrodes were sonicated in nanopure water for 10 minutes before being rinsed with nanopure water and dried under an N₂ stream.

The electropolymerization solutions were made up of a saturated (~1 mM) solution of TPTCrCl₃ or a 1 mM solution of TPT in 0.1 M nBu₄NPF₆ in dichloromethane. The solution was vortexed until the monomer dissolved. The solution was then used for electropolymerization within 24 hrs and stored in the freezer when not in use. All electropolymerizations were conducted in a single cell beaker with the working GCE, counter graphite rod electrode, and Ag/AgNO₃ (1.0 mM in MeCN with 0.1 M nBu₄NPF₆) nonaqueous reference electrode held in close proximity to minimize solution resistance. The working electrode was then held at 1.2 V vs Ag/AgNO₃ (1.06 V vs Fc⁺⁰) until 20 mC was passed. The working electrode was then held at 0 V vs Ag/AgNO₃ (-0.140 V vs Fc⁺⁰) for 60 seconds to discharge the system. The electrode was then removed from the deposition solution, rinsed with dichloromethane, and dried under an N₂ stream. Between each deposition a small amount of dichloromethane was added to the deposition solution in order to maintain concentration consistency. Additionally, we found that the TPTCrCl₃ monomer would slowly clog the CoralPor frit on the reference electrode. In order to increase the lifetime of the electrode, after each deposition the frit was gently polished with water on a silicon carbide abrasive paper (CarbiMet 2, 600/P1200, Buehler). CoralPor frits were still replaced every 1-2 weeks depending on usage.

Surface Coverage Estimation. The surface coverage of the catalyst was estimated in two ways. The first was solely from the charge passed during deposition. In theory the electropolymerization of thiophenes consumes 2 electrons per monomer with an additional 0.25 electrons per thiophene subunit as a reversible oxidative doping during the anodic deposition process.^{32, 33} As each of our monomers contain 3 thiophene subunits each monomer should consume approximately 2.75 electrons. However, this method fails to account for the formation of soluble oligomers which do not precipitate out of solution and onto the electrode surface and

therefore is likely an overestimation of the surface coverage. With a standard deposition charge of 20 mC we can estimate a surface coverage of approximately 1.16×10^{17} molecules cm^{-2} using this method. Additionally, we also calculated the area under the Cr III/II and II/I cathodic peak using a baseline correction. The combination of the two peaks was used because with a deposition of 20 mC the peaks overlap. Using this method a surface coverage of $4.41 \times 10^{16} \pm 0.77 \times 10^{16}$ molecules cm^{-2} was estimated. We believe that this is closer to the true value for surface coverage due to the aforementioned drawbacks of the charge deposition method. Both methods however clearly indicate the improved surface coverage compared to a single monolayer deposition which usually fall in the 10^{14} molecules cm^{-2} range.³⁴

Cyclic Voltammetry (CV) Measurements. Working electrodes were used in combination with a Pine Research Instrumentation E6-series change-disk rotating disk electrode (RDE) assembly attached to a Pine Research Instrumentation MSR rotator. Before each cyclic voltammetry measurement, the electrochemical cells were sparged with N_2 for a minimum of 10 minutes prior to use, and the solution was blanketed with N_2 during each measurement. Unless otherwise noted, the scan rate was 0.1 V s^{-1} for each CV measurement.

Sealed Cell Electrolysis Measurements. Sealed cell electrolyses were conducted in the previously described custom built 2 compartment cell. All cell components and electrodes were rinsed with copious nanopure water prior to assembly. Electrodes for electrolysis experiments were made immediately prior to use. In order to remove adventitious ammonia from the Nafion membrane prior to electrolysis the membranes were pre-treated by 30-minute sequential sonications in 5 % hydrogen peroxide, nanopure water, 0.5 M H_2SO_4 , and nanopure water.³⁵ Treated membranes were stored in nanopure water for up to 2 months and used without any further treatment. The stir bars used were always Fisherbrand Egg-Shaped Bars (19 mm length, 9.5 mm

diameter), and the stir plates used were always Thermo Scientific RT Touch Series Magnetic Stirrers (4 L capacity, 30-2000 RPM). The cells were sparged with UHP argon for 30 minutes prior to electrolyses and were kept sealed throughout the experiment. After the electrolysis was complete a sample of the headspace was removed and analyzed via gas chromatography for HER. Then, a small sample of the electrolyte was removed and massed. This sample (usually 4-5 ml) was then used for detection of liquid products. The headspace of the main chamber was measured by mass balance with water. Detection of nitrite and hydroxylamine was achieved using colorimetric methods and ¹⁵N ammonia was detected with NMR spectroscopy as described below. All workup was completed within ~1.5 hours of electrolysis completion.

Faradaic efficiencies were calculated with the following equation:

$$FE = \frac{c * V * n * F}{Q * MW} * 100$$

where c is the experimentally determined product concentration, V is the electrolyte volume, n is the number of electrons passed, F is Faraday's constant, Q is the total charge passed, and MW is the relative molecular weight.

5.4.5 Product Detection

Detection of Nitrite. Nitrite was detected using the Greiss Reagent which was prepared as follows: 6 ml phosphoric acid, 2g of sulfanilamide, and 0.2 g N-(1-naphthyl)ethylene hydrochloride were dissolved in 100 ml total volume of nanopure water. The reagent should be stored in the dark and cold for up to 3 weeks. For analysis 2 ml of sample was combined with 2 ml of Greiss Reagent, briefly shaken, and stored in the dark for 30 minutes. Afterwards the absorbance at 548 nm taken using nanopure water as the blank. A calibration curve was prepared using different concentrations of sodium nitrite in 0.1 M pH 6 phosphate buffer and can be found in the SI (S5.1). All calibration

curve standards were prepared in triplicate. For samples obtained from bulk electrolysis measurements a dilution of the electrolyte was necessary. All samples were diluted 1:10 with 100 mM pH 6 phosphate buffer with the exception of the electrolyses ran at -0.55 V vs RHE which were diluted 1:2, the electrolyses conducted on unmetalled TPT which were diluted 1:4, and the electrolyses conducted on bare glassy carbon which were diluted 1:100.

Detection of Hydroxylamine. Hydroxylamine was detected using the 8-hydroxyquinoline method. This method involves two solutions prepared as follows: Solution A was prepared by dissolving 1g of 8-hydroxyquinoline in ethanol to 100 ml total volume, and Solution B was prepared by dissolving 10.6 g of Sodium Carbonate in nanopure water to 100 ml total volume. Solution A was stored in the dark and cold for up to 3 weeks. Solution B required no special storage procedures and was replaced at the same time as Solution A. For analysis 1 ml of sample was combined with 1 ml of Solution A and briefly mixed followed by 1 ml of Solution B. After all solutions were added, the mixture was vigorously shaken to incorporate oxygen and let to sit for 60 minutes. Afterwards the absorbance at 700 nm was taken using nanopure water as the blank. A calibration curve was prepared using different concentrations of hydroxylamine hydrochloride in 0.1 M pH 6 phosphate buffer and can be found in the SI (Figure S5.2). All calibration curve standards were prepared in triplicate. Electrolysis samples were not diluted prior to measurements.

A Note on Hydroxylamine stability. Hydroxylamine solutions are known to be fairly unstable, with the rate of decomposition increasing with basicity of the solution. We performed a stability study of hydroxylamine in several different pH phosphate buffer solutions by measuring initial hydroxylamine concentration after an electrolysis and then taking repeat measurements at different time points. As seen in SI Figure S5.3 at pH 7 only ~70 percent of the initial hydroxylamine concentration remained after 2 hours while at pH 6 ~94 percent of the initial

hydroxylamine concentration remained. Based on these results we chose to use pH 6 phosphate buffer for our experiments to minimize the effects of hydroxylamine decomposition.

Detection of ^{15}N Ammonia. In order to ensure that all ammonia measured was due to the electrochemical reduction of nitrate and not do to either polymer decomposition or ammonia contamination, all substrates used for electrolyses were ^{15}N labeled. In order to perform high-throughput detection of ^{15}N ammonia we adapted a method previously published by Macfarlane, Simonov, and co-workers.³⁶ This method uses a specific solvent suppression sequence that comes standard with all Bruker NMRs along with a nitrogen or helium cooled cryoprobe to obtain rapid ammonia quantification. The following solutions were prepared in advance and stored in the dark for up to 2 weeks. Solution A was a 50 μM Maleic Acid solution in DMSO-d_6 prepared by dissolving 11.6 mg of Maleic Acid in 50 ml of DMSO then diluting a 50 μl aliquot of the maleic acid solution with 1.950 ml of DMSO-d_6 . Solution B was 4M H_2SO_4 in DMSO-d_6 prepared by adding 450 μl of conc sulfuric acid to 1.55 ml of DMSO-d_6 . In order to prepare a sample for analysis the following was added to a Bel-Art SP Scienceware 5mm O.D. Thin-Walled Precision NMR tube in the following order: 750 μl of DMSO-d_6 , 125 μl of Solution A, 50 μl of Solution B, and 125 μl of sample. After all components were added the NMR tube was sealed with a cap and vigorously shaken. The NMR tube was then briefly (2-3 seconds) sonicated to remove bubbles formed during the mixing with can interfere with the solvent suppression. Electrolysis samples were not diluted prior to $^{15}\text{NH}_3$ quantification with the exception of samples collected after of $^{15}\text{NH}_2\text{OH}\cdot\text{HCl}$ reduction which were diluted 1:4 with 100 mM pH 6 phosphate buffer prior to data collection.

The NMR was then collected on a Bruker 600 MHz spectrometer with a liquid nitrogen cooled Prodigy broadband probe using the `lc1pncwps` pulse sequence. All parameters were

unchanged with the exception of the interscan delay (d1) being set to 1.5s and the number of scans (ns) being set to 1024 scans. The larger number of scans compared to the referenced paper is due to the decreased signal of the nitrogen cooled probe used for this study compared to the helium cooled probe referenced in the paper. However, we found that with the increased number of scans quantitative ^{15}N ammonia data was readily obtained.

All NMR data was worked up in MestreNova version 14.1.2 (Mestrelab Research). First the spectrum was referenced to the maleic acid peak (6.25 ppm vs TMS). Phase correction was manually applied and then a baseline correction using the Whittaker Smoother function between 7.4 and 6.1 ppm. The following integrals were then measured: Maleic Acid between 6.26 and 6.24 ppm, ^{15}N ammonia peak 1 between 7.130 and 7.095 ppm, and ^{15}N ammonia peak 2 between 7.245 and 7.210 ppm. The ratio of the ^{15}N peaks to the maleic acid peak were then compared to a calibration curve to determine the concentration of ammonia. The calibration curve was prepared using different concentrations of ^{15}N ammonium chloride in 0.1 M pH 6 phosphate buffer and can be found in the SI (Figure S5.4). All calibration curve standards were prepared in triplicate. Representative spectra for the NMR calibration curve can also be found in the SI (Figures S5.5 – S5.11).

5.5 Results and Discussion

The TPTCrCl₃ monomer complex was synthesized by first preparing the TPT ligand according to a procedure adapted from previously reported methods,²⁹ and then metalating with a chromium salt (Figure 5.2a). Briefly, the TPT ligand was synthesized by coupling a boronic acid functionalized terpyridine with a bromine functionalized terthiophene (Figure 5.1a). The TPT ligand was then metalated by exposing the ligand to CrCl₃•3THF. The crystal structure of the TPTCrCl₃ monomer is found in Figure 5.2b. Full details of the synthetic methods and full characterization data can be found in the experimental section.

Electropolymerization solutions were prepared by dissolving 1.0 mM TPTCrCl₃ in CH₂Cl₂ with 0.1 M nBu₄NPF₆ supporting electrolyte. Higher concentrations of TPTCrCl₃ led to precipitation of the monomer during the electropolymerization process. Electropolymerization of the TPTCrCl₃ monomer was conducted in a single chamber cell in a three-electrode configuration with a 0.195 cm² glassy carbon (GC) working electrode, a single junction Ag/AgNO₃ (1.0 mM with 0.1 M nBu₄NPF₆)/MeCN reference electrode, and a carbon rod auxiliary electrode. The GC working electrode was held at a constant potential of 1.06 V vs Fc⁺⁰ until the desired charge was passed, typically 0.020 C unless otherwise noted (Figure S5.12). Electropolymerization can also be achieved via repeated cyclic voltammograms to oxidizing conditions (Figure S5.13), the controlled potential method we used results in more reproducible polymer films. Note that electropolymerization was successfully achieved using only CH₂Cl₂ as a solvent, consistent with other studies that show electropolymerization occurs preferentially in CH₂Cl₂ compared to other common solvents.^{29, 37}

The electropolymerized p-TPTCrCl₃ was characterized by X-ray photoelectron spectroscopy (XPS), scanning electron microscopy (SEM), and cyclic voltammetry (CV).

Representative high-resolution XPS of the N 1s, S 2p, Cr 2p, and Cl 2p regions are shown in Figure 5.2d. The ratios of the integrated peaks, corrected for the respective relative sensitivity factors, are shown in Table S5.1. The XPS results closely match the predicted elemental ratios based on the TPTCrCl₃ monomer. In particular, the measured N:Cr ratio is 3.23 ± 0.05 compared to a 3:1 predicted ratio, and the measured S:Cr ratio is 2.63 ± 0.12 compared to a 3:1 predicted ratio. The XPS results suggest the deposited film has the same compositional structure as the TPTCrCl₃ monomer, which is expected for the p-TPTCrCl₃ film. A representative SEM image in Figure S5.14 shows a distinct polymer film formation on the electrode surface.

CVs of the p-TPTCrCl₃ film were conducted in a three-electrode configuration in a single chamber cell with the p-TPTCrCl₃-modified GC working electrode, a single-junction Ag/AgCl/KCl(sat.) aqueous reference electrode, and a carbon rod auxiliary electrode with an N₂-saturated 0.1 M pH 6 phosphate buffer as electrolyte. All potentials are referenced to RHE using the procedure described in the experimental section in the supplementary information. Representative CVs of the p-TPTCrCl₃ film in the presence and absence of 0.1 M NaNO₃ are shown in Figure 5.2d. In the absence of NaNO₃, a broad, quasireversible redox feature is observed at ~ -0.35 V vs RHE that is attributed to the reduction and corresponding reoxidation of the p-TPTCrCl₃ film. In the presence of 0.1 M NaNO₃, there is a large, irreversible reduction peak attributed to the electrocatalytic reduction of NO₃⁻ by the p-TPTCrCl₃ film.

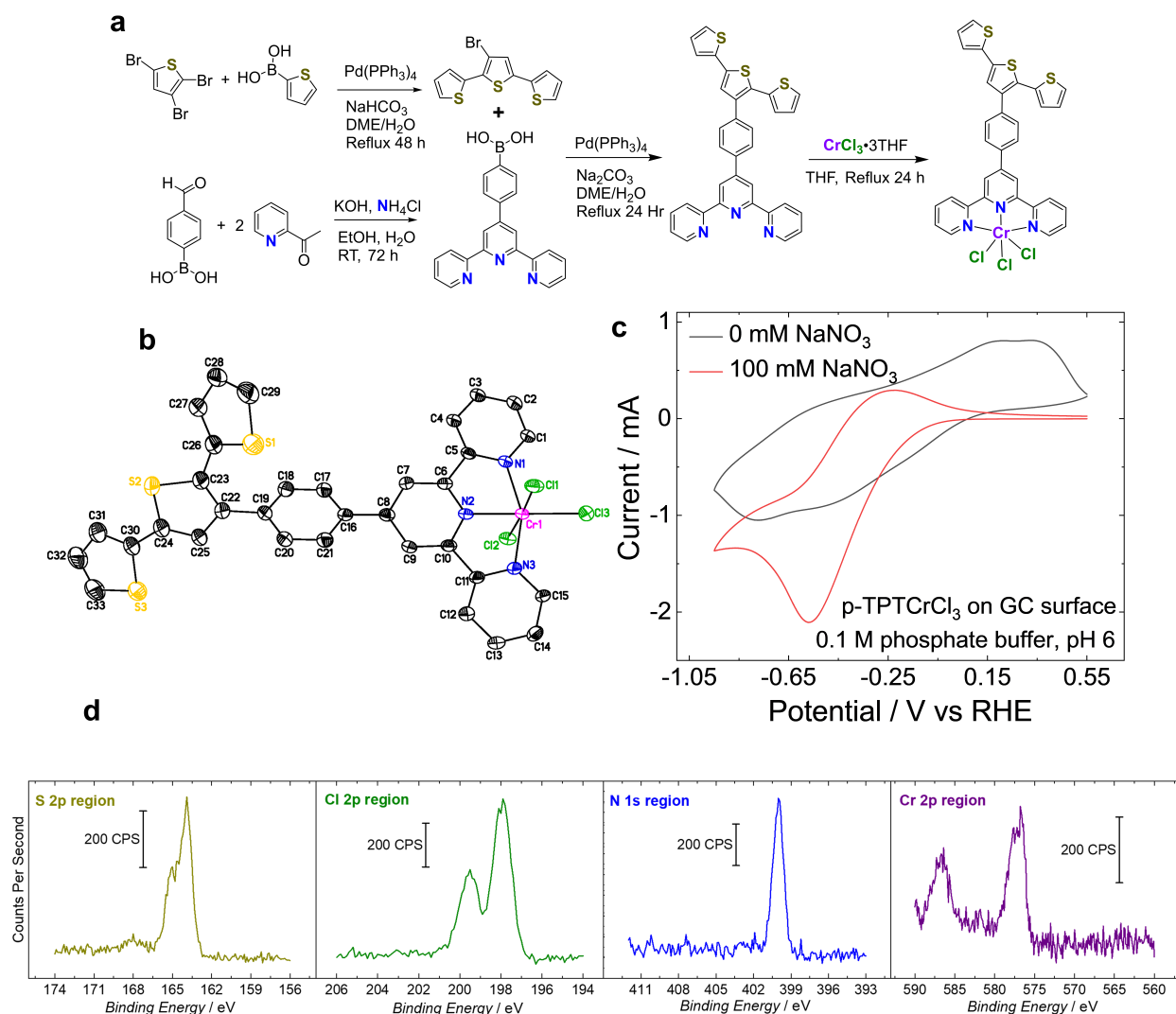


Figure 5.2 (a) General scheme for the synthesis of the TPTCrCl₃ monomer. Further synthetic details are in the experimental section of the supplemental information. (b) Single crystal structure of the TPTCrCl₃ monomer complex, based on single crystals suitable for X-ray analysis grown from acetonitrile/hexanes/diethyl ether. (c) Representative CVs of p-TPTCrCl₃ films in 0.1 M phosphate buffer at a scan rate of 0.1 V/s in the absence and presence of 0.1 M NaNO₃. The p-TPTCrCl₃ film was formed from a 20 mC electrodeposition. (d) Representative XPS of a p-TPTCrCl₃ film formed from a 20 mC electrodeposition.

To quantify further the activity and selectivity for NO_3^- reduction, we conducted a series of 2-h controlled potential electrolysis (CPE) experiments. CPE experiments were conducted in a previously described sealed two-chamber electrochemical cell²⁸ in which the p-TPTCrCl₃-modified GC working electrode and single junction Ag/AgCl/KCl(sat.) reference electrode were located in the first chamber, the carbon rod auxiliary electrode was located in the second chamber, and the two chambers were separated by a pre-treated Nafion membrane (see experimental for details). The first chamber also contained a magnetic Fisherbrand Egg-Shaped Bar (19 mm length, 9.5 mm diameter), and the stir rate was controlled using a Thermo Scientific RT Touch Series Magnetic Stirrer (4 L capacity, 30-2000 RPM). All results from the CPE experiments are summarized in Tables S5.2-S5.4 in the SI and Figure 5.3 below.

Note that we used exclusively isotopically labeled ¹⁵N species (e.g. ¹⁵NO₃⁻, ¹⁵NO₂⁻, and ¹⁵NH₂OH) in our CPE experiments to ensure that any ammonia detected was due solely to substrate reduction and not from adventitious ammonia or catalyst decomposition.^{38,39} Electrocatalytically-generated ¹⁵NH₃ product was quantified using a recently-reported low-temperature ¹H-NMR method in which a specific solvent suppression sequence is combined with pH control of the sample in order to obtain a quantitative ratio between an internal standard (maleic acid) and the proton doublets specific to ¹⁵NH₃.³⁶ Using this ¹H-NMR method with a liquid N₂-cooled Bruker 600 MHz NMR enabled us to obtain quantitative ¹⁵NH₃ data in 40 minutes. NO₂⁻ and NH₂OH were quantified using colorimetric methods,^{40,41} and H₂ produced from the competitive hydrogen evolution reaction (HER) was quantified using gas chromatography. Further details of these methods including calibration curves for the UV-vis and NMR methods can be found in the experimental section.

For all CPE measurements, the p-TPTCrCl₃ films were formed from a 20 mC electrodeposition. The potential dependence product distribution of NO₃ reduction by p-TPTCrCl₃ film in a 0.1 M phosphate buffer at pH 6 and a stir rate of 250 rpm is shown in Figures 5.3a-5.3b. Representative ¹⁵N NMR measurements can be found in the SI (Figures S5.15-S5.20). Significant average current density for the NO₃RR in the CPE measurements is observed at potentials more negative than -0.55 V vs. RHE (Figure 5.3b), consistent with onset potential of the NO₃RR observed in the catalytic CVs (Figure 5.2e). The highest Faradaic efficiency for NH₃ production is FE = 86 ± 2 achieved at -0.75 V vs RHE (Figure 5.3a). At potentials more negative than -0.75 V vs RHE, the Faradaic efficiency for NH₃ production decreases due to the onset of competitive hydrogen evolution. Importantly, the average partial current density going to NH₃ production remains constant or even slightly increasing at these more negative potentials, suggesting that the competitive HER does not inhibit the NO₃RR. Small amounts of NO₂⁻ and NH₂OH were observed at every potential negative of -0.55 V vs. RHE, but these intermediate products accounted for < 20% of the Faradaic efficiency.

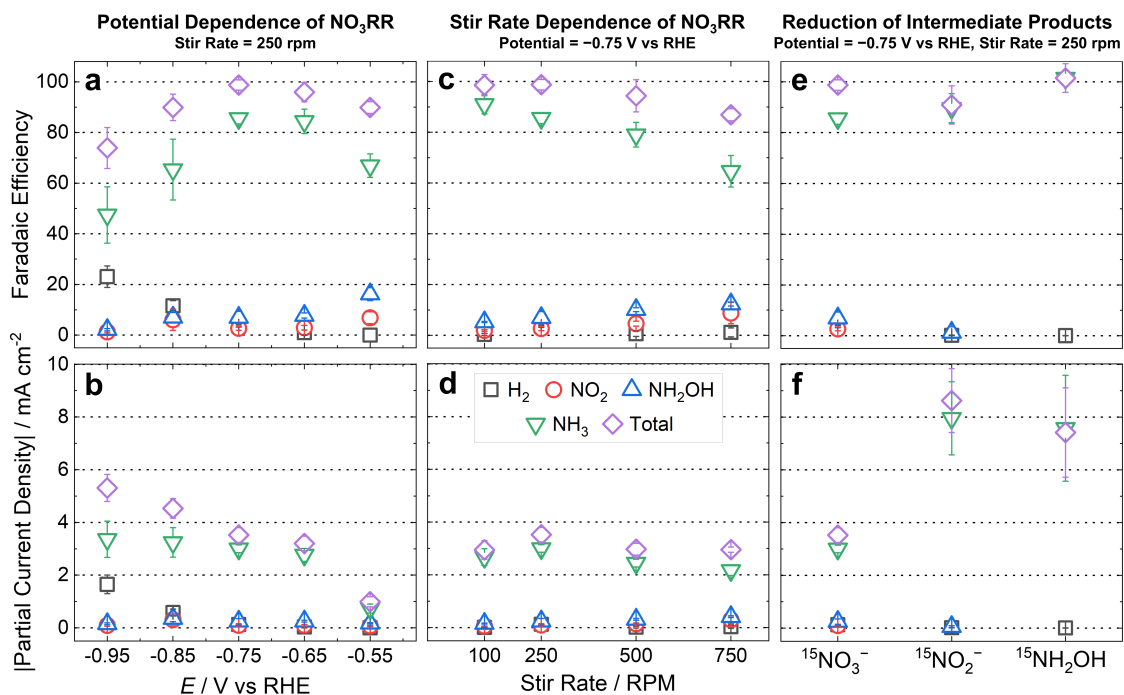


Figure 5.3 Product distributions from CPE measurements of NO_3RR by p-TPTCrCl₃ films formed from a 20 mC electrodeposition. Unless otherwise noted, all CPEs were conducted in pH 6 phosphate buffer with 0.1 M of ^{15}N -labeled substrate for 2 h. **(a)** Faradaic efficiencies and **(b)** average partial current densities for products of $^{15}\text{NO}_3^-$ reduction as a function of applied potential at a stir rate of 250 rpm. **(c)** Faradaic efficiencies and **(d)** average partial current densities products of $^{15}\text{NO}_3^-$ reduction as a function of stir rate at -0.75 V vs RHE. **(e)** Faradaic efficiencies and **(f)** average partial current densities for products of the reduction of 0.1 M $^{15}\text{NO}_3^-$, 0.1 M $^{15}\text{NO}_2^-$, and 0.1 M $^{15}\text{NH}_2\text{OH}$ at -0.75 V vs RHE and a stir rate of 250 rpm. The CPEs for $^{15}\text{NO}_3^-$ and $^{15}\text{NO}_2^-$ were conducted for 2 h, and the CPEs for NH_2OH were conducted for 1 h. All data in these figures are also included in Table S5.2-S5.4.

Because we observed small amounts of both NO_2^- and NH_2OH as products in our electrolysis experiments, we hypothesized that the p-TPTCrCl₃ system may reduce NO_3^- using a cascade catalysis mechanism, in which NO_3^- is sequentially reduced through various intermediates to the final NH_3 product. A similar mechanism has been proposed for another NO_3RR catalyst system.⁴² To test this hypothesis, we first measured the product distribution for the NO_3RR by p-TPTCrCl₃ in CPE experiments at different stir rates (Figures 5.3c-d). Representative ^{15}N NMR measurements can be found in the SI (Figures S5.21-S5.23). We postulated that at slower stir rates, the various reduced intermediates would be retained near the electrode surface and undergo

further reduction, resulting in larger observed Faradaic efficiencies for NH_3 . Conversely, at faster stir rates, we postulated that the reduced intermediates would be swept from the electrode surface, leading to larger Faradaic efficiencies for NO_2^- and NH_2OH . The results shown in Figure 5.3c are consistent with our hypothesis—there is a decrease in Faradaic efficiency for NH_3 and increase in Faradaic efficiencies for NO_2^- and NH_2OH as a function of increasing stir rate. Note that a decrease in the total Faradaic efficiency is also observed at the fastest stir rates. We attribute this to the production of NO , another NO_3RR intermediate that we did not attempt to quantify due to its short lifetime and difficulty in detection.⁴³

To further test our hypothesis that NO_3RR by p-TPTCrCl₃ occurs via a cascade catalysis mechanism, we confirmed whether the catalyst film was able to reduce NO_2^- and NH_2OH , the proposed intermediates, to the final NH_3 product. We conducted CPE experiments with 0.1 M $^{15}\text{NO}_2^-$ and 0.1 M $^{15}\text{NH}_2\text{OH}$ at -0.75 V vs RHE and a stir rate of 250 rpm in a pH 6 aqueous phosphate buffer. Note that a shorter 1-h CPE time was used for $^{15}\text{NH}_2\text{OH}$ to limit the extent of its thermal degradation to $^{15}\text{NH}_3$ under the experimental conditions.⁴⁴ The resulting product distributions for NO_2^- and NH_2OH reduction are shown in Figures 5.3e-f, along with the NO_3RR results under identical conditions for comparison. Representative ^{15}N NMR measurements can be found in the SI (Figures S5.24-S5.25). The p-TPTCrCl₃ film was able to reduce both NO_2^- and NH_2OH to NH_3 with high Faradaic efficiency (Figure 5.3e), providing additional support that NO_2^- and NH_2OH are possible intermediates for NO_3RR . Importantly, p-TPTCrCl₃ reduces NO_2^- and NH_2OH with higher average current densities than NO_3^- , suggesting that consumption of these intermediates occurs at faster rates than their production during the NO_3RR . This result is consistent with a cascade catalysis mechanism with a rate-determining NO_3^- activation step.¹⁹

To ensure that the NO₃RR we measured in our experiments was due to the p-TPTCrCl₃, we conducted a series of control experiments, the results of which can be found in the SI. CPEs performed with bare glassy carbon electrodes without the p-TPTCrCl₃ film showed surprisingly high activity for NO₃RR to NO₂⁻, with > 75% Faradaic efficiency and > 3.5 mA cm⁻² average partial current density for NO₂⁻ production (Figures S5.26 and S5.27). However, < 5% Faradaic efficiency for any other N-containing product was detected. We believe this is one of the first reports that glassy carbon itself is an efficient and selective catalyst for the 2-electron reduction of NO₃⁻ to NO₂⁻. Nevertheless, this control experiment confirmed that the glassy carbon electrode was not responsible for the NH₃ production observed in the presence of the p-TPTCrCl₃ films. In another control experiment, CPEs conducted with the TPT polymer (p-TPT) without chromium metalation showed very low activity for the NO₃RR, < 0.25 mA cm⁻² total average current density (Figures S5.28 and S5.29), over an order of magnitude lower than the ~3.5 mA cm⁻² total average current density measured with p-TPTCrCl₃. This result suggests that the p-TPT film suppresses any background activity by the glassy carbon electrode, and that Cr incorporation into the film is necessary for NO₃RR activity. Finally, CPEs conducted with p-TPTCrCl₃ in the absence of NO₃⁻ showed low activity of < 0.30 mA cm⁻² total average current density and no N-containing products (Figure SS.30).

The p-TPTCrCl₃ system shows continuous activity for NO₃RR during the course of the CPE experiments. However, there is a ~2-fold decrease in measured current during the course of the 2-h CPE (Figure S5.31). XPS measurements conducted after the CPE measurements show a complete loss of Cl signal, and an appreciable decrease in the peak heights for Cr, N, and S (Figure S5.32). The loss of Cl in the catalytic cycle during the catalytic cycle is both expected and necessary to free up coordination sites on Cr for substrate binding. However, the loss of Cr, N,

and S peak intensity in the XPS suggests some level of film degradation may be occurring. Additionally, there is a moderate decrease in the S:Cr ratio from the XPS measurements of the post-CPE p-TPTCrCl₃ films compared to the as-synthesized films (Table S5.1), and this could indicate modest demetalation during the CPE experiments. There is also a moderate increase in the N:Cr and N:S ratios, but interpretation of these results is complicated by the possible incorporation of residual NO₃⁻ or NH₃ in the films post-CPE. CVs measured of TPTCrCl₃ post-electrolysis also show a change in the voltammetric peaks associated with the p-TPTCrCl₃ after CPE, and a modest decrease in catalytic activity for the NO₃RR (Figure S5.33). Together, these measurements suggest a modest level of catalyst deactivation occurs during the CPE measurements, possibly due to Cr demetalation or some other film degradation. Additional studies are necessary to determine the mechanism of this modest film degradation, and to determine modifications to the p-TPTCrCl₃ system to prevent activity loss and catalyst deactivation.

The p-TPTCrCl₃ system compares favorably to state-of-the-art NO₃RR catalysts for NH₃ production on the basis of both activity and selectivity (Figure 5.4 and Table S5.5) and is, to this date, the only molecular catalyst to do so. The catalytic activity of p-TPTCrCl₃ for the NO₃RR to NH₃ is 0.29 ± 0.053 mmol NH₃ mg_{cat}⁻¹ h⁻¹ at -0.75 V vs RHE and 0.27 ± 0.053 mmol NH₃ mg_{cat}⁻¹ h⁻¹ at the more positive -0.65 V vs RHE. These activities are comparable to several state-of-the-art catalyst systems (Figure 5.4). Importantly, the p-TPTCrCl₃ has not been optimized for activity as have many of these previously reported solid-state catalysts for the NO₃RR. Future work on this system will focus on optimizing performance by studying the influence of film thickness on catalytic activity and selectivity, and polymerizing the p-TPTCrCl₃ films onto nanostructured surfaces to improve active site exposure.

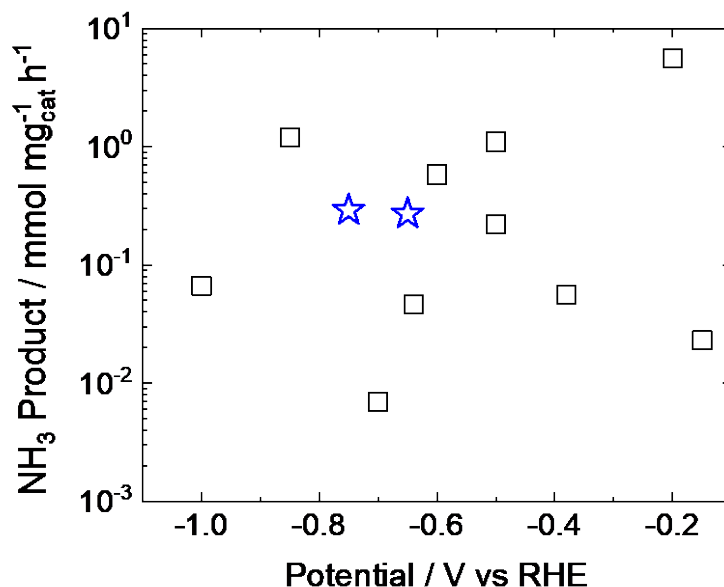


Figure 5.4 Comparison of NO₃RR activity to NH₃ by p-TPTCrCl₃ films from this study (blue stars) to that of selected previously reported catalysts (black squares). All data from this figure along with relevant citations are included in Tables S5.5.

5.6 Conclusion

In summary, we have developed a bio-inspired polymeric Cr catalyst that shows high activity and selectivity for NO₃⁻ reduction to NH₃ with negligible competitive HER. The catalyst likely operates via cascade catalyst mechanism, in which NO₃⁻ is sequentially reduced to key intermediates such as NO₂⁻ and NH₂OH, and finally to NH₃. This work hallmarks a new paradigm in electrochemical NO₃RR for nutrient recovery, showing that molecular catalysts in conductive polymer-catalyst composite films can operate with competitive activity and selectivity to solid-state catalysts. The high activity and selectivity of the p-TPTCrCl₃ catalyst was obtained without the extensive systems optimization and engineering seen in most other reports of active and selective solid-state catalysts for NO₃RR to NH₃, suggesting that there is significant room to improve the p-TPTCrCl₃ system. Future work with the p-TPTCrCl₃ system will include studies to elucidate the mechanism of the modest catalyst deactivation and improve stability, and to increase

active site exposure and overall activity by electropolymerizing the film onto microstructured and nanostructured supports.

5.7 Supporting Information

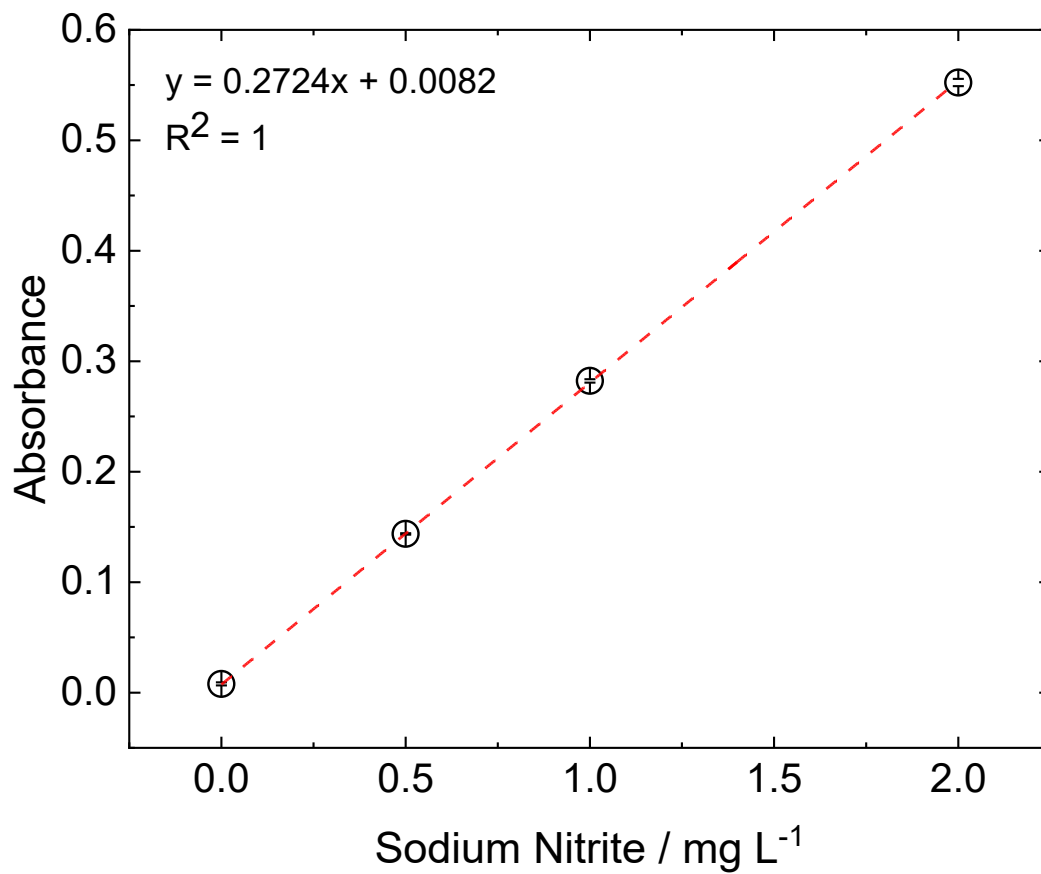


Figure S5.1 Calibration curve for absorbance at 548 nm versus sodium nitrite concentration as obtained using the Greiss method for nitrite quantitation. All reported values are averages of 3 independently prepared samples, and all errors are standard deviations.

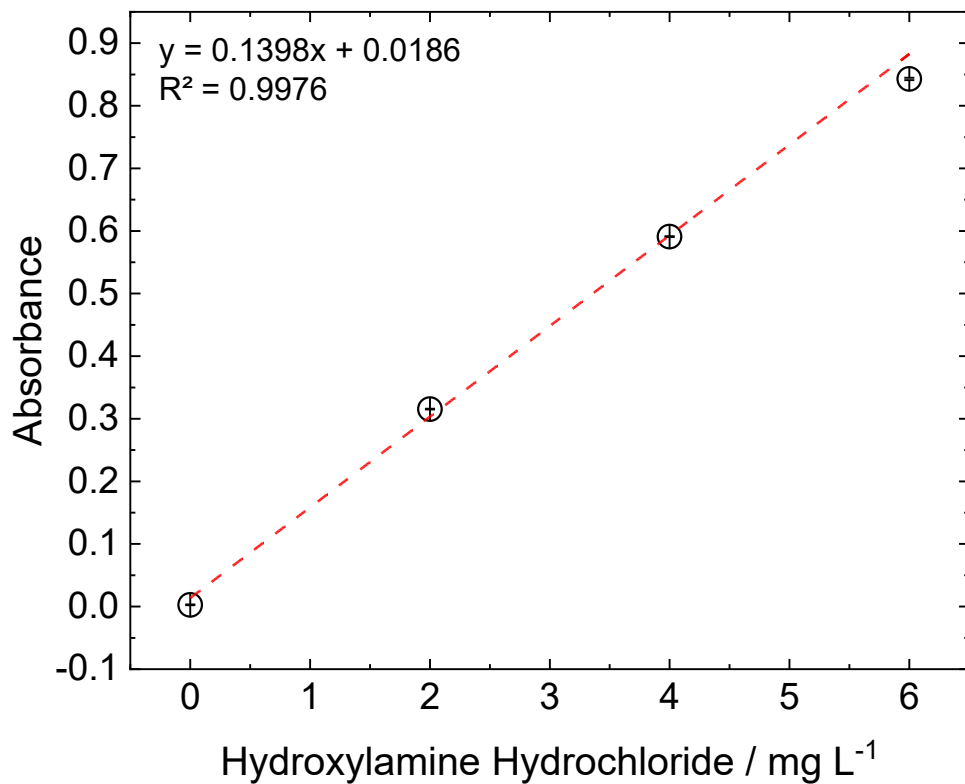


Figure S5.2 Calibration curve for absorbance at 700 nm versus hydroxylamine hydrochloride concentration as obtained using the 8-hydroxyquinoline method for hydroxylamine quantitation. All reported values are averages of 3 independently prepared samples, and all errors are standard deviations.

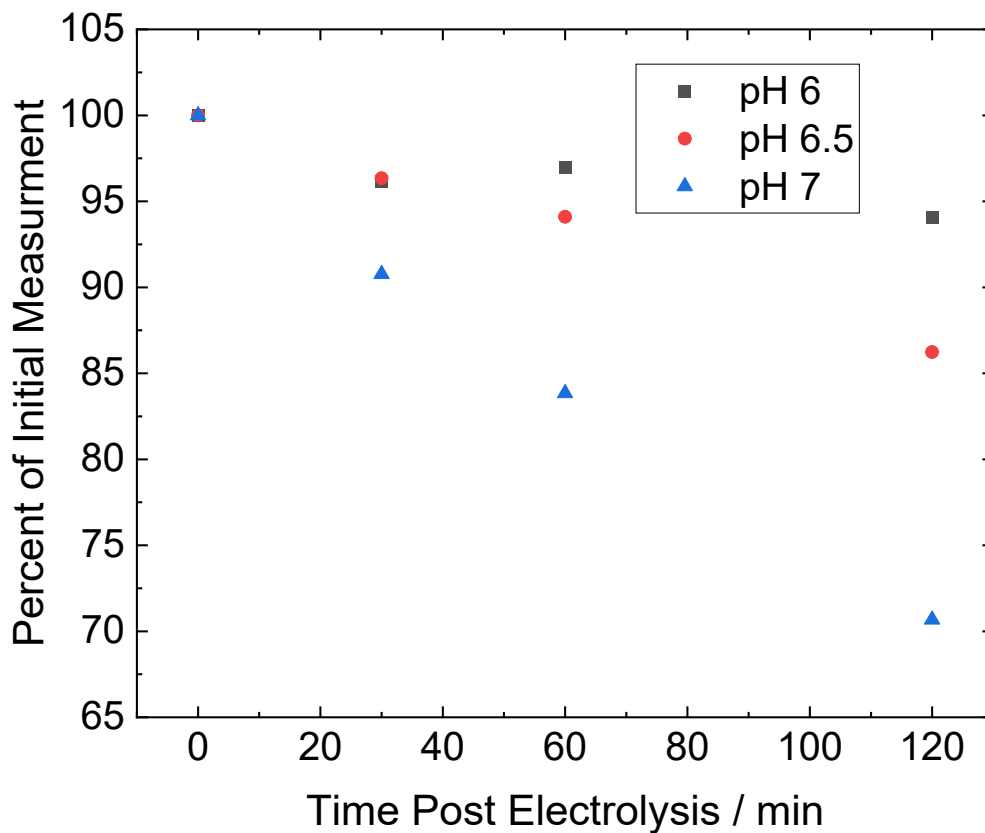


Figure S5.3 Representative data showing the concentration of hydroxylamine in the electrolyte solution over time after reduction of NaNO_3 by p-TPTCrCl_3 . All values are reported as a percent of the initial concentration determined immediately after electrolysis completed. The electrolyte was 100 mM phosphate buffer titrated to various pH values. Due to the drastic increase in stability of hydroxylamine at pH 6 all electrolyses in this paper use pH 6 100 mM phosphate buffer as the electrolyte.

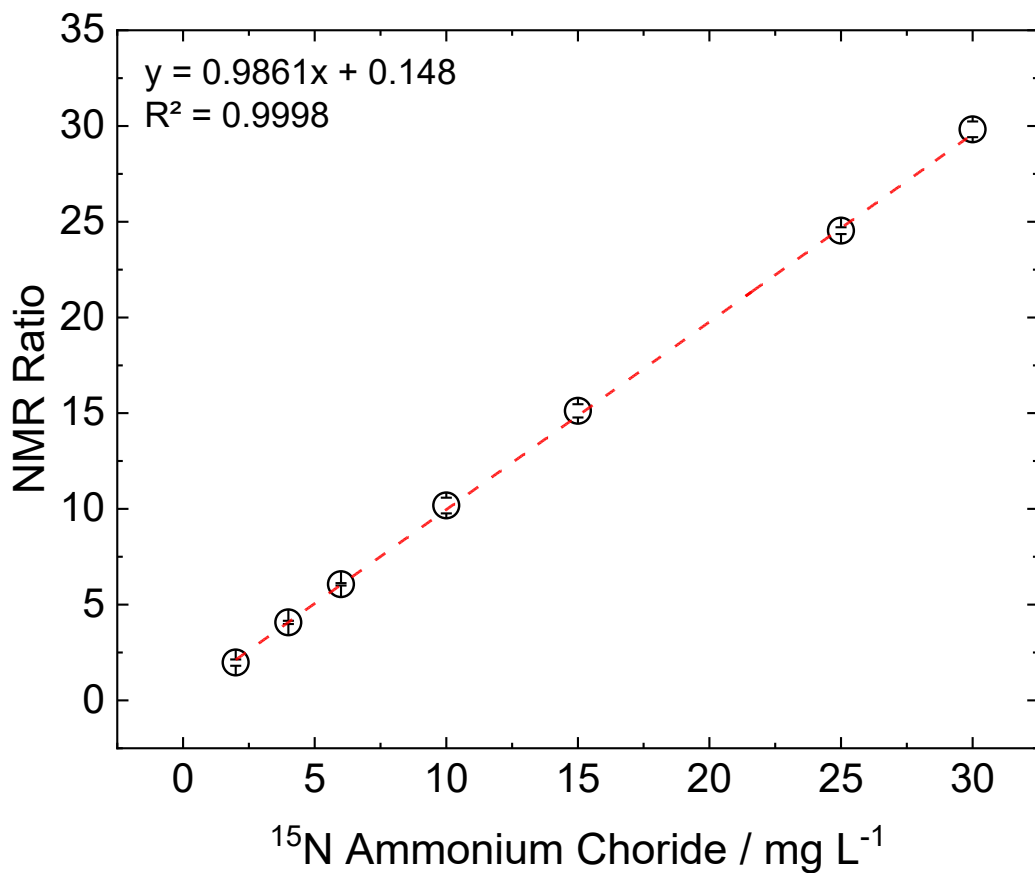


Figure S5.4 Calibration curve for the quantification of isotopically labeled $^{15}\text{NH}_4\text{Cl}$ via H-NMR. All values are reported as a ratio between the $^{15}\text{NH}_4$ peaks and the maleic acid internal standard. All reported values are averages of 3 independently prepared samples, and all errors are standard deviations.

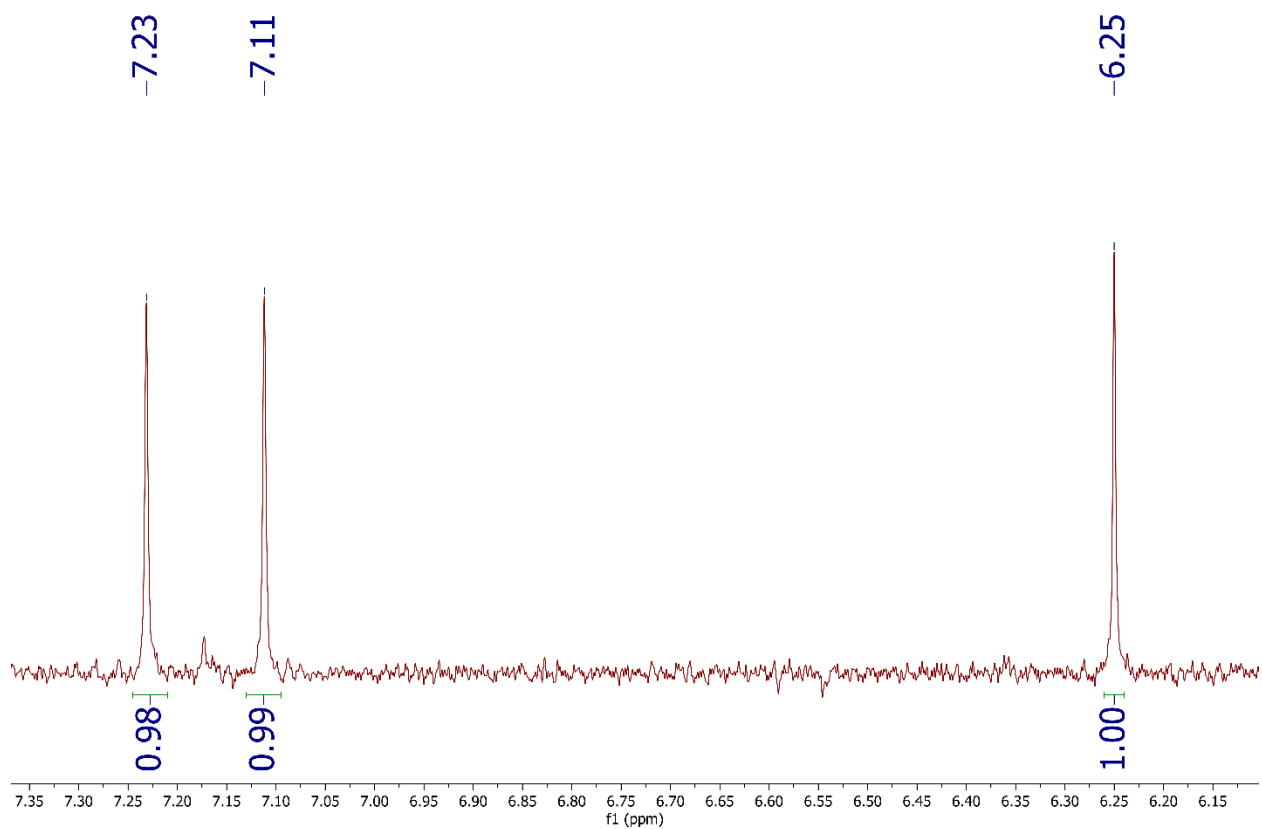


Figure S5.5 Representative H-NMR of a calibration standard containing 2 mg L⁻¹ isotopically labeled ¹⁵NH₄Cl. The peaks at 7.23 and 7.11 ppm are from the ¹⁵NH₄Cl and the peak at 6.25 ppm is the maleic acid internal standard.

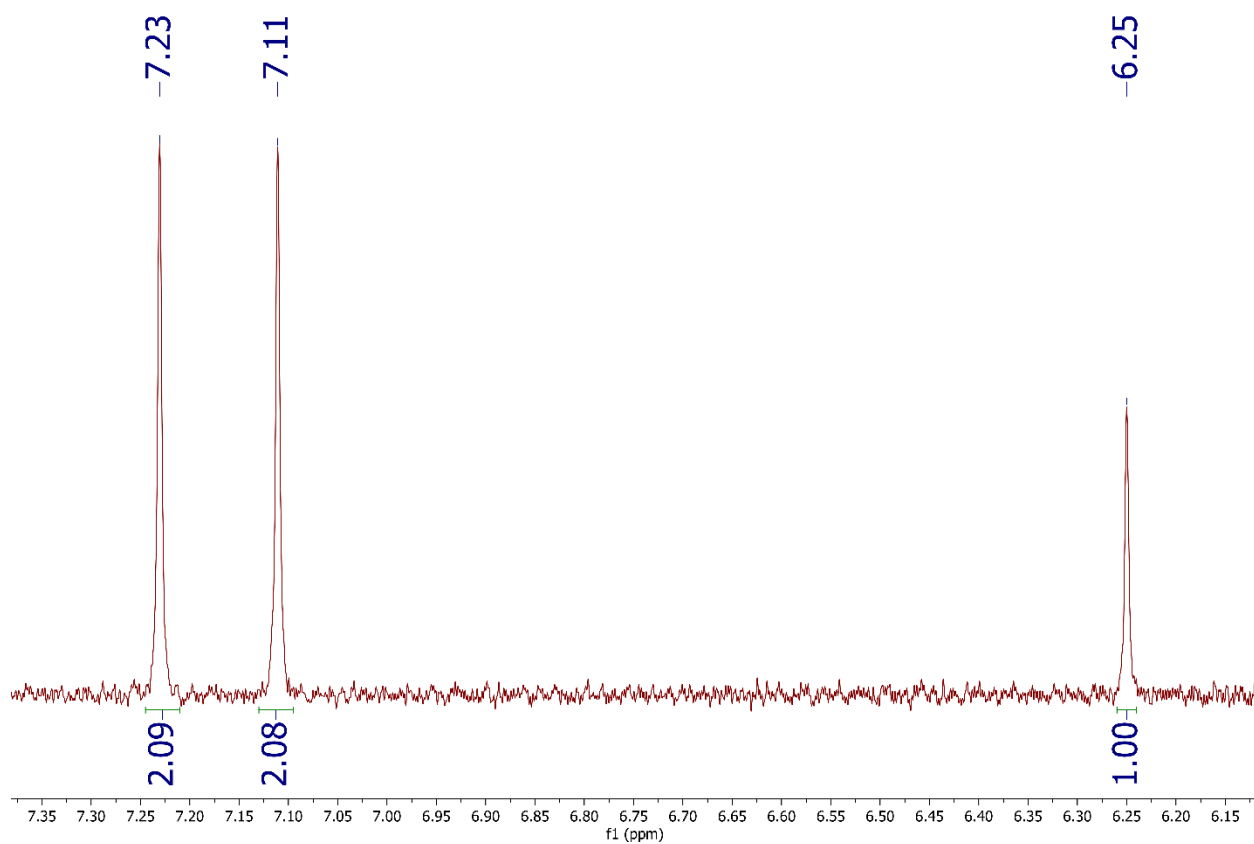


Figure S5.6 Representative H-NMR of a calibration standard containing 4 mg L⁻¹ isotopically labeled ¹⁵NH₄Cl. The peaks at 7.23 and 7.11 ppm are from the ¹⁵NH₄Cl and the peak at 6.25 ppm is the maleic acid internal standard.

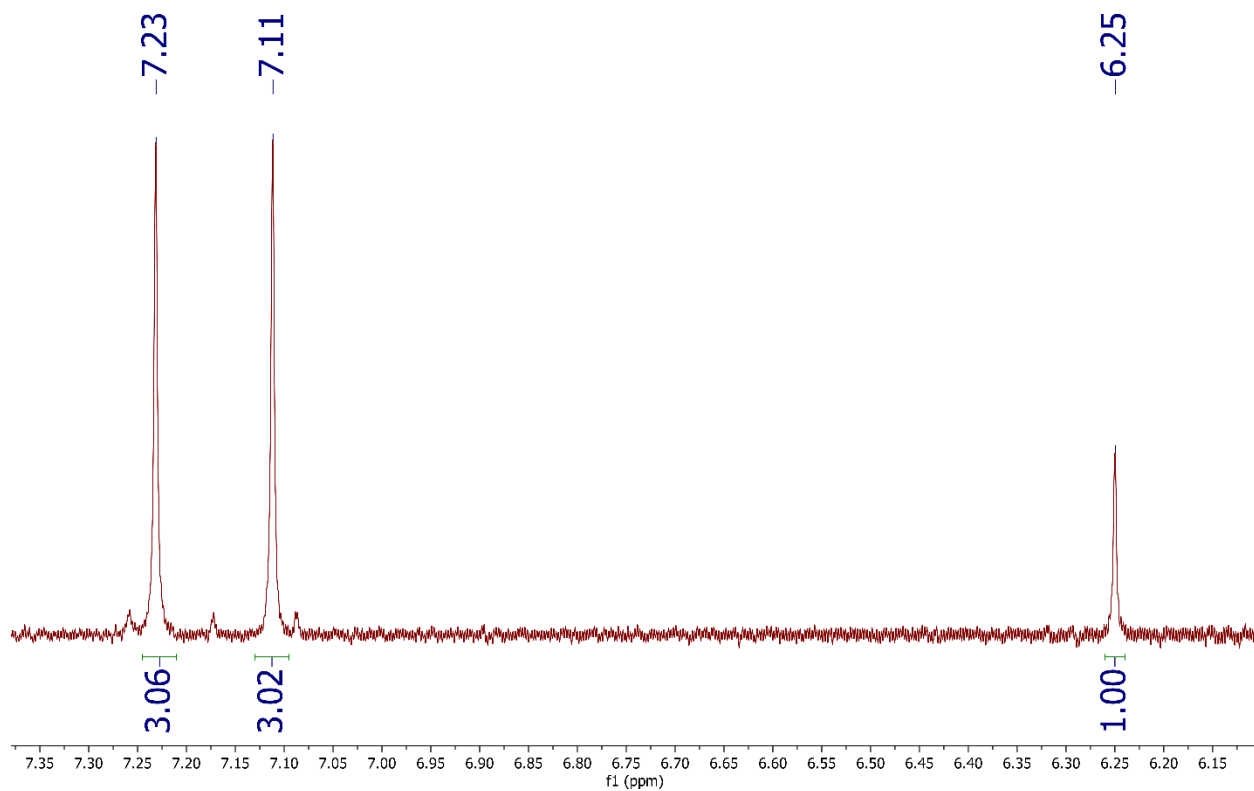


Figure S5.7 Representative H-NMR of a calibration standard containing 6 mg L⁻¹ isotopically labeled ¹⁵NH₄Cl. The peaks at 7.23 and 7.11 ppm are the from ¹⁵NH₄Cl and the peak at 6.25 ppm is the maleic acid internal standard. The small triplet interspaced with the ¹⁵NH₄Cl doublet is due the presence of trace amounts of ¹⁴NH₄.

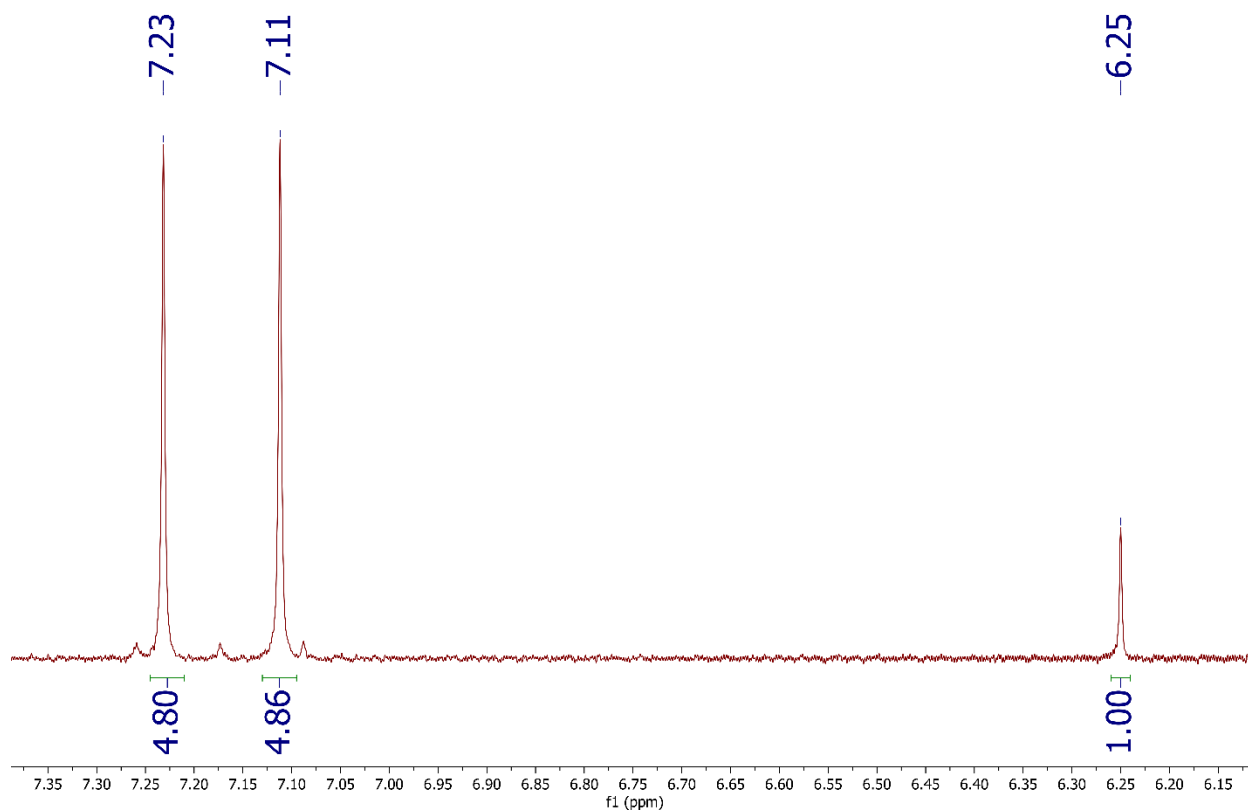


Figure S5.8 Representative $^1\text{H-NMR}$ of a calibration standard containing 10 mg L^{-1} isotopically labeled $^{15}\text{NH}_4\text{Cl}$. The peaks at 7.23 and 7.11 ppm are from the $^{15}\text{NH}_4\text{Cl}$ and the peak at 6.25 ppm is the maleic acid internal standard. The small triplet interspaced with the $^{15}\text{NH}_4\text{Cl}$ doublet is due the presence of trace amounts of $^{14}\text{NH}_4$.

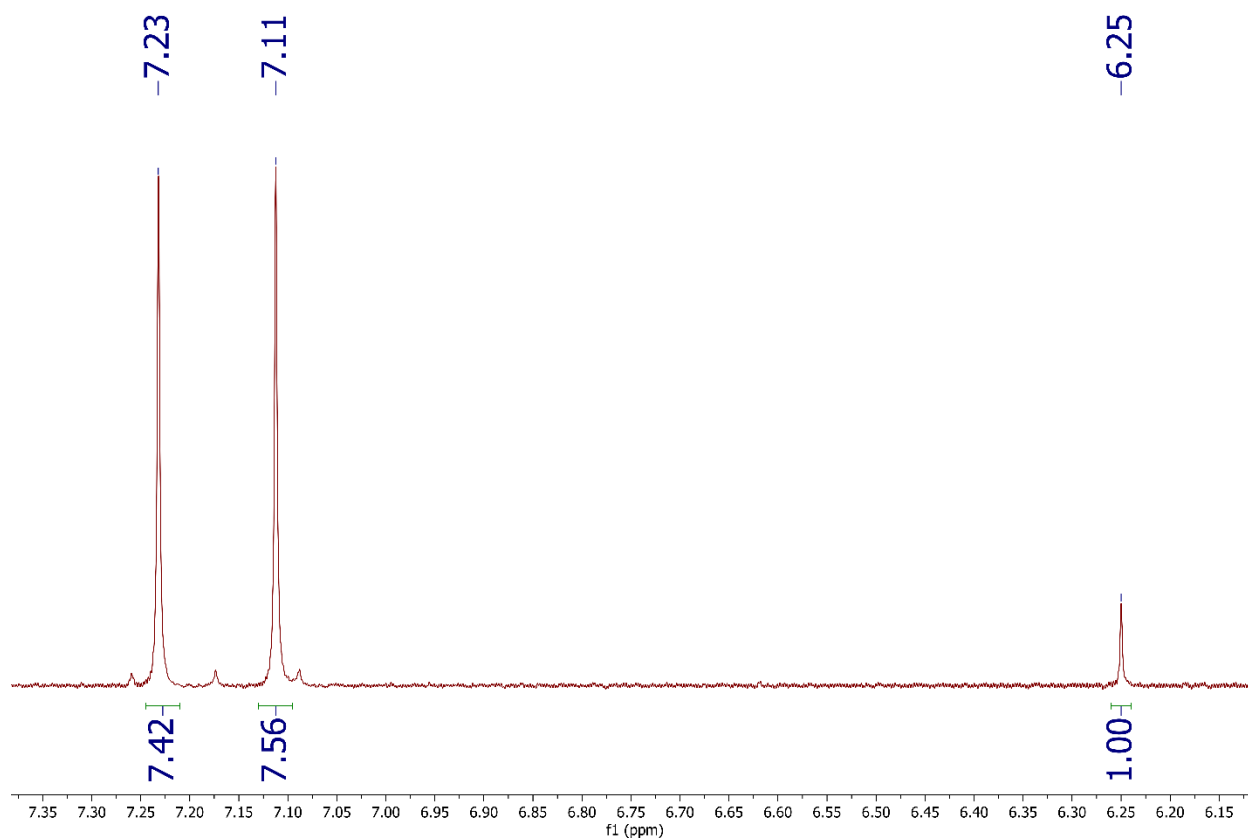


Figure S5.9 Representative $^1\text{H-NMR}$ of a calibration standard containing 15 mg L^{-1} isotopically labeled $^{15}\text{NH}_4\text{Cl}$. The peaks at 7.23 and 7.11 ppm are from the $^{15}\text{NH}_4\text{Cl}$ and the peak at 6.25 ppm is the maleic acid internal standard. The small triplet interspaced with the $^{15}\text{NH}_4\text{Cl}$ doublet is due the presence of trace amounts of $^{14}\text{NH}_4$.

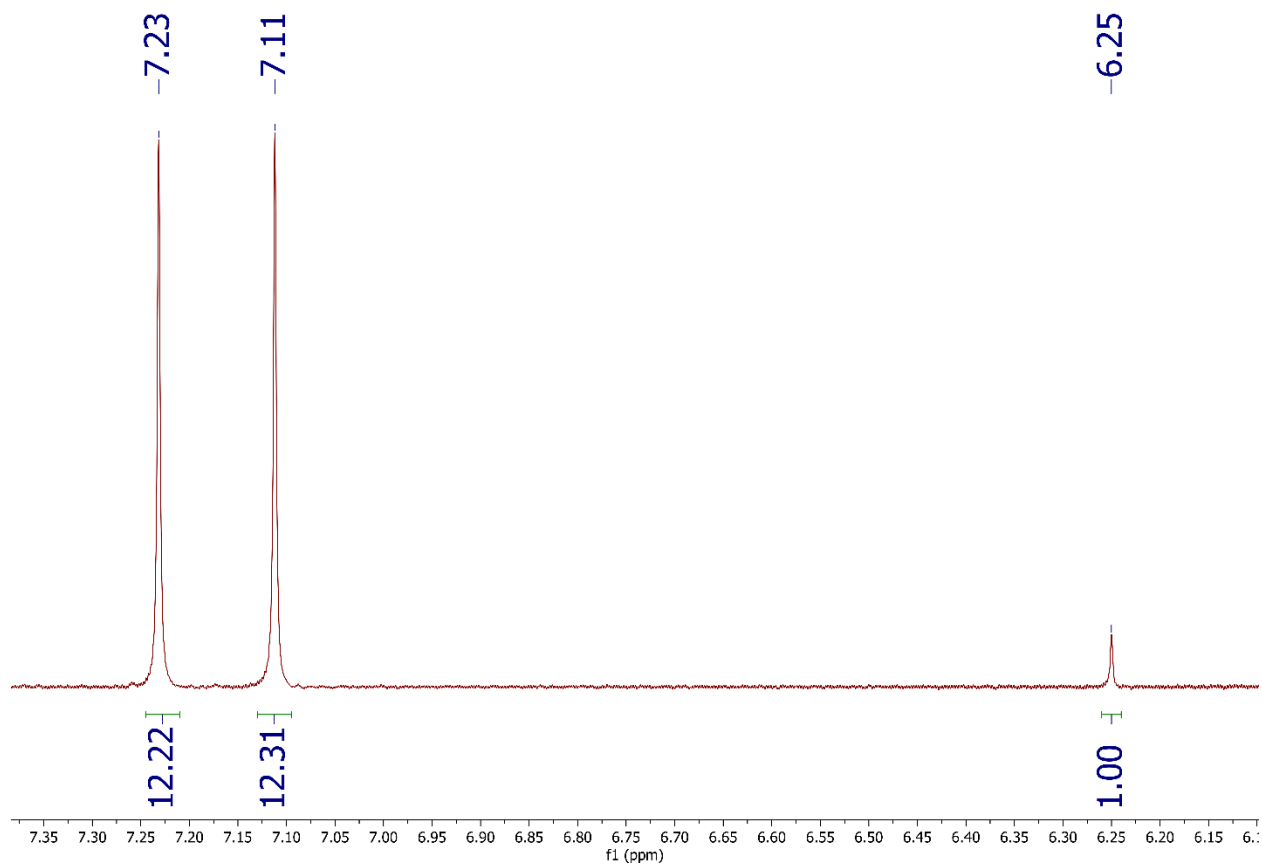


Figure S5.10 Representative H-NMR of calibration standard containing 25 mg L⁻¹ isotopically labeled ¹⁵NH₄Cl. The peaks at 7.23 and 7.11 ppm are from the ¹⁵NH₄Cl and the peak at 6.25 ppm is the maleic acid internal standard. The small triplet interspaced with the ¹⁵NH₄Cl doublet is due the presence of trace amounts of ¹⁴NH₄.

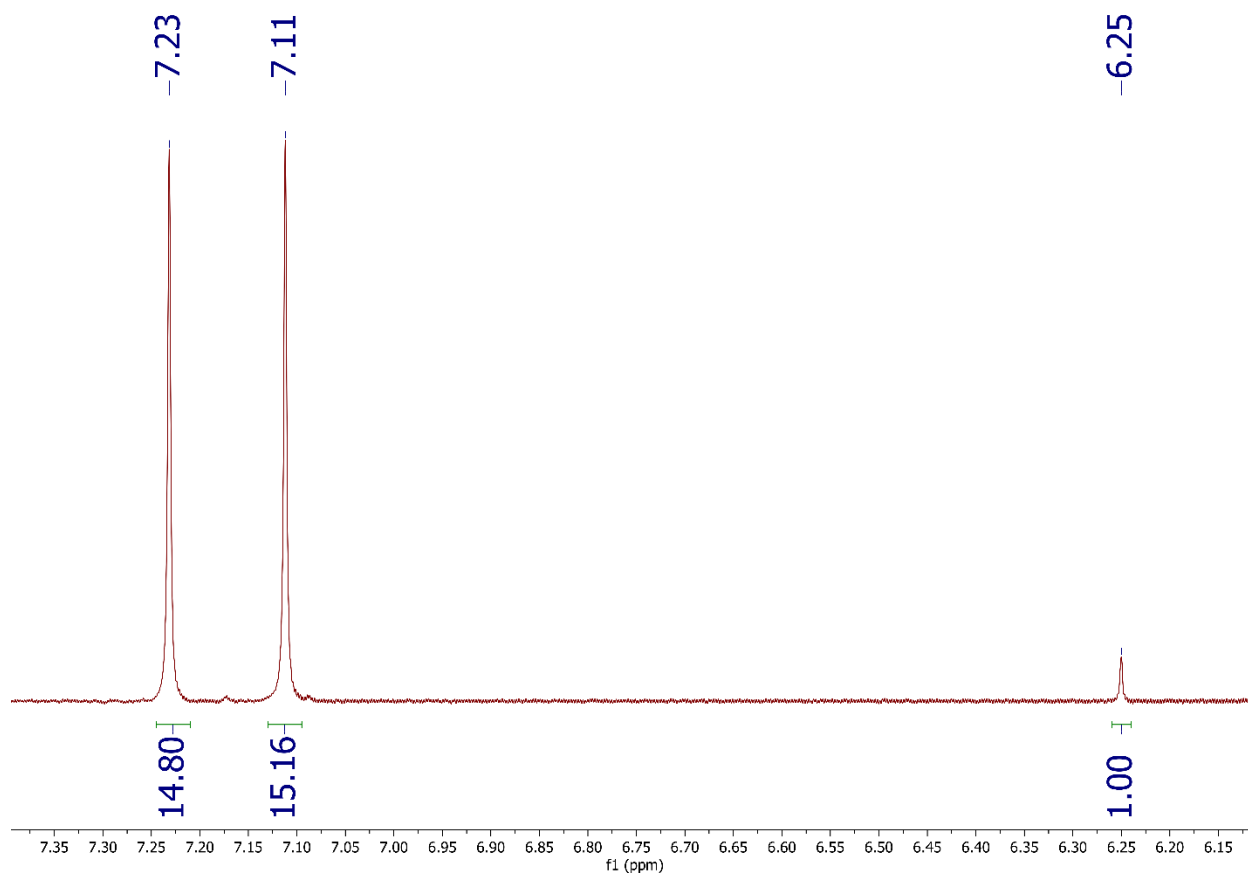


Figure S5.11 Representative $^1\text{H-NMR}$ of a calibration standard containing 30 mg L^{-1} isotopically labeled $^{15}\text{NH}_4\text{Cl}$. The peaks at 7.23 and 7.11 ppm are from the $^{15}\text{NH}_4\text{Cl}$ and the peak at 6.25 ppm is the maleic acid internal standard. The small triplet interspaced with the $^{15}\text{NH}_4\text{Cl}$ doublet is due the presence of trace amounts of $^{14}\text{NH}_4$.

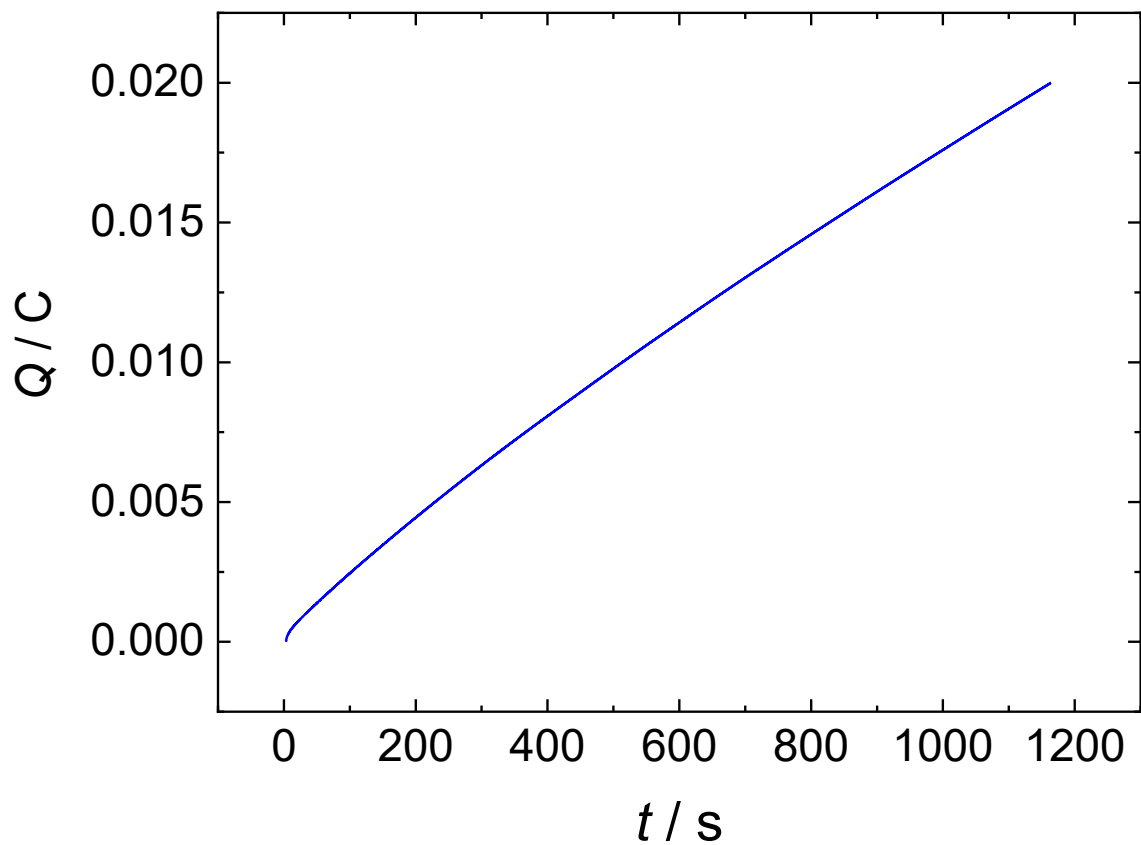


Figure S5.12 Representative potentiostatic p-TPTCrCl₃ deposition. The deposition solution consisted of 1 mM TPTCrCl₃ dissolved in dichloromethane with 0.1 M tetrabutylammonium hexafluorophosphate as the electrolyte. The deposition potential was 1.06 V vs Fc⁺⁰ and the total charge passed was 0.02 C.

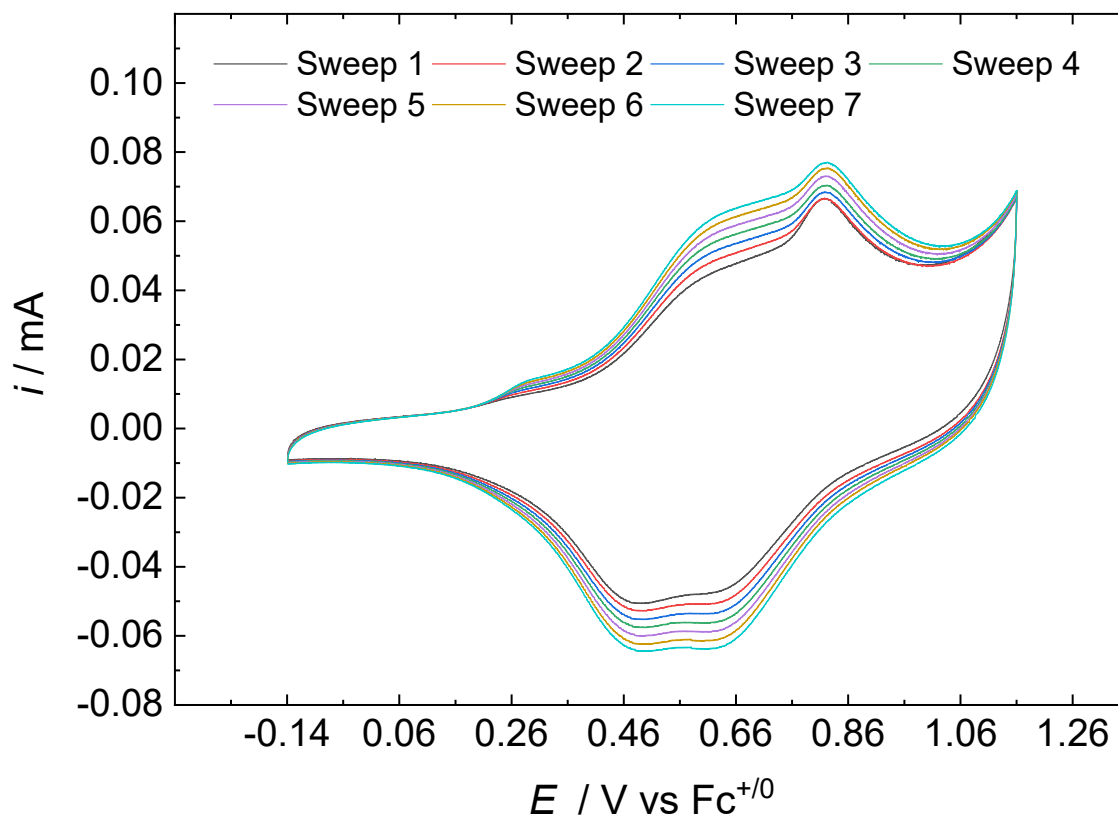


Figure S5.13 Representative cyclic voltammetry data showing the growth of the TPTCrCl₃ polymer during oxidative electropolymerization. The deposition solution consisted of 1 mM TPTCrCl₃ dissolved in dichloromethane with 0.1 M tetrabutylammonium hexafluorophosphate as the electrolyte.

Table S5.1 Average XPS ratios of p-TPTCrCl₃ films both directly after polymerization and after a standard 2-hour electrolysis. The lack of Cl ratios for post electrolysis polymers is due to an absence of the chlorine peak in those samples. All reported values are averages of at least 3 independently prepared samples and all errors are standard deviations

Compared Elements	Predicted Ratio	Fresh Polymer	Post Electrolysis Polymer
N:Cr	3:1	3.22 ± 0.05	3.72 ± 0.28
N:S	1:1	1.23 ± 0.08	1.62 ± 0.16
S:Cr	3:1	2.62 ± 0.13	2.31 ± 0.23
Cl:N	1:1	0.87 ± 0.04	N/A
Cl:S	1:1	1.07 ± 0.04	N/A
Cl:Cr	3:1	2.80 ± 0.10	N/A

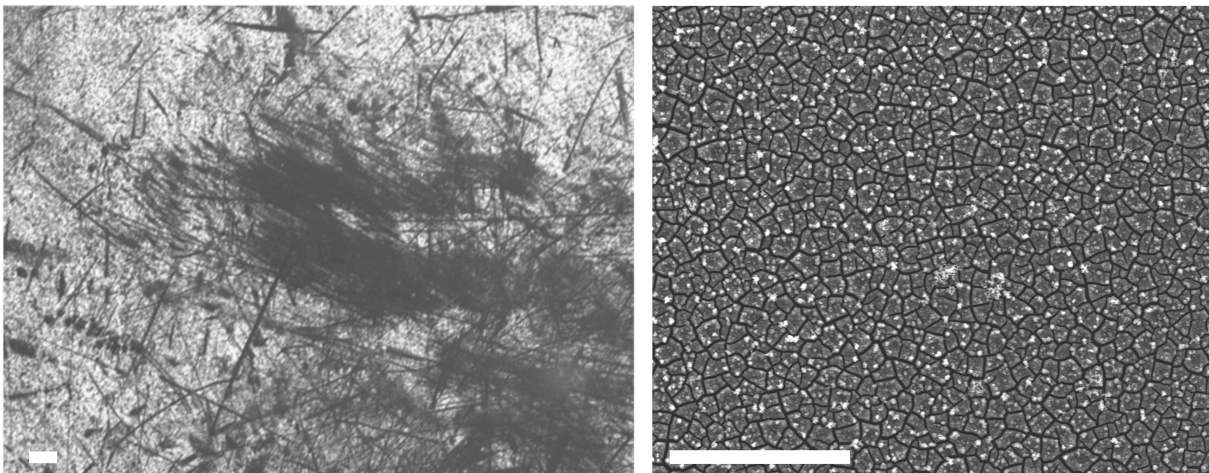


Figure S5.14 Representative SEM of a bare glassy carbon electrode (Left) and a glassy carbon electrode coated with a film of electropolymerized TPTCrCl₃ (Right). The white bars represent 100 μm.

Table S5.2 Faradaic efficiencies and current densities for the potential dependent reduction of nitrate by electropolymerized p-TPTCrCl₃ films. All electrolyses were conducted for 2 hours in argon sparged 0.1 M pH 6 phosphate buffer containing 0.1 M Na¹⁵NO₃. The stir rate was 250 RPM. All reported values are the average of 3 independently conducted electrolyses and all errors are standard deviations. The data in this table corresponds to Figures 5.3a and 5.3b in the main text.

Applied Potential (V vs RHE)	-0.55 V	-0.65 V	-0.75 V	-0.85 V	-0.95 V
FE NH ₃	66.89 ± 4.62	84.36 ± 4.82	85.56 ± 2.22	65.34 ± 11.98	47.44 ± 11.13
FE NH ₂ OH	16.17 ± 2.58	7.73 ± 0.99	6.93 ± 2.41	6.99 ± 1.93	2.12 ± 0.47
FE NO ₂	6.80 ± 2.35	2.91 ± 0.89	2.67 ± 0.79	6.01 ± 4.18	1.24 ± 0.36
FE H ₂	0	0.94 ± 1.0	3.58 ± 0.43	11.56 ± 2.07	23.08 ± 4.25
FE Total	89.87 ± 2.36	95.93 ± 3.83	98.74 ± 2.03	89.91 ± 5.23	73.88 ± 8.10
Partial Current Density NH ₃ (mA cm ⁻²)	0.72 ± 0.17	2.77 ± 0.25	3.00 ± 0.14	3.24 ± 0.56	3.36 ± 0.69
Partial Current Density NH ₂ OH (mA cm ⁻²)	0.17 ± 0.02	0.25 ± 0.04	0.25 ± 0.10	0.35 ± 0.11	0.15 ± 0.03
Partial Current Density NO ₂ (mA cm ⁻²)	0.07 ± 0.2	0.10 ± 0.03	0.09 ± 0.03	0.30 ± 0.22	0.09 ± 0.03
Partial Current Density H ₂ (mA cm ⁻²)	0	0.03 ± 0.03	0.13 ± 0.02	0.58 ± 0.13	1.65 ± 0.35

Table S5.3 Faradaic efficiencies and current densities for the stir rate dependent reduction of nitrate by electropolymerized p-TPTCrCl₃ films. All electrolyses were conducted for 2 hours in argon sparged 0.1 M pH 6 phosphate buffer containing 0.1 M Na¹⁵NO₃. The applied potential was -0.75 V vs RHE. All reported values are the average of 3 independently conducted electrolyses and all errors are standard deviations. The data in this table corresponds to Figures 5.3c and 5.3d in the main text.

Stir Rate (RPM)	100	250	500	750
FE NH ₃	91.00 ± 3.75	85.56 ± 2.22	79.05 ± 4.86	64.62 ± 6.22
FE NH ₂ OH	5.25 ± 0.24	6.93 ± 2.41	10.11 ± 0.76	12.34 ± 0.82
FE NO ₂	1.94 ± 0.32	2.67 ± 0.79	4.60 ± 0.96	8.76 ± 4.18
FE H ₂	0.39 ± 0.39	3.58 ± 0.43	0.61 ± 1.05	1.15 ± 1.76
FE Total	98.89 ± 4.19	98.74 ± 2.03	94.37 ± 6.35	86.87 ± 2.38
Partial Current Density NH ₃ (mA cm ⁻²)	2.67 ± 0.32	3.00 ± 0.14	2.45 ± 0.15	2.17 ± 0.19
Partial Current Density NH ₂ OH (mA cm ⁻²)	0.15 ± 0.02	0.25 ± 0.10	0.31 ± 0.33	0.41 ± 0.03
Partial Current Density NO ₂ (mA cm ⁻²)	0.06 ± 0.00	0.09 ± 0.3	0.14 ± 0.04	0.30 ± 0.15
Partial Current Density H ₂ (mA cm ⁻²)	0.01 ± 0.01	0.13 ± 0.2	0.02 ± 0.03	0.04 ± 0.06

Table S5.4 Faradaic efficiencies and current densities for the reduction of select NO_x species by electropolymerized p-TPTCrCl₃ films. All electrolyses were conducted for 2 hours in argon sparged 0.1 M pH 6 phosphate buffer containing 0.1 M substrate except for the reduction of ¹⁵NH₂OH•HCl which was conducted for 1 hour. The applied potential was -0.75 V vs RHE and the stir rate was 250 RPM. All reported values are the average of 3 independently conducted electrolyses and all errors are standard deviations. The data in this table corresponds to Figures 5.3e and 5.3f in the main text.

Substrate	Na ¹⁵ NO ₃	Na ¹⁵ NO ₂	¹⁵ NH ₂ OH•HCl
FE NH ₃	85.56 ± 2.22	67.70 ± 2.86	99.66 ± 5.55
FE NH ₂ OH	6.93 ± 2.41	0.76 ± 0.50	N/A
FE NO ₂	2.67 ± 0.79	N/A	N/A
FE H ₂	3.58 ± 0.43	0.15 ± 0.10	0.05 ± 0.05
FE Total	98.74 ± 2.03	68.61 ± 3.30	99.71 ± 5.56
Partial Current Density NH ₃ (mA cm ⁻²)	3.00 ± 0.14	4.17 ± 0.73	10.59 ± 2.81
Partial Current Density NH ₂ .OH (mA cm ⁻²)	0.25 ± 0.10	0.05 ± 0.03	N/A
Partial Current Density NO ₂ (mA cm ⁻²)	0.09 ± 0.3	N/A	N/A
Partial Current Density H ₂ (mA cm ⁻²)	0.13 ± 0.2	0.01 ± 0.01	0.005 ± 0.006

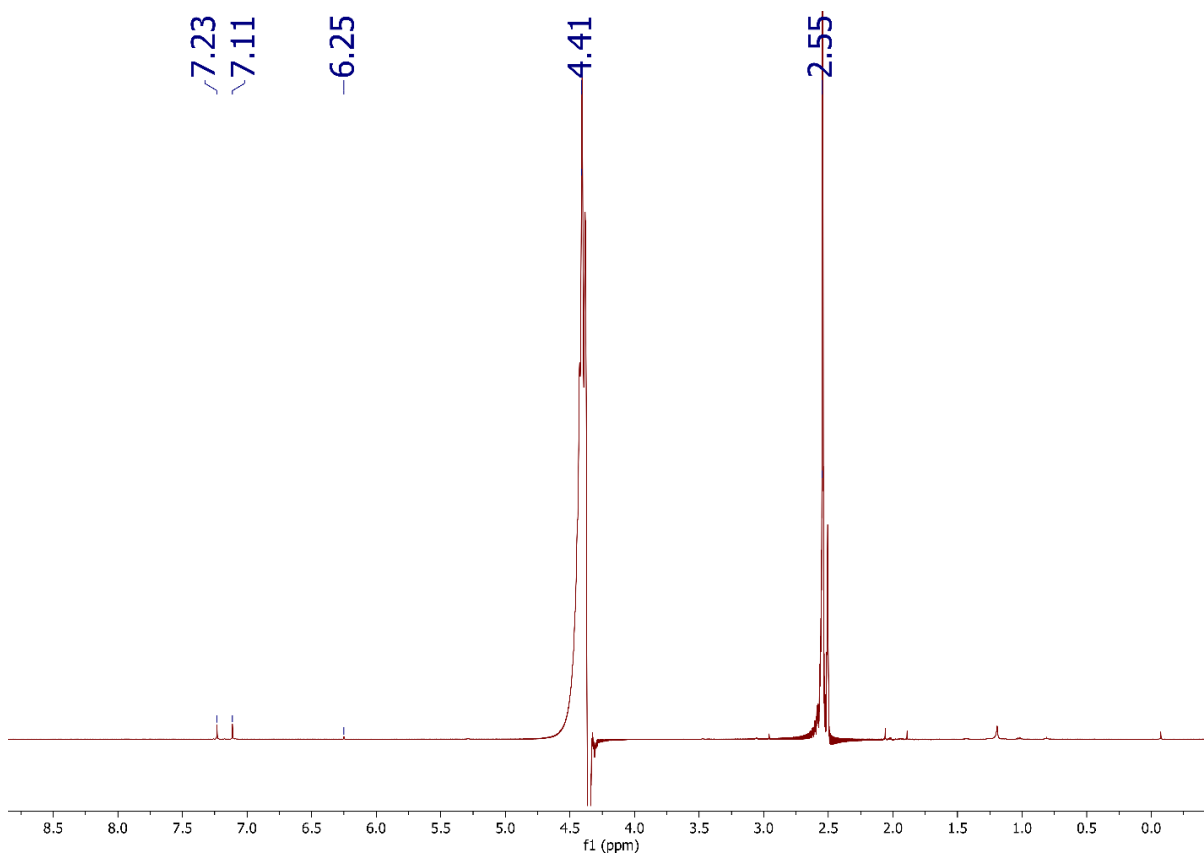


Figure S5.15 Representative raw (prior to any processing) $^1\text{H-NMR}$ of the electrolyte solution obtained after a 2-hour controlled potential electrolysis (CPE) at -0.75 V vs RHE and 250 RPM of isotopically labeled NO_3^- on a glassy carbon electrode modified with p-TPTCrCl₃. The electrolysis was conducted in a sealed cell containing 100 mM $\text{Na}^{15}\text{NO}_3$ dissolved in 0.1 M pH 6 phosphate buffer that was sparged with Argon for 30 minutes. The peaks at 7.23 and 7.11 ppm are from $^{15}\text{NH}_3$ and the peak at 6.25 ppm is from the maleic acid internal standard. The peak at 4.41 ppm is from water, and the peak at 2.55 ppm is from DMSO.

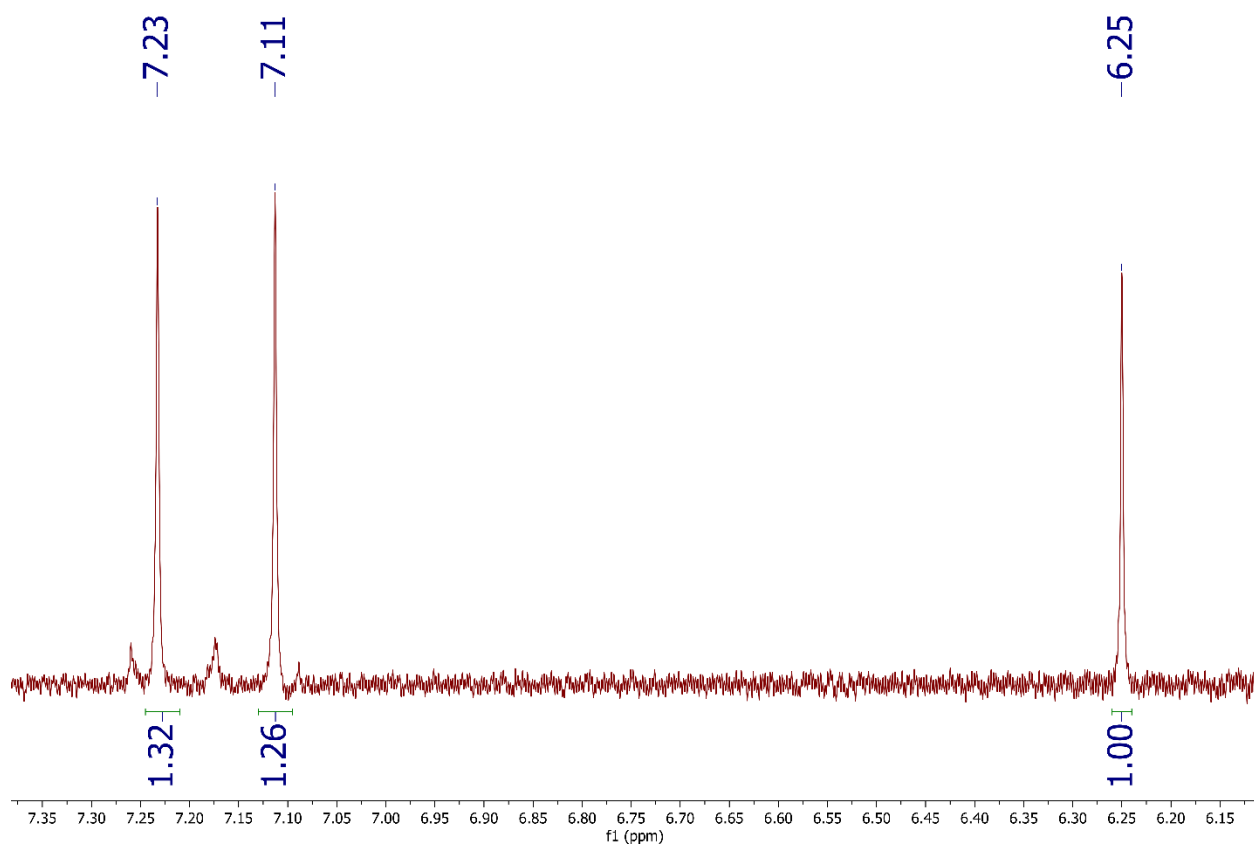


Figure S5.16 Representative $^1\text{H-NMR}$ of the electrolyte solution obtained after a 2-hour controlled potential electrolysis (CPE) at -0.55 V vs RHE and 250 RPM of isotopically labeled NO_3^- on a glassy carbon electrode modified with a p-TPTCrCl₃ film. The electrolysis was conducted in a sealed cell containing 100 mM $\text{Na}^{15}\text{NO}_3$ dissolved in 0.1 M pH 6 phosphate buffer that was sparged with Argon for 30 minutes. The peaks at 7.23 and 7.11 ppm are from $^{15}\text{NH}_3$ and the peak at 6.25 ppm is from the maleic acid internal standard. The small triplet interspaced with the $^{15}\text{NH}_3$ doublet is due the presence of trace amounts of $^{14}\text{NH}_4$.

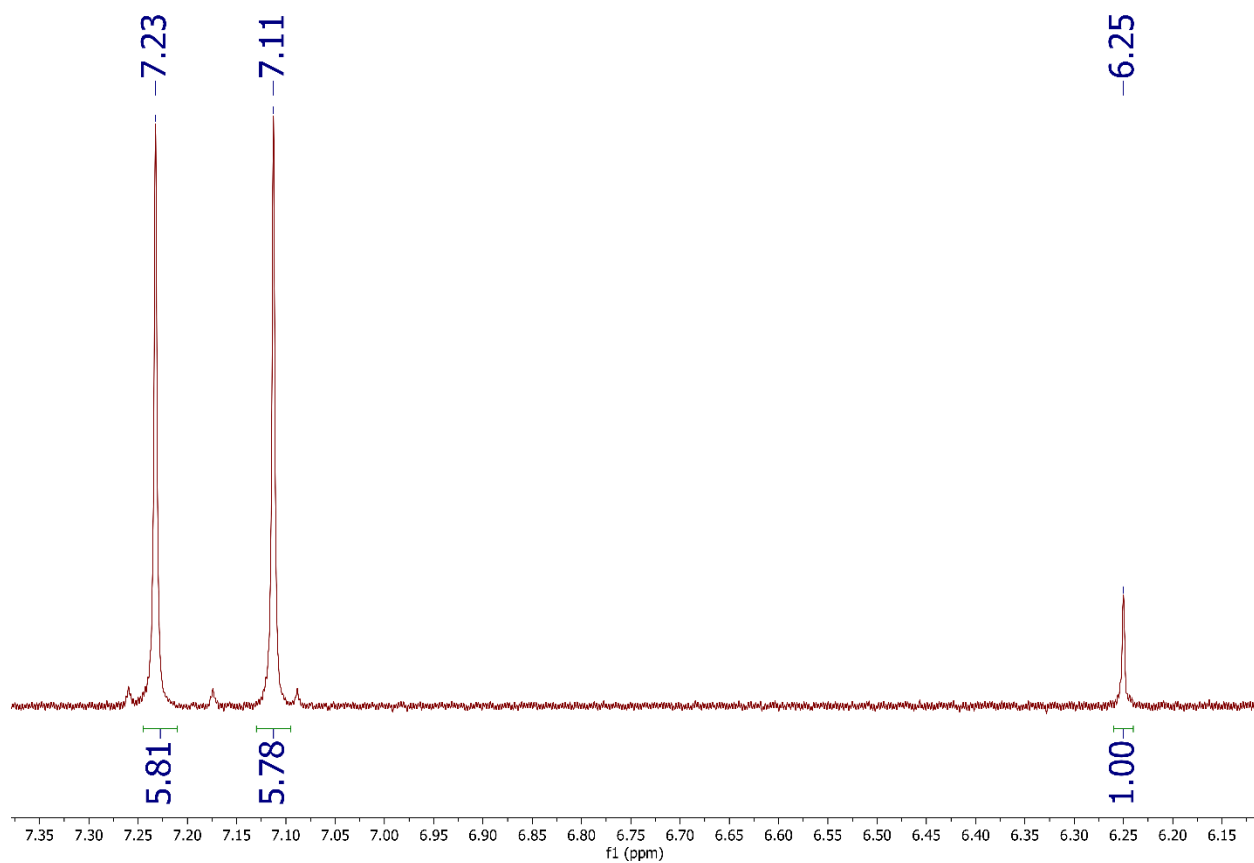


Figure S5.17 Representative $^1\text{H-NMR}$ of the electrolyte solution obtained after a 2-hour controlled potential electrolysis (CPE) at -0.65 V vs RHE and 250 RPM of isotopically labeled NO_3^- on a glassy carbon electrode modified with a p-TPTCrCl₃ film. The electrolysis was conducted in a sealed cell containing 100 mM $\text{Na}^{15}\text{NO}_3$ dissolved in 0.1 M pH 6 phosphate buffer that was sparged with Argon for 30 minutes. The peaks at 7.23 and 7.11 ppm are from $^{15}\text{NH}_3$ and the peak at 6.25 ppm is from the maleic acid internal standard. The small triplet interspaced with the $^{15}\text{NH}_3$ doublet is due the presence of trace amounts of $^{14}\text{NH}_4$.

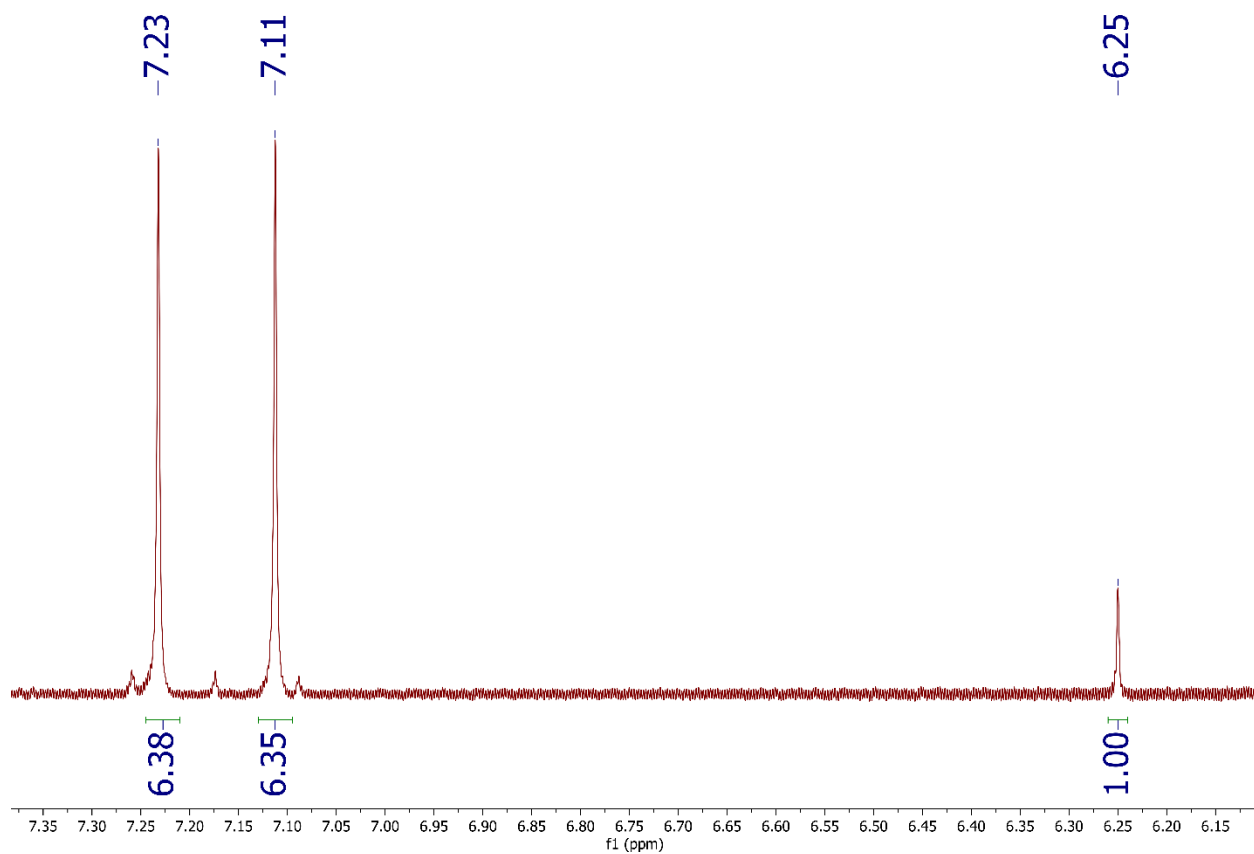


Figure S5.18 Representative $^1\text{H-NMR}$ of the electrolyte solution obtained after a 2-hour controlled potential electrolysis (CPE) at -0.75 V vs RHE and 250 RPM of isotopically labeled NO_3^- on a glassy carbon electrode modified with a p-TPTCrCl₃ film. The electrolysis was conducted in a sealed cell containing 100 mM $\text{Na}^{15}\text{NO}_3$ dissolved in 0.1 M pH 6 phosphate buffer that was sparged with Argon for 30 minutes. The peaks at 7.23 and 7.11 ppm are from $^{15}\text{NH}_3$ and the peak at 6.25 ppm is from the maleic acid internal standard. The small triplet interspaced with the $^{15}\text{NH}_3$ doublet is due the presence of trace amounts of $^{14}\text{NH}_4$.

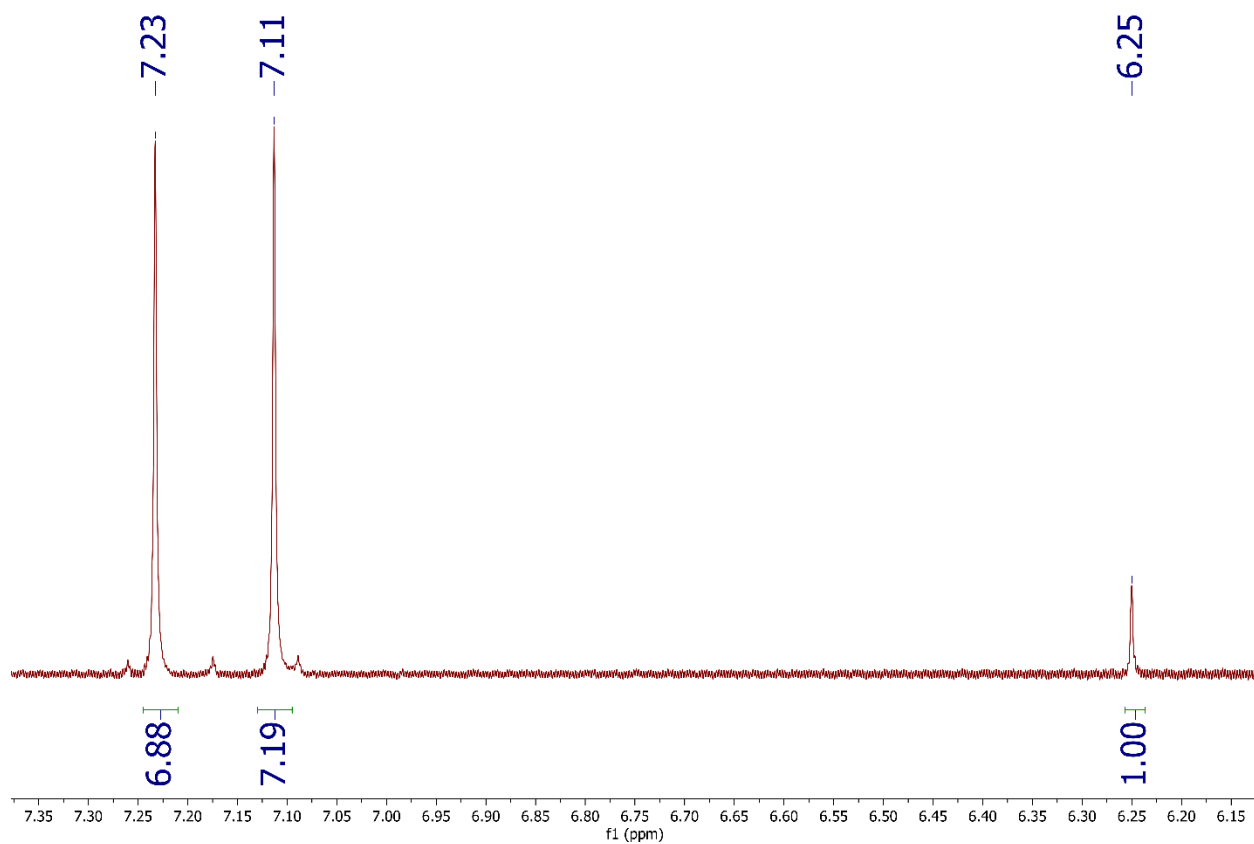


Figure S5.19 Representative $^1\text{H-NMR}$ of the electrolyte solution obtained after a 2-hour controlled potential electrolysis (CPE) at -0.85 V vs RHE and 250 RPM of isotopically labeled NO_3^- on a glassy carbon electrode modified with a p-TPTCrCl₃ film. The electrolysis was conducted in a sealed cell containing 100 mM $\text{Na}^{15}\text{NO}_3$ dissolved in 0.1 M pH 6 phosphate buffer that was sparged with Argon for 30 minutes. The peaks at 7.23 and 7.11 ppm are from $^{15}\text{NH}_3$ and the peak at 6.25 ppm is from the maleic acid internal standard. The small triplet interspaced with the $^{15}\text{NH}_3$ doublet is due the presence of trace amounts of $^{14}\text{NH}_4$.

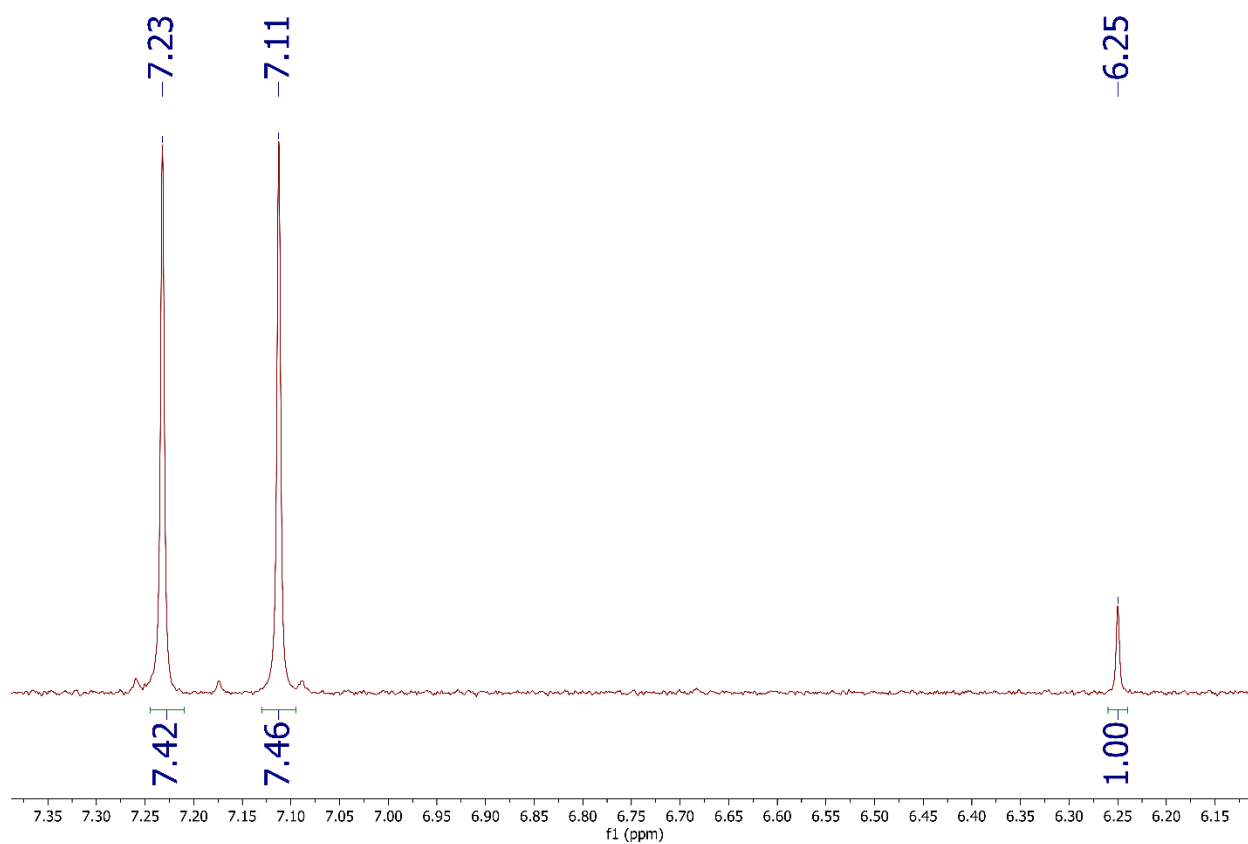


Figure S5.20 Representative $^1\text{H-NMR}$ of the electrolyte solution obtained after a 2-hour controlled potential electrolysis (CPE) at -0.95 V vs RHE and 250 RPM of isotopically labeled NO_3^- on a glassy carbon electrode modified with a p-TPTCrCl₃ film. The electrolysis was conducted in a sealed cell containing 100 mM $\text{Na}^{15}\text{NO}_3$ dissolved in 0.1 M pH 6 phosphate buffer that was sparged with Argon for 30 minutes. The peaks at 7.23 and 7.11 ppm are from $^{15}\text{NH}_3$ and the peak at 6.25 ppm is from the maleic acid internal standard. The small triplet interspaced with the $^{15}\text{NH}_3$ doublet is due the presence of trace amounts of $^{14}\text{NH}_4$.

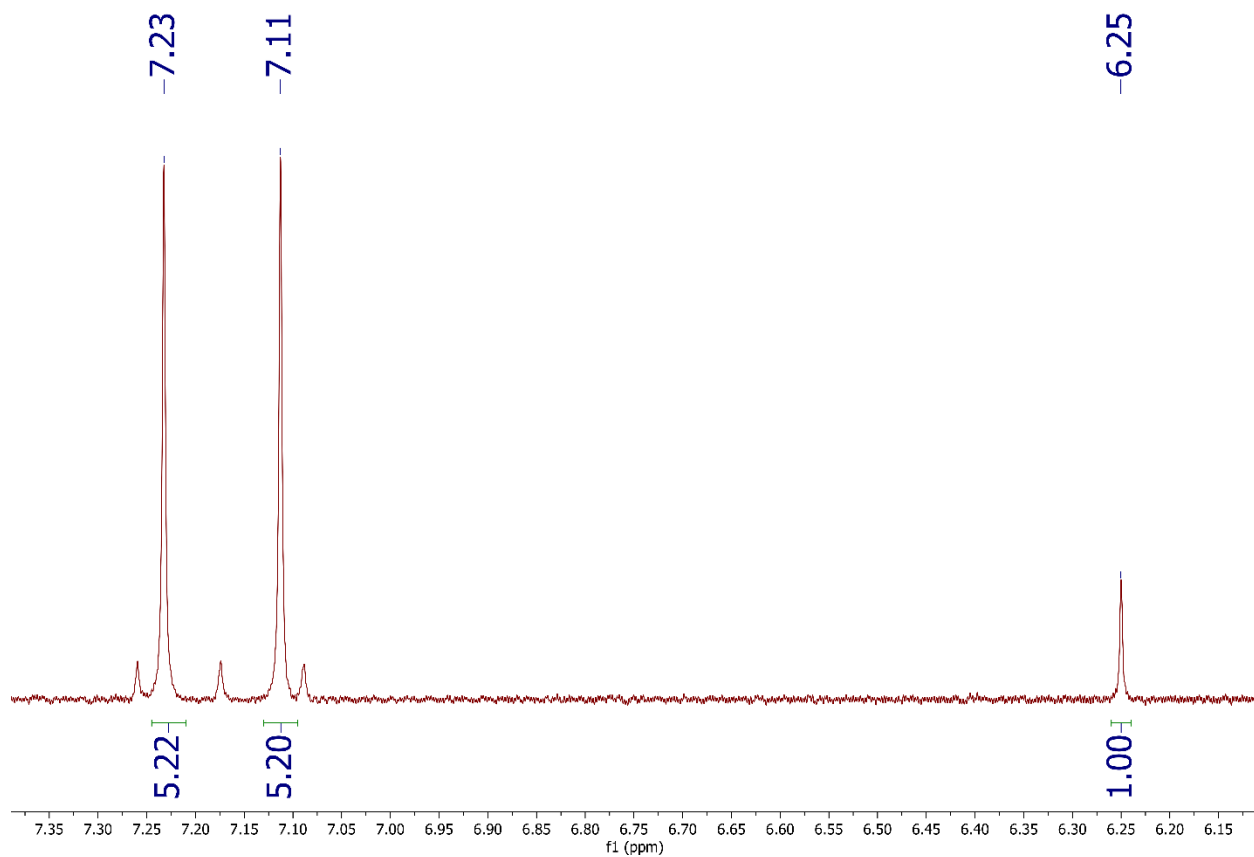


Figure S5.21 Representative $^1\text{H-NMR}$ of the electrolyte solution obtained after a 2-hour controlled potential electrolysis (CPE) at -0.75 V vs RHE and 100 RPM of isotopically labeled NO_3^- on a glassy carbon electrode modified with a p-TPTCrCl₃ film. The electrolysis was conducted in a sealed cell containing 100 mM $\text{Na}^{15}\text{NO}_3$ dissolved in 0.1 M pH 6 phosphate buffer that was sparged with Argon for 30 minutes. The peaks at 7.23 and 7.11 ppm are from $^{15}\text{NH}_3$ and the peak at 6.25 ppm is from the maleic acid internal standard. The small triplet interspaced with the $^{15}\text{NH}_3$ doublet is due the presence of trace amounts of $^{14}\text{NH}_4$.

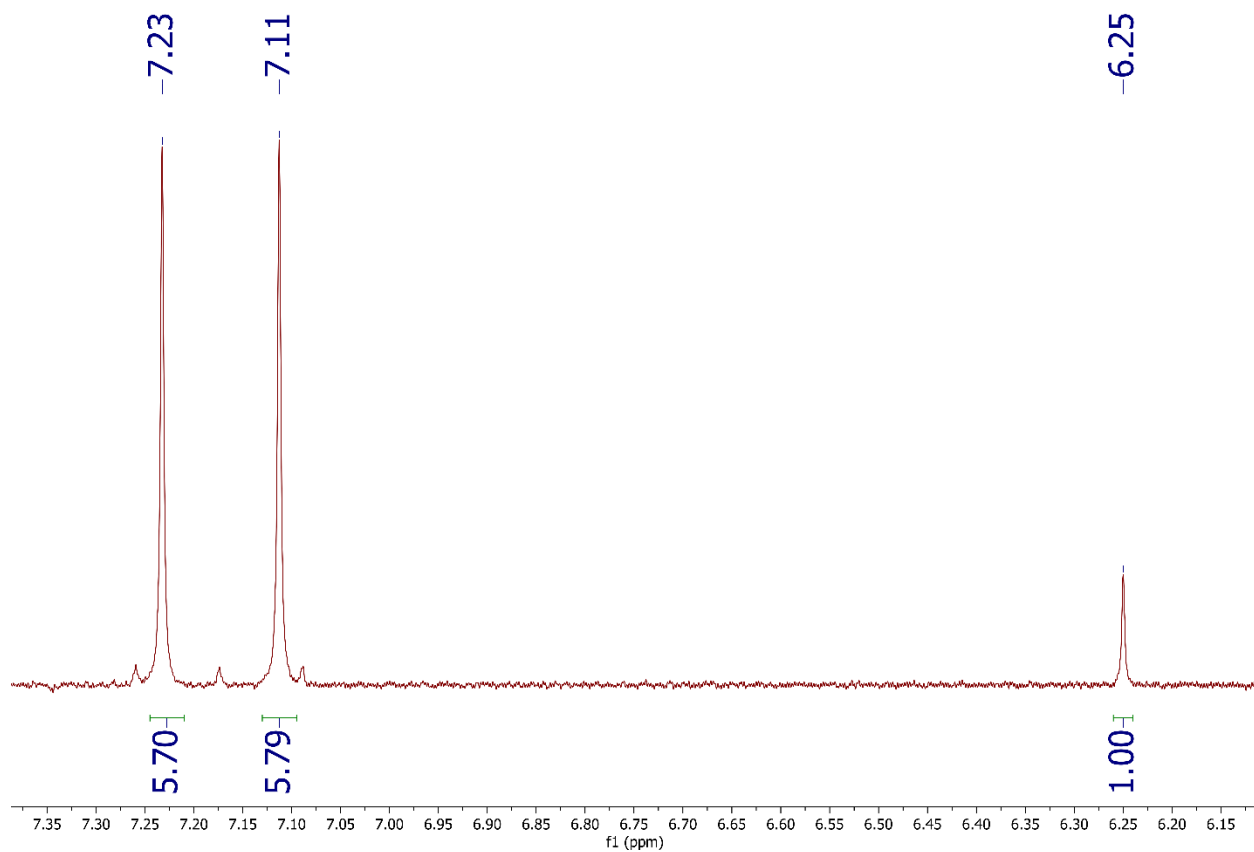


Figure S5.22 Representative $^1\text{H-NMR}$ of the electrolyte solution obtained after a 2-hour controlled potential electrolysis (CPE) at -0.75 V vs RHE and 500 RPM of isotopically labeled NO_3^- on a glassy carbon electrode modified with a p-TPTCrCl₃ film. The electrolysis was conducted in a sealed cell containing 100 mM $\text{Na}^{15}\text{NO}_3$ dissolved in 0.1 M pH 6 phosphate buffer that was sparged with Argon for 30 minutes. The peaks at 7.23 and 7.11 ppm are from $^{15}\text{NH}_3$ and the peak at 6.25 ppm is from the maleic acid internal standard. The small triplet interspaced with the $^{15}\text{NH}_3$ doublet is due the presence of trace amounts of $^{14}\text{NH}_4$.

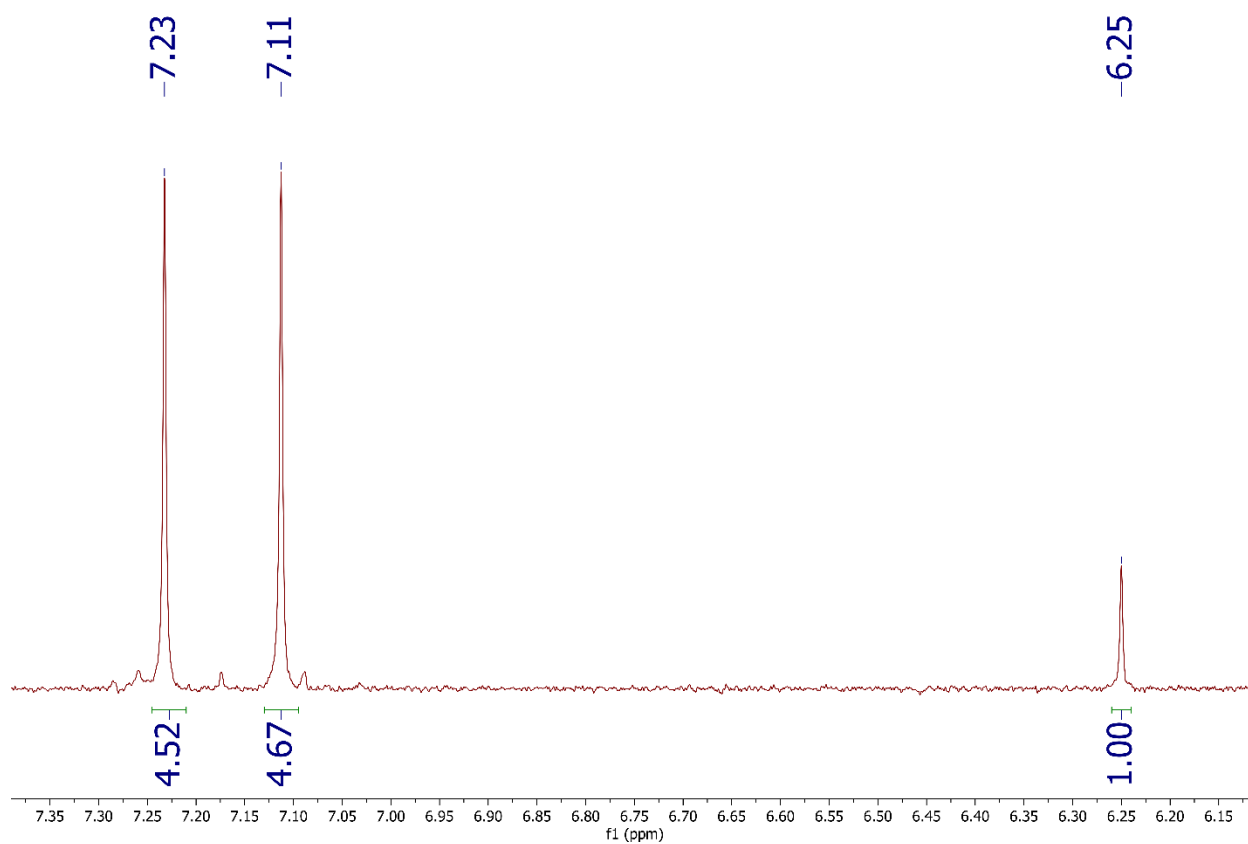


Figure S5.23 Representative $^1\text{H-NMR}$ of the electrolyte solution obtained after a 2-hour controlled potential electrolysis (CPE) at -0.75 V vs RHE and 750 RPM of isotopically labeled NO_3^- on a glassy carbon electrode modified with a p-TPTCrCl₃ film. The electrolysis was conducted in a sealed cell containing 100 mM $\text{Na}^{15}\text{NO}_3$ dissolved in 0.1 M pH 6 phosphate buffer that was sparged with Argon for 30 minutes. The peaks at 7.23 and 7.11 ppm are from $^{15}\text{NH}_3$ and the peak at 6.25 ppm is from the maleic acid internal standard. The small triplet interspaced with the $^{15}\text{NH}_3$ doublet is due the presence of trace amounts of $^{14}\text{NH}_4$.

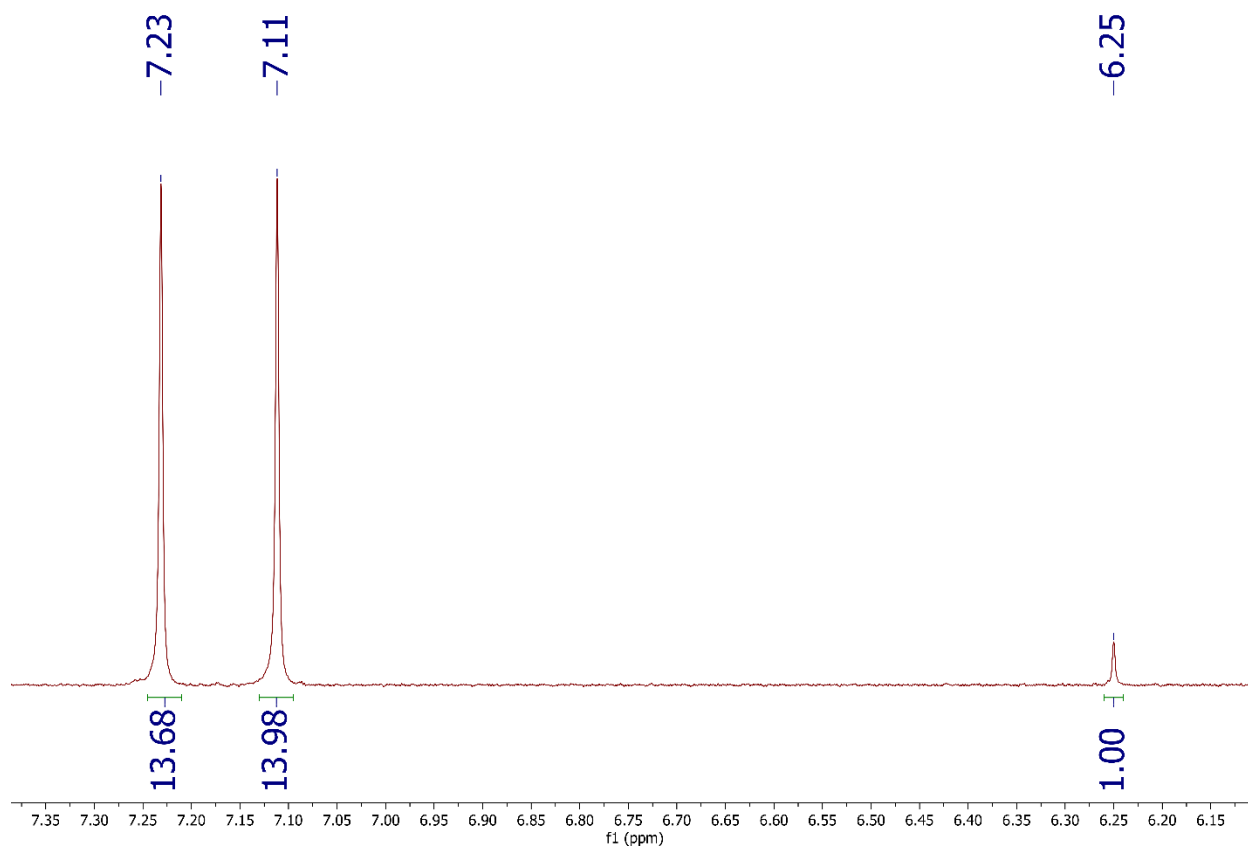


Figure S5.24 Representative $^1\text{H-NMR}$ of the electrolyte solution obtained after a 2-hour controlled potential electrolysis (CPE) at -0.75 V vs RHE and 250 RPM of isotopically labeled NO_2^- on a glassy carbon electrode modified with a p-TPTCrCl₃ film. The electrolysis was conducted in a sealed cell containing 100 mM $\text{Na}^{15}\text{NO}_2$ dissolved in 0.1 M pH 6 phosphate buffer that was sparged with Argon for 30 minutes. The peaks at 7.23 and 7.11 ppm are from $^{15}\text{NH}_3$ and the peak at 6.25 ppm is from the maleic acid internal standard. The small triplet interspaced with the $^{15}\text{NH}_3$ doublet is due the presence of trace amounts of $^{14}\text{NH}_4$.

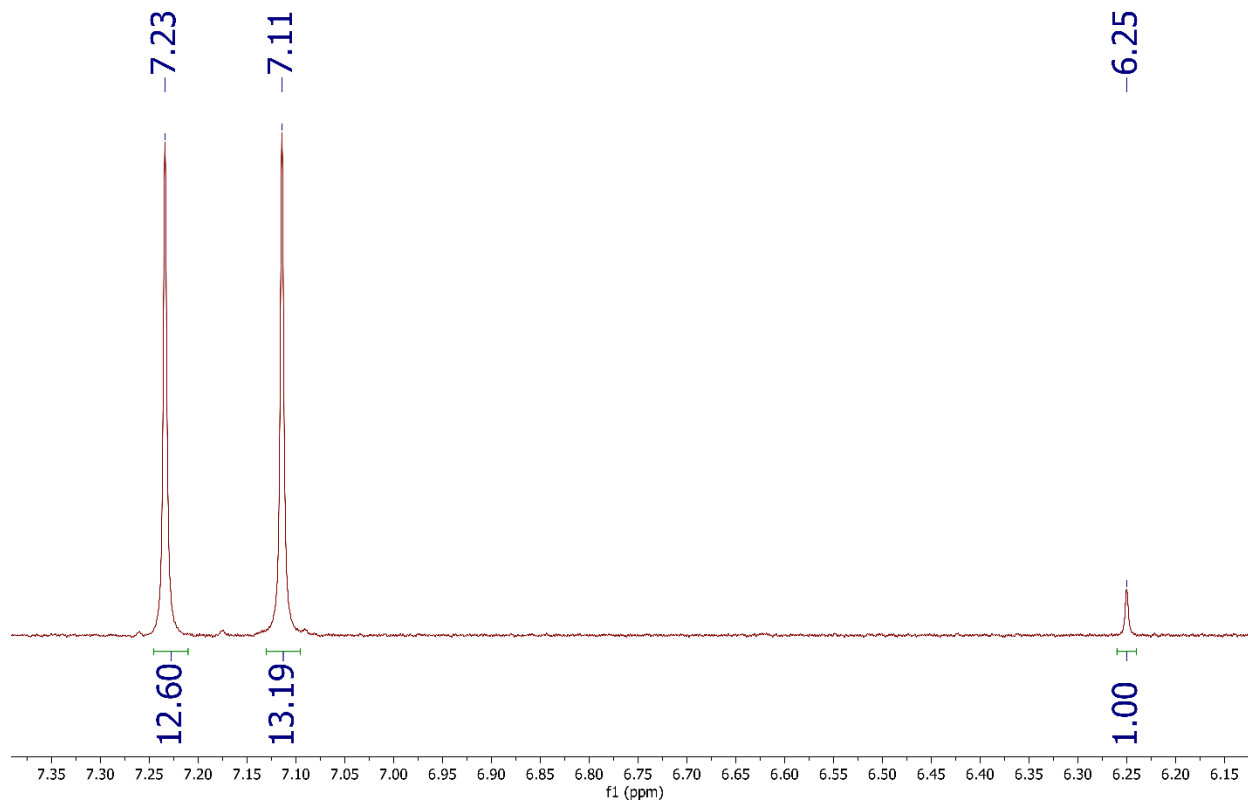


Figure S5.25 Representative $^1\text{H-NMR}$ of an electrolyte solution obtained after a 1-hour controlled potential electrolysis (CPE) at -0.75 V vs RHE and 250 RPM of isotopically labeled $^{15}\text{NH}_2\text{OH}$ on a glassy carbon electrode modified with a p-TPTCrCl₃ film. The electrolysis was conducted in a sealed cell containing 100 mM $\text{Na}^{15}\text{NH}_2\text{OH}\cdot\text{HCl}$ dissolved in 0.1 M pH 6 phosphate buffer that was sparged with Argon for 30 minutes. The resulting electrolyte was diluted 1:4 with 100 mM pH 6 phosphate buffer prior to analysis. The peaks at 7.23 and 7.11 ppm are from $^{15}\text{NH}_3$ and the peak at 6.25 ppm is from the maleic acid internal standard. The small triplet interspaced with the $^{15}\text{NH}_3$ doublet is due the presence of trace amounts of $^{14}\text{NH}_4$.

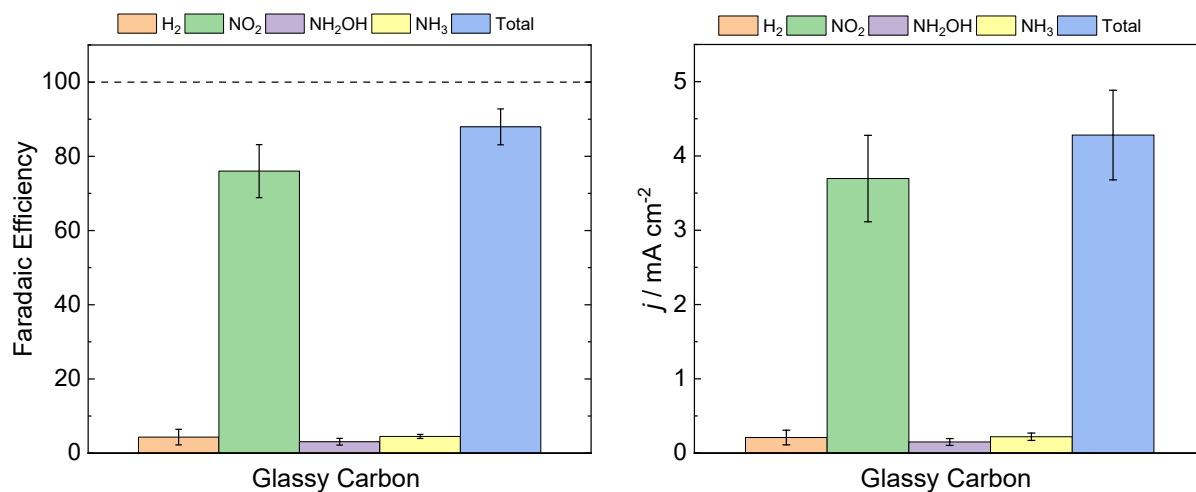


Figure S5.26 Faradaic efficiencies (a) and partial current densities (b) obtained from 2-hour controlled potential electrolyses (CPE) at -0.75 V vs RHE of isotopically labeled NO_3^- on bare glassy carbon electrodes. Electrolyses were conducted in a sealed cell containing 100 mM $\text{Na}^{15}\text{NO}_3$ dissolved in 0.1 M pH 6 phosphate buffer that was sparged with Argon for 30 minutes. All reported values are averages of 3 independently conducted measurements, and all errors are standard deviations.

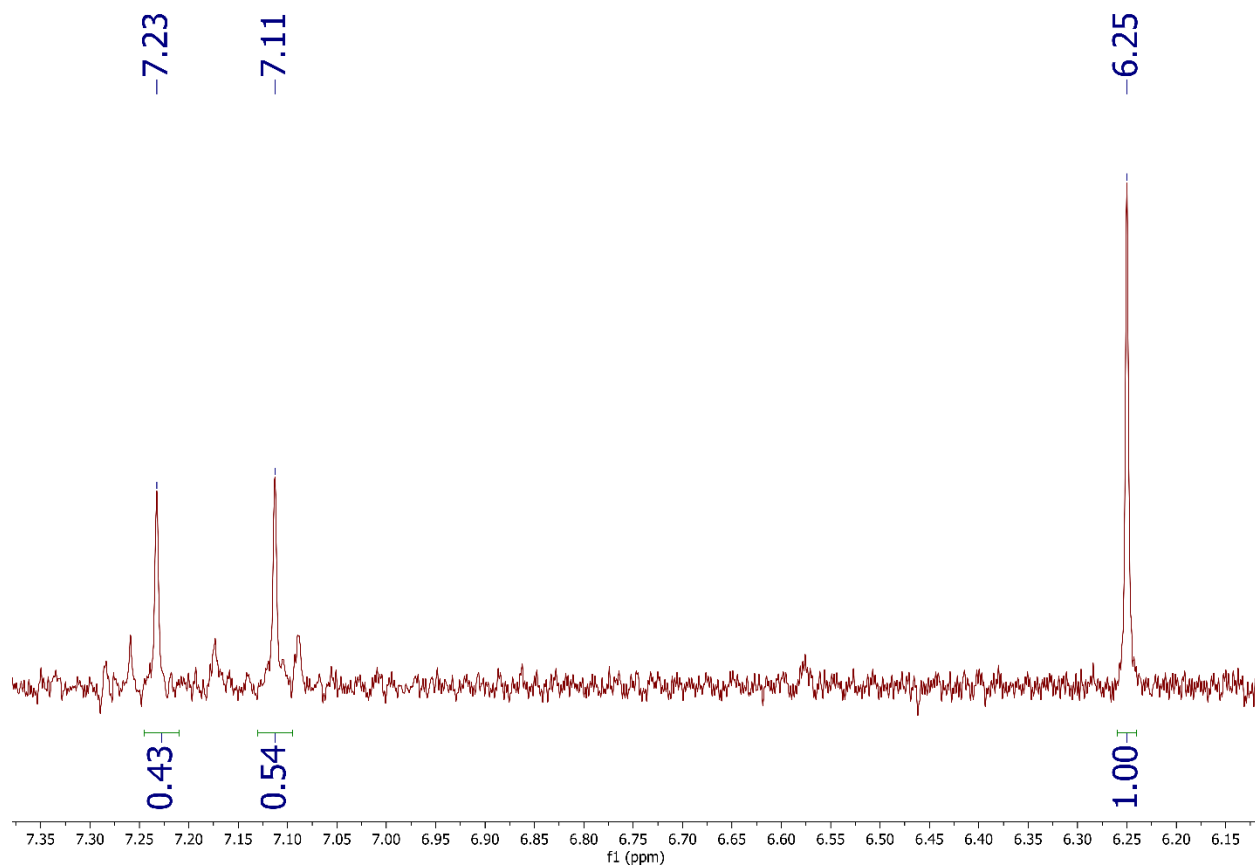


Figure S5.27 Representative $^1\text{H-NMR}$ of the electrolyte solution obtained after a 2-hour controlled potential electrolysis (CPE) at -0.75 V vs RHE and 250 RPM of isotopically labeled NO_3^- on a bare glassy carbon electrode. The electrolysis was conducted in a sealed cell containing $100\text{ mM Na}^{15}\text{NO}_3$ dissolved in 0.1 M pH 6 phosphate buffer that was sparged with Argon for 30 minutes. The peaks at 7.23 and 7.11 ppm are from $^{15}\text{NH}_3$ and the peak at 6.25 ppm is from the maleic acid internal standard. The small triplet interspaced with the $^{15}\text{NH}_3$ doublet is due the presence of trace amounts of $^{14}\text{NH}_4$.

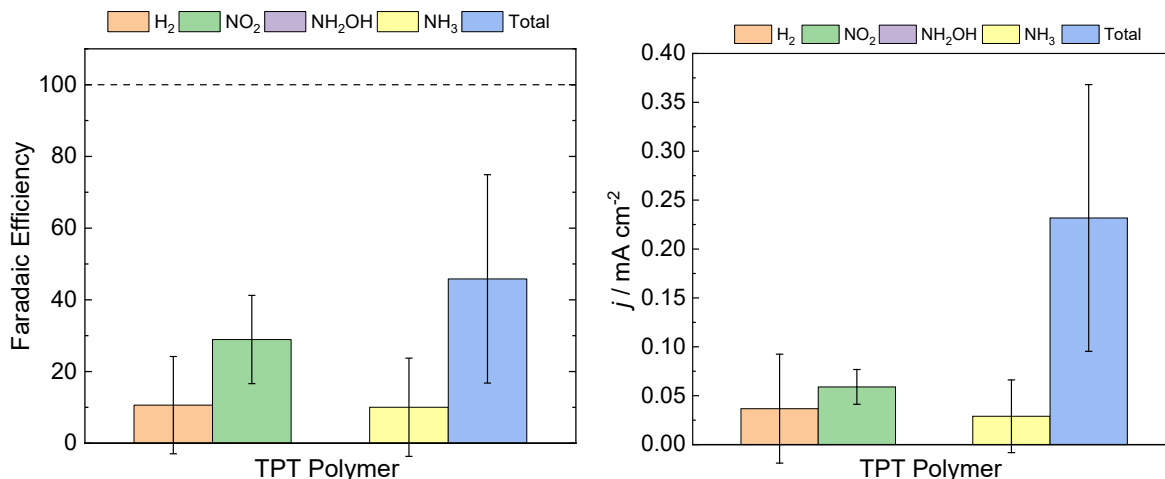


Figure S5.28 Faradaic efficiencies (a) and partial current densities (b) obtained from 2-hour controlled potential electrolyses (CPE) at -0.75 V vs RHE of isotopically labeled NO_3^- on glassy carbon coated with p-TPT (poly-4'-4-([2,2':5',2''-terthiophen]-3'-yl)phenyl)-2,2':6',2''-terpyridine). Electrolyses were conducted in a sealed cell containing $100 \text{ mM Na}^{15}\text{NO}_3$ dissolved in $100 \text{ mM pH } 6$ phosphate buffer that was sparged with Argon for 30 minutes. All reported values are averages of 3 independently conducted measurements, and all errors are standard deviations. The very low currents seen during the electrolysis suggest that the TPT film is not catalytically active.

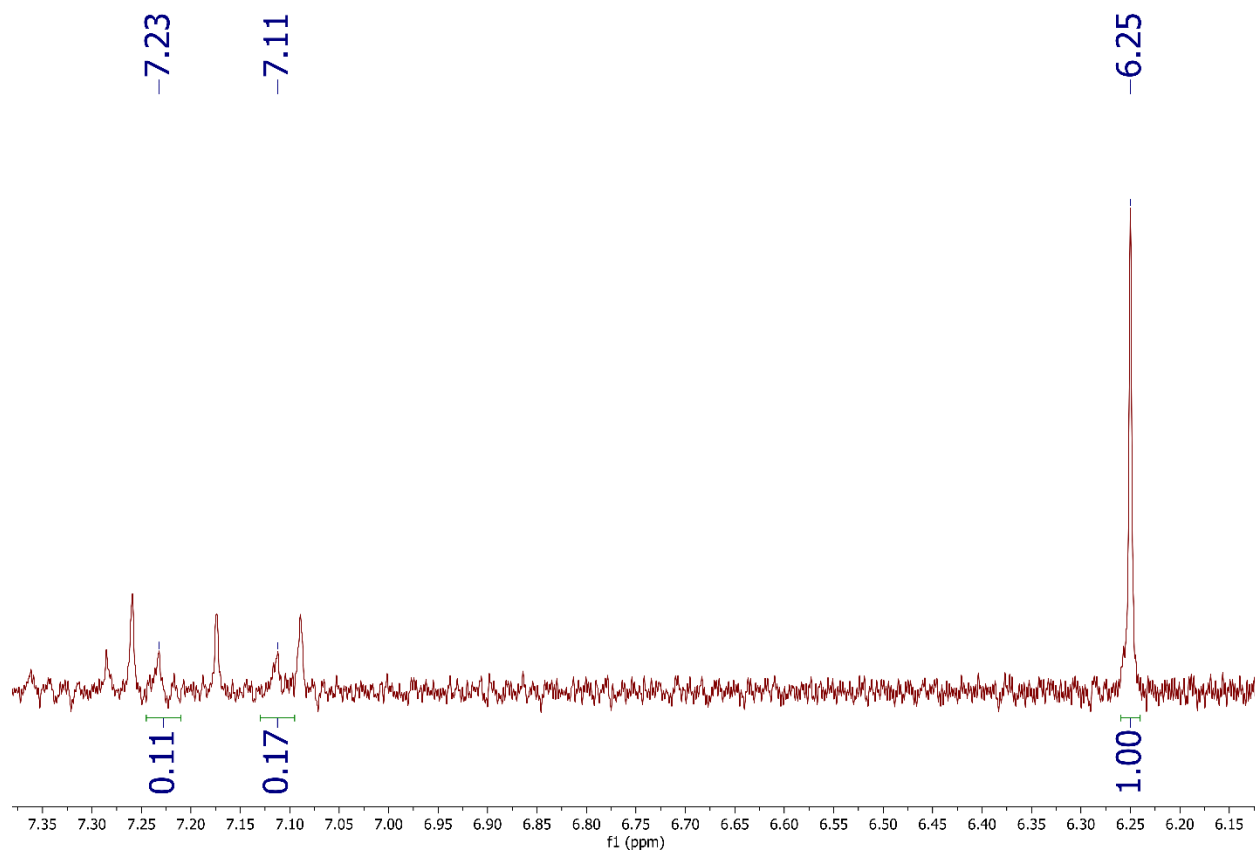


Figure S5.29 Representative $^1\text{H-NMR}$ of an electrolyte solution obtained after a 2-hour controlled potential electrolysis (CPE) at -0.75 V vs RHE and 250 RPM of isotopically labeled $^{15}\text{NO}_3^-$ on a glassy carbon electrode modified with an unmetalled TPT film. The electrolysis was conducted in a sealed cell containing 100 mM $\text{Na}^{15}\text{NO}_3$ dissolved in 0.1 M pH 6 phosphate buffer that was sparged with Argon for 30 minutes. The peaks at 7.23 and 7.11 ppm are from $^{15}\text{NH}_3$ and the peak at 6.25 ppm is from the maleic acid internal standard. The small triplet interspaced with the $^{15}\text{NH}_3$ doublet is due the presence of trace amounts of $^{14}\text{NH}_4$.

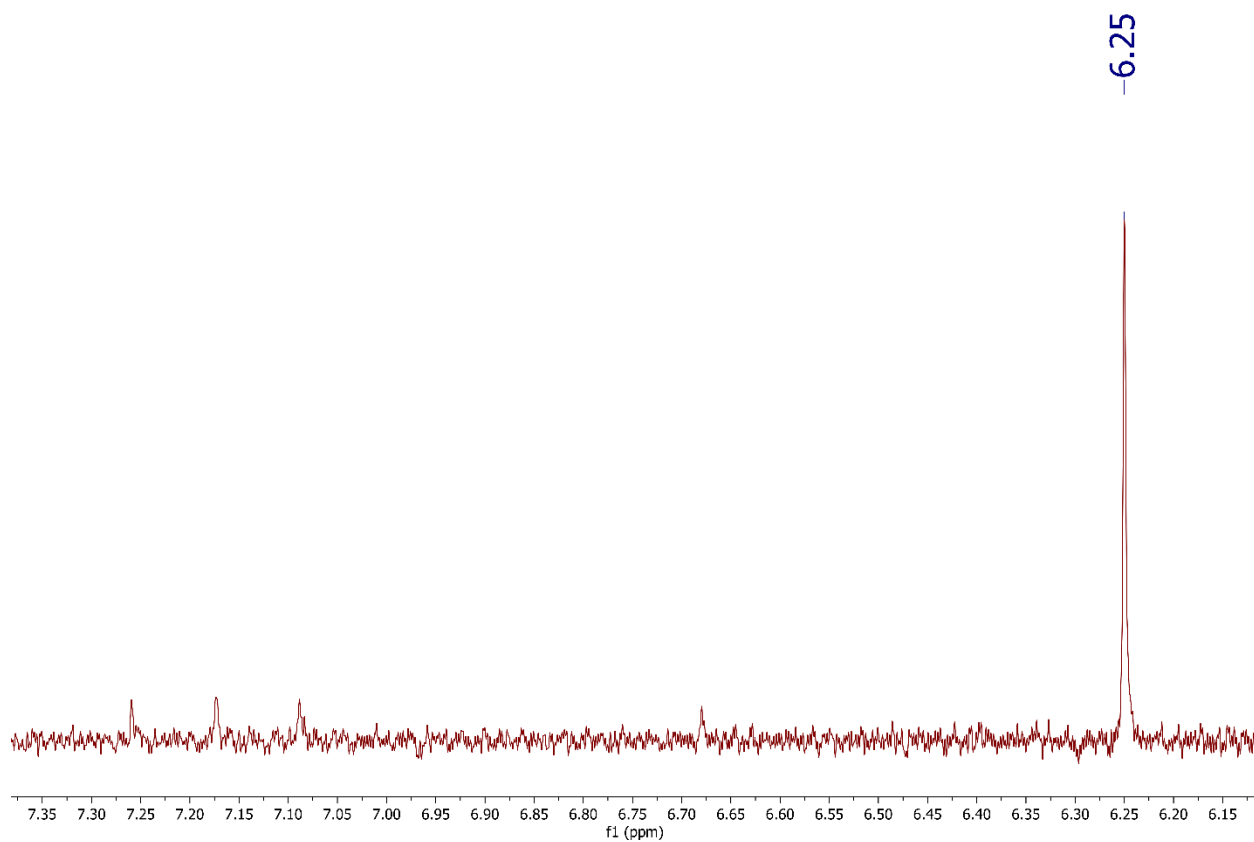


Figure S5.30 Representative $^1\text{H-NMR}$ of the electrolyte solution obtained after a 2-hour controlled potential electrolysis (CPE) at -0.75 V vs RHE and 250 RPM in nitrate-free electrolyte on a glassy carbon electrode modified with a p-TPTCrCl₃ film. The electrolysis was conducted in a sealed cell containing 0.1 M pH 6 phosphate buffer that was sparged with Argon for 30 minutes. No $^{15}\text{NH}_4$ was detected. The small triplet present at $\sim 7.17\text{ ppm}$ is due the presence of trace amounts of $^{14}\text{NH}_4$.

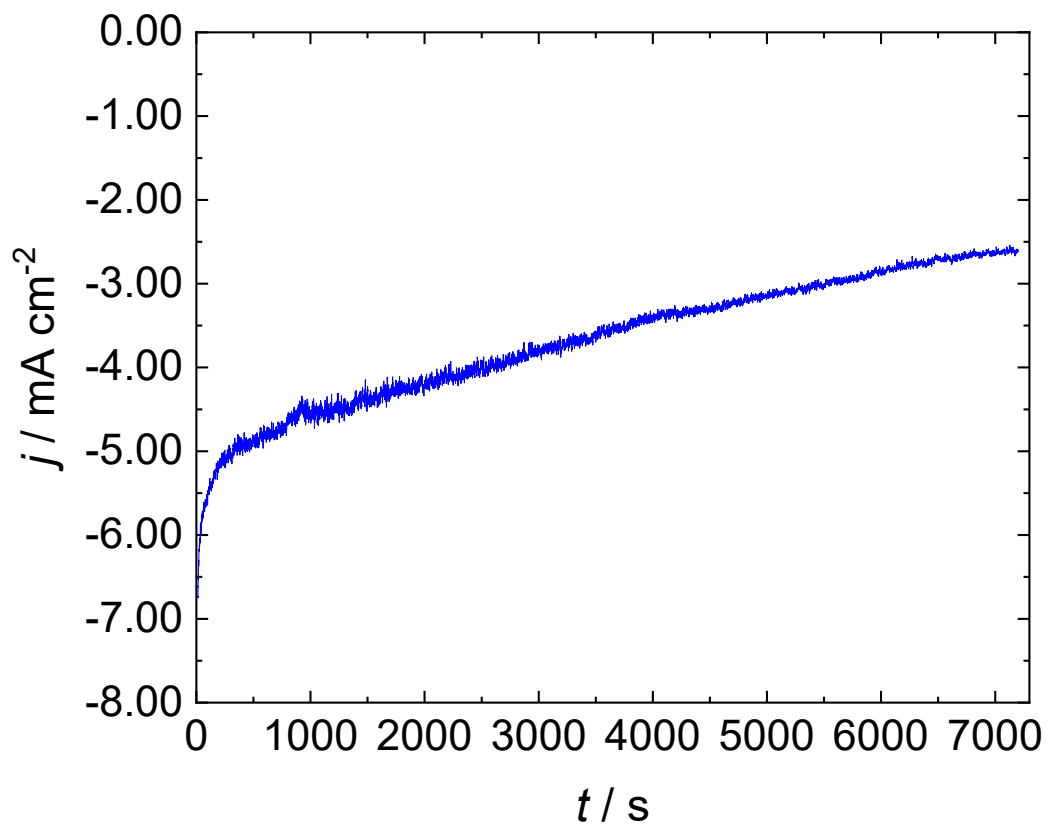


Figure S5.31 Representative current density of a 2-hour controlled potential electrolysis (CPE) at -0.75 V vs RHE and 250 RPM of isotopically labeled NO_3^- on a glassy carbon electrode modified with a p-TPTCrCl₃ film. The electrolysis was conducted in a sealed cell containing 100 mM $\text{Na}^{15}\text{NO}_3$ dissolved in 0.1 M pH 6 phosphate buffer that was sparged with Argon for 30 minutes.

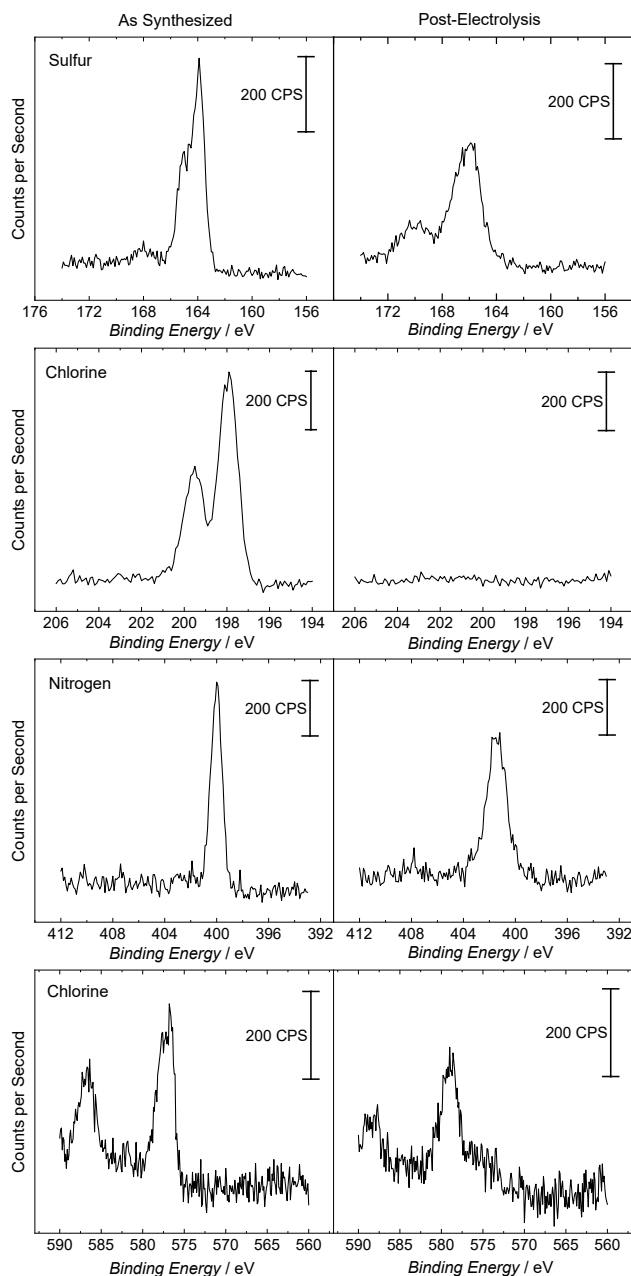


Figure S5.32 Representative XPS of (left) a freshly synthesized p-TPTCrCl₃ film on a glassy carbon electrode and (right) a p-TPTCrCl₃ film on a glassy carbon electrode after a 2-hour controlled-potential electrolysis (CPE) at -0.75 V vs RHE and 250 RPM of isotopically labeled ¹⁵NO₃⁻. The electrolysis was conducted in a sealed cell containing 100 mM Na¹⁵NO₃ dissolved in 0.1 M pH 6 phosphate buffer that was sparged with Argon for 30 minutes. The XPS supports the presence of some degradation over the course of the electrolysis but also demonstrates that a large part of the film remains intact. Additionally, the loss of chlorine is also clearly shown. This suggests that chlorine loss is part of the catalytic cycle and is necessary to free up active sites for NO₃RR.

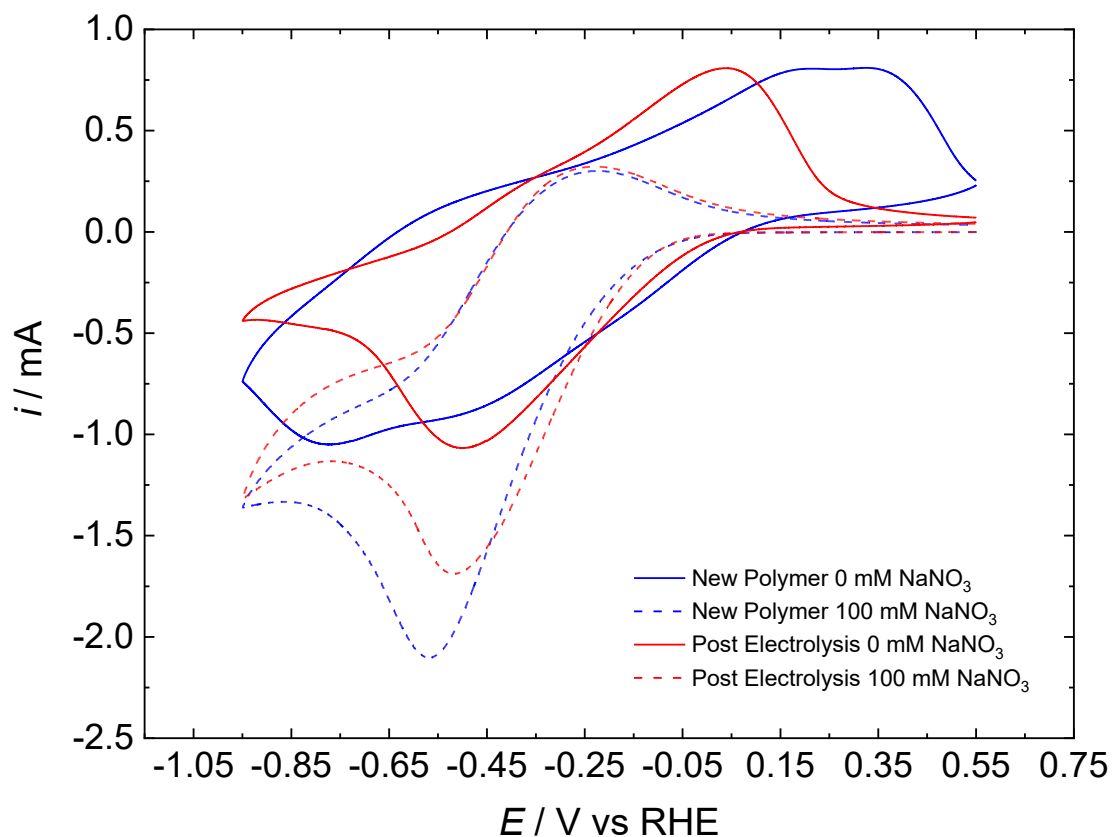


Figure S5.33 Representative data showing the relative stability of the p-TPTCrCl₃ post 2-hour controlled potential electrolysis (CPE) at -0.75 vs RHE in 100 mM pH 6 phosphate buffer containing 100 mM Na¹⁵NO₃. All CVs were conducted in 100 mM pH 6 phosphate buffer that was sparged with N₂ for at least 10 minutes. The blue CVs are of a freshly prepared glassy carbon electrode coated with p-TPTCrCl₃ and the red CVs are of an identically prepared electrode after a CPE. The results suggest that some degradation of the film occurred, but that it was still catalytically active post-electrolysis.

Table S5.5 Activity and Selectivity Measurements of selected State-of-the-Art Solid-State Electrocatalysts for Nitrate Reduction to Ammonia¹

Activity and Selectivity Measurements of selected State-of-the-Art Solid-State Electrocatalysts for Nitrate Reduction to Ammonia¹

<i>Electrode</i>	Maximum FE to NH ₃	Partial Current Density to NH ₃	Maximum NH ₃ Production Reported	Conditions	Reference
<i>^{a,b,c}p-TPTCrCl₃</i>	91%	3 mA cm ⁻² (86% FE)	0.29 mmol mg _{cat} ⁻¹ hr ⁻¹ (0.014 mmol hr ⁻¹ cm ⁻²) (86% FE)	100 mM ¹⁵ NO ₃ ⁻ 100 mM pH 6 Na ₂ PO ₄ -0.75 V vs RHE	This Work
<i>TiO_{2-x}</i>	85%	-	0.045 mmol mg _{cat} ⁻¹ hr ⁻¹	3.6 mM NO ₃ ⁻ 0.5 M Na ₂ SO ₄ -1 V vs RHE	45
<i>TiO₂</i>	66.3%	-	0.024 mmol mg _{cat} ⁻¹ hr ⁻¹	3.6 mM NO ₃ ⁻ 0.5 M Na ₂ SO ₄ -1 V vs RHE	45
<i>Cu/Cu₂O NWAs</i>	95.8%	-	0.2449 mmol h ⁻¹ cm ⁻¹	14.3 mM NO ₃ ⁻ 0.5 M Na ₂ SO ₄ -0.85 V vs RHE	46
<i>^dCopper-nickel alloys</i>	99%	-90 mA cm ⁻²	-	100 mM NO ₃ ⁻ 1M KOH, pH 14, -0.1 V vs RHE	47
<i>^eTi</i>	82%	-22 mA cm ⁻²	-	0.3 M KNO ₃ , 0.1 M HNO ₃ , acidic pH, -1 V vs RHE	48
<i>^eCu-incorporated PTCDA</i>	85.9%	-	0.0256 mmol h ⁻¹ cm ⁻² (77% FE)	36 mM NO ₃ ⁻ , 0.1mM PBS, pH 7, -0.4 V vs RHE	40
<i>^eStrained Ru nanoclusters</i>	~100%	-120 mA cm ⁻²	5.56 mmol mg _{cat} ⁻¹ hr ⁻¹ (1.17 mmol hr ⁻¹ cm ⁻²)	1M NO ₃ ⁻ , 1 M KOH, -0.2 V vs RHE	49
<i>^eFe Single Atom Catalyst</i>	75%	-100 mA cm ⁻² (65% FE)	1.2 mmol mg _{cat} ⁻¹ hr ⁻¹ (0.46 mmol cm ⁻² hr ⁻¹) (65% FE)	0.1 M K ₂ SO ₄ , 0.5 M KNO ₃ -0.85 V vs RHE	50
<i>^eOxide-derived Co</i>	92%	-565 mA cm ⁻²	-	1 M KNO ₃ 1 M KOH -0.8 V vs RHE	51
<i>Cobalt Phosphide Nanoshuttles</i>	94.24%	-	1.1 mmol g _{cat} ⁻¹ hr ⁻¹	0.5 M K ₂ S ₂ O ₄ 0.05 M KNO ₃ -0.5 V vs RHE	52

<i>Au/C</i>	26%	-	0.06 $\mu\text{mol h}^{-1} \text{cm}^{-2}$	0.5 M K_2SO_4 0.001 M KNO_3 -0.3 V vs RHE	53
<i>Cu nanosheets</i>	99.7%	5 mA cm^{-2}	0.023 $\text{mmol h}^{-1} \text{mg}_{\text{cat}}^{-1}$	0.1 M KOH 0.01 M KNO_3 -0.15 V vs RHE	54
<i>Co₃O₄@NiO bifunctional electrodes</i>	54.97	-	0.007 $\text{mmol mg}_{\text{cat}}^{-1} \text{h}^{-1}$	0.5M Na_2SO_4 0.89 M NaNO_3 -0.7 V vs RHE	55
<i>Pothole-rich Cu nanosheets</i>	82%	-	0.046 $\text{mmol mg}_{\text{cat}}^{-1} \text{h}^{-1}$	0.5 M K_2SO_4 0.5 mM KNO_3 -0.64 V vs RHE	56
<i>Ultrathin CoO_x Nanosheets</i>	93.4%	-	4.8 $\text{mmol mg}_{\text{cat}}^{-1} \text{h}^{-1}$	0.1 M KOH 0.1 M KNO_3 -0.3 V vs RHE	57
<i>BCN encapsulated Cu nanoparticles</i>	88.9 %	-	0.58 $\text{mmol mg}_{\text{cat}}^{-1} \text{h}^{-1}$	0.1 M KOH 0.1 M KNO_3 -0.6 V vs RHE	58
<i>Indium in sulfur-doped graphene</i>	75%	-	0.22 $\text{mmol mg}_{\text{cat}}^{-1} \text{h}^{-1}$	1 M KOH 0.1 M KNO_3 -0.5 V vs RHE	59
<i>Nickel Phosphide</i>	99.23%	-	0.056 $\text{mmol mg}_{\text{cat}}^{-1} \text{h}^{-1}$	0.5 M Na_2SO_4 1.3 mM NO_3^- -0.38 vs RHE	60

^a All experiments carried out with ¹⁵N labeled substrate, ^b Surface coverage determined from CV peak area (See Experimental), ^c Activity normalized to geometric electrode surface area, ^d Activity normalized to experimentally determined ECSA

5.8 References

1. van Langevelde, P. H.; Katsounaros, I.; Koper, M. T. M., Electrocatalytic Nitrate Reduction for Sustainable Ammonia Production. *Joule* **2021**, 5 (2), 290-294.
2. Mulholland, P. J.; Helton, A. M.; Poole, G. C.; Hall, R. O.; Hamilton, S. K.; Peterson, B. J.; Tank, J. L.; Ashkenas, L. R.; Cooper, L. W.; Dahm, C. N.; Dodds, W. K.; Findlay, S. E. G.; Gregory, S. V.; Grimm, N. B.; Johnson, S. L.; McDowell, W. H.; Meyer, J. L.; Valett, H. M.; Webster, J. R.; Arango, C. P.; Beaulieu, J. J.; Bernot, M. J.; Burgin, A. J.; Crenshaw, C. L.; Johnson, L. T.; Niederlehner, B. R.; O'Brien, J. M.; Potter, J. D.; Sheibley, R. W.; Sobota, D. J.; Thomas, S. M., Stream denitrification across biomes and its response to anthropogenic nitrate loading. *Nature* **2008**, 452 (7184), 202-205.
3. Canfield, D. E.; Glazer, A. N.; Falkowski, P. G., The Evolution and Future of Earth's Nitrogen Cycle. *Science* **2010**, 330 (6001), 192-196.
4. Sebilo, M.; Mayer, B.; Nicolardot, B.; Pinay, G.; Mariotti, A., Long-term fate of nitrate fertilizer in agricultural soils. *Proceedings of the National Academy of Sciences of the United States of America* **2013**, 110 (45), 18185-18189.
5. Gu, B.; Chang, J.; Min, Y.; Ge, Y.; Zhu, Q.; Galloway, J. N.; Peng, C., The role of industrial nitrogen in the global nitrogen biogeochemical cycle. *Scientific Reports* **2013**, 3 (1), 2579.
6. Katsounaros, I.; Dortsiou, M.; Kyriacou, G., Electrochemical reduction of nitrate and nitrite in simulated liquid nuclear wastes. *Journal of Hazardous Materials* **2009**, 171 (1), 323-327.
7. Breitburg, D.; Levin, L. A.; Oschlies, A.; Grégoire, M.; Chavez, F. P.; Conley, D. J.; Garçon, V.; Gilbert, D.; Gutiérrez, D.; Isensee, K.; Jacinto, G. S.; Limburg, K. E.; Montes, I.; Naqvi, S. W. A.; Pitcher, G. C.; Rabalais, N. N.; Roman, M. R.; Rose, K. A.; Seibel, B. A.; Telszewski, M.; Yasuhara, M.; Zhang, J., Declining oxygen in the global ocean and coastal waters. *Science* **2018**, 359 (6371), eaam7240.
8. Diaz, R. J.; Rosenberg, R., Spreading Dead Zones and Consequences for Marine Ecosystems. *Science* **2008**, 321 (5891), 926-929.
9. Carpenter, S. R., Eutrophication of aquatic ecosystems: Bistability and soil phosphorus. *Proceedings of the National Academy of Sciences of the United States of America* **2005**, 102 (29), 10002.
10. Li, C.; Narayanan, V.; Harriss, R. C., Model estimates of nitrous oxide emissions from agricultural lands in the United States. *Global Biogeochemical Cycles* **1996**, 10 (2), 297-306.
11. Beaulieu, J. J.; Tank, J. L.; Hamilton, S. K.; Wollheim, W. M.; Hall, R. O.; Mulholland, P. J.; Peterson, B. J.; Ashkenas, L. R.; Cooper, L. W.; Dahm, C. N.; Dodds, W. K.; Grimm, N. B.; Johnson, S. L.; McDowell, W. H.; Poole, G. C.; Valett, H. M.; Arango, C. P.; Bernot, M. J.; Burgin, A. J.; Crenshaw, C. L.; Helton, A. M.; Johnson, L. T.; O'Brien, J. M.; Potter, J. D.; Sheibley, R. W.; Sobota, D. J.; Thomas, S. M., Nitrous oxide emission from denitrification in stream and river networks. *Proceedings of the National Academy of Sciences* **2011**, 108 (1), 214-219.
12. Dore, J. E.; Popp, B. N.; Karl, D. M.; Sansone, F. J., A large source of atmospheric nitrous oxide from subtropical North Pacific surface waters. *Nature* **1998**, 396 (6706), 63-66.
13. Ward Mary, H.; deKok Theo, M.; Levallois, P.; Brender, J.; Gulis, G.; Nolan Bernard, T.; VanDerslice, J., Workgroup Report: Drinking-Water Nitrate and Health—Recent Findings and Research Needs. *Environmental Health Perspectives* **2005**, 113 (11), 1607-1614.

14. Kapoor, A.; Viraraghavan, T., Nitrate Removal From Drinking Water—Review. *Journal of Environmental Engineering* **1997**, *123* (4), 371-380.
15. Mohseni-Bandpi, A.; Elliott, D. J.; Zazouli, M. A., Biological nitrate removal processes from drinking water supply—a review. *Journal of Environmental Health Science and Engineering* **2013**, *11* (1), 35.
16. Ghafari, S.; Hasan, M.; Aroua, M. K., Bio-electrochemical removal of nitrate from water and wastewater—A review. *Bioresource Technology* **2008**, *99* (10), 3965-3974.
17. Duca, M.; Koper, M. T. M., Powering denitrification: the perspectives of electrocatalytic nitrate reduction. *Energy & Environmental Science* **2012**, *5* (12), 9726-9742.
18. Singh, N.; Goldsmith, B. R., Role of Electrocatalysis in the Remediation of Water Pollutants. *ACS Catalysis* **2020**, *10* (5), 3365-3371.
19. Garcia-Segura, S.; Lanzarini-Lopes, M.; Hristovski, K.; Westerhoff, P., Electrocatalytic reduction of nitrate: Fundamentals to full-scale water treatment applications. *Applied Catalysis B: Environmental* **2018**, *236*, 546-568.
20. Wang, Y.; Wang, C.; Li, M.; Yu, Y.; Zhang, B., Nitrate electroreduction: mechanism insight, in situ characterization, performance evaluation, and challenges. *Chemical Society Reviews* **2021**, *50* (12), 6720-6733.
21. Greenlee, L. F., Recycling fertilizer. *Nature Energy* **2020**, *5* (8), 557-558.
22. Bertero, M. G.; Rothery, R. A.; Palak, M.; Hou, C.; Lim, D.; Blasco, F.; Weiner, J. H.; Strynadka, N. C. J., Insights into the respiratory electron transfer pathway from the structure of nitrate reductase A. *Nature Structural & Molecular Biology* **2003**, *10* (9), 681-687.
23. Elliott, S. J.; Hoke, K. R.; Heffron, K.; Palak, M.; Rothery, R. A.; Weiner, J. H.; Armstrong, F. A., Voltammetric Studies of the Catalytic Mechanism of the Respiratory Nitrate Reductase from *Escherichia coli*: How Nitrate Reduction and Inhibition Depend on the Oxidation State of the Active Site. *Biochemistry* **2004**, *43* (3), 799-807.
24. Hille, R., The Mononuclear Molybdenum Enzymes. *Chemical Reviews* **1996**, *96* (7), 2757-2816.
25. Kepp, K. P., A Quantitative Scale of Oxophilicity and Thiophilicity. *Inorganic Chemistry* **2016**, *55* (18), 9461-9470.
26. Liu, Y.; Leung, K. Y.; Michaud, S. E.; Soucy, T. L.; McCrory, C. C. L., Controlled Substrate Transport To Electrocatalyst Active Sites For Enhanced Selectivity In The Carbon Dioxide Reduction Reaction. *Comments Inorg. Chem.* **2019**, 1-28.
27. Kramer, W. W.; McCrory, C. C. L., Polymer coordination promotes selective CO₂ reduction by cobalt phthalocyanine. *Chem. Sci.* **2016**, *7* (4), 2506-2515.
28. Liu, Y.; McCrory, C. C. L., Modulating the mechanism of electrocatalytic CO₂ reduction by cobalt phthalocyanine through polymer coordination and encapsulation. *Nat. Commun.* **2019**, *10* (1), 1683.
29. Manca, P.; Pilo, M. I.; Casu, G.; Gladiali, S.; Sanna, G.; Scanu, R.; Spano, N.; Zucca, A.; Zanardi, C.; Bagnis, D.; Valentini, L., A new terpyridine tethered polythiophene: Electrosynthesis and characterization. *Journal of Polymer Science Part A: Polymer Chemistry* **2011**, *49* (16), 3513-3523.
30. McCrory, C. C. L.; Jung, S.; Kallick, J., Chapter 5 Evaluating Electrocatalysts for Solar Water-splitting Reactions. In *Integrated Solar Fuel Generators*, The Royal Society of Chemistry: 2019; pp 154-181.
31. Bard, A. J.; Faulkner, L. R., *Electrochemical Methods: Fundamentals and Applications*, 2nd Edition. John Wiley & Sons, Incorporated: 2000.

32. Zotti, G.; Gallazzi, M. C.; Zerbi, G.; Meille, S. V., Conducting polymers from anodic coupling of some regiochemically defined dialkoxy-substituted thiophene oligomers. *Synthetic Metals* **1995**, *73* (3), 217-225.
33. Marrec, P.; Fabre, B.; Simonet, J., Electrochemical and spectroscopic properties of new functionalized polythiophenes electroformed from the oxidation of dithienyls linked by long chain polyether spacers. *Journal of Electroanalytical Chemistry* **1997**, *437* (1), 245-253.
34. Kallick, J. D.; Feng, W.-J.; McCrory, C. C. L., Controlled Formation of Multilayer Films of Discrete Molecular Catalysts for the Oxygen Reduction Reaction Using a Layer-by-Layer Growth Mechanism Based on Sequential Click Chemistry. *ACS Applied Energy Materials* **2020**, *3* (7), 6222-6231.
35. Hanifpour, F.; Sveinbjörnsson, A.; Canales, C. P.; Skúlason, E.; Flosadóttir, H. D., Preparation of Nafion Membranes for Reproducible Ammonia Quantification in Nitrogen Reduction Reaction Experiments. *Angewandte Chemie International Edition* **2020**, *59* (51), 22938-22942.
36. Hodgetts, R. Y.; Kiryutin, A. S.; Nichols, P.; Du, H.-L.; Bakker, J. M.; Macfarlane, D. R.; Simonov, A. N., Refining Universal Procedures for Ammonium Quantification via Rapid 1H NMR Analysis for Dinitrogen Reduction Studies. *ACS Energy Letters* **2020**, *5* (3), 736-741.
37. Manca, P.; Scanu, R.; Zucca, A.; Sanna, G.; Spano, N.; Pilo, M. I., Electropolymerization of a Ru(II)-terpyridine complex ethynyl-terthiophene functionalized originating different metallopolymers. *Polymer* **2013**, *54* (14), 3504-3509.
38. Andersen, S. Z.; Čolić, V.; Yang, S.; Schwalbe, J. A.; Nielander, A. C.; McEnaney, J. M.; Enemark-Rasmussen, K.; Baker, J. G.; Singh, A. R.; Rohr, B. A.; Statt, M. J.; Blair, S. J.; Mezzavilla, S.; Kibsgaard, J.; Vesborg, P. C. K.; Cargnello, M.; Bent, S. F.; Jaramillo, T. F.; Stephens, I. E. L.; Nørskov, J. K.; Chorkendorff, I., A rigorous electrochemical ammonia synthesis protocol with quantitative isotope measurements. *Nature* **2019**, *570* (7762), 504-508.
39. Qing, G.; Ghazfar, R.; Jackowski, S. T.; Habibzadeh, F.; Ashtiani, M. M.; Chen, C.-P.; Smith, M. R.; Hamann, T. W., Recent Advances and Challenges of Electrocatalytic N₂ Reduction to Ammonia. *Chemical Reviews* **2020**, *120* (12), 5437-5516.
40. Chen, G.-F.; Yuan, Y.; Jiang, H.; Ren, S.-Y.; Ding, L.-X.; Ma, L.; Wu, T.; Lu, J.; Wang, H., Electrochemical reduction of nitrate to ammonia via direct eight-electron transfer using a copper–molecular solid catalyst. *Nature Energy* **2020**, *5* (8), 605-613.
41. Stamler, J. S.; Feelisch, M., *Methods in nitric oxide research*. J. Wiley: New York, 1996; p xix, 712 p.
42. Wu, Y.; Jiang, Z.; Lin, Z.; Liang, Y.; Wang, H., Direct electrosynthesis of methylamine from carbon dioxide and nitrate. *Nature Sustainability* **2021**, *4* (8), 725-730.
43. Feelisch, M.; Stamler, J., *Methods in nitric oxide research*. J. Wiley: New York :, 1996; Vol. New York :
44. Wang, Q.; Wei, C.; Pérez, L. M.; Rogers, W. J.; Hall, M. B.; Mannan, M. S., Thermal Decomposition Pathways of Hydroxylamine: Theoretical Investigation on the Initial Steps. *The Journal of Physical Chemistry A* **2010**, *114* (34), 9262-9269.
45. Jia, R.; Wang, Y.; Wang, C.; Ling, Y.; Yu, Y.; Zhang, B., Boosting Selective Nitrate Electroreduction to Ammonium by Constructing Oxygen Vacancies in TiO₂. *ACS Catalysis* **2020**, *10* (6), 3533-3540.
46. Wang, Y.; Zhou, W.; Jia, R.; Yu, Y.; Zhang, B., Unveiling the Activity Origin of a Copper-based Electrocatalyst for Selective Nitrate Reduction to Ammonia. *Angewandte Chemie International Edition* **2020**, *59* (13), 5350-5354.

47. Wang, Y.; Xu, A.; Wang, Z.; Huang, L.; Li, J.; Li, F.; Wicks, J.; Luo, M.; Nam, D.-H.; Tan, C.-S.; Ding, Y.; Wu, J.; Lum, Y.; Dinh, C.-T.; Sinton, D.; Zheng, G.; Sargent, E. H., Enhanced Nitrate-to-Ammonia Activity on Copper–Nickel Alloys via Tuning of Intermediate Adsorption. *Journal of the American Chemical Society* **2020**, *142* (12), 5702-5708.
48. McEnaney, J. M.; Blair, S. J.; Nieland, A. C.; Schwalbe, J. A.; Koshy, D. M.; Cargnello, M.; Jaramillo, T. F., Electrolyte Engineering for Efficient Electrochemical Nitrate Reduction to Ammonia on a Titanium Electrode. *ACS Sustainable Chemistry & Engineering* **2020**, *8* (7), 2672-2681.
49. Li, J.; Zhan, G.; Yang, J.; Quan, F.; Mao, C.; Liu, Y.; Wang, B.; Lei, F.; Li, L.; Chan, A. W. M.; Xu, L.; Shi, Y.; Du, Y.; Hao, W.; Wong, P. K.; Wang, J.; Dou, S.-X.; Zhang, L.; Yu, J. C., Efficient Ammonia Electrosynthesis from Nitrate on Strained Ruthenium Nanoclusters. *Journal of the American Chemical Society* **2020**, *142* (15), 7036-7046.
50. Wu, Z.-Y.; Karamad, M.; Yong, X.; Huang, Q.; Cullen, D. A.; Zhu, P.; Xia, C.; Xiao, Q.; Shakouri, M.; Chen, F.-Y.; Kim, J. Y.; Xia, Y.; Heck, K.; Hu, Y.; Wong, M. S.; Li, Q.; Gates, I.; Siahrostami, S.; Wang, H., Electrochemical ammonia synthesis via nitrate reduction on Fe single atom catalyst. *Nature Communications* **2021**, *12* (1), 2870.
51. Kani, N. C.; Gauthier, J. A.; Prajapati, A.; Edgington, J.; Bordawekar, I.; Shields, W.; Shields, M.; Seitz, L. C.; Singh, A. R.; Singh, M. R., Solar-driven electrochemical synthesis of ammonia using nitrate with 11% solar-to-fuel efficiency at ambient conditions. *Energy & Environmental Science* **2021**.
52. Jia, Y.; Ji, Y.-G.; Xue, Q.; Li, F.-M.; Zhao, G.-T.; Jin, P.-J.; Li, S.-N.; Chen, Y., Efficient Nitrate-to-Ammonia Electroreduction at Cobalt Phosphide Nanoshuttles. *ACS Applied Materials & Interfaces* **2021**, *13* (38), 45521-45527.
53. Choi, J.; Du, H.-L.; Nguyen, C. K.; Suryanto, B. H. R.; Simonov, A. N.; MacFarlane, D. R., Electroreduction of Nitrates, Nitrites, and Gaseous Nitrogen Oxides: A Potential Source of Ammonia in Dinitrogen Reduction Studies. *ACS Energy Letters* **2020**, *5* (6), 2095-2097.
54. Fu, X.; Zhao, X.; Hu, X.; He, K.; Yu, Y.; Li, T.; Tu, Q.; Qian, X.; Yue, Q.; Wasielewski, M. R.; Kang, Y., Alternative route for electrochemical ammonia synthesis by reduction of nitrate on copper nanosheets. *Applied Materials Today* **2020**, *19*, 100620.
55. Wang, Y.; Liu, C.; Zhang, B.; Yu, Y., Self-template synthesis of hierarchically structured Co₃O₄@NiO bifunctional electrodes for selective nitrate reduction and tetrahydroisoquinolines semi-dehydrogenation. *Science China Materials* **2020**, *63* (12), 2530-2538.
56. Xu, Y.; Wang, M.; Ren, K.; Ren, T.; Liu, M.; Wang, Z.; Li, X.; Wang, L.; Wang, H., Atomic defects in pothole-rich two-dimensional copper nanoplates triggering enhanced electrocatalytic selective nitrate-to-ammonia transformation. *Journal of Materials Chemistry A* **2021**, *9* (30), 16411-16417.
57. Wang, J.; Cai, C.; Wang, Y.; Yang, X.; Wu, D.; Zhu, Y.; Li, M.; Gu, M.; Shao, M., Electrocatalytic Reduction of Nitrate to Ammonia on Low-Cost Ultrathin CoO_x Nanosheets. *ACS Catalysis* **2021**, 15135-15140.
58. Zhao, X.; Hu, G.; Tan, F.; Zhang, S.; Wang, X.; Hu, X.; Kuklin, A. V.; Baryshnikov, G. V.; Ågren, H.; Zhou, X.; Zhang, H., Copper confined in vesicle-like BCN cavities promotes electrochemical reduction of nitrate to ammonia in water. *Journal of Materials Chemistry A* **2021**, *9* (41), 23675-23686.

59. Lei, F.; Xu, W.; Yu, J.; Li, K.; Xie, J.; Hao, P.; Cui, G.; Tang, B., Electrochemical synthesis of ammonia by nitrate reduction on indium incorporated in sulfur doped graphene. *Chemical Engineering Journal* **2021**, *426*, 131317.
60. Yao, Q.; Chen, J.; Xiao, S.; Zhang, Y.; Zhou, X., Selective Electrocatalytic Reduction of Nitrate to Ammonia with Nickel Phosphide. *ACS Applied Materials & Interfaces* **2021**, *13* (26), 30458-30467.

Chapter 6 Conclusions and Future Directions

6.1 Introduction

The work in this thesis focuses on heterogenization of molecular electrocatalysts for small-molecule transformations. In **Chapter 1** we discussed some of the many methods for attaching molecular electrocatalysts to surfaces along with some of the benefits and limitations of the process. In **Chapter 2** we discussed some of the methods used in in this Thesis to analyze both the modified surface and any products produced during experimentation. **Chapter 3** focused on using multilayer films formed through the CuAAC “click” reaction to overcome the surface coverage limitation of heterogenization of molecular catalysts. By adding multiple layers of catalyst we could increase the catalyst loading resulting in a system that operated with the specificity and tunability of molecular catalysts and the activity of solid-state catalysts. Our results were partially successful. We were able to form double layer films of copper phenanthroline that operated with a higher activity than the mono layer films of the same. However, we were unable to produce triple layer films due to steric inhibition from the double layer. **Chapter 4** discusses our work on attaching TEMPO complexes to glassy carbon electrodes using the same technique as Chapter 1. TEMPO is a known molecular electrocatalyst for alcohol oxidation and we planned to use the TEMPO modified electrode for that reaction. Unfortunately, while we were able to successfully attach several TEMPO complexes to glassy carbon electrodes, we found that the TEMPO complexes rapidly decomposed under oxidative

conditions. While the system cannot be used for alcohol oxidation at this stage, it does demonstrate very clearly one of the drawbacks of molecular systems: stability. Finally, in **Chapter 5** we explored using electropolymerization of terthiophene as a method for surface modification with molecular electrocatalysts. By attaching a terthiophene moiety to a terpyridine chromium molecular electrocatalyst we were able to form conductive films on an electrode surface that were catalytically active for the selective reduction of nitrate to ammonia. While our control over the film is more limited this method results in much higher loadings than the previously click method. As one of the first examples of a molecular system capable of this reaction and one of the most active examples of a polythiophene based system this work opens up whole new avenues to explore.

6.2 Next Steps for NO₃RR by TPTCrCl₃ Films

While there are several different directions that this work could go, I think that further efforts should initially focus on gaining a deeper understanding of the polymer itself. The main reason for this is that as discussed in Chapter 5, notable degradation of the TPTCrCl₃ film occurs during electrolyses and we currently do not have a good understanding of why. Initial experiments suggest that the degradation appears to be attenuated by larger substrate concentrations and some preliminary XPS results on this subject can be seen in Figure 6.1. While XPS cannot give quantitative decomposition results (See Chapter 2) the changes in the peaks can give insight into the polymer degradation. The largest attenuation to the XPS peaks occurs when there is no substrate present, when the applied potential is more negative than -0.75 V vs RHE, or more positive than the onset potential of about -0.65 V vs RHE. This suggests that if the potential is too positive for substrate reduction or there is no substrate present the film decomposes more rapidly. Our current hypothesis is that when the film is reduced without the

presence of substrate (or when the applied potential is only negative enough to reduce to film but not catalyze the reduction of substrate) the charge within the polymer ends up degrading the film. However, when enough substrate is present the charge is more likely to go towards competitive substrate reduction instead. Additionally, applying a potential that is too negative also results in increased degradation. This may be due to the applied potential itself, or because the kinetic limit of the catalyst is too slow to keep up with the applied potential resulting in more charge going towards competitive film degradation.

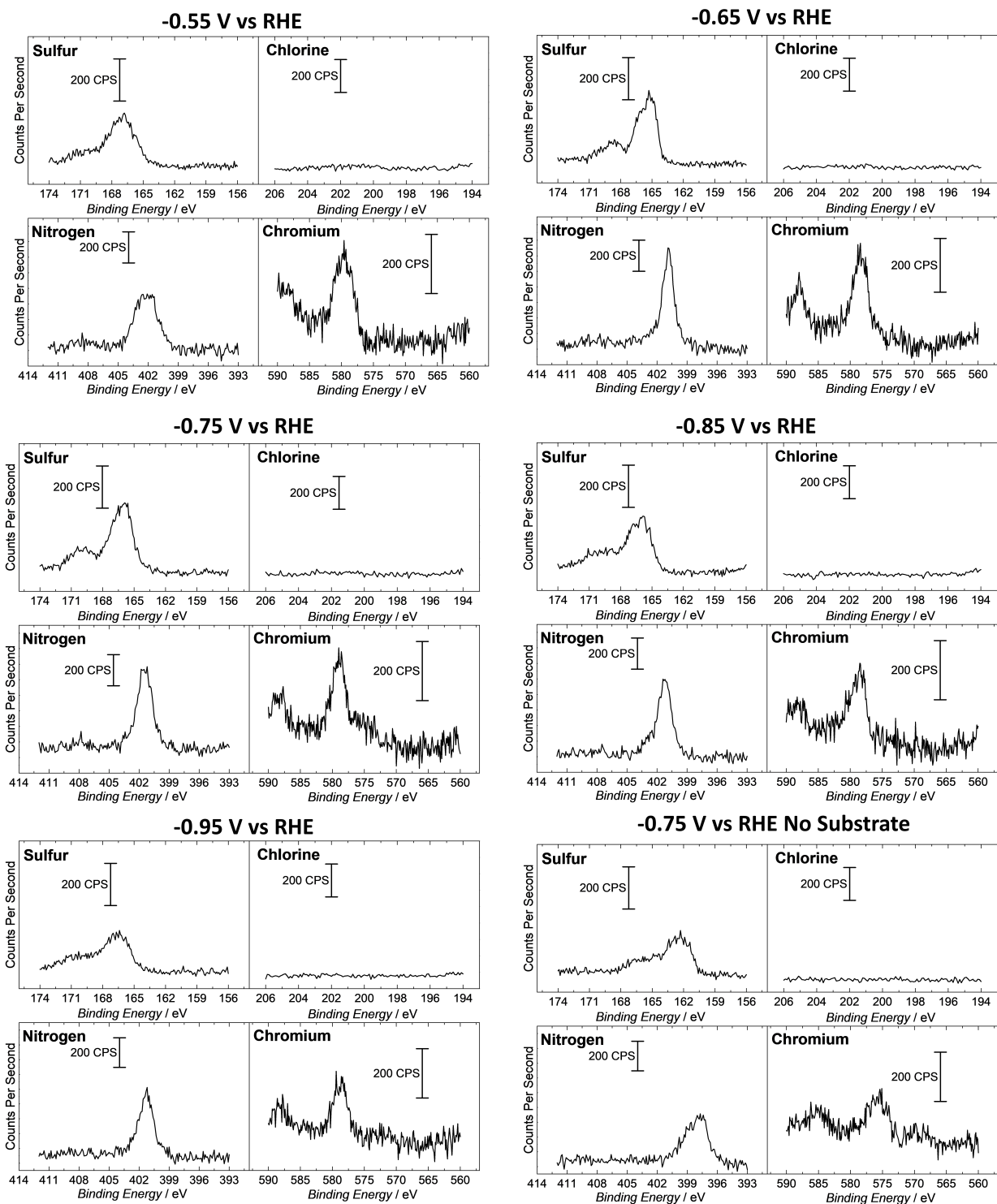


Figure 6.1 Representative XPS of p-TPTCrCl₃ films on a glassy carbon electrode post-electrolysis under varying applied potentials and substrate concentration. All controlled-potential electrolyses (CPE) were conducted for 2-hours with a stir rate of 250 RPM in a sealed cell with 0.1 M pH 6 phosphate buffer that was sparged with Argon for 30 minutes. The substrate was 100 mM Na¹⁵NO₃ unless otherwise noted. XPS of a freshly prepared film is also included for comparison.

First steps for elucidating the degradation method should start by investigating if it is the catalyst, the thiophene backbone, or both that are degrading. The first step should be to run a series of electrolyses similar to those in Chapter 5 with unmetalated p-TPT films and compare the XPS as synthesized and post-electrolysis. If degradation of the film is apparent it suggests that the backbone is degrading. A second set of electrolysis should also be run with the TPT film metalated with a redox inactive metal such as zinc. This should be relatively easy to synthesize as terpyridine zinc dichloride is already a known compound. This would be useful data as it not only helps to determine whether the presence of the chromium has any effect on the degradation process but is also further confirmation that chromium is necessary for the NO₃RR. Within this set of investigations it is also important to see if the conductivity of the backbone has any effect on the activity and stability of the film. It may be the case that the conductivity of the film is not necessary for activity but does contribute to the degradation. In order to test for this a terpyridine monomer modified with a vinyl group should be synthesized. A simple path would be to slightly modify the synthesis used to create compound 2 ((4-([2,2':6',2''-terpyridin]-4'-yl)phenyl)boronic acid) from Chapter 5 by replacing the 4-formylphenyl boronic acid with the commercially available 1-(4-vinylphenyl)ethenone (Figure 6.2). After metalation with chromium trichloride this monomer should be capable of electropolymerization similar to the electropolymerization previously reported by Abrūna et al.^{1,2} The resulting film should also be non-conductive and by comparing the activity, selectivity, and stability to the conductive thiophene film a great deal of insight could be gained. In particular, the results should help determine the comparative benefits and drawbacks of each method and which method will result in the most active and stable film. In this vein, a series of electrolyses with different film thicknesses for both the conductive and non-conductive films should be ran and the TOFs for each calculated. The work by Abrūna et al

suggested that non-conductive films result in a lower TOF with a larger film thickness due to sluggish electron transport through the films.² The results from the thickness dependence experiments described above could help determine if the lower TOF was due to solely electron transport or if substrate or ion transport through the film plays a role as well as those effects should be present for both the conductive and non-conductive films

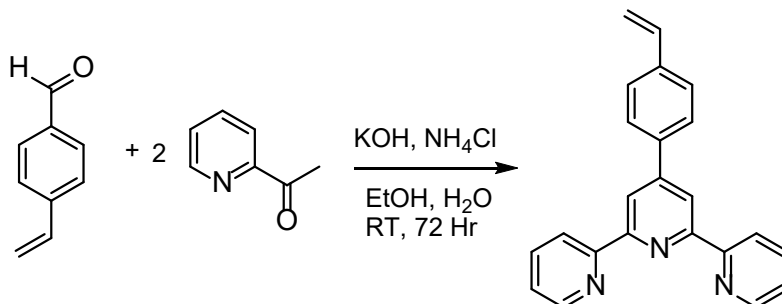


Figure 6.2 Proposed synthetic scheme for 4'-(4-vinylphenyl)-2,2':6',2''-terpyridine

One last topic of interest in the initial experiments should be to determine if the encapsulation of the catalyst within a polymer is beneficial towards the activity and selectivity. An ideal method for comparison would be to run electrolyses with the monomer dissolved in the electrolyte. Unfortunately the solubility of chromium terpyridine trichloride and the TPTCrCl₃ monomer in aqueous solution is negligible. However, by modifying a terpyridine with solvating groups such as sulfonyl moieties or replacing the chlorides with triflates it may be possible to synthesize a more water-soluble monomer. If this is successful, then electrolyses should be run using the dissolved complex. These results would help illuminate the effects of the polymer encapsulation. In addition, post-mortem analysis by XPS and SEM/EDX could be used to test for catalyst decomposition on the surface which would help elucidate the stability of the monomer.

Taken together these experiments should give a well-rounded understanding of the system which could be used for the polymerization of other molecular electrocatalysts.

Finally, while these should wait until the system is further investigated, there are also engineering considerations. These includes things such as setting up the system for larger-scale electrolyses using a flow cell and improving the surface coverage through polymerization onto high surface area materials such as nano-structured surfaces or carbon foams. There should be some focus on how to use the system for real-world applications such as nutrient reclamation from nuclear wastewater and agricultural run-off but these studies should be held off until after system optimization.

6.3 Alternative Catalyst Systems

During my time in graduate school I have also worked on several other catalytic systems that show promise for small-molecule transformations. The first of which is a ruthenium bipyridine (Figure 6.3) covalently attached to a glassy carbon electrode using similar methodology as those used in both Chapter 2 and Chapter 3. XPS of the surface post modification shows a nitrogen to ruthenium ratio of 5.3:1 very close to the expected value of 5:1 (Figure 6.4). Cyclic voltammograms of the modified electrode in nitrogen and carbon dioxide suggest that it is active for CO₂RR (Figure 6.5). The Kubiak group have also shown that a similar ruthenium complex is also active for CO₂RR when heterogenized³ providing further evidence that this avenue of research may be worth exploring.

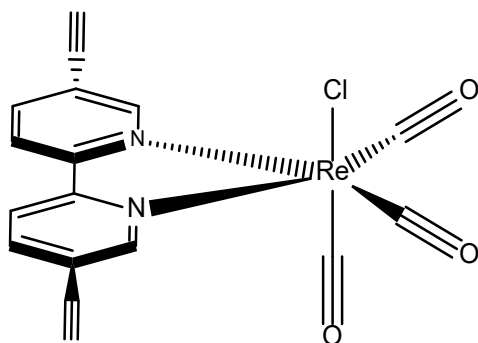


Figure 6.3 Rhenium Bipyridine Complex

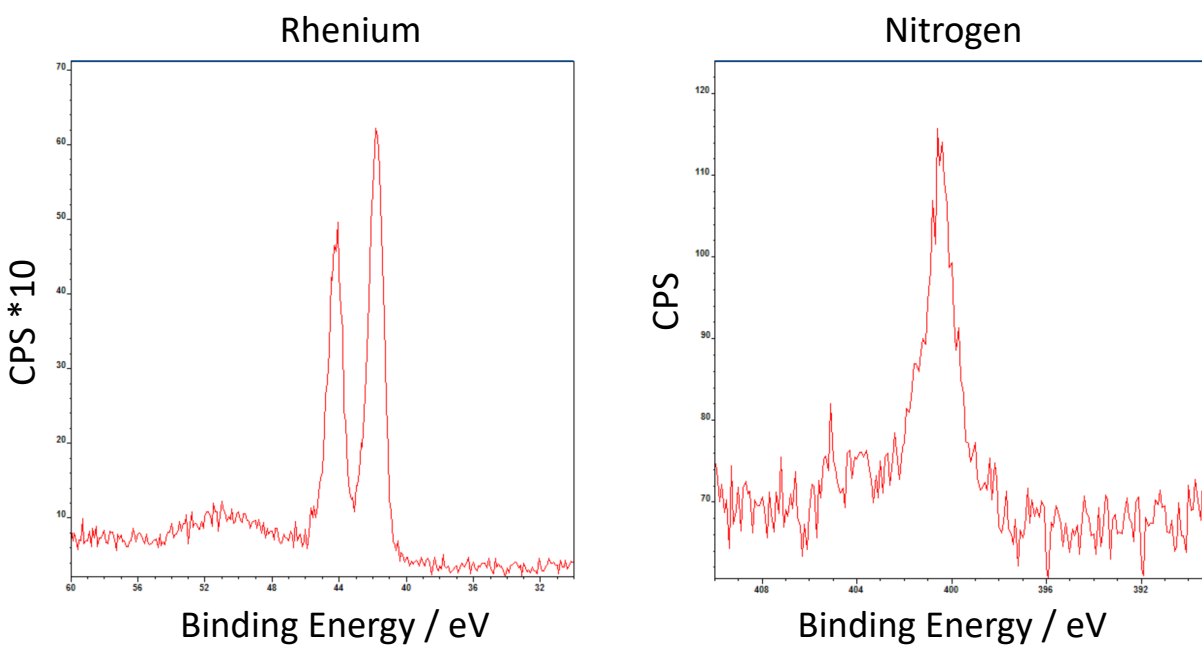


Figure 6.4 Representative XPS of a glassy carbon electrode covalently modified with a diethynyl rhenium bipyridine complex

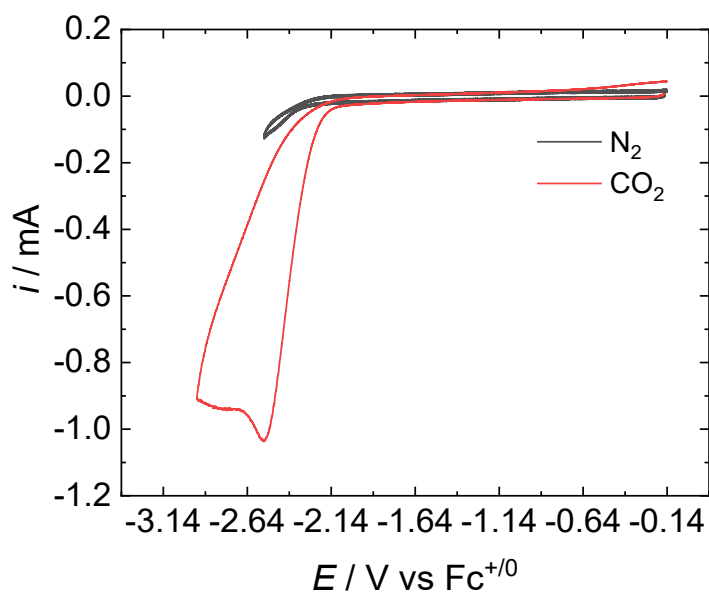


Figure 6.5 Representative Cyclic Voltammogram of a glassy carbon electrode covalently modified with a rhenium diethynylbipyridine complex. The electrolyte is 100 mM tetrabutylammonium hexafluorophosphate in acetonitrile with 5% H₂O added as a proton source.

I also found that while the TPTCrCl₃ system was not capable of CO₂ reduction, other chromium terpyridine systems may be more active. In particular, bis-chromium terpyridine appears to be much more active for the reaction. However, it has limited solubility in aqueous solutions. One of the other main projects in our lab is the encapsulation of cobalt phthalocyanine complexes in poly-4-vinylpyridine for CO₂ reduction. I found that by replacing the cobalt phenanthroline with a bis-chromium terpyridine complex I was able to create a system that also appeared capable of CO₂RR (Figure 6.6). What is particularly interesting about this is that electropolymerized films of chromium terpyridine have been reported to be capable of the electrochemical reduction of CO₂ to formaldehyde.² Further exploration into this project should explore the possibility that this system is capable of that same transformation.

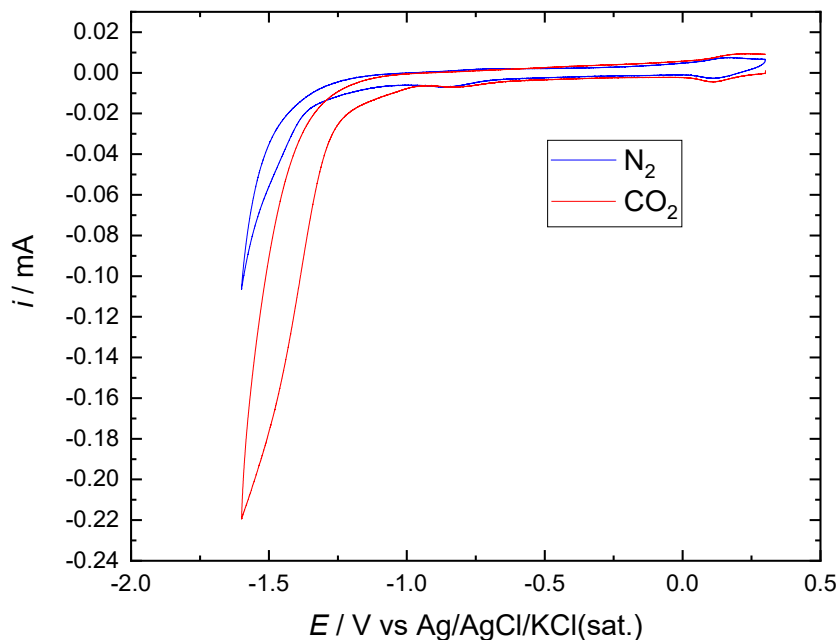


Figure 6.6 Representative Cyclic Voltammogram of bis-chromium terpyridine PF₆ complex encapsulated in poly-4-vinylpyridine and dropcast onto a glassy carbon electrode. The electrolyte is 0.1 M pH 7 phosphate buffer sparged with either N₂ or CO₂ for 10 minutes.

6.4 References

1. Potts, K. T.; Usifer, D. A.; Guadalupe, A.; Abruna, H. D., 4-Vinyl-, 6-vinyl-, and 4'-vinyl-2,2':6',2''-terpyridinyl ligands: their synthesis and the electrochemistry of their transition-metal coordination complexes. *Journal of the American Chemical Society* **1987**, *109* (13), 3961-3967.
2. Ramos Sende, J. A.; Arana, C. R.; Hernandez, L.; Potts, K. T.; Keshevarz-K, M.; Abruna, H. D., Electrocatalysis of CO₂ Reduction in Aqueous Media at Electrodes Modified with Electropolymerized Films of Vinylterpyridine Complexes of Transition Metals. *Inorganic Chemistry* **1995**, *34* (12), 3339-3348.
3. Zhanaidarova, A.; Ostericher, A. L.; Miller, C. J.; Jones, S. C.; Kubiak, C. P., Selective Reduction of CO₂ to CO by a Molecular Re(ethynyl-bpy)(CO)₃Cl Catalyst and Attachment to Carbon Electrode Surfaces. *Organometallics* **2019**, *38* (6), 1204-1207.